

# **Kinetic and Affinity Analysis of Hybridization Reactions Between PNA Probes and DNA Targets Using Surface Plasmon Field-Enhanced Fluorescence Spectroscopy (SPFS)**

Dissertation zur Erlangung des Grades  
‘Doktor der Naturwissenschaft’

am Fachbereich Chemie und Pharmazie  
der Johannes Gutenberg-Universität Mainz

Hyeyoung Park  
Geboren in Pusan, Korea

Mainz, September 2005

# TABLE OF CONTENTS

---

## CHAPTER 1 INTRODUCTION

1.1	Genetically Modified Organism	1
1.2	Biosensor Technology	4
1.3	Outline of the Thesis	5
1.4	References	7

## CHAPTER 2 THEORY AND BACKGROUND

2.1	Surface Plasmon Resonance	10
2.1.1	<i>Evanescent wave</i>	10
2.1.2	<i>Plasmon surface polaritons at a noble metal/dielectric interface</i>	12
2.1.3	<i>Analytical application</i>	17
2.2	Surface Plasmon Field Enhanced Fluorescence Spectroscopy	19
2.2.1	<i>Fluorescence</i>	20
2.2.2	<i>Quantum yield</i>	22
2.2.3	<i>Fluorescence Quenching</i>	22
2.2.4	<i>Resonance Energy Transfer</i>	23
2.2.5	<i>Excitation of chromophore by surface plasmon evanescent field</i>	23
2.2.6	<i>Fluorescence at the Metal/dielectric Interface</i>	25
2.3	Self-Assembled Monolayers	26
2.3.1	<i>Principle of self-assembly</i>	27
2.3.2	<i>Self-assembled monolayers of alkanethiol on Au (111)</i>	27
2.4	Biotin-Streptavidin Interaction	28
2.5	Analysis of Biomolecular Interaction on the Surface	30
2.5.1	<i>Simple Langmuir Model</i>	30
2.5.2	<i>Global Analysis</i>	31
2.5.3	<i>Langmuir adsorption isotherm</i>	32
2.6	Nucleic Acids	33
2.6.1	<i>DNA</i>	35
2.6.2	<i>PNA</i>	36
2.6.3	<i>Stability of nucleic acids duplex</i>	37
2.6.4	<i>DNA Amplification- Polymerase Chain Reaction</i>	38
2.7	References	40

## CHAPTER 3 EXPERIMENTAL SECTION

3.1	Instrumental	44
3.1.1	<i>Flow cell</i>	45
3.1.2	<i>Sample assembly</i>	45
3.1.3	<i>Temperature control</i>	46
3.2	Strategic Sensor Matrix	48
3.2.1	<i>Cleaning of glass substrate</i>	50
3.2.2	<i>Thermal evaporation of gold on glass substrate</i>	50
3.2.3	<i>Sensor matrix on gold substrate</i>	50

3.2.4	<i>Characterization of sensor matrix by SPR</i>	51
3.2.5	<i>Specific and unspecific binding on the sensor matrix</i>	53
3.3	<b>PNAs Synthesis</b>	54
3.4	<b>Polymerase Chain Reaction</b>	55
3.4.1	<i>Amplification from RR GMO and natural soybean</i>	55
3.4.2	<i>Amplification for Mu –159</i>	56
3.4.3	<i>Agarose gel Electrophoresis</i>	57
3.4.4	<i>UV-Vis. Sprctrum</i>	58
3.4.5	<i>How to get single-stranded PCR?</i>	59
3.5	<b>Kinetic Measurement</b>	60
3.6	<b>References</b>	62

## **CHAPTER 4 PNA/DNA HYBRIDIZATION**

4.1	<b>Motivation</b>	63
4.2	<b>Immobilization of PNA Probe</b>	65
4.3	<b>Kinetic Analysis of Binding Data</b>	67
4.4	<b>Dependence of Ionic Strength for PNA/DNA hybridization</b>	68
4.4.1	<i>PNA/DNA hybridization (MM0)</i>	68
4.4.2	<i>PNA-11mer/DNA-11mer (MM1)</i>	71
4.5	<b>Influence of Ionic Strength for Fluorescence Intensity</b>	72
4.5.1	<i>PNA-11mer/DNA-11mer (MM0)</i>	72
4.5.2	<i>PNA-11mer/DNA-11mer hybridization in water (MM0)</i>	76
4.5.3	<i>Fluorescence intensity at different ionic strength</i>	77
4.6	<b>Effect of Length</b>	79
4.7	<b>Mismatch Discrimination</b>	80
4.8	<b>Effect of Temperature</b>	81
4.8.1	<i>Titration analysis for PNA-11mer/DNA-11mer (MM0)</i>	81
4.8.2	<i>Langmuir adsorption isotherm</i>	89
4.8.3	<i>Gibbs free energy</i>	90
4.9	<b>Conclusion</b>	91
4.10	<b>References</b>	92

## **CHAPTER 5 DETECTION OF OLIGONUCLEOTIDES AND GENETICALLY MODIFIED DNA AMPLICONS**

5.1	<b>Motivation</b>	94
5.2	<b>Kinetic Experiments for PNA/DNA Hybridization</b>	98
5.3	<b>Hybridization of PNA/ Oligomer DNA</b>	99
5.3.1	<i>Global analysis</i>	99
5.3.2	<i>Ionic strength dependence</i>	102
5.3.3	<i>Titration measurement</i>	103
5.3.4	<i>Single Kinetic analysis</i>	106
5.3.5	<i>Effect of PNA probes</i>	108
5.3.6	<i>Sequence dependence</i>	110
5.4	<b>Ionic Strength Influence for DNA/DNA Hybridization</b>	112
5.5	<b>Detection of PCR Amplicons from Round-up Ready<sup>TM</sup> Soybean</b>	114
5.5.1	<i>Kinetic-titration analysis for P-RR-15/T-RR-125</i>	116

5.5.2	<i>Kinetic-titration analysis for P-RR-15/T-RR 169</i>	119
5.5.3	<i>Mismatch discrimination</i>	121
5.5.4	<i>Effect of PNA probe</i>	122
5.5.5	<i>Limit of detection for PCR target on the sensor surface</i>	125
5.5.6	<i>Detection limit for mixed PCR targets on the sensor surface</i>	127
5.5.7	<i>Detection of GMO on array by Surface plasmon fluorescence microscopy</i>	130
5.5.8	<i>Morphology study by AFM</i>	131
5.6	Conclusion	137
5.7	References	140

## **CHAPTER 6 SUMMARY** 145

## **CHAPTER 7 SUPPLEMENT**

7.1	Abbreviations	147
7.2	List of Figures	148
7.3	List of Tables	150

## **CURRICULUM VITAE**

## **ACKNOWLEDGEMENTS**



# CHAPTER 1

## INTRODUCTION

---

### 1.1 Genetically Modified Organism (GMO)

Advances in molecular biology since the early 1970s have resulted in the growth of a wide variety of techniques, which result in genetic modification. Genetically modified organism (GMO) can be defined as organisms in which the genetic material (DNA) has been altered in a way that does not occur naturally by mating or natural recombination including medicines and vaccines, foods and food ingredients, feeds, and fibers, i.e. by being genetically modified (GM) or by recombinant DNA technology [1]. In the few years since the first commercial introduction of a genetically modified organism, the cultivation of several transgenic crop species were planted rapidly to more than 40 million ha worldwide, i.e. approximately 4% of the total world acreage with transgenic crops, the principal ones being herbicide and insecticide resistant soybeans, corn, cotton, and canola [1-3]. Other crops grown commercially or field-tested are a sweet potato resistant to a virus that could decimate most of the African harvest, rice with increased iron and vitamins that may alleviate chronic malnutrition in Asian countries, and a variety of plants able to survive weather extremes [3].

While all impacts have not been fully researched, specific aspects have been documented in benefits and controversies (Table 1.1). The most obvious benefits to consumers are the cheap price of the products due to increasing of efficiency and productivity. Moreover, biotechnology of gene allows for the opportunity of creating plants and producing food that is more nutritious like “Golden rice” which contains beta-carotene, a source of vitamin A and iron. However, there are also some known (allergic reaction with genetically modified organisms) and unknown risks. When humans consume a GMO that has a gene spliced into its genetic structure, the human body cells cannot discern what is a gene from a “natural” or genetically modified organism because they are completely unbound from the original plant. It would be difficult whether there is an affect of GMO to human health. Controversies surrounding GM foods and crops commonly focus on human and environmental safety, labeling and consumer choice, intellectual property rights, ethics, food security, poverty reduction, and environmental conservation (Table 1.1) [2].

**Table 1.1** GMO Products: Benefits and Controversies

<b>Benefits</b>	
<b>Crops</b>	<ul style="list-style-type: none"><li>• Enhanced taste and quality reduced maturation time</li><li>• Increased nutrients, yields, and stress tolerance</li><li>• Improved resistance to disease, pests, and herbicides</li><li>• New products and growing techniques</li></ul>
<b>Animals</b>	<ul style="list-style-type: none"><li>• Increased resistance, productivity, hardiness, and feed efficiency</li><li>• Increased better yields of meat eggs, and milk</li><li>• Improved animal health and diagnostic methods</li></ul>
<b>Environment</b>	<ul style="list-style-type: none"><li>• Friendly" bioherbicides and bioinsecticides</li><li>• Conservation of soil, water, and energy</li><li>• Bioprocessing for forestry products</li><li>• Better natural waste management</li><li>• More efficient processing</li></ul>
<b>Society</b>	<ul style="list-style-type: none"><li>• Increased food security for growing populations</li></ul>

<b>Controversies</b>	
<b>Safety</b>	<ul style="list-style-type: none"><li>• Potential human health impact: allergens, transfer of antibiotic resistance markers, unknown effects</li><li>• Potential environmental impact: unintended transfer of transgenes through cross-pollination, unknown effects on other organisms</li></ul>
<b>Ethics</b>	<ul style="list-style-type: none"><li>• Violation of natural organisms' intrinsic values</li><li>• Tampering with nature by mixing genes</li><li>• Objections to consuming animal genes in plants</li><li>• Stress for animal</li></ul>
<b>Labelling</b>	<ul style="list-style-type: none"><li>• Not mandatory in some countries (e.g., United States)</li><li>• Mixing GM crops with non-GM confounds labeling attempts</li></ul>
<b>Society</b>	<ul style="list-style-type: none"><li>• New advances may be skewed to interests of rich countries</li></ul>

Products consisting of or containing GMOs and food products obtained from GMOs which have been authorised on the basis of the procedure under regulations so-called

“threshold regulation” specifies that foodstuffs must be subject to labelling where material derived from these GMOs is present in food ingredients in a proportion above 1% of the food ingredients [3].

The need to monitor and verify the presence and the amount of GMOs in agricultural crops and in products derived has generated a demand for analytical methods capable of detecting, identifying and quantifying either the DNA introduced or the protein(s) expressed in transgenic plants, because these components are considered fundamental constituents [4-7]. In addition, for certain types of GM food such as vegetable oils with altered fatty acid profiles, chemical analysis, such as chromatography and near infrared spectroscopy, may be a complementary or alternative tool for GMO detection.

Numerous analytical methods, both qualitative and quantitative, have been developed to determine reliably the presence and/or the amount of genetically modified organisms (GMOs) in agricultural commodities, in raw agricultural materials and in processed and refined ingredients. In addition to the methods for DNA and protein analysis, e.g. polymerase chain reaction [8-11] and enzyme linked immunosorbent analysis [12-15], certain types of GMO-containing matrices can be profiled by complementary chemical analysis methods such as chromatography [16-18] and near infrared spectroscopy [19,20].

Since the European Union allows importation only to GM –maize, soybean and forbid to cultivate GMOs in Europe, it is important to detect, identify and quantify genetically modified organism in the novel food. To this purpose the European Union has financed a 3 years project, named "DNA-TRACK", in order to develop and validate techniques for these kinds of inspections [21]. This thesis is involved in the project deeply to detect Roundup Ready<sup>TM</sup> soybean.

Soybean plants tolerant to glyphosate herbicide were produced by inserting an expression cassette encoding a native glyphosate-tolerant EPSPS (5-enol-pyruvylshikimate-3-phosphate synthase) isolated from *Agrobacterium sp.* strain into the genome of soybean. This resulted in the glyphosate tolerant, Round-up Ready<sup>TM</sup> (RR) soybean (event 40-3-2) [22-24]. Herbicide tolerant soybean has been the most dominant transgenic crop grown commercially in several countries (USA, Argentina, Canada, Mexico, Romania, and Uruguay) (James, 2000). The molecular characterization of RR soybean has been extended using more sensitive and precise methods, including genome walking, higher sensitivity Southern blot analysis, genomic cloning, nucleotide sequencing, PCR, and northern blot analysis [25].

## 1.2 Biosensor Technology

Research in the field of biosensors has enormously increased over the recent years. Since the development of the first biosensor by Clark in 1962, where an oxygen electrode was immobilized with an enzyme (glucose oxidase) [26], many efforts have been invested to create detection systems. These systems often benefit from the coupling of the unique recognition and signal-amplification abilities of biological systems that have been developed and optimized during millions of years of evolution, with detection and amplification system. Thus, the combination of knowledge in bio- and electrochemistry, solid-state and surface physics, bioengineering, integrated circuit silicon technology and data processing offers the possibility of a new generation of highly specific, sensitive, selective and reliable micro (bio-) chemical sensors and sensor arrays. Moreover, the rapid development of silicon technology has stimulated the fabrication of miniaturized analytical systems such as  $\mu$ TAS (micro total analysis system), ‘lab on chip’ sensors, electronic tongue devices and electronic noses [27-31].

Biosensors represent functional hybrid systems, generally combining two basic components connected in series, namely a biological (molecular) recognition system and a physico-chemical transducer. The recognition system is often also called the bioreceptor, because in the natural chemical senses, the recognition phenomenon is performed by a chemoreceptive cell. The biosensor is usually constructed by attaching a biologically sensitive material to a suitable transducing system [32].

Biosensors combine the specificity of biology with the processing power of modern electronics to provide powerful analytical tools that are able to rapidly detect tiny amounts of particular substances. With appropriate development and commercialisation, biosensors are expected to have a significant impact on reducing costs and increasing efficiency within industry [33].

A typical biosensor (Figure 1.1) consists of a receptor (biological component, eg an enzyme or antibody) and an electronic device (ie the transducer) that converts the signal into a measurable output. The biological part of the sensor reacts with a particular substance of interest (ie the analyte) to produce a physical or biochemical change that is detected and converted to an electrical signal by the transducer. The amplifier increases the intensity of the signal so that it can be readily measured. These components are usually housed within a single portable unit that can be placed at fixed strategic locations. The biosensor display can be tailored to meet the needs of the application and can range from a simple output such as

switching on (or off) a light-emitting diode to a quantitative result displayed in a graphical format. The biological component is usually an enzyme, an antibody or a micro-organism, although it can be DNA or even biological tissues. The type of transducer used depends on the parameters being measured, but typically involves electrochemical [34], optical [35-36], mass [37] or thermal [38] measurements.

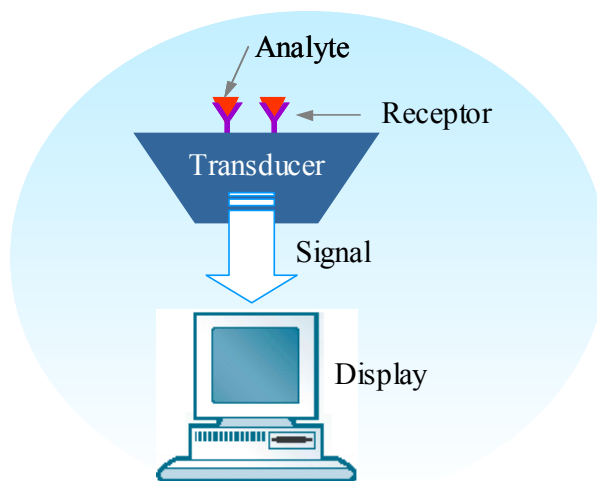


**Figure 1.1** A typical biosensor consists of a receptor and an electronic device that converts the biological signal into a measurable output.

Biosensor technology is having an increasing impact on manufacturing industry and there is a significant opportunity for expansion of this potentially large market. The application in areas where rapid detection, high sensitivity and high specificity are important should provide a continuing driver for scientific development as well as commercialization. Biosensors in market require: (1) cost-effectiveness, (2) sensitivity, (3) specificity, and (4) rapid response times.

### 1.3 Outline of the Thesis

Sequence specific analysis of biomolecular has become very useful to detect single nucleotide polymorphisms (SNPs) and to identify genes driven by the human genome project. Due to the enormous number of base-pairs that need to be analysed, sensitive and efficient screening methods are needed that are capable of processing DNA samples in a convenient way. Most of the detection formats include the interaction of immobilized probes and targets with surfaces. The analysis of the kinetic behavior of oligonucleotides at the sensor surface is hence of major importance for the improvement of known detection schemes.

Recently, the surface plasmon field-enhanced fluorescence spectroscopy (SPFS) [39,40] was developed as a kinetic analysis and a detection method with dual- monitoring of the change of reflectivity and fluorescence signal for the interfacial phenomenon (chapter 2).

By using SPFS, kinetic measurements for the hybridization between peptide nucleic acid (PNA), which is a synthesized DNA mimic of nucleic acid forming more a stable duplex with DNA, and deoxyribonucleic acid (DNA) were carried out on the sensor surface (chapter 3). Based on the Langmuir model, rate constants were determined for the binding of oligomer DNA targets (chapter 4) and PCR targets (chapter 5) to PNA with a complementarily matched sequence as well as a mismatched sequence by performing different experiments (single-, global-, and titration-experiment). Furthermore, influences of ionic strength and temperature for PNA/DNA hybridization were demonstrated in kinetic analysis (chapter 4).

In order to detect GMOs from food, DNA amplicons were amplified by polymerase chain reaction (PCR) [41] using a template gene extracted from Monsanto's Round-up Ready<sup>TM</sup> soybean (chapter 5). The effect of probe PNAs immobilized on the surface was investigated for better sensing properties. Also, reliable detection limits for PCR target detection was measured on the PNA bound sensor surface as well as the quantitative kinetic analysis on account of the high sequence specificity and stability of the duplex.

Finally, the specific binding of functional molecules on a planar substrate was characterized by tapping-mode AFM in air. The surface morphology change after the hybridization from PNA layers gives the clear demonstration for the existence of bound target DNA to the PNA immobilized surface (chapter 5).

## 1.4 References

- [1] Anklam, E.; Gadani, F.; Heinze, P.; Pijnenburg, H.; Eede, G. D. *Eur Food Res Technol.* **2002**, 214, 3–26.
- [2] [http://www.ornl.gov/sci/techresources/Human\\_Genome/elsi/gmfood.shtml](http://www.ornl.gov/sci/techresources/Human_Genome/elsi/gmfood.shtml).
- [3] Commission Regulation (EC) 65/2004 establishing a system for the development and assignment of unique identifiers for genetically modified organisms. *Off. J. Eur. Union* **2004**, L10, 5–10.
- [4] Gachet, M.; Martin, G. G.; Vigneau, F.; Meyer, G. *Trends Food Sci Technol.* **1999**, 9, 380–388.
- [5] Lüthy, J. *Food Control.* **1999**, 10, 359–361.
- [6] Gilbert, J. *Food Control.* **1999**, 10, 363–365.
- [7] Meyer, R. *Food Control.* **1999** 10, 391–399.
- [8] Hemmer, W. Foods derived from genetically modified organisms and detection methods. BATS-Report **1997**, Agency for Biosafety Research and Assessment of Technology Impacts of the Swiss Priority Programme Biotechnology of the Swiss National Science Foundation, Basel, Switzerland.
- [9] Pietsch, K.; Waiblinger, H. U.; Brodmann, P.; Wurz, A. *Lebensm Rundsch.* **1997**, 93, 35–38.
- [10] Hupfer, C.; Hotzel, H.; Sachse, K.; Engel, K. H. *Z Lebensm Unters Forsch.* **1997**, 205, 442–445.
- [11] Anklam, E. *Anal Chim Acta.* **1999**, 393, 177–179.
- [12] Steinkellner, H.; Korschhineck, I. Detection of recombinant viral coat protein in transgenic plants. In: Cunningham C, Porter AJR (eds) *Methods in biotechnology. Recombinant proteins from plants*, vol. 3. Humana, Totowa, New Jersey, **1998**, 65–75.
- [13] Brett, G. M.; Chamber, S. J.; Huang, L.; Morgan, M. R. A. *Food. Control.* **1999**, 10, 401–406.
- [14] Wood, D. C.; Vu, L. V.; Kimack, N. M.; Glennon, J. R.; Ream, J. E.; Nickson, T. E. *J Agric Food Chem.* **1995**, 43, 1105–1109.
- [15] Stave, J. *Food Control.* **1999**, 10, 367–374.
- [16] Byrdwell, W. C.; Neff, W. E. *J Liq Chromatogr Relat Technol.* **1996**, 19, 2203–2225.
- [17] Neff, W. E.; Selke, E.; Mounts, T. L.; Rinsch, W. M.; Frankel, E. N.; Zeitoun, M. A. M. *J Am Oil Chem Soc.* **1992**, 69, 111–118.
- [18] Neff, W. E.; Mounts, T. L.; Rinsch, W. M.; Konishi, H.; El-Agaimy, M. A. *J Am Oil Chem Soc.* **1994**, 71, 1101–1109.
- [19] Sanders, G. W. H.; Manz, A. *Trends Anal Chem.* **2000**, 19, 364–378.

- [20] Hurburgh, C. R.; Rippke, G. R.; Heithoff, C.; Roussel, S. A.; Hardy, C. L. Detection of genetically modified grains by nearinfrared spectroscopy. Proceedings PITTCO 2000 – Science for the 21st Century, #1431. New Orleans, La. **2000**, 12–17.
- (a) Commission Regulation (EC) 258/97 of the European Parliament and of the Council concerning Novel Foods and Novel Food Ingredients. *Off. J. Eur. Communities* **1997**, L 43, 1-5.
- (b) Commission Regulation (EC) 50/2000 of Jan 10, 2000, on the labeling of foodstuffs and food ingredients containing additives and flavorings that have been genetically modified or have been produced from genetically modified organisms. *Off. J. Eur. Communities* **2000**, L 6, 15.
- (c) Regulation (EC) 1829/2003 of the European Parliament and the Council of the European Union on genetically modified food and feed. *Off. J. Eur. Union* **2003**, L268, 1-23.
- (d) The European Parliament and the Council of the European Union Regulation (EC) 1831/2003 concerning the traceability and labeling of genetically modified organisms and the traceability of food and feed products produced from genetically modified organisms and amending Directive 2001/ 18/EC. *Off. J. Eur. Union* **2003**, L268, 24-28.
- [21] Amerhein, N. et al. *Plant Physiology*, 1980, 65, 830-834.
- [22] Torres, A. C. et al. *Pesq. agropec.* **2003**, 38, 1053-1057.
- [23] Monsanto Company, *Study number 99-01-30-22*, 10.
- [24] Ayala, L. et al. *Seed Science & Technology*, **2002**, 30, 431-436.
- [25] Clark, L. C.; Lyons, C. *Ann. N.Y. Acad. Sci.*, **1962**, 102, 29–45.
- [26] Manz, A.; Gruber, N.; Widmar, H. M. *Sens. Actuators, B*, **1990**, 1, 244–248.
- [27] van den Berg, A.; Lammerink, T. S. J. *Top. Curr. Chem.*, **1997**, 194, 21–49.
- [28] Jain, K. K. *Trends Biotechnol.* **2000**, 18, 278–280.
- [29] Toko, K. *Biosens. Bioelectron.* **1998**, 13, 701–709.
- [30] Göpel, W. *Sens. Actuators, B*. **1998**, 52, 125–142.
- [31] Ziegler, C.; Göpel, W. *Curr. Opin. Chem. Biol.* **1998**, 2, 585-591.
- [32] Thevenot, D. R.; Toth, K.; Durst, R. A.; Wilson, G. S. *Biosens. Bioelectron.* **2001**, 16, 121–131.
- [33] McDonnell, J. M. *Curr. Opin. Chem. Biol.* **2001**, 5, 572–577.
- [34] Mugweru, A.; Wang, B. –Q.; Rusling, J. *Anal. Chem.* **2004**, 76, 5557-5563.
- [35] Buerk, D. G. *Biosensors*, Technomic Publishing AG, Lancaster, USA, **1992**.
- [36] Yeung, E. S. *The Chemical Record*. **2001**, 1, 123–139.
- [37] Ha, T. -H.; Kim, S.; Lim, G.; Kim, K. *Biosens. Bioelectron.* 2004, 20, 378-389



- [38] Doyle, M. L. *Curr. Opin. Biotechnol.* **1997**, 8, 31-35.
- [39] Liebermann, T.; Knoll, W. *Colloid Surf. A.* **2000**, 171, 115–130.
- [40] Hegner, M.; Wagner, P.; Semenza, G. *Surf. Sci.* **291**, 39 ~1993.
- [41] Saiki, R. K.; Scharf, S.; Faloona, F.; Mullis, K. B.; Horn, G. T.; Erlich, H. A.; Arnheim, N. *Science* **1985**, 230, 1350-1354.

## CHAPTER 2

# THEORY AND BACKGROUND

---

### 2.1 Surface Plasmon Resonance (SPR)

Surface plasmon resonance (SPR) spectroscopy has been widely used as a detection technique in sensors as well as for characterizing molecular interactions at the interface between the analyte and the sensor surface. Many efforts have been directed to the development of various SPR combinations for improving the sensitivity and allowing for quantitative measurement. For instance, SPR spectroscopy combined with diffraction method [1-4], fluorescence detection [5-9], electrochemical measurement [10-12], and quartz crystal microbalance measurements (QCM) [13-15] have been developed by several groups.

SPR is a quantum optical-electrical phenomenon arising from the interaction of light with a metal surface. Under certain conditions the energy carried by photons of light is transferred to packets of electrons, called plasmons, on a metal surface. Energy transfer occurs only at a specific resonance wavelength of light. That is, the wavelength where the quantum energy carried by the photons exactly equals the quantum energy level of the plasmon. If a light beam hits a prism, the light is bend towards the plane of interface, when it is passing form a denser medium to a less dense one. Changing the incidence angle ( $\theta$ ) changes the out coming light until a critical angle ( $\theta_c$ ) is reached. At this point all the incoming light is reflected within the prism. This is called total internal reflection (TIR).

#### 2.1.1 *Evanescent wave*

In TIR, the reflected photons create an electric field on the opposite site of the interface. This field is called evanescent wave because it decays exponentially with distance. The evanescent wave optics is a number of optical phenomena and techniques associated with the total internal reflection of light at the boundary between two media of different optical properties with their different dielectric functions,  $\epsilon_i$ . A plane wave, e.g. from a laser light source (wavelength,  $\lambda$ ) impinging upon that interface from the glass side, i.e. from the side of

the material with the higher refractive index,  $n_p = \sqrt{\epsilon_p}$ , will be totally (internally) reflected if the angle of incidence exceeds a critical value  $\theta_c$ .

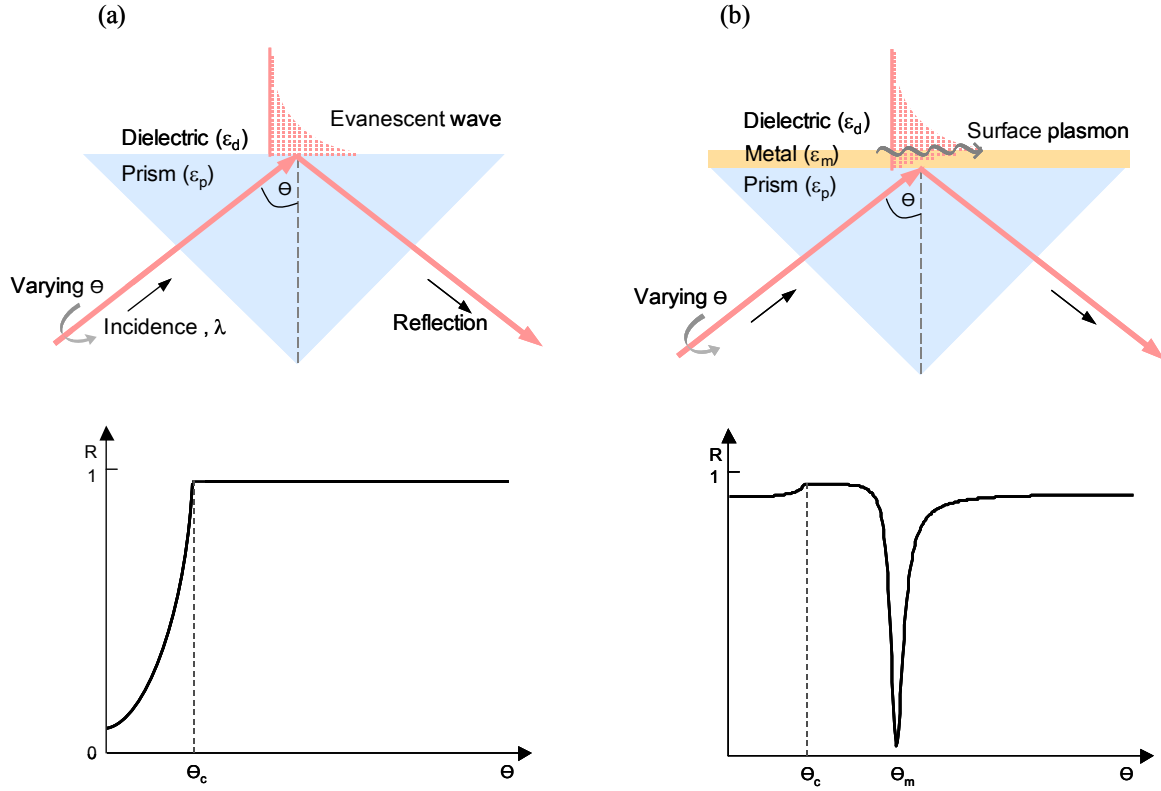


**Figure 2.1.** (a) Total internal reflection of a plane wave of wavelength  $\lambda$  and intensity  $I_{in}$  at a glass prism with  $\epsilon_p$  in contact with a dielectric medium of  $\epsilon_d < \epsilon_p$ . The reflected light is monitored with a detector. For incident angles  $\theta > \theta_c$ , the critical angle for total internal reflection, the evanescent field at the interface decays exponentially into the dielectric. (b) Attenuated total internal reflection (ATR) construct for surface plasmon excitation in the Kretschmann geometry. A thin metal film is evaporated onto the prism and acts as a resonator driven by the photon field incident at an angle  $\theta$ . Note the decreasing of reflectivity until an angle  $\theta_m$ , where maximum coupling of the surface plasmon in surface plasmon spectroscopy.

Figure 2.1 shows a typical evanescent excitation. At incident angles smaller than  $\theta_c$ , most of the incoming light is transmitted and hence the reflected intensity is low. As one approaches  $\theta_c$ , however, the reflectivity  $R$  reaches unity.  $\theta_c$  is given by Snell's law and depends on the refractive indices of the two media. In the case of a glass/water interface, one obtains  $\sin \theta_c = \frac{n_d}{n_p}$  with  $n_p = \sqrt{\epsilon_p}$  being the refractive index of the water. Beyond the

critical angle, the electric field distribution in the vicinity of the interface does not fall abruptly to zero but instead there is a harmonic wave that travels parallel to the surface with

amplitude that decays exponentially. The penetration depth,  $l$ , of this wave is given by the following equation:

$$l = \frac{\lambda}{2\pi\sqrt{(n \cdot \sin \theta)^2 - 1}}, \theta > \theta_c \quad (1)$$

This propagating electromagnetic field distribution is called an evanescent wave.

### **2.1.2 Plasmon surface polaritons at a noble metal/dielectric interface**

The prism is coated with a thin gold film on the reflection site. When the energy of the photon electrical field is just right it can interact with the free electron constellations in the gold surface. The surface plasmon phenomenon exists when polarized light reaches the interface between a thin metal film and a high density medium in Kretschmann geometry. The electric field within the light causes oscillation of the electrons in the dielectric material. This oscillation produces evanescent waves that are non-propagating spatially decaying fields, in turn causing oscillations in the free delocalized electron density of the metal called surface plasmons [16-20] (Figure 2.1 (b) and Figure 2.2). The metal acts as an oscillator by the free electron gas in the metal film, leading to resonant excitation by a coupling between the electron oscillation and the incident light. This resonant excitation of a coupled state is called plasmon surface polaritons (PSPs). Due to the resonance coupling, the electric field at the interface is enhanced by about 15-20 times in case of gold and about 80 times in the case of silver film [20].

An interface is demonstrated in the xy-plane between two half-infinite spaces, 1 and 2, of materials the optical properties of which are described by their complex frequency-dependent dielectric functions (Figure 2.2). Ignoring magnetic materials, surface polaritons can only be excited at such an interface if the dielectric displacement  $\vec{D}$  of the electromagnetic mode has a component normal to the surface can induce a surface charge density  $\sigma$ ,

$$(\vec{D}_2 - \vec{D}_1) \cdot \vec{z} = 4\pi\sigma \quad (2)$$

The Maxwell equations are given by

$$\nabla \cdot \vec{H} = 0, \quad (3)$$

$$\nabla \cdot \vec{E} = 0, \quad (4)$$

$$\nabla \cdot \vec{E} + \frac{1}{c} \frac{\partial \vec{H}}{\partial t} = 0, \quad (5)$$

$$\nabla \cdot \vec{H} + \frac{\omega}{c} \frac{\partial \vec{E}}{\partial t} = 0 \quad (6)$$

with  $c$  being the speed of light in vacuum,  $c = 1/\sqrt{\mu \cdot \varepsilon}$ .  $\mu$  is a magnetic permeability.

The electrical field,  $\vec{E}$  in case of plane waves, is presented by

$$\vec{E} = \vec{E}_0 e^{i(\vec{k} \cdot \vec{r} - \omega \cdot t)} \quad (7)$$

where  $\vec{E}_0$  is the electric field amplitude,  $\vec{r}$  is a position vector,  $\omega$  is the angular frequency ( $\omega = 2\pi f$ ,  $f$ =frequency),  $t$  is a time, and  $\vec{k}$  is the wavevector which is in direction of the propagation.

S-polarized (transversal electric, TE) light propagate along the x-direction with only electric field components,  $\vec{E}_i = (0, E_y, 0)$ , parallel to the surface, hence, is unable to excite surface polaritons. Only p-polarized light (transversal magnetic, TM) modes with electric field,  $E = (E_x, 0, E_z)$  or, magnetic field,  $\vec{H} = (0, H_y, 0)$ , can couple to such modes. Considering the dielectric ( $\varepsilon_1 > 0$ , medium 1)/metal ( $\varepsilon_2 = \varepsilon_2' + i \cdot \varepsilon_2''$ , medium 2) interface, the electromagnetic fields are expressed by:

$$\begin{aligned} E_1 &= (E_{x1}, 0, E_{z1}) e^{i(k_{x1} \cdot x + k_{z1} \cdot z - \omega \cdot t)} \\ H_1 &= (0, H_{y1}, 0) e^{i(k_{x1} \cdot x + k_{z1} \cdot z - \omega \cdot t)} \quad , \quad Z > 0 \end{aligned} \quad (8)$$

$$\begin{aligned} E_2 &= (E_{x2}, 0, E_{z2}) e^{i(k_{x2} \cdot x + k_{z2} \cdot z - \omega \cdot t)} \\ H_2 &= (0, H_{y2}, 0) e^{i(k_{x2} \cdot x + k_{z2} \cdot z - \omega \cdot t)} \quad , \quad Z < 0 \end{aligned} \quad (9)$$

Both fields  $\vec{E}$  and  $\vec{H}$  have to be equal at the interface, i.e.

$$\vec{E}_{x1} = \vec{E}_{x2} \quad (10)$$

and

$$\vec{H}_{y1} = \vec{H}_{y2}. \quad (11)$$

From Equation 10 it follows  $k_{x1} = k_{x2} = k_x$ . Inserting from the equation 8 into 6 and 9 into 6, one obtains:

$$k_{z1} H_{z1} = \frac{\omega}{c} \cdot \varepsilon_1 \cdot E_{x1} \quad (12)$$

and

$$k_{z2} H_{z2} = -\frac{\omega}{c} \cdot \epsilon_2 \cdot E_{x2}. \quad (13)$$

This leads to the only nontrivial solution if:

$$\frac{k_{z1}}{k_{z2}} = -\frac{\epsilon_1}{\epsilon_2}. \quad (14)$$

This indicates that surface electromagnetic modes can only be excited at interfaces between two media with dielectric constants of opposite sign with the interface between a metal ( $\tilde{\epsilon}_m = \epsilon'_m + i \cdot \epsilon''_m$ ) and a dielectric material ( $\tilde{\epsilon}_d = \epsilon'_d + i \cdot \epsilon''_d$ ) by coupling the collective plasma oscillations of the nearly free electron gas in a metal to an electromagnetic field [21]. These excitations are called plasmon surface polaritons (PSP) or surface plasmons. From the equations 8, 9, 12, and 13 one obtains the dispersion relation of PSP:

$$k_x^2 + k_{zd}^2 = \left(\frac{\omega}{c}\right)^2 \cdot \epsilon_d \quad (15)$$

or

$$k_{zd} = \sqrt{\epsilon_d \cdot \left(\frac{\omega}{c}\right)^2 - k_x^2}. \quad (16)$$

The dispersion relationship is obtained (i.e. the energy momentum relation) for surface plasmons at a metal/dielectric interface:

$$k_x = \frac{\omega}{c} \cdot \sqrt{\frac{\epsilon_m \cdot \epsilon_d}{(\epsilon_m + \epsilon_d)}}. \quad (17)$$

The PSP modes propagating along a metal/dielectric interface exhibit a finite propagation length,  $L_x$ , given by  $L_x = 1/2 \cdot k_x''$ . This decay has a strong impact on lateral resolution that we want to obtain in the characterization of laterally structured samples investigated with plasmon or waveguide light in a microscopic applications [22].

In the frequency (spectral) range of interest we have:

$$\sqrt{\frac{\epsilon_m \cdot \epsilon_d}{(\epsilon_m + \epsilon_d)}} \geq \sqrt{\epsilon_d}. \quad (18)$$

The surface plasmon is a bound, non-radiative evanescent wave with field amplitude, the maximum of which is at the interface ( $z=0$ ) and which is decaying exponentially into the dielectric (and into the metal). The mode is propagating as a damped oscillatory wave (Figure 2.2). All parameters characterizing the properties of PSPs can be quantitatively described on the basis of the dielectric functions of the involved materials.

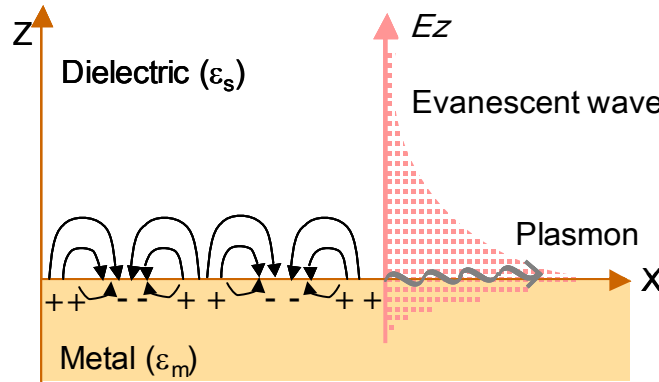


**Figure 2.2.** Schematic drawing of the charges and the electromagnetic field of surface plasmons propagating on a surface in the x-direction at the interface between a metal and a dielectric media. The electric field along z-direction decay exponentially, here shown for the  $E_z$  component.

The dispersion relation of a free photon in a dielectric ( $\epsilon_d$ ) is

$$k_{ph} = \frac{\omega}{c} \cdot \sqrt{\epsilon_d} , \quad (19)$$

which is always smaller than the momentum of a surface plasmon mode,  $k_{sp}$ , propagating along an interface between that same medium and the metal (see Figure 2.3 (a)). The dispersion of photons is described by the light line,  $\omega = c_d \cdot k_{ph}$  (Figure 2.3 (b)), with  $c_d = c / \sqrt{\epsilon_d}$ .

For the excitation of surface plasmons, the optical momentum at the surface could match by prism coupling. The dispersion curves before and after enhancement by the prism are shown as curve (1) and (2) in Figure 2.3 (b)

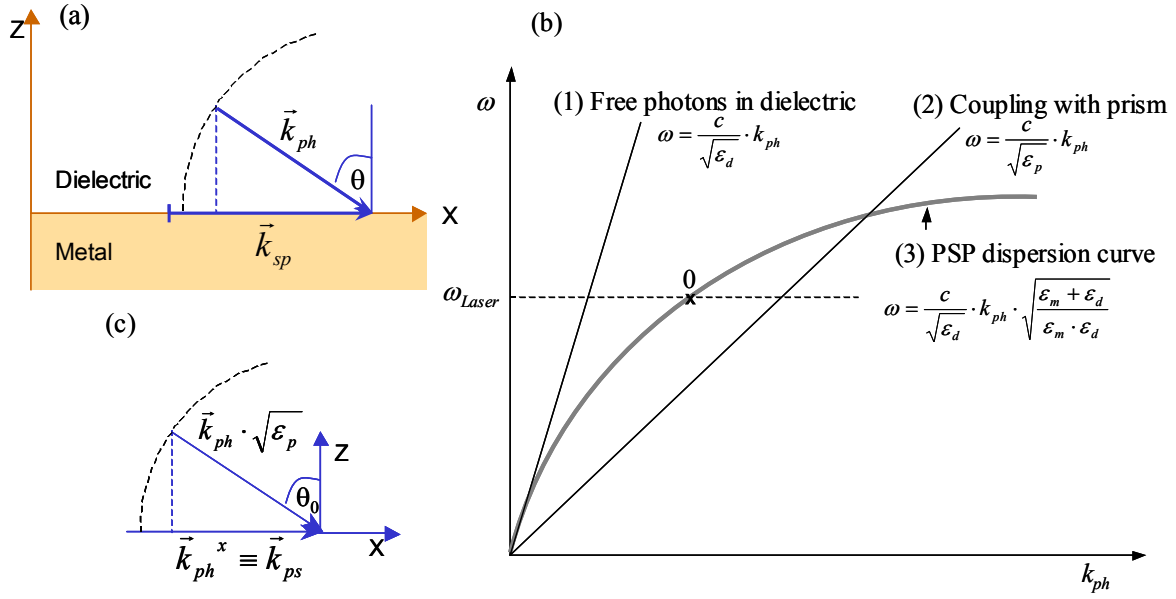


**Figure 2.3.** (a) Momentum relation between a surface plasmon,  $\vec{k}_{sp}$ , propagating along  $x$  and a photon,  $\vec{k}_{ph}$ , incident at the metal/ dielectric interface at an angle  $\theta$ .  $|\vec{k}_{sp}| < |\vec{k}_{ph}|$ . (b) Dispersion relation of a photon traveling as a plane wave in the dielectric medium, of a photon propagating in the prism, and of the surface plasmonmode propagating along the metal/dielectric interface. (c) Wavevector matching condition for the resonant coupling of photons traveling in the prism at the incident angle  $\theta_0$ .

The PSP dispersion curve (gray curve (3) in Figure 2.3 (b)) asymptotically reaches the light line, whereas for higher energies it approaches the cutoff angular frequency  $\omega$  determined by the plasma frequency of the employed metal,  $\omega_p$ :

$$\omega = \frac{\omega_p}{\sqrt{1 + \epsilon_d}}. \quad (20)$$

Photons are not coupled directly to the metal/dielectric interface, but via the evanescent tail of light totally internally reflected at the base of a high-index prism (with  $\epsilon_p > \epsilon_d$ ). This light is characterized by a larger momentum (Figure 2.3 (b), *dashed line*) that for a certain spectral range can exceed the momentum of the PSP to be excited at the metal surface. So, by choosing the appropriate angle of incidence  $\theta_0$  (point 0 in Figure 2.3 (b)), resonant coupling between evanescent photons and surface plasmons can be obtained. The corresponding momentum matching condition is schematically given in Figure 2.3 (c).

This resonant coupling is observed by monitoring, as a function of the incident angle, the laser light of energy  $\hbar \cdot \omega_L$  that is reflected by the base of the prism, which shows a sharp



minimum (see also  $\theta_m$  in Figure 2.1 (b)). This configuration is the need to get the metal surface close enough to the prism base, typically to within  $\sim 200$  nm. Even a few dust particles can act as spacers, thus preventing efficient coupling [23].

The surface plasmon spectroscopy is based on the configuration introduced by Kretschmann and Raether [19]. Qualitatively, the angular dependence of the reflectivity can be simulated by Fresnel's equations for the layers of glass/metal-layer/dielectric.

### 2.1.3 Analytical application

Applications of SPR have been reported in the scientific literatures [1-4]. SPR can be used as a sensor which is capable of sensitive and quantitative measurement of a broad spectrum of chemical and biological adsorption. It offers a number of important practical advantages over analytical techniques. A sensor format may be used for immunological, nucleic acid binding, enzymatic, chemical, and gas adsorption. Some of the potential areas of application include medical diagnostics, environmental monitoring, agriculture pesticide and antibiotic monitoring, food additive testing, military and civilian airborne biological and chemical agent testing, and real time chemical and biological production process monitoring.

During a binding analysis SPR changes occur at a sensor chip. To perform an analysis, the sensor surface is faced to one wall of a flow cell (Figure 2.4 (b)). Sample containing analyte is injected over this surface in a precisely controlled flow. The binding events are detected as changes in the particular angle where SPR creates extinction of light. This change is measured continuously to form a sensorgram, which provides a complete record of the progress of association or dissociation of the interactants.

The deposition of an ultrathin layer of a material with an index of refraction  $n_{layer} = \sqrt{\epsilon_{layer}}$  larger than that of the ambient dielectric, e.g. air  $n=1$ , for a surface plasmon mode is equivalent to an increase of the overall effective index integrated over the evanescent field. The net effect is a slight shift of the dispersion curve corresponding to an increase of  $k_{sp}$  for any  $\omega_{Laser}$ . This is depicted in Figure 2.4 (a) (*dashed curve* labeled PSP<sub>2</sub>). As a consequence, the angle of incidence that determines the photon wave vector projection along the PSP propagation direction has to be slightly increased (from  $\theta_1$  and point 1 on curve PSP<sub>1</sub> to  $\theta_2$  and point 2 on curve PSP<sub>2</sub> in Figure 2.4) in order to again couple resonantly to PSP modes [24].

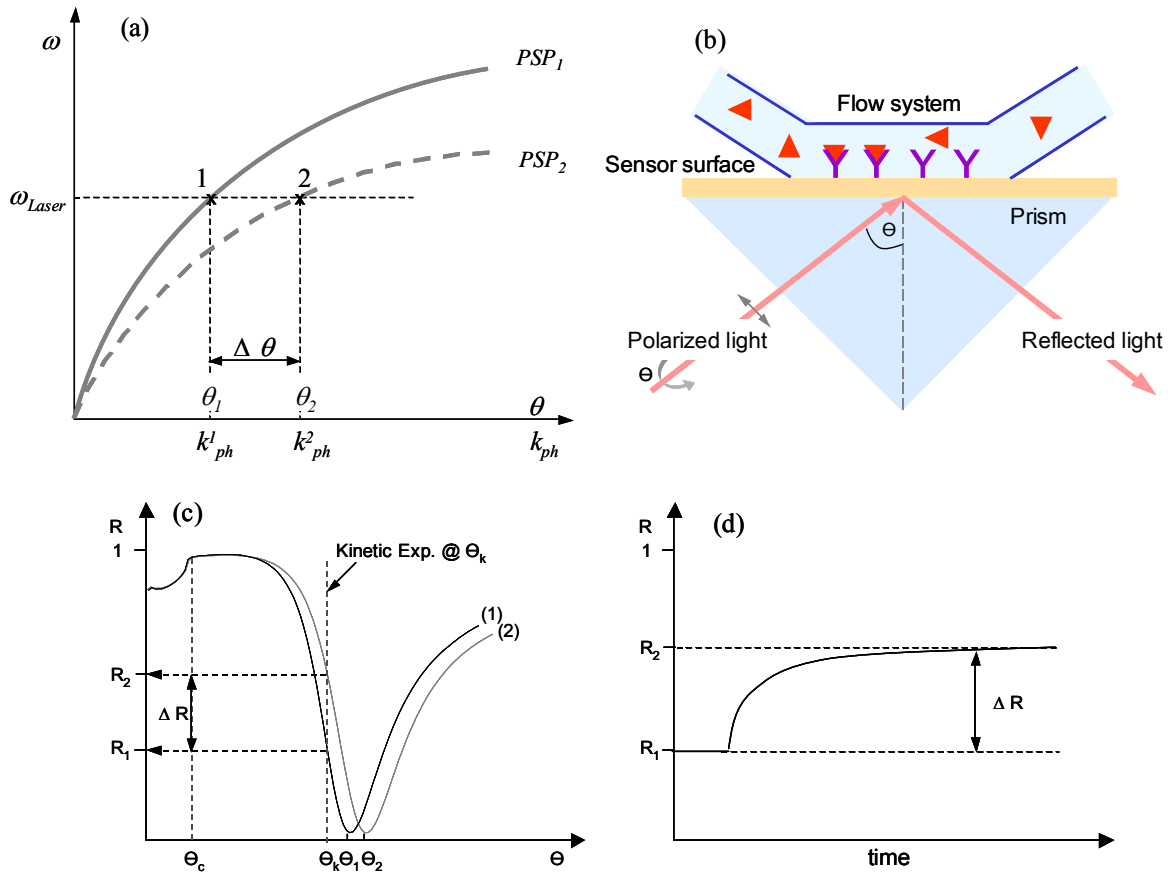


**Figure 2.4.** (a) Dispersion relation,  $\omega$  vs.  $k_{sp}$ , of plasmon surface polaritons (PSP) at a metal/dielectric interface before (gray plot,  $PSP_1$ ) and after (gray dashed plot,  $PSP_2$ ) the adsorption of an analyte layer. Laser light of energy  $\hbar\omega_{Laser}$  couples at angles  $\theta_0$  and  $\theta_1$ , given by the energy and momentum matching condition (see the intersection of the horizontal line at  $\omega_{Laser}$  with the two dispersion curves). (b) Schematic drawing of analytical experiment in flow system using SPR (c) Reflectivity curves (angular scans) of surface plasmon spectroscopy before (1) and after (2) binding of analyte on the sensor surface. (d) The corresponding kinetic mode recording the reflected intensity at a fixed angle (normally 30% of reflectivity because this linear region is sensitive and reliable) of incidence as a function of time.

A p-polarized laser beam of wavelength,  $\lambda$  on the noble-metal-coated base of the prism is reflected, and the intensity of the reflected light is monitored with a detector as a function of  $\theta$ . A typical reflectivity scan-curves are given in Figure 2.4 (c). The curve labeled (1) in Figure 2.4 (c) was taken in water on a bare Au-film evaporation-deposited onto the prism base. For  $\theta < \theta_c$  the reflectivity is rather high compared to the total internal reflection discussed in Figure 2.1 (a) because the evaporated metal layer acts as a mirror with little transmission. The deposition of an ultrathin analyte layer from solution to the Au-surface

results in a shift of the dispersion curve for PSP running along this modified interface and hence in a shift of the resonance angle (from  $\theta_1$  to  $\theta_2$ , see Figure 2.4 (a) and (c)).

The angular dependence of the overall reflectivity can be computed and compared with the measured curves (Figure 2.4 (c)). If the refractive index ( $n$ ) of the material is known, the geometrical thickness ( $d$ ) can be determined by the resonance angle shift:

$$\Delta\theta \propto n \cdot d. \quad (21)$$

During the interaction between the surface and analyte, the binding kinetics can be measured with changes of reflectivity at fixed angle,  $\theta_k$  as a function of time (Figure 2.4 (d)).

## 2.2 Surface Plasmon Field Enhanced Fluorescence Spectroscopy

The field enhanced mechanisms operating at resonance excitation of surface plasmon mode at a metal/dielectric interfaces are well established and widely used in surface enhanced Raman spectroscopy (SERS) [25-27]. As a combination of SPR and fluorescence technique, surface plasmon fluorescence spectroscopy (SPFS) was recently introduced [28-30], which uses greatly enhanced electromagnetic field obtained at the surface plasmon resonance to excite the fluorescent dyes in the vicinity of the metal/dielectric interface. Most of the intriguing features of fluorescence, such as high-sensitivity, multiplexing detection, can be directly inherited by SPFS. SPFS has become a very powerful tool for detection and quantitative evaluation of interfacial binding reaction.

Analytical methods based on fluorescence detection are widely used in chemical as well as biochemical research due to the extraordinary sensitivity and the favourable time scale on which fluorescence occurs. A number of molecular processes can be observed by monitoring their influence on a fluorescent probe during the fluorescence lifetime, which is typically in the range of 10 ns.

Several photophysical parameters of fluorescent probes have been exploited to monitor analyte binding events. These include fluorescence polarisation [31], fluorescence quenching [32,33], fluorescence enhancement [34] and resonant energy transfer (RET) [35,36]. Combining one of these fluorescence schemes with other optical or electrical detection methods of interest can lead to an improvement in the sensitivity and detection limit of these

methods. Since fluorescence detection has been utilized extensively in this study, the principles about fluorescence will be explained in the following.

### **2.2.1 Fluorescence**

The absorption of electromagnetic radiation is a universal property of matter. If light in the ultraviolet/visible part of the electromagnetic spectrum is passed through a sample in solution, some light energy may be absorbed. Any molecule absorbs light in some wavelength range. However, for any selected wavelength, certain types of chemical groups usually dominate the observed spectrum. These groups are called chromophors.

The electronic transitions are restricted by spin selection rules. In the electronic ground state of a molecule the orbitals of lowest energy are usually occupied by two electrons. According to Pauli's principle, the spins of the two electrons that occupy the same orbital must be antiparallel i.e., the electrons are paired and the intrinsic angular momenta (spins) of the electrons add to give a resultant spin of zero. These states are characterized by a total spin quantum number  $S=0$ , which has a multiplicity  $2S + 1 = 1$  and are called singlet (S) states. Another important configuration is the triplet state (T) in which the electrons have parallel spins leading to a spin quantum number 1 and multiplicity  $2S + 1 = 3$ . Transitions between energy states and hence their lifetimes, are governed by selection rules. For a spin allowed transition,  $\Delta S = 0$ , which means that the multiplicity must be conserved. A change in multiplicity i.e., a spin forbidden transition (triplet to singlet state) can occur by a strong internal magnetic field arising from the orbital movement of electrons. This spin-orbit interaction becomes more effective when atoms with higher nuclear charge are introduced in a molecule, such as halogens, metals, sulfur or phosphorus.

All processes that involve the emission of electromagnetic radiation are called luminescence which is of two types (Figure 2.5): Fluorescence and Phosphorescence, depending upon the nature of the ground and excited states. Fluorescence is the emission which results from the transition between singlet states. These high emissive rates result in fluorescence lifetimes of nearly  $10^{-8}$  s (10 ns). Phosphorescence is the emission which results from transition between states of different multiplicity, generally a triplet excited state returning to singlet ground state. Such transitions are not allowed and emissive rates are very low. Typical phosphorescent lifetimes range from milliseconds to seconds.

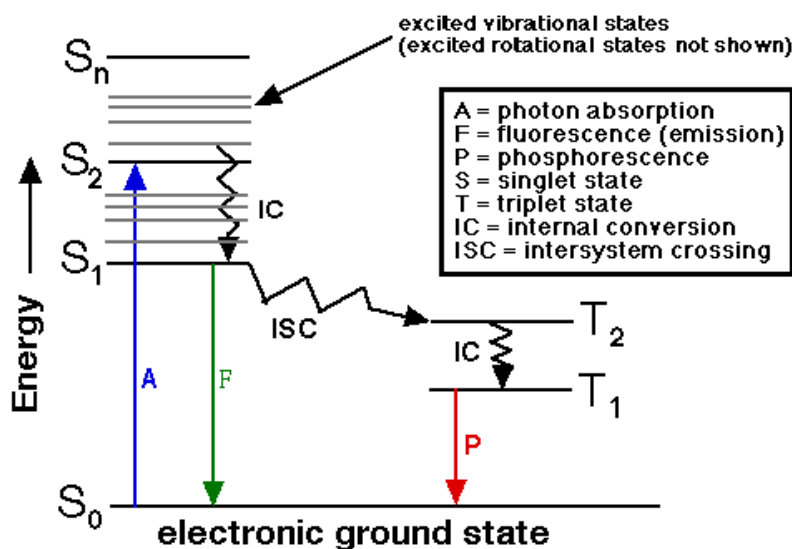


Figure 2.5. Jablonski diagram

The absorption and emission of light is illustrated by the energy level diagram suggested by Jablonski. The diagram shows the excitation of an electron from the electronic-vibrational ground state  $S_0$  to excited states  $S_1$ ,  $S_2$  ... which are characterized by different electronic energies and by different vibrational states of the molecule. The absorption to a triplet state is forbidden as a consequence of quantum theory, because it would require a reversal of the electron spin. Such a spin reversal in the transition from the ground state ( $S_0 \rightarrow T_1$ ) is very improbable since the antiparallel electrons are strongly coupled to the ground state.

Upon excitation, electrons in ground state absorb a photon and jump to higher vibrational energy levels of the excited singlet state. The transition from  $S_0$  to higher excited levels  $S_n$  is responsible for the visible and ultraviolet absorption spectra observed. The absorption of photon is highly specific and it takes place in about  $10^{-15}$  second. This time is too short for any significant displacement of nuclei (Frank-Condon principle).

Excitation is followed by a return to the lower vibrational levels of the excited state. With a few rare exceptions, generally all molecules rapidly relax to the lowest vibrational level of  $S_1$ . This process is called internal conversion and occurs in about a picosecond ( $10^{-12}$  s). Typical values of excited-state lifetimes are in the range of nanoseconds ( $10^{-9}$  s). Thus the internal conversion is generally complete before emission takes place. The result is that all observed fluorescence normally originates from the lowest vibrational level of the lowest

excited singlet state. This means that the spectrum of the emitted light should be independent of the excitation wavelength.

From the excited singlet state, the chromophore (chromophore that can fluoresce, also called fluor) returns to the electronic ground state with the emission of the photon. However, the state to which the chromophore decays are not always the lowest vibrational state of the ground state, but it is an equilibrium distribution of vibrational levels. An interesting consequence of these considerations is that the absorption spectrum of the molecule reflects the vibrational levels of the electronically excited states and the emission spectrum reflects the vibrational levels of the ground electronic state.

### 2.2.2 Quantum yield

The quantum yield,  $Q$  is calculated by:

$$Q = \frac{\text{Number of photons emitted}}{\text{Number of photons absorbed}} = \frac{\text{Rate of fluorescence}}{\text{Rate of absorption}}. \quad (22)$$

$Q$  is a measure of a molecule's probability of fluorescence following excitation and takes values in the range 0 to 1. Under a given set of conditions,  $Q$  will usually have a fixed value for a particular chromophore. Molecules with larger quantum yields exhibit stronger fluorescence. The quantum yield is a parameter which depends on the immediate environment of the chromophore.

The number of excited molecules at the exciting wavelength  $\lambda_e$  is proportional to the number of photons absorbed i.e., proportional to  $(I_0 - I)$  where  $I_0$  is the incident intensity and  $I$  is the transmitted intensity. The Beer-Lambert law can be rewritten as,

$$I = I_0 e^{\varepsilon(\lambda_e) \cdot c \cdot l} \quad (23)$$

where  $\varepsilon(\lambda_e)$  is the extinction coefficient at the exciting wavelength,  $\lambda_e$ . The concentration of the absorbing molecules is  $c$  and  $l$  is the path length.

### 2.2.3 Fluorescence Quenching

Information about the properties of macromolecules and their interactions with other molecules can be obtained from studies of the fluorescent spectra. There are many environmental factors that affect fluorescent efficiency. Only a proportion of the light energy

originally absorbed is emitted as radiation, since some energy may be lost in vibrational transitions. Two further processes can diminish or quench the amount of light energy emitted from the sample. Internal quenching is due to some intrinsic structural feature of the excited molecule involving, for example, structural rearrangement. External quenching arises either from interaction of the excited molecule with another molecule present in the sample or absorption of exciting or emitted light by another chromophore present in the sample. All forms of quenching result in a non-radiative loss of energy. External quenching may be due to contaminants present in the preparations. Hence great care must be taken in carrying out fluorescence measurements to ensure the absence of quenchers from the sample and all solutions used.

#### **2.2.4 Resonance Energy Transfer**

Since chromophore has characteristic optical values in both its absorbance and emission spectra, it is possible to establish an experiment in which the emission of one chromophore (A) overlaps with the absorbance of a second chromophore (B). If these separate chromophores have unique locations in a protein or macromolecular complex, it is possible for emission light energy from chromophore A to be absorbed by chromophore B and to be emitted as part of B's emission spectrum. This phenomenon is called resonance energy transfer and since it is strongly dependent on the distance,  $R$ , between the chromophores, it may be used to measure distances in proteins, membranes and macromolecular assemblies especially in the range of 10-80 Å. The efficiency of the energy transfer,  $E$  called Förster transfer depends on the distance  $R$  between the two chromophores.

The efficiency of energy transfer,  $E$  is expressed as following:

$$E = \frac{R_0^6}{R_0^6 + R^6} \quad (24)$$

where  $R$  is the distance between the donor and acceptor molecules and  $R_0$  is a constant related to the donor-acceptor pair which can be calculated from their absorption and emission spectra.

#### **2.2.5 Excitation of chromophore by surface plasmon evanescent field**

The surface plasmon evanescence field can be used to excite the chromophore within the vicinity of the interface. The emitted fluorescence is a strong function of the optical

evanescent field at a given wavelength and the probability of the radiative decay of the chromophore from its excited to the ground state. The optical excitation of the chromophore follows the strength of the evanescent field and since the strength of evanescent field is maximum near the resonance angle, a characteristic increase in the fluorescence signal is observed, which reaches its peak near the resonance angle and then starts decaying as the system moves away from resonance. The peak fluorescence intensities are observed at a slightly lower angle than the actual resonance angle due to certain phase modulations introduced by the nature of the PSP excitation.

It has been shown that chromophores close to the metal surface experience this enhanced evanescent plasmon field and consequently will be excited resonantly [37-40]. Such excitation of fluorescence *via* surface plasmons has been observed for planar systems using prism coupling [41] as well as for grating coupling [47]. Only a few studies are known which use the surface sensitive enhancement for sensing purposes [47,36]. As discussed in chapter 2.1 the evanescent field decays exponentially into the dielectric layer adjacent to the metal film. The penetration depth into the dielectric, at which the surface field intensity drops down to  $1/\epsilon$  of the interface value, is in the order of the used wavelength. Thus, surface sensitive fluorescence measurements are possible, since only dyes in the proximity to the metal film contribute significantly to a measurable signal. Chromophores further away from the metal surface cannot be excited due to a negligible evanescent field.

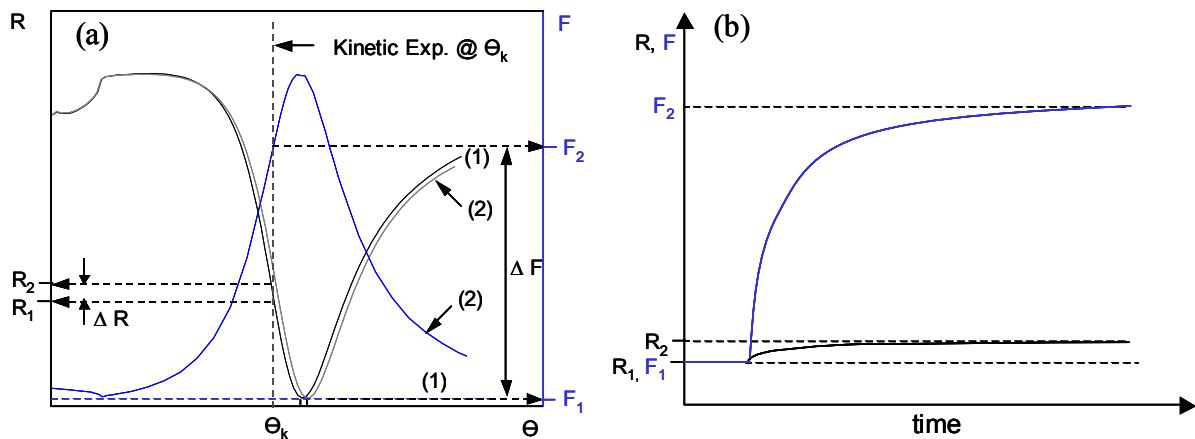


**Figure 2.6.** Fluorescence scan curves (a) and corresponding fluorescence kinetics (b) before (1) and after (2) adsorption of fluorescent labelled analyte onto the sensor surface. Due to the low molecular weight of the analyte change in reflectivity is not significant ( $\Delta R$ ), while the excited fluorescence causes a clear signal difference ( $\Delta F$ ) in both scan and in the kinetics.



In cases where SPS alone is not sensitive alone to detect the adsorption of low molecular fluorescent dyes, a theoretical calibration approach is rather difficult. However, the difference between the observed fluorescence increase during the adsorption of the labelled analyte and the virtually unchanged reflectivity demonstrates the sensitivity enhancement of surface plasmon spectroscopy (SPS) by the additional fluorescence detection in SPFS (Figure 2.6).

### 2.2.6 Fluorescence at the Metal/dielectric Interface

A chromophore is excited by either direct illumination or evanescent surface plasmon fields in front of a planar metallic surface. Since the metal film serves as a mirror the reflected field interferes with the emitting dipole. If the reflected field is in phase with the dipole oscillations, it will be excited by the reflected electromagnetic wave. The dipole will be driven harder and consequently the emission will be enhanced. If the reflected field is out of phase, the emission will be hindered. Thus, the dipole can be considered as a forced, damped, dipole oscillator [42]: it is forced in the way that the field reflected by the boundary provides a driving term for the oscillation of the dipole and it is damped because the oscillator radiates power. With increasing distance between the dipole and the metal surface the phase difference between incident and reflected light alters, which results in an oscillating emission rate of the dipole. Furthermore, with increasing distance of the dye to the metal the strength of the oscillation will decrease. The radiation field of the dipole at the surface weakens with increasing distance to the surface and thus the strength of the reflected field will also decrease. In addition strong quenching of the fluorescence light was found for small emitter-surface separations. Figure 2.7 summarizes the fluorescence according to the distance dependent [43].

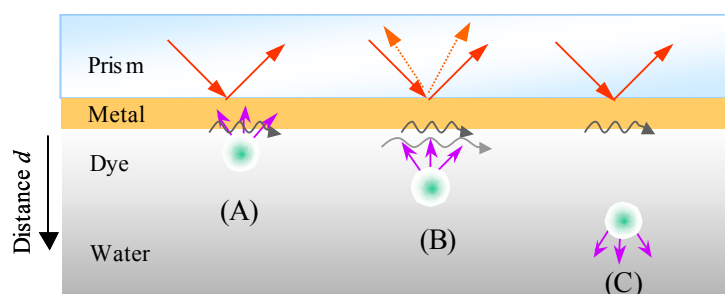


**Figure 2.7.** Schematic of fluorescence near metallic surfaces at different distance from metal to chromophors. (A) Non-radiative transition and exciton coupling, (B) coupling to surface plasmon modes, (C) emission of photons.

If the chromophore is very close to the metal within 10 nm (Figure 2.7 (A)), a substantial de-excitation (radiation-less) with corresponding reduction of radiative lifetime and the fluorescence intensity is found. The fluorescence is quenched dissipating the excitation energy in the metal as heat.

In an intermediate distance ( $<20$  nm, Figure 2.7 (B)), the optically excited chromophores can couple back effectively to surface plasmon polaritons, by fulfilling momentum-matching conditions. However, some of the excitation energy is dissipated in the chromophore. The corresponding back-coupled surface plasmon is red-shifted relative to the excitation and re-radiates (dashed arrows) *via* a prism at a slightly smaller angle.

At sufficient separation distances ( $>20$  nm, Figure 2.7 (C)), free emission of the chromophore dominates. The fluorescence yield depends on the intensity of evanescent field which is decreased exponentially as the distance increases and the fluorescence emission oscillates reflected from metal.

## 2.3 Self-Assembled Monolayers

Molecular self-assembly is a process in which molecules spontaneously form ordered aggregates and involves no human intervention; the interactions involved usually are noncovalent. In molecular self-assembly, the molecular structure determines the structure of the assembly [44]. Self-assembly is scientifically interesting and technologically important for several reasons. The first is that it is important in life. The cell contains an astonishing range of complex structures such as lipid membranes, folded proteins, structured nucleic acids, protein aggregates, molecular machines, and many others that form by self-assembly [45]. The second is that self-assembly provides routes to a range of materials with regular structures: molecular crystals [46], liquid crystals [47], and semicrystalline and phase-separated polymers [48] are examples. Third, self-assembly also occurs widely in systems of components larger than molecules, and there is great potential for its use in materials and condensed matter science [49]. Fourth, self-assembly seems to offer one of the most general strategies available for generating nanostructures. Thus self-assembly is important in a range of fields: chemistry, physics, biology, materials science, nanoscience, and manufacturing.

### 2.3.1 Principle of self-assembly

A self-assembling system consists of a group of molecules or segments of a macromolecule that interact with one another. These molecules or molecular segments may be the same or different. Their interaction leads from some less ordered state (a solution, disordered aggregate, or random coil) to a final state (a crystal or folded macromolecule) that is more ordered [50].

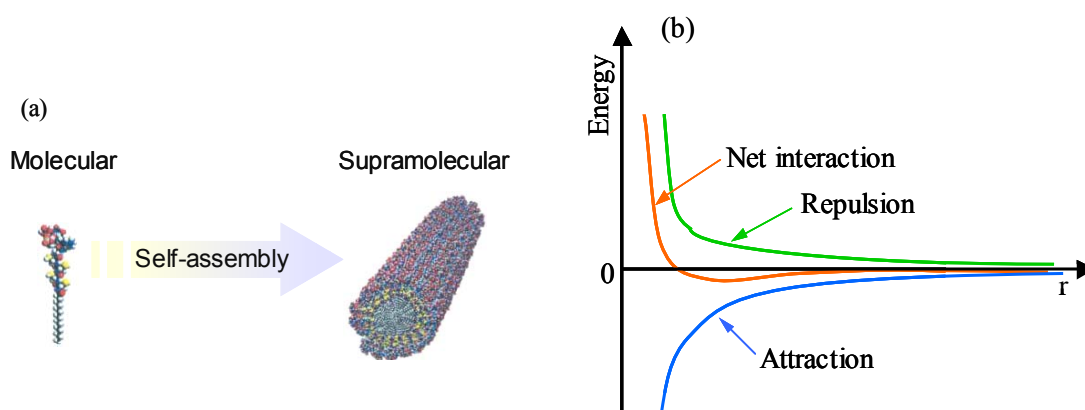
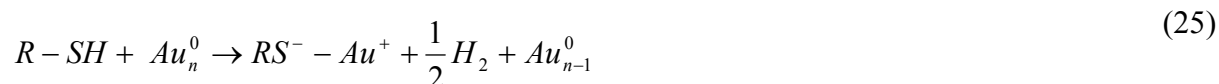


**Figure 2.8.** Aggregation occurs when there is a net attraction and an equilibrium separation between the components. The equilibrium separation normally represents a balance between attraction and repulsion. These two interactions are fixed in molecular self-assembly but can be engineered independently in macroscopic self-assembly.

Self-assembly occurs when molecules interact with one another through a balance of attractive and repulsive interactions (Figure 2.8 (b)). These interactions are generally weak and noncovalent (van der Waals and Coulomb interactions, hydrophobic interactions, and hydrogen bonds for self-assembly [51,52].

### 2.3.2 Self-assembled monolayers of alkanethiol on Au (111)

Among the known SAMs, alkanethiols  $[\text{CH}_3(\text{CH}_2)_n\text{SH}]$  on Au(111) are one of the most studied systems due, mainly, to their stability and ease of preparation on atomically flat Au surfaces. From a chemical point of view, the attachment of the thiol to the Au surface is believed to proceed through a Au-S bonding mechanism, which is known to be sufficiently strong and stable, with bond energies typically of  $\sim 48 \text{ kcal/mol}^{-1}$  [53,54]. Extensive X-ray photoelectron spectroscopic (XPS) experiments suggest that chemisorption of alkanethiols on gold (0) surfaces yields the gold (I) thiolate (R-S-) species. The presumed adsorption chemistry is:



which infers an oxidative addition of the S-H bond to the Au surface, followed by a reductive elimination of the hydrogen. Thus, the liquid-phase formation of the monolayers is a two-step process involving chemical bonding of the molecules by diffusion to the surface followed by selfassembly aided by van der Waals interactions [72].

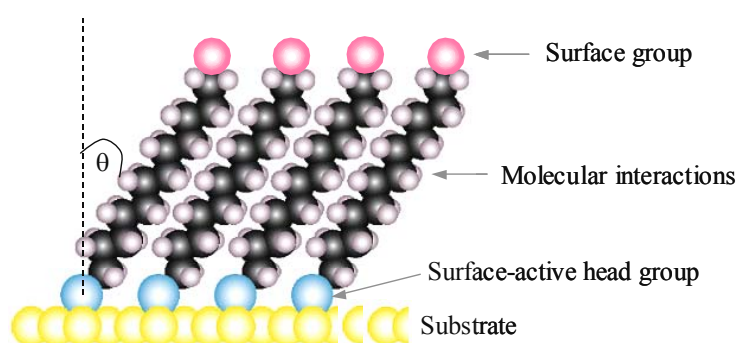


**Figure 2.9.** Self-assembled monolayers of alkanethiols on substrate (gold). The angular orientation of assembled molecules is  $30^\circ$  with respect to the surface normal. The surface-active head group (sulfur) is adsorbed chemically to the substrate. Van der Waals interactions are the main force in the simple alkyl chains. The surface group (tail group) could be modified with functional group (-OH, -COOH, -NH<sub>2</sub>, and so on) for further investigation.

The typical tilt angles for alkanethiols on gold consisting of methylene side chains is ca.  $30^\circ$  with respect to the surface normal (Figure 2.9). This orientation is preferred since it minimizes the van der Waals interactions between the side chain units.

## 2.4 Biotin-Streptavidin Interaction

Streptavidin is a protein produced by the bacterium *Streptomyces avidinii* and isolated by purification from fermentation broth. The protein consists of 4 identical subunits, each bearing an active binding site for biotin [55-58] with high affinity constant ( $K_A \sim 10^{13} \text{ M}^{-1}$ ) [59-61]. Streptavidin is non-glycosylated and do not react unspecifically with endogeneous lectins when used in immunological assays on cells and tissues. Streptavidin is non- or very low charged around pH 7, reducing nonspecific binding to charged molecules to a very

limited level [62-64]. The dimensions of the protein were determined by X-ray scattering [77,65] to be 5.6nm x 4.2nm x 4.2nm [66].

Biotin (B-vitamin, 244 g/mol) plays an essential role in a number of important body processes. Biotin also helps produce certain enzymes. Biotin is synthesized by bacteria, yeast and other fungi, algae and certain plant species. The biotins are found in so many foods, including rice, barley, oatmeal, whole wheat, soy products, and cauliflower. Biotin deficiency results such as brittle nails and lackluster hair [67].

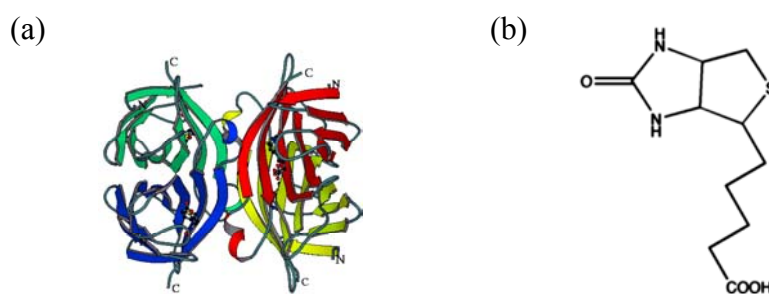


**Figure 2.10.** Structures of (a) tetrameric streptavidin and (b) biotin. copyright © Stefanie Freitag.

The binding pocket is constructed showing three different binding motifs with the ligand as reported in the structures of the streptavidin-biotin complex by Weber et al., 1989 and Hendrickson et al., 1989 and also observed in structures [67-70]: (a) hydrophobic and van der Waals interactions of mainly four streptavidin tryptophan side chains, (b) an effective hydrogen bonding network, (c) a binding surface loop, which folds over the ligand (Figure 2.11).

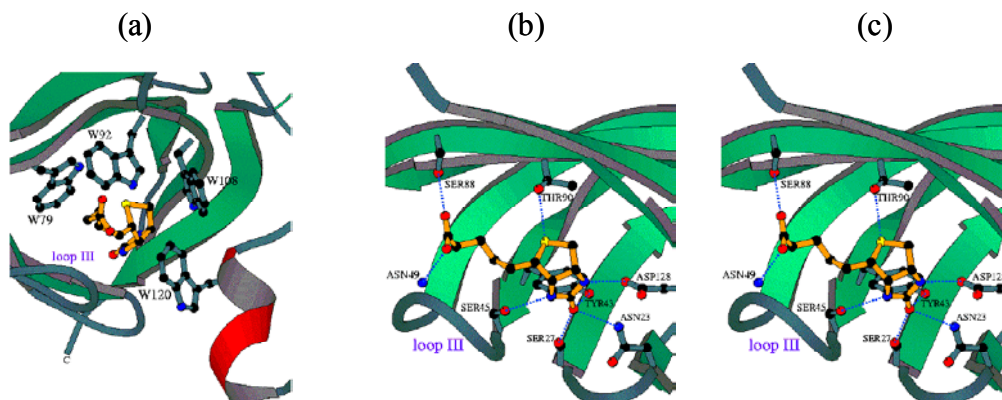


**Figure 2.11.** Interactions between streptavidin and biotin. copyright © Stefanie Freitag

## 2.5 Analysis of Biomolecular Interaction on the Surface

### 2.5.1 Simple Langmuir Model

The Langmuir model [71,72] was used in this study to analysis kinetics and equilibrium constants in the case of specific interaction between immobilized probe PNA and target DNA in solution. The Langmuir model assumes that all binding sites are equivalent and already occupied sites do not influence the binding reaction in adjacent places and the surface is homogenously covered by monolayers.

In a basic SPR biosensor experiment, PNA probes (A) are attached to the sensor surface. Then DNA targets (B) interact with PNA probes (A) forming a complex (AB) with increasing of response. Figure 2.12 shows the interactions that occur at the sensor surface. Because binding responses are recorded in real time, it is possible to interpret kinetic information about the interaction [73].

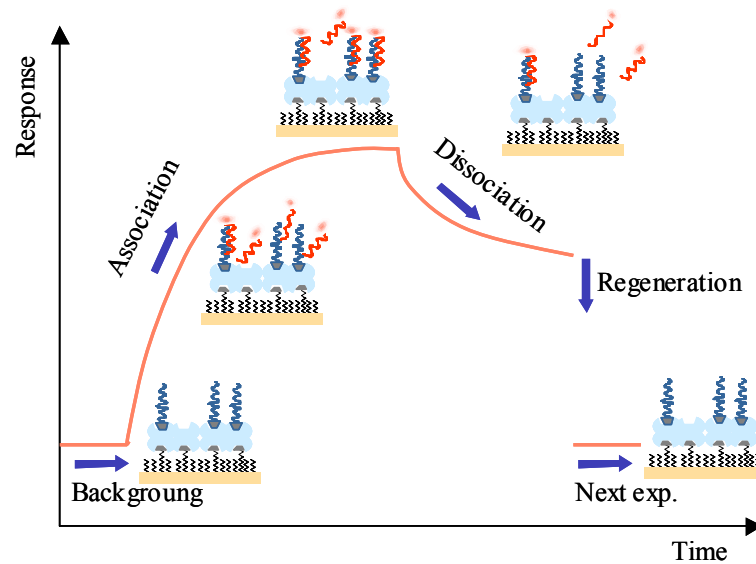


**Figure 2.12.** A typical kinetic curve of molecular interaction on the surface; after short background measurement, the association phase is observed by introduce of target to probe immobilized sensor surface, then dissociation phase is carried out by changing the target solution to fresh buffer solution. For next experiment the surface is regenerated by chemical solution (strong acid or base).

The processes at the surface can be described by the rate constants of the adsorption,  $k_{on}$  and the one of dissociation,  $k_{off}$  from the surface (Figure 2.12). The resulting time dependent surface coverage  $\Theta$  can be described by the following equation:

$$\frac{\partial \Theta}{\partial t} = c_0 \cdot k_{on} (1 - \Theta) - k_{off} \Theta \quad (27)$$

where  $c_0$  is the concentration of the binding species in solution. According to this equation the surface will be occupied until all binding sites are blocked. Then  $(1-\Theta)$  equals zero and this will occur the fastest when the concentration in solution is high. On the other hand, dissociation is only dependent on the rate  $k_{off}$  and on the actual number of covered binding sites. Integration of (Equation. 27) with the initial condition  $\Theta = 0$  at  $t = 0$  leads to

$$\Theta(t) = \frac{c_0 \cdot k_{on}}{c_0 \cdot k_{on} + k_{off}} (1 - \exp(-(k_a)t)), \quad k_a = k_{on} \cdot c_0 + k_{off}. \quad (28)$$

In the case of a real experiment the dissociation process can be followed separately by exchanging the analyte solution against pure buffer, since then the concentration  $c_0$  equals zero. Thus, the rate constant  $k_{off}$  can be determined according to:

$$\Theta(t) = \Theta_0 \exp(-k_{off} \cdot t) \quad (29)$$

where  $\Theta_0$  is the surface coverage at the beginning of the dissociation process. Here it is assumed that the desorbed molecules are prevented from re-adsorption by continuous rinsing with pure buffer solution. Practically, the dissociation process should be fitted simultaneously with the simulation of the adsorption process. Thus, dissociation rate,  $k_{off}$  is assured to be identical in both processes.

### 2.5.2 Global Analysis

For a detailed kinetic analysis, it is important to perform a suitable experiment which gives a reliable value. Kinetic information could be collected from SPR (or SPFS) data by fitting to the obtained binding responses for a simple one-to-one interaction model [74-77]. It has been shown that fitting association and dissociation phase data for a series of concentrations simultaneously (referred to as global analysis) can be used to determine the rate constants [88]. Global analysis was first used to interpret protein-DNA interactions [78]

and this analytical method was successful in fitting two different antigen-antibody interactions to a simple one-to-one reaction model [79,80].

In this study, the association kinetics is quantified with respect to the concentration dependence starting every initial probe surface (by regeneration) during the beginning (first 10 min) of binding process. Fitting the association phase data recorded from starting the injection of target to changing the pure buffer with equation (28) the rate constants  $k_a = k_{on} \cdot c_0 + k_{off}$  were obtained individually at different target concentrations. The time-dependent dissociation is described by equation (29): The dissociation is sufficiently enhanced and leads to a measurable loss of response intensity even within the 10 min of the rinsing phase of the analysis (Figure 2.13).

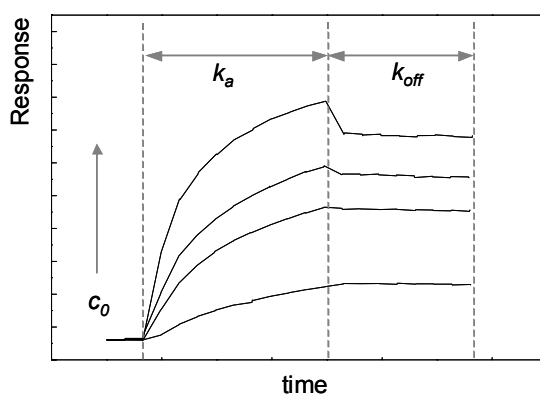


**Figure 2.13.** A typical set of global analysis. By increasing the target concentration, the reliable data set with association and dissociation phase is measured for short time.

The global analysis turned out to be the fastest and most reliable method to determine association rate constant because it analyses only early stages of the binding. For rather stable complexes (for zero mismatched oligonucleotides target to probe) a 10 min rinsing phase is not sufficient to see a significant dissociation that can be analyzed quantitatively. However, it is very well suited to obtain the dissociation rate in the case of a single base mismatched double strand during the rinsing step resulting in a visible loss of response that allows for a quantitative determination of  $k_{off}$  in addition to  $k_{on}$ , and hence can also give the affinity constant  $K_A$ .

### 2.5.3 Langmuir adsorption isotherm

It is possible to monitor the complete Langmuir adsorption isotherm if the surface is saturated stepwise. For this the sample is immersed in solutions of increasing concentration of



the adsorbing species and the system is allowed to be equilibrium before a further increase in bulk concentration. Thus, the starting value of the surface coverage for the individual adsorption curves is larger than zero for the subsequent steps. In case of such stationary surface coverage a simple correlation to the equilibrium constant  $K$  of the reaction can be derived:

$$\Theta = \frac{c_0 \cdot K}{1 + c_0 \cdot K} \quad (30)$$

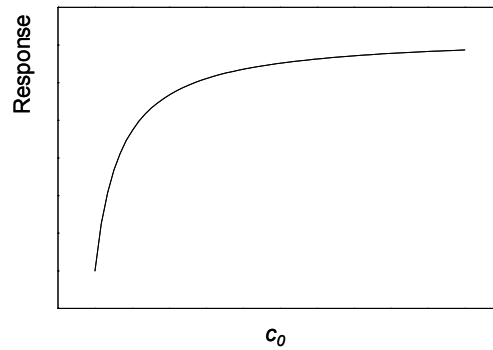


**Figure 2.14.** A typical curve of Langmuir adsorption isotherm taken titration experiment. The surface coverage is dependent on the target concentration.

The typical titration experiment allows for the determination of the Langmuir adsorption isotherm (Figure 2.14) and, hence, the affinity constant  $K_A$  based on the evaluation of surface coverages.

## 2.6 Nucleic Acids

In 1868, almost a century before the Nobel Prize was awarded to Watson, Crick, Wilkins, and Friedrich isolated something no one had ever seen before from the nuclei of cells [92]. He called the compound "nuclein." This is today called nucleic acid, the "NA" in DNA (deoxyribo-nucleic-acid) and RNA (ribo-nucleic-acid). Our bodies are formed from between 50 and 100 trillion cells (a trillion is a thousand billion, or a thousand, thousand million). These cells are organized into tissues, such as skin, muscle, and bone. Each cell contains all of the organism's genetic instructions stored as deoxyribonucleic acid (DNA) (Figure 2.15). The long DNA molecule is tightly wound and packaged as a chromosome. Humans have two sets of 23 chromosomes in every cell, one set inherited from each parent. A human cell therefore contains 46 of these chromosomal DNA molecules. Each DNA molecule that forms a

chromosome can be viewed as a set of shorter DNA sequences. These are the units of DNA function, called genes, each of which guides the production of one particular component of an organism.

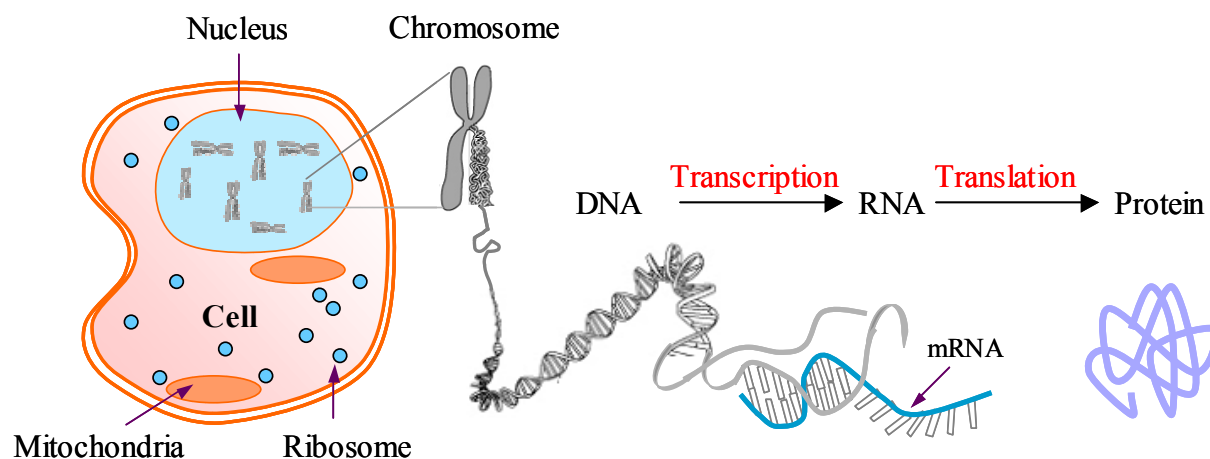


**Figure 2.15.** This drawing provides a graphic overview of the steps involved in transcription and translation. Within the nucleus of the cell, genes (DNA) are transcribed into RNA. This RNA molecule is then subject to post-transcriptional modification and control, resulting in a mature mRNA molecule that is then transported out of the nucleus and into the cytoplasm where it undergoes translation into a protein. mRNA molecules are translated by ribosomes that match the three-base codons of the mRNA molecule to the three-base anti-codons of the appropriate tRNA molecules.

A set of human chromosomes contains one copy of each of the roughly 30,000 genes in the human "genome" the term used to refer to the complete genetic instructions for an organism. Within a gene, the sequence of nucleotides along a DNA strand defines a protein, which an organism is liable to manufacture or "express" at one or several points in its life using the information of the sequence. The relationship between the nucleotide sequence and the amino-acid sequence of the protein is determined by simple cellular rules of translation, known collectively as the genetic code. The genetic code is made up of three letter 'words' formed from a sequence of three nucleotides (eg. ACT, CAG, TTT). These codons can then be translated with messenger RNA and then transfer RNA, with a codon corresponding to a particular amino acid. Since there are 64 possible codons, most amino acids have more than one possible codon. There are also three 'stop' or 'nonsense' codons signifying the end of the coding region.

### 2.6.1 DNA

Deoxyribonucleic acid (DNA) is a nucleic acid which carries genetic instructions for the biological development of all cellular forms of life and many viruses. The nucleotides are linked together by phosphodiester bonds to form a polynucleotide chain. Each nucleotide consists of a phosphate group, a five-carbon sugar deoxyribose and one of four different nitrogenous bases, i.e. Adenine (A), Guanine (G), Cytosine (C) and Thymine (T). The native state of the DNA duplex is known as a double helix, which essentially resembles a twisted ladder structure. In the double helix, two polynucleotide chains combine via base-pairing between nucleotide units in the individual chains (Figure 2.16).

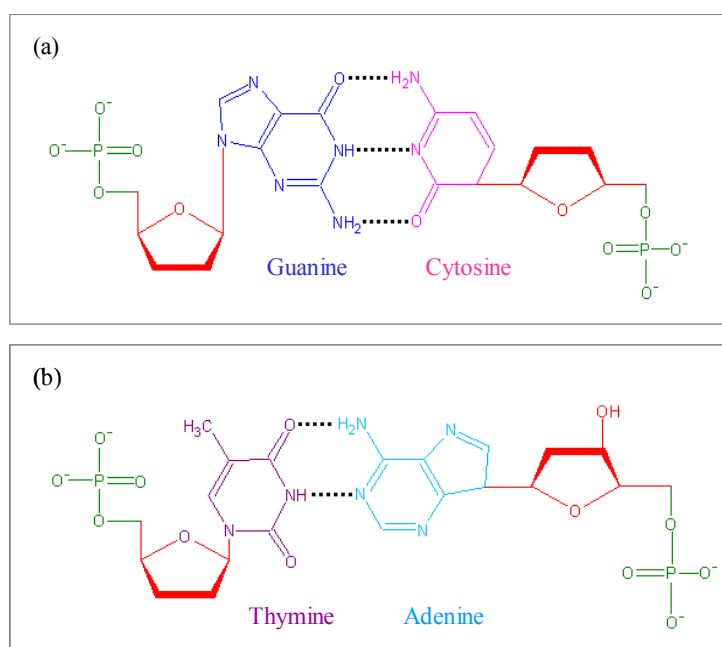


**Figure 2.16.** The base pairs of G-C and A-T.

The orientation of the two chains are antiparallel: one chain runs from 3' to 5' and the other runs from 5' to 3'. According to Chargaff's rule, the sum of the purine bases (A, G) in a duplex equals the sum of pyrimidines (T, C). The reason for this is the characteristic Watson-Crick's basepair formation between the adenine- thymine, and guanine-cytosine by hydrogen bonds [81].

The DNA helix can assume one of three slightly different geometries (A, B and Z), of which the "B" form described by James D. Watson and Francis Crick is believed to predominate in cells. It is 2 nanometres wide and extends 3.4 nanometres per 10 bp of sequence (Figure 2.17). This is also the approximate length of sequence in which the helix makes one complete turn about its axis. This frequency of twist (known as the helical *pitch*) depends largely on stacking forces that each base exerts on its neighbors in the chain. The B form of the DNA helix twists  $360^\circ$  per 10.6 bp in the absence of strain. But many molecular biological processes can induce strain. A DNA segment with excess or insufficient helical twisting is referred to, respectively, as positively or negatively "supercoiled". DNA *in vivo* is typically negatively supercoiled, which facilitates the unwinding of the double-helix required for RNA transcription.

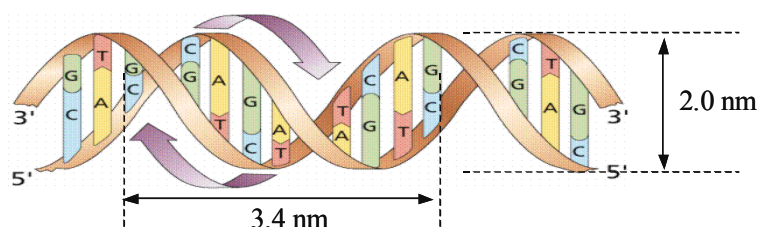


**Figure 2.17.** The B form of the DNA helix.

### 2.6.2 PNA

Synthetic oligonucleotides have shown immense promise and have been extremely useful in gene activation and repression strategies over the past 20 years. However, several factors have limited their potential, most importantly the susceptibility to nuclease digestion. Less than 10 years ago, Nielsen and colleagues developed an oligonucleotide analog in which the phosphodiester backbone was replaced with a polyamide to create a peptide nucleic acid (PNA) (Figure 2.18) [82-85]. PNAs are nucleic acid analogs in which the phosphodiester backbone has been replaced with a polyamide backbone made up of repeating *N*-(2-aminoethyl)glycine units [93]. The purine and pyrimidine bases are attached to the backbone and extend out in a conformation that is remarkably similar, both in spacing and geometry, to DNA. PNAs can bind to either single-stranded DNA or RNA, in which the resulting hybrid resembles the B-form of DNA [86-89]. Like DNA base-pairing (bp) affinity of the PNA–DNA or PNA–RNA complex is determined by the base pair composition of base pairs.

This modified oligonucleotide, PNA displayed high affinity and specificity of binding to DNA and RNA and showed great resistance to both nucleases and proteases. Although initially designed to function as antisense and antigene reagents, these molecules have recently found more applications that make them ideal for the development of a variety of novel gene therapy approaches, including gene activation and plasmid delivery.

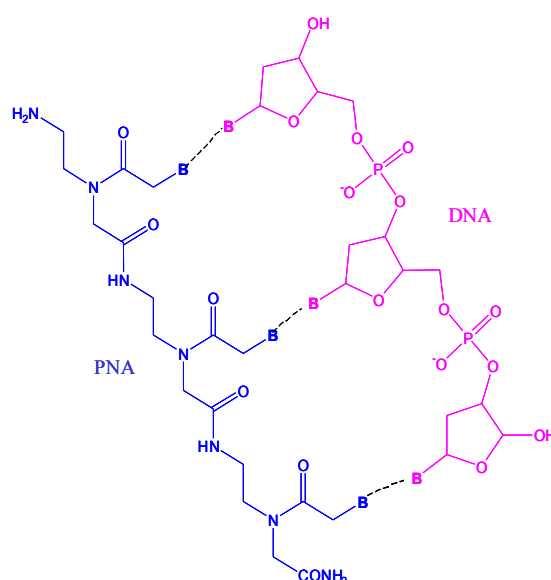


**Figure 2.18.** Structures of double strand of PNA and DNA hybridization.

### 2.6.3 Stability of nucleic acids duplex

The stability of duplex (DNA or PNA) is dependent on temperature, pH, ionic strength or chaotropic agents the hydrogen bonds or the hydrophobic interactions are disrupted. If double stranded DNA is subjected to extreme conditions, the DNA could be denatured and changed from a double strand to a random coil of single strands. The temperature at which 50% of all strands are separated into ssDNA (single strand DNA) is called the melting temperature  $T_m$ . The bases in the DNA strands absorb light at 260nm. This absorption is partially suppressed in double stranded DNA due to stacking interaction of the bases. The increase in absorbance upon melting is referred to as hyper-chromic effect and can be used to monitor DNA melting quantitatively by UV spectroscopy.

The stability of duplex DNA and hence the melting temperature is dependent on several factors [90,91]:

- (C+G) content of the DNA: Since a G-C pair has three hydrogen bonds and T-A only two, the stability of the duplex is influenced by the content of cytosine and guanine.
- Length of the sequence: with increasing chain length  $T_m$  increases and the slope of the melting curve at  $T_m$  becomes steeper.
- Sequence dependent nearest neighbour and end effects: the stacking interaction between two neighboured bases along the chain is dependent on their identity.
- Presence of hydrogen bond disrupting agents like formamide or urea.
- Mismatches: If a double strand contains one or more non-complementary base pair combinations like AA, AC, GG, CT etc. the stability of the duplex is reduced. The number of hydrogen bonds is reduced and the cooperative stacking effect is influenced. Hence the stability of the whole strand is affected. The destabilising effect of a single mismatch decreases as the chain length increases. As a rule of thumb, 1% mismatch causes a decrease of about 1°C in  $T_m$  for duplexes < 100 bp.
- Ionic strength and pH of the solvent: At high salt concentrations, the negative charges in the DNA backbone are screened; the melting temperature is increased and the melting curve shows a sharp transition.

#### **2.6.4 DNA Amplification- Polymerase Chain Reaction**

In 1985, Kary B. Mullis invented a sensational method for multiplying DNA, and called it Polymerase Chain Reaction (PCR, Figure 2.19) [92-94]. The PCR allows the million-fold amplification of a target DNA fragment in a highly sensitive and specific manner. Therefore, two primers (synthetic oligonucleotides) frame the target sequence. Each primer is complementary to either one of the two strands from the double stranded DNA target. Starting from a primer attached to the target sequence, an enzyme (*Taq*-polymerase) can generate a complementary copy of this sequence. This allows the duplication of the target sequence in each reaction cycle. In consecutive reaction cycles the number of target sequences grows exponentially according to the number of cycles.

The PCR is subdivided into three steps.

- (1) **Denaturation:** During denaturation, the template-DNA is separated (denaturated) into its two separate strands by heating up the temperature to 94°C.

- (2) **Annealing:** The temperature is lowered to a degree (calculated in advance) specific for the primer (oligonucleotide), which generally lies between 55°C and 70°C. This guarantees, that the primer takes its place at the specific DNA-recognition-sequence (according to their complementary) of the single-stranded DNA-template-sequence (annealing).
- (3) **Extension:** The third step, the synthesizing, takes place at a temperature of 72°C degrees. This corresponds to the optimal temperature for the Taq-polymerase enzyme to work. The polymerase ensuingly prolongues the paired short oligonucleotides according to the DNA-matrix, until the double-stranded DNA-molecule is complete again.

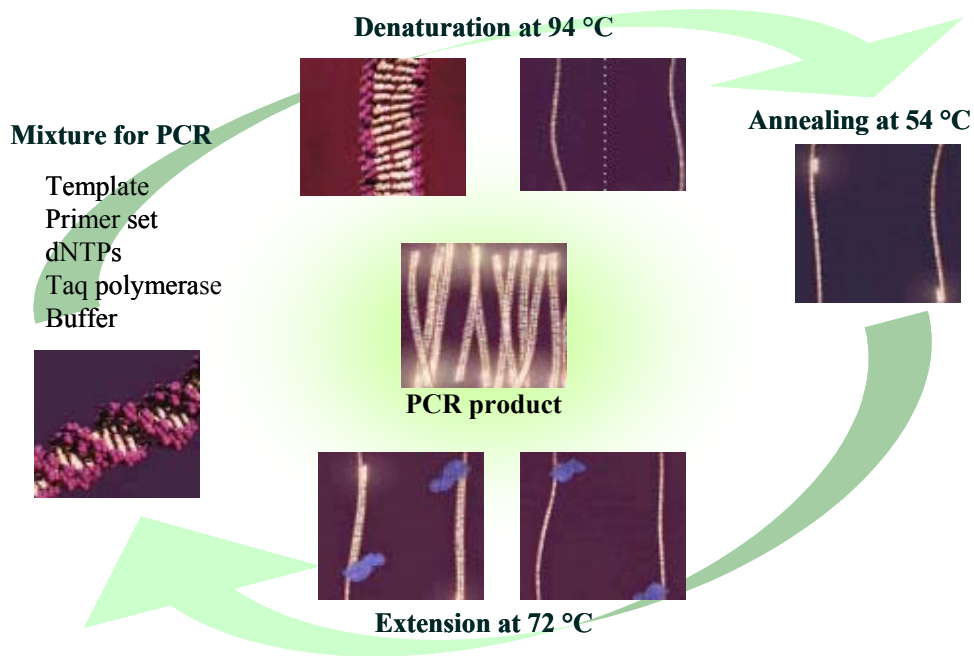


**Figure 2.19.** Schematic drawing of PCR

The number of amplified products is described [95]:

$$N_f = N_0(1 + Y)^n \quad (31)$$

where  $N_f$  is the copy number of the amplified sequence after  $n$  cycles of amplification,  $N_0$  is the initial copy number of target sequence in the DNA template, and  $Y$  is the efficiency of amplification (normally 70%) per cycle. Generally, the number of amplification is  $10^{12}$  copies of PCR products after 29 cycles with  $3 \times 10^5$  of template.

## 2.7 References

- [1] Rothenhäusler, B.; Knoll, W. *Nature*, **1988**, 332, 615-617.
- [2] Nakajima, F.; Hirakawa, Y.; Kaneta, T.; Imasaka, T. *Anal. Chem.*, **1999**, 71, 2262-2265.
- [3] Homola, J.; Koudela, I.; Yee, S. S. *Sens. Actuator B.*, **1999**, 54, 16-24.
- [4] Yu, F.; Yao, D.; Knoll, W. *Nucleic Acids Res.*, **2004**, Vol. 32, No. 9 e75.
- [5] Culha, M.; Stokes, D. L.; Griffin, G.D.; Vo-Dinh, T. *Biosens. Bioelectron.* **2004**, 19, 1007-1012.
- [6] Fang, X. H.; Sen, A.; Vicens, M.; Tan, W. H. *Chembiochem.* **2003**, 4, 829-834.
- [7] Liebermann, T.; Knoll, W. *Colloid. Surface. A.* **2000**, 171, 115–130.
- [8] Kroger, K.; Jung, A.; Reder, S.; Gauglitz, G. *Anal. Chim. Acta.* 2002, 469, 37-48.
- [9] Shipman, L. L. *Biophys. J.* **1978**, 21, A107-A107.
- [10] Tadjeddine, A.; Kolb, D. M.; Kötz, R. *Surf. Sci.* **1980**, 101, 277.
- [11] Gordon, J. G., II; Ernst, S. *Surf. Sci.* **1980**, 101, 499.
- [12] Iwasaki, Y.; Horiuchi, T.; Morita, M.; Niwa, O. *Electroanalysis*, **1997**, 9, 1239.
- [13] Laschitsch, A.; Menges, B.; Johannsmann, D. *Appl. Phys. Lett.* **2000**, 77, 2252-2254.
- [14] Bund, A.; Baba, A.; Berg, S. et al. *J. Phys. Chem. B.* **2003**, 107, 6743-6747.
- [15] Bailey, L.E.; Kambhampati, D.; Kanazawa, K.K. et al. *Langmuir*, **2002**, 18, 479-489.
- [16] Wood, R. W. *Proceeding of the Physical Society of London*, **1902**, 269-275.
- [17] Otto, A. *Z. Phys.* **1968**, 216, 398.
- [18] Kretschmann, E.; Raether, H. *Zeitschrift für Naturforschung Part A*, **1968**, A23, 2135.
- [19] Agarwal, G. S. *Physical review B.* **1973**, 8, 4768-4779.
- [20] Knoll, W. *Annu. Rev. Phys. Chem.* **1998**, 49, 569-638.
- [21] Burstein, E.; Chen, W.P.; Chen, Y. J.; Hartstein A. . *J. Vac. Sci. Technol.* **1972**, 11, 1004-1019.
- [22] Aust, E.; Ito, S.; Knoll W. *Scanning*, **1994**, 16, 353–361.
- [23] Hickel, W.; Rothenhäusler, B.; Knoll, W. *J. Appl. Phys.* **1989**, 66, 4832–4836.
- [24] Gordon, J. G II; Swalen, J. D. *Opt. Commun.* **1977**, 22, 374–78.
- [25] Bryant, M. A.; Pemberton, J. *J. Am. Chem. Soc.* **1991**, 113, 8284.
- [26] Nemetz, A.; Knoll, w.; *J. Raman Spectrosc.* **1996**, 27, 587-592.



- [27] Nemetz, A.; Fernandez, U.; Knoll, W. *J. Appl. Phys.* **1994**, 75, 1582-1585.
- [28] Liebermann, T.; Knoll, W. *Colloid. Surface. A.* **2000**, 171, 115–130.
- [29] Mol, N. -J.; Plomp, E.; Fischer, M. -J. -E.; Ruijtenbeek, R. *Anal. Biochem.* **2000**, 279, 61-70.
- [30] Kambhampati, D.; Nielsen P. -E.; Knoll, W. *Biosens. Bioelectron.* **2001**, 16, 1109-1118.
- [31] Christopoulos, T. K. & Diamandis, E. P. *Immunoassay*, Academic Press, San Diego, **1996**.
- [32] Smith, D. J. *FEBS. Lett.* **77**, **1997**.
- [33] Lin, M. & Nielsen, K. J. *Bioconjugate Chem.* **1997**, 4.
- [34] Smith, D. J. *FEBS. Lett.* **1977**, 25-27.
- [35] Ullman, E. F.; Schwarzberg, M.; Rubenstein, K. E. *J. Biol. Chem.* **1976**, 251, 4172-4178.
- [36] Lazowski, K. W., Kaczmarek, L. *Antisense Nucleic Acid Drug Dev.* **2000**, 10, 97-103.
- [37] Kitson, S. C.; Barnes, W. L.; Sambles, J. R.; Cotter, N. P. K. *Journal of modern optics.* **1996**, 43, 573-582.
- [38] Knobloch, H.; Brunner, H.; Leitner, A.; Aussenegg, F.; Knoll, W. *J. Chem. Phys.* **1993**, 98, 10093-10095.
- [39] Attridge, J. W.; Daniels, P. B.; Deacon, J. K.; Robinson, G. A.; Davidson, G. P. *Biosens Bioelectron.* **1991**, 6, 201-14.
- [40] Eagen, C. F.; Weber, W. H.; McCarthy, S. L.; Terhune, R. W. *Chemical Physical Letters.* **1980**, 75, 274-277.
- [41] Benner, R. E.; Dornhaus, R.; Chang, R. K. *Optics. Commun.* **1979**, 30, 145.
- [42] Barnes, W. L. *Journal of Modern optics.* **1998**, 45, 661-699.
- [43] Neumann, T.; Johansson, M. -L.; Kambhampati, D.; Knoll, W. *Adv. Funct. Mater.* **2002**, 12, 575-586.
- [44] Whitesides, G. M.; Simanek, E. E.; Gorman, C. B. in *NATO Advanced Study Institute on Chemical Synthesis: Gnosis to Prognosis*, **1990**, 565–588.
- [45] Alberts, B.; Bray, D.; Lewis, J.; Raff, M.; Roberts, K.; Watson, J. D. *Molecular Biology of the Cell*, Garland, New York, **1994**.
- [46] Schwiebert, K. E.; Chin, D. N.; MacDonald, J. C.; Whitesides, G. M. *J. Am. Chem. Soc.* **1996**, 118, 4018–4029.
- [47] Schmidt-Mende, L.; Fechtenkotter, A.; Mullen, K.; Moons, E.; Friend, R. H.; MacKenzie, J. D. *Science*, **2001**, 293, 1119–1122.
- [48] De Rosa, C.; Park, C.; Thomas, E. L.; Lotz, B. *Nature*, **2000**, 405, 433–437.

- [49] Whitesides, G. M. *Sci. Am.* **1995**, 273, 146–149.
- [50] Whitesides, G. M.; Boncheva, M. *Proc. Natl. Acad. Sci.* **2002**, 99, 4769–4774.
- [51] Olenyuk, B.; Whiteford, J. A.; Fechtenkötter, A.; Stang, P. J. *Nature*, **1999**, 398, 796–799.
- [52] Lehn, J.-M. *NATO ASI Ser. Ser. E.* **1990**, 320, 511–524.
- [53] Dubois, L. H.; Nuzzo, R. G. *Ann. Phys.* **1992**, 43, 437.
- [54] Schlenoff, J. B.; Li, M.; Ly, H. *J. Am. Chem. Soc.* **1995**, 117, 12528.
- [55] Bayer, E. A.; Wilchek, M. *Trends Biochem. Sci.* **1978**, 3, 237–239.
- [56] Skutelsky, E.; Bayer, E. A. *Biol. Cellul.* **1979**, 36, 237–252.
- [57] Bayer, E. A.; Wilchek, M. *Methods Biochem. Anal.* **1980**, 26, 1–45.
- [58] Wilchek, M.; Bayer, E. A. *Immunol. Today.* **1984**, 5, 39–43.
- [59] Skutelsky, E.; Bayer, E. A. *J. Med. Sci.* **1979**, 15, 675–686.
- [60] Bayer, E. A.; Wilchek, M. *J. Chromatogr.* **1990**, 510, 3–11.
- [61] Balass, M., E.; M., Bayer, E. A.; Fuchs, S.; Wilchek, M.; Katchalski-Katzir, E. *Anal. Biochem.* **1996**, 243, 264–269.
- [62] Athappilly, F.K.; Hendrickson, W. A. *Protein Science*, **1997**, 6, 1338–1342.
- [63] Wilchek, M.; Bayer, E. A. *Trends Biochem. Sci.* **1989**, 14, 408–412.
- [64] Wilchek, M.; Bayer, E. A. *Anal. Biochem.* **1988**, 171, 1–32.
- [65] Hendrickson, W. A.; *Proc. Natl. Acad. Sci.* **1989**, 85, 2190–2194.
- [66] Ebersole, R. C.; Miller, J. A.; Moran, J. R.; Ward, M. d. *J. Am. Chem. Soc.* **1990**, 112, 3239.
- [67] Weber, P. C.; Wendoloski, J. J.; Pantoliano, M. W.; Salemme, F. R. *J. Am. Chem. Soc.* **1992**, 114, 3197–3200.
- [68] Weber, P. C.; Ohlendorf, D. H.; Wendoloski, J. J.; Salemme, F. R. *Science*, **1989**, 243, 85–88.
- [69] Hendrickson W.A. *Science*, **1991**, 254, 51–58.
- [70] Weber P. C.; Pantoliano, M. W.; Thomson L.D. *Biochemistry*, **1992**, 31, 9350–9354.
- [71] Atkins, P. W. *Physikalische Chemie*, VCH, **1990**.
- [72] Ulman, A. *An Introduction to Ultrathin Organic Films*, Academic Press, **1991**.
- [73] Myszkowski, D. G. *Current Opinion in Biotechnology* **1997**, 8, 50–57.

- [74] O'Shannessy, D.; Brigham-Burke, M.; Soneson, K. K.; Hensley, P.; Brooks, I. *Anal Biochem* **1993**, 212, 457-468.
- [75] O'Shannessy, D.; Winzor, D. J. *Anal Biochem* **1996**, 236, 275-283.
- [76] Cheskis, B.; Freedman, L. P. *Biochemistry* **1996**, 35, 3309-3318.
- [77] Morton, T. A.; Myszka, D. G.; Chaiken, I. M. *Anal Biochem* **1995**, 227, 176-185.
- [78] Fisher, R. J.; Fivash, M.; Casas-Finet, J.; Erickson, J. W. et al. *Science* **1994**, 3, 257-266.
- [79] Roden, L. D.; Myszka, D. G. *Biochem Biophys Res Commun* **1996**, 225, 1073-1077.
- [80] Karlsson, R.; Falt A. *J. Immunol Methods* **1997**, 200, 121-133.
- [81] Watson, J. D.; Crick, F. H. C. *Nature*. **1953**, 71, 737-738.
- [82] Nielsen, P.E.; Egholm, M.; Berg, R.H. *Science* **1991**, 254, 1497.
- [83] Nielsen, P.E.; Egholm, M. *Bioconjugate Chem.* **1994**, 5, 3.
- [84] Hyrup, B.; Nielsen, P.E. *Biomed. Chem.* **1996**, 4, S-23.
- [85] Petersen, K.H.; Buchardt, O.; Nielsen, P.E. *Bioorg. Med. Chem. Lett.* **1996**, 6, 793.
- [86] Brown, S.C.; Thomson, S.A.; Veal, J.M.; Davis, D.G. *Science* **1994**, 265, 777-780.
- [87] Wittung, P.; Nielsen, P.E.; Buchardt, O.; Egholm, M.; Norden, B. *Nature* **1994**, 368, 561-563.
- [88] Cherny, D.; Belotserkovskii, D.Y.; Frank- Kamenetskii, M.D.; Egholm, M.; Buchardt, O.; Berg, R.H.; Nielsen, P.E. *Proc. Natl. Acad. Sci.* **1993**, 90, 1667.
- [89] Nielsen, P.E.; Egholm, M.; Buchardt, O. *J. Mol. Recognition* **1994**, 7, 165.
- [90] Neumann, T. *dissertation*, Univ. Mainz, Germany, **2001**.
- [91] Tenover, F. C. in *Manual of Clinical Microbiology* Washington, **1991**, 119-127.
- [92] Saiki, R. K.; Scharf, S.; Faloona, F.; Mullis, K. B.; Horn, G. T.; Erlich, H. A.; Arnheim, N. *Science* **1985**, 230, 1350-1354.
- [93] Saiki, R. K.; Gelfand, D. H.; Stoffel, S. et al. *Science* **1988**, 239, 487-491.
- [94] Mullis, K. B., Faloona, F. A. *Methods Enzymol.* **1987**, 155, 335-350.
- [95] Sambrook, J. and Russell, D. W. *Molecular cloning, third edition*, Cold spring harbor, New York.

## CHAPTER 3

# EXPERIMENTAL SECTION

---

### 3.1 Instrumental

Based on the surface plasmon resonance optics, a surface plasmon field-enhanced fluorescence spectroscopy (SPFS set-up) was built to investigate the hybridization interactions as shown in Figure 3.1.

A HeNe laser beam (5 mW,  $\lambda = 632.8$  nm, Uniphase) passes through a chopper that is connected to a lock-in amplifier (EG&G) in order to allow for reduced noise and daylight independent measurements of the reflected intensity. The intensity and polarisation of the incident light were adjusted by two polarizers (Glan-Thompson). The exposure time was controlled by placing the shutter in front of the sample in order to minimize any photobleaching of the fluorescent dyes. Typically, the shutter was open for 5 sec and closed for 3 min, except for the global analysis. The incident laser is reflected off the base plane of the coupling prism ( $90^\circ$ , LaSFN9, Schott), and the reflected intensity is focussed by a lens ( $f = 50$  mm, Owis) for detection by a photodiode. The laser intensity is also modulated by the chopper and the reflected intensity is also measured by a photo-diode detector coupled to a lock-in amplifier. The sample is mounted onto a 2-phase goniometer (Huber) that can be rotated in  $\Delta\theta = 0.001^\circ$  steps. The two co-axial goniometers enable an independent tuning of the incident angle of the laser and/or the detection angle. Both motors rotate in a  $\theta/2\theta$  fashion for the usual SPR angular scans.

In order to detect the fluorescence emission of the sample, a collecting lens focuses the emitted light through an interference filter ( $\lambda = 670$  nm, LOT) into a photomultiplier tube (PMT, Hamamatsu), which is mounted towards the backside of the sample. Note that the interference filter is specifically designed for commercially versatile fluorophores such as Cy5 (Cyanine 5, from Amersham Pharmacia Inc.). The fluorescence detection unit is mounted towards the base of the prism, rotating together with the prism (sample) at  $\theta$ , while the photodiode detecting the reflected light rotates at  $2\theta$ . The temperature in the cell was sensed by thermocouple (PT 100), which is posited in the center of the flow cell.

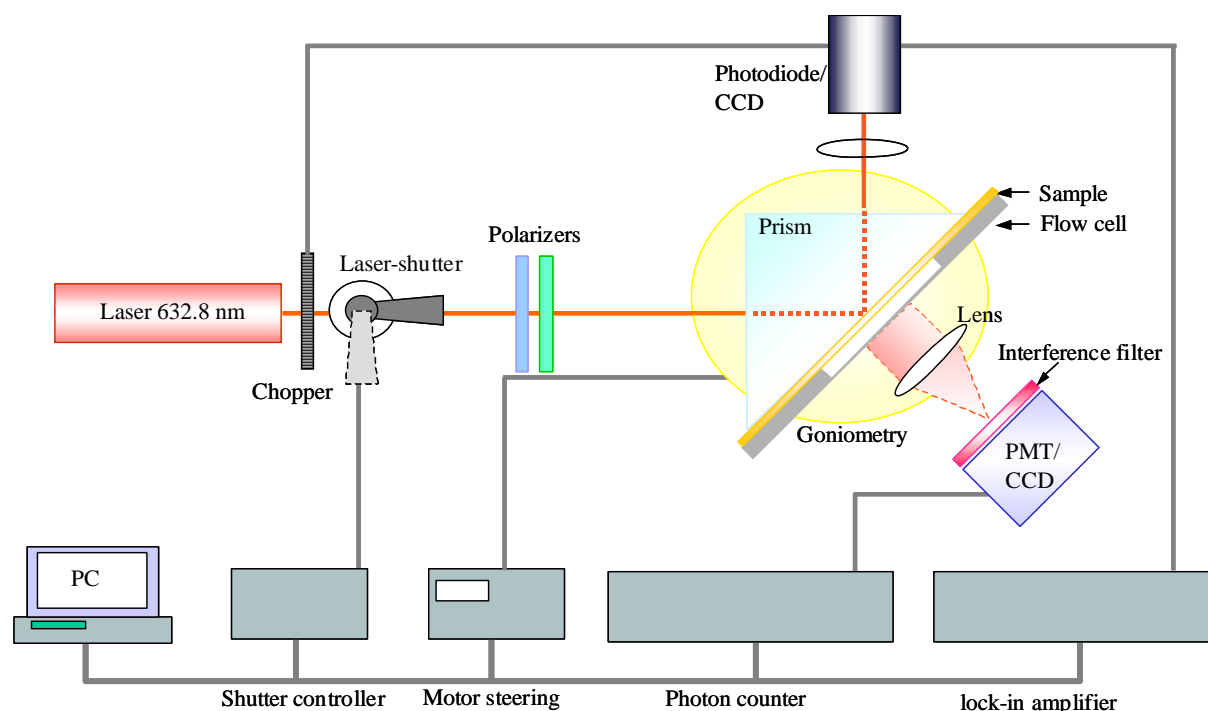


**Figure 3.1.** Schematic draw of the surface plasmon field-enhanced fluorescence spectroscopy.

### 3.1.1 Flow cell

As schematically shown in Figure 3.2 (a) the flow cell (26 x 26 x 3 mm) made with quartz glass (Herasil, Schott) has a hole connected with an inlet and outlet to circulate the target solution. The flow cell is attached, via Tygon® tubing with an inner diameter of 0.76 mm, to a peristaltic pump (Ismatec, Switzerland) which can control the flow rate and the sample tube, forming a closed circulation loop. The total volume including the tube is around 400  $\mu\text{L}$ . Buffer and sample solutions can only be manually exchanged. Once the exchange is completed, the whole loop is closed and completely sealed allowing for a long interaction time.

### 3.1.2 Sample assembly

All experiments were performed by using a flow cell coupled prism in the Kretschmann configuration (Figure 3.2 (b)). For practical reason the gold layer was evaporated on the glass slide that has the same refractive index as the prism (LaSFN9,  $n=1.845$ ). The interface between prism and glass slide was matched with high refractive index matching oil

(Hydrogenated terphenyl 1-bromonaphthalene, Cargille,  $n=1.700$ ). This fluid oil should have a similar refractive index as the prism and the glass in order to allow for unperturbed coupling. For practical reasons a less volatile index match liquid is frequently used with the drawback of a lower refractive index and thus non optimal match. The gold side was placed towards the flow cell for specific binding of molecules to the gold. Then, the flow cell was placed onto a low-fluorescent quartz glass slide (Herasil, Schott) and sealed by O-rings (Viton) made of Teflon.

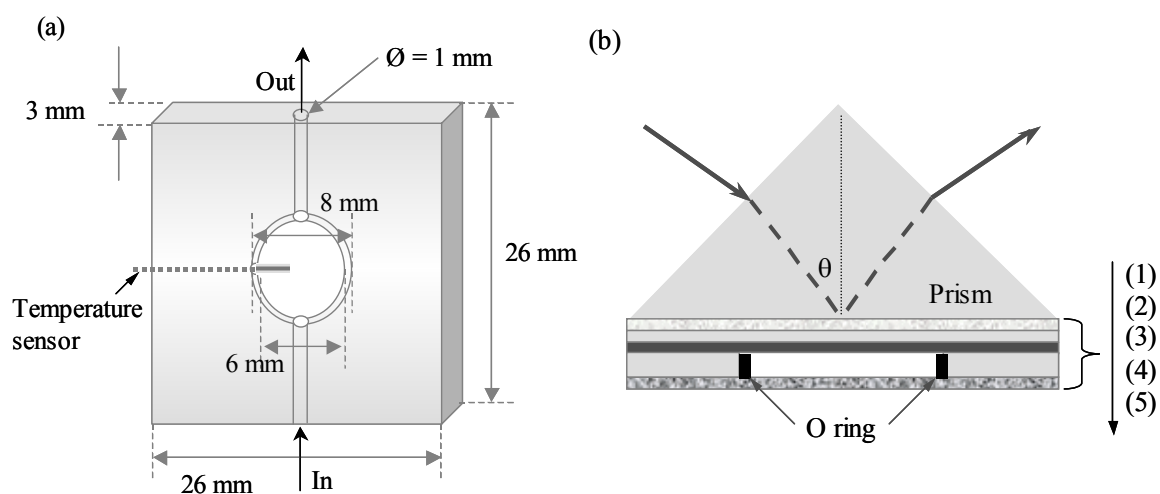


**Figure 3.2.** (a) Schematic draw of flow cell. (b) Sample assembly consistent of prism, (1) refractive index matching oil, (2) glass slide, (3) evaporated gold, (4) flow cell, and (5) quartz glass in Kretschmann configuration.

### 3.1.3 Temperature control

The temperature in the cell can be controlled by preheating the solution using a thermostat (Eppendorf). The temperature in the cell was sensed by a thermocouple (PT 100), which is posited in the middle of the flow cell (Figure 3.3). The sample window (16 mm, Figure 3.3) in the flow cell used for the temperature experiments is larger than a normal cell (6 mm, Figure 3.2 (a)) because the temperature sensor should be posited avoiding to be hit by the laser beam. The total volume including the tube is around 700  $\mu\text{L}$ . In order to generate desired constant temperature, the conditions such as flow rate, volume of solution and temperature of thermostat need to be optimized systematically. Table 3.1 shows the optimized conditions to control the temperature. The used sample volume is about 2 mL. Normally, the temperature in

the cell is normally  $24 \pm 0.5$  °C at a flow rate of 10  $\mu\text{L}/\text{sec}$ . The temperature below room temperature was controlled by using an ice bath in order to get  $20 \pm 0.5$  °C.

**Table 3.1.** The optimized conditions to get desired temperature.

Desired Temp. °C	Flow rate $\mu\text{L}/\text{sec}$	Temp. of thermostat °C
29	50	37
32	20	56
40	70	56

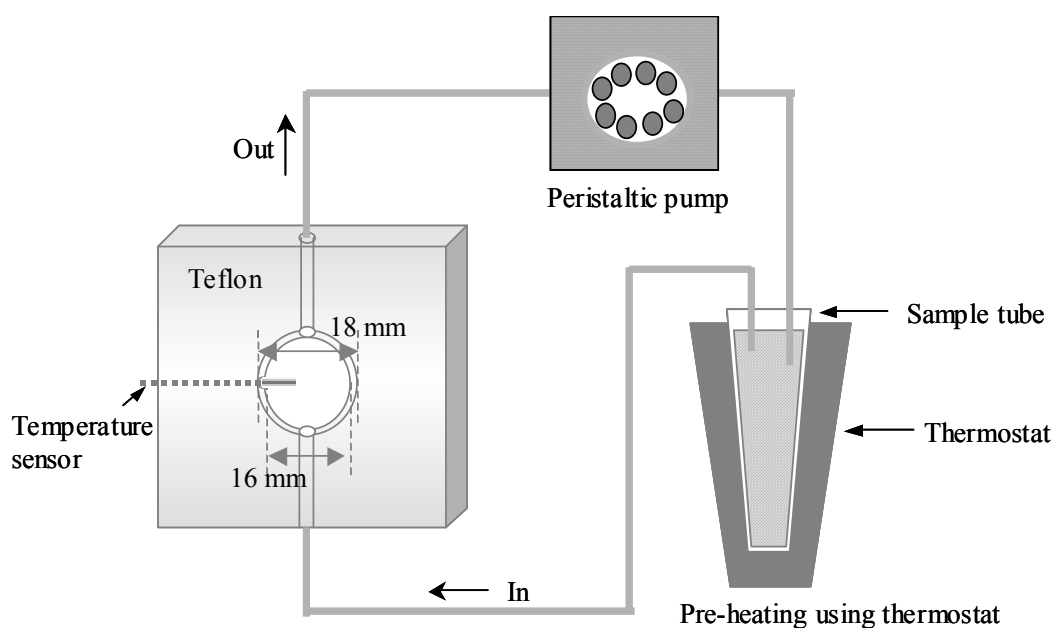


**Figure 3.3.** Schematic draw of flow system for temperature experiment. The temperature in the cell is controlled by pre-heated sample solution using thermostat.

Figure 3.4 shows the angular scan curves taken of the sensor matrix upon varying the temperature from 20 to 45 °C in order to check the stability of the sensor matrix assembled with a mixed SAM employing the biotin/streptavidin system. At  $R=0.3$  the angle shift

between the value at 20 °C and 45 °C was 0.1 deg. This small shift of angle is due to the change of refractive index change of water at different temperatures. From the SPR measurement the temperature in the range of 20-45 °C does not influence the stability of the sensor surface.

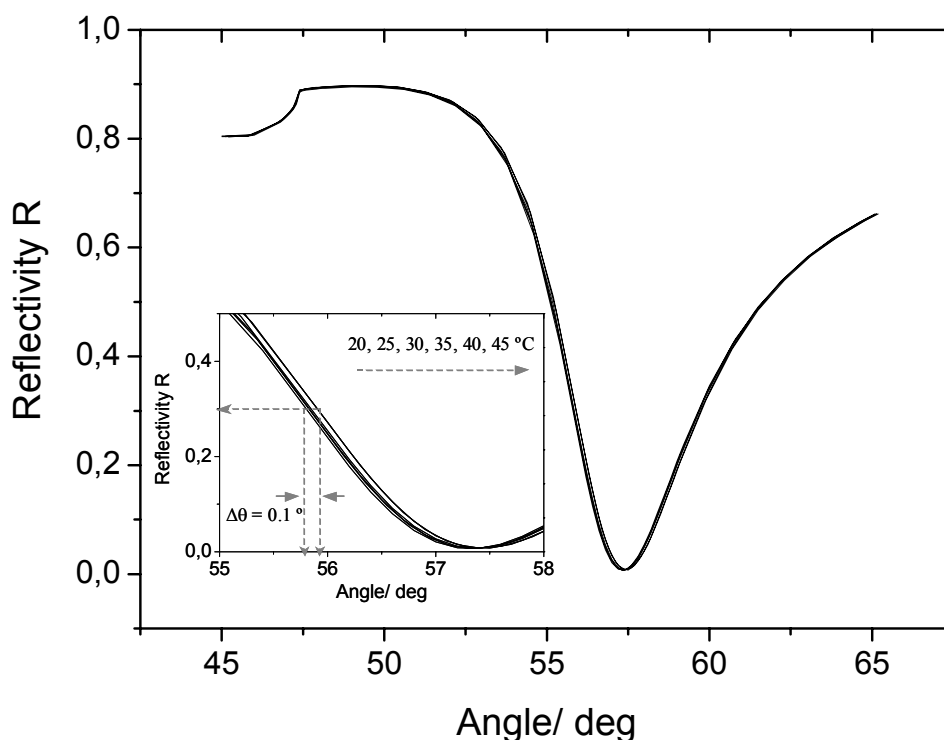


**Figure 3.4.** Angular scan curves of the reflectivity R according to the temperature. The inset shows a zoom-in to the angles between 55 ° and 58 °. At 0.3 of reflectivity, the observed angle shift was 0.1 deg.

### 3.2 Strategic Sensor Matrix

Although streptavidin can adsorb directly onto gold surfaces in an unspecific way, such relatively disordered physisorbed protein layers should be avoided. Rather, the formation of the complex organised sensor architecture must be controlled using appropriate anchoring layers. A very convenient way of providing binding sites for the streptavidin on the surface is the use of biotinylated thiols. Thiols are known to form SAMs very facile onto gold (chapter 2.3) and the biotin-moiety assures binding of the adjacent protein layer in a specifically ordered and controlled way. An optimal protein self-assembled protein layer is obtained only,



if the distance between the biotin-moieties corresponds to the distance of the streptavidin binding pockets in the protein layer. A too high biotin density was found to inhibit the formation of proper protein layers. Thus, the biotin sites on the surface were diluted with a thiol of identical core structure, in which the biotin was exchanged by a hydroxyl end group.

By varying the ratio of both thiols in solution the density of the biotin-moieties on the surface can be controlled. If the lateral dilution of the biotinylated thiol is too small, the accessibility of the binding sites is reduced and improper protein layer formation is observed. On the other hand, if the surface concentration of the biotin sites is too small, the consequent density of the bound streptavidin molecules is decreased and the formation of a complete monolayer is hindered.

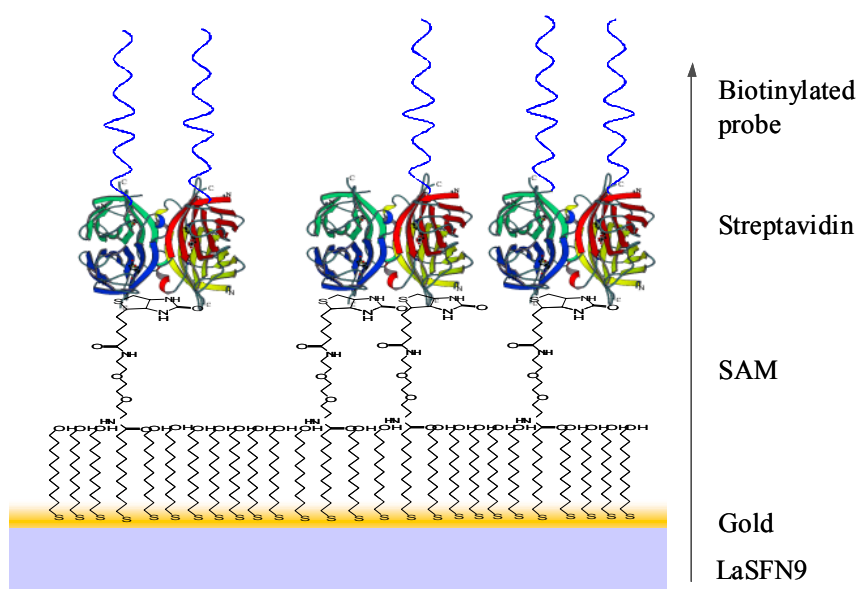


**Figure 3.5.** Illustration of the self-assembled sensor matrix.

The streptavidin layer provides a defined and stable binding matrix that can be used to immobilise a variety of biotinylated molecules for sensing purposes. As has been discussed in chapter 2.2.6, the fluorescence intensity of fluorophores near metal surfaces is strongly dependent on the metal-dye distance. It is important to note that in the used architecture the protein matrix separates the DNA bound fluorophores from the gold surface. SPFS can hence be conducted with only moderate losses of the fluorescence signal. Therefore, the sensor matrix assembled with mixed SAM employing biotin/streptavidin system was the architecture of choice (Figure 3.5).

### **3.2.1 Cleaning of glass substrate**

The glass substrates were carefully cleaned the by following procedure:

- 1) sonication for 10 min each in 2% alkaline detergent solution (Helmanex, Helma, Germany; sonification apparatus Super RK510, Sonorex, Germany),
- 2) sonication for 15 min in MilliQ water (18 M $\Omega$ / cm),
- 3) 15 min sonification in ethanol (Chromasolv, Riedel-de Haehn, Germany),
- 4) cleaned samples were blown dry in a stream of nitrogen.

In order to recycle of the glass substrate after the experiments, the used substrates were carefully cleaned by following procedure:

- 1) gold films were removed by mechanical rubbing with smooth optical paper immersed in ethanol.
- 2) in case of resistant gold films, a 20 times diluted solution of 50 mL of MilliQ water, 40 g of potassium iodine, and 10 g of iodine, (Aldrich) was used.

The chromium films were removed by a treatment with an aqueous solution of ammonium cerium (IV) nitrate (Aldrich).

### **3.2.2 Thermal evaporation of gold on glass substrate**

Gold (99.9999%, Balzers) was deposited onto clean LaSFN9 slides by thermal evaporation at a deposition rate of 0.1 nm/s under UHV conditions ( $p < 10^{-6}$  mbar) in an evaporation apparatus (Edwards). In order to improve the adhesion of the gold film to the glass substrate a chromium film of approximately 2 nm was evaporated if necessary.

### **3.2.3 Sensor matrix on gold substrate**

For the preparation of the self-assembled monolayers (SAM), the gold surface was incubated overnight in a binary mixed thiol solution of a biotinylated thiol (Biotinamino-capronacid-amidodioctyl-mercaptopropionamide, Figure 3.6) and a spacer thiol (11-Mercapto-1-undecanol, Aldrich, Figure 3.6) at a molar ratio of 1: 9 and a total concentration of 0.5 mM in absolute ethanol (Aldrich) in order to control the surface density and to

minimize non-specific adsorption of analyte (target) molecules. Then, the streptavidin solution (1  $\mu$ M, Kem-En-Tec Diagnostics) was injected into the flow cell system in order to allow for binding to the self-assembled thiol layer at a flow rate of 10  $\mu$ L/sec. Subsequently, biotinylated PNAs (500 nM) were immobilized on the streptavidin layer as catcher probes via the streptavidin/biotin binding.

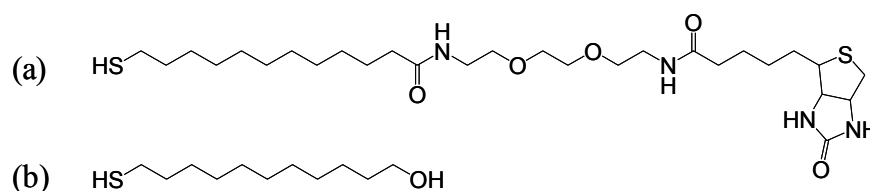


**Figure 3.6.** Molecular structures of (a) biotinylated thiol and (b) spacer thiol.

### 3.2.4 Characterization of the sensor matrix by SPR

In Figure 3.7 (a) typical adsorption kinetics of all individual layers are given before and after each adsorption process. The surface architecture was characterised by means of thickness determination using the simulation software WINSPALL2.0. The scan curves and the corresponding simulations are depicted in Figure 3.7 (b). The used optical constants and the resulting optical thickness of the layers are summarised in Table 3.2.

**Table 3.2.** Optical constants and determined thickness of sensor matrix measured by SPR.

Layer	<i>d</i> / nm	$\epsilon'$	$\epsilon''$
Gold	57.5	-12.38	1.38
SAM	1.5	2.25	0
SA	3.3	2.10	0
PNA probe (15mer)	1.3	2.10	0
Water		1.78	0

In this study we make use of the streptavidin-matrix as supporting layer for measuring binding reactions between probe and target oligonucleotides. In addition to the stable

immobilisation of the probe DNA, the use of the streptavidin platform assures that the immobilised probes are diluted on the surface. It is assumed that due to steric and electrostatic constraints only one of two neighbouring binding pockets can be occupied by a biotinylated DNA strand. From the calculations we can derive a density of one probe strand per  $44 \text{ nm}^2$ . Thus, the obtained dilution is large enough to permit duplex formation. Furthermore, interactions like crowding effects between the probes are reduced by this high lateral dilution of the immobilized probe on the surface.

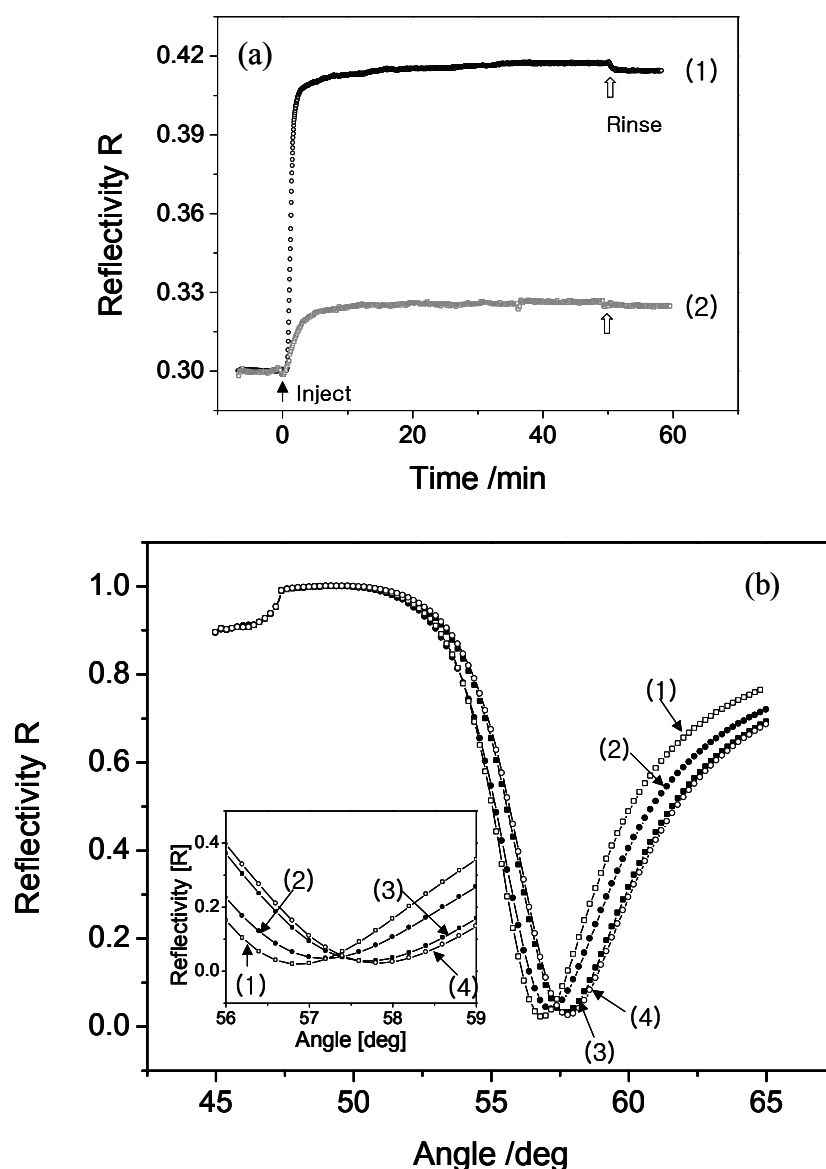


**Figure 3.7.** (a) Kinetic SPR curves taken at  $\theta = 55.7^\circ$  (at this angle, the reflectivity changes approximately linearly with the bound optical mass) (1) Streptavidin binding to a biotinylated thiol SAM, (2) biotinylated PNA probes binding to a streptavidin layer. (b) Angular scan curves of the reflectivity  $R$ ; (1) reference gold, (2) mixed SAMs (full circles), (3) streptavidin layers, (4) PNA probe layers (open circles). The inset shows a zoom-in to the angles between  $56^\circ$  and  $59^\circ$ .

The determined thickness of the thiol and streptavidin layers were 1.3 nm and 3.3 nm, respectively. The refractometric measurements gave 53% of a surface coverage of streptavidin [1]. By ellipsometric measurements of a streptavidin monolayer on a biotinylated lipid interface and in twodimensional streptavidin crystals coverage of 65% and 66% was found, respectively [1]. Therefore we have to assume that the streptavidin layer in our architecture is not as highly ordered as in a crystal and that defects in the layer structure are apparent.

### 3.2.5 Specific and unspecific binding to the sensor matrix

It is necessary to check unspecific adsorption of the chromophore labelled DNA target to the sensor surface. Figure 3.8 shows the SPFS kinetic curve to investigate unspecific binding of DNA target with mixed thiol SAM layer and with streptavidin (SA) layer and the specific binding with the PNA probe (MM1) sensor matrix in PBS.

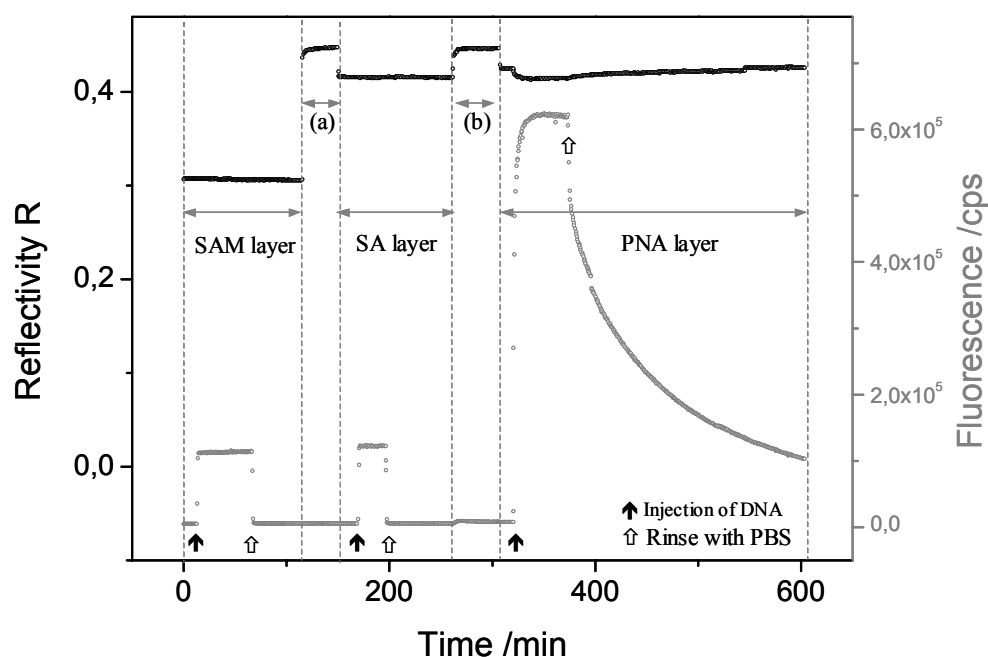


**Figure 3.8.** SPFS measurement for specific and unspecific binding of DNA target to sensor surface. (a) is the immobilization process of streptavidin (SA) onto biotinylated SAM layer and (b) is the immobilization process of PNA probe onto SA layer.

As shown in Figure 3.8, the fluorescence signal jumps up to  $1.1 \times 10^5$  cps upon the sample injection of DNA target (500 nM) to SAM layer (or SA) and then the fluorescence intensity

goes back immediately to the baseline level ( $1.3 \times 10^3$  cps) by replacing with fresh buffer solution without any target. The signal jump up is due to the emission from chromophores in the bulk excited by the SPR evanescent tail and randomly scattered surface plasmon light.

In contrast, the target DNA gradually binds to the PNA probe immobilized at the surface in PBS, and showed typical association phase. After hybridization the dissociation was observed by rinsing with fresh buffer solution.

Therefore, any unexpected adsorption between DNA target and SAM (or SA) was not observed.

### 3.3 PNAs synthesis

The PNA probe was synthesised [2-4] using solid-phase synthesis with a 433A Peptide Synthesizer (Applied Biosystems) with the BOC strategy and *O*-(1*H*-7-azabenzotriazolyl)-*N,N,N',N'*-tetramethyluronium hexafluorophosphate (HATU, Aldrich) coupling and *N,N*-diisopropylethylamine (DIEA, Aldrich) as base, using commercially available PNA monomers (Applied Biosystems), (4-methylbenzhydryl)amine (MBHA) resin (Novabiochem) as solid support. After the PNA part was completed, two coupling steps were performed using the protected linker [2-(*N*-Boc-2-amioethoxy)ethoxyacetic acid dicyclohexylammonium salt (AEEA, Applied Biosystems), and a coupling step using biotin (Aldrich). Cleavage of the PNA from the resins was then carried out manually using a mixture of a trifluoroacetic acid (TFA) and trifluoromethanesulfonic acid (TFMSA): thianisole: *m*-cresol 6:2:1:1. Swelling, downloading and cleavage of the PNAs from the resin were done manually. The crude product was purified by reversed phase HPLC using a Phenomenex C18 peptide column (3  $\mu$ m, 250 mm  $\times$  10 mm) with a binary gradient (flow rate: 4mL/min); eluent A: water /TFA = 100 : 0.1; eluent B: water/acetonitrile/TFA = 60 : 40 : 0.1; detector UV (260 nm). The purified product was then identified by Mass Spectrometry (*Micromass ZMD*). The sequences of all probes and targets used in this study are given in Table 3.2.

**Table 3.3.** The sequences of PNA probes.

Name	Sequence
<b>P-RR-11</b>	Biotin-AEEA-AEEA - AGAGTCAGCTT- NH <sub>2</sub>
<b>P-RR-13</b>	Biotin-AEEA-AEEA - CAGAGTCAGCTTG- NH <sub>2</sub>
<b>P-RR-15</b>	Biotin-AEEA-AEEA -GCAGAGTCAGCTTGT- NH <sub>2</sub>
<b>P-RR-11</b>	Biotin-AEEA-AEEA - AGAGTCAGCTT -NH <sub>2</sub>
<b>P-RR-13</b>	Biotin-AEEA-AEEA - CTAGAGTCAGCTT -NH <sub>2</sub>
<b>P-RR-15</b>	Biotin-AEEA-AEEA -TGCTAGAGTCAGCTT -NH <sub>2</sub>
<b>P-RR-mis-11</b>	Biotin-AEEA-AEEA - AGAGCCAGCTT -NH <sub>2</sub>
<b>P-RR-mis-13</b>	Biotin-AEEA-AEEA - CTAGAGCCAGCTT -NH <sub>2</sub>
<b>P-RR-mis-15</b>	Biotin-AEEA-AEEA -TGCTAGAGCCAGCTT -NH <sub>2</sub>

### 3.4 Polymerase Chain Reaction

Polymerase chain reaction, or PCR, uses repeated cycles of heating and cooling to make many copies of a specific region of a DNA. First, the temperature is raised to near boiling, causing the double-stranded DNA to separate, or denature, into single strands. If the temperature is decreased, short DNA sequences known as primers bind, or anneal, to complementary matches on the target DNA sequence. The primers bracket the target sequence to be copied. At a slightly higher temperature, the enzyme Taq polymerase, binds to the primed sequences and adds nucleotides to extend the second strand. This completes the first cycle. In subsequent cycles, the process of denaturing, annealing and extending are repeated to make additional DNA copies. After three cycles, the target sequence defined by the primers begins to accumulate. After 30 cycles, as many as a billion copies of the target sequence are produced from a single starting molecule.

For GMO detection, target DNAs were amplified by polymerase chain reaction (PCR) using a template gene extracted from Monsanto's Round-up Ready<sup>TM</sup> soybean.

#### 3.4.1 Amplification from RR GMO and natural soybean

The PCR protocol was optimized on the thermocycler (Biometra) by designing the primer sequences and adjusting the annealing temperature and the concentration of each component. 50  $\mu$ L of a mixture of Taq polymerase (5 U, Qiagen), buffer, primers (0.5  $\mu$ M, MWG-Biotech, Table 3.4.), dNTPs (0.2 mM, Fermentas), template (150 ng, extracted from soybean certified reference material, Fluka), and sterilized water were prepared. Using a thermocycler 40 PCR cycles are run as follows: denaturation at 95 °C for 50 s, annealing at 58 °C for 50 s,

and elongation at 72 °C for 1 min. The PCR products were analyzed by agarose gel (2%, 0.5 x TBE buffer) electrophoresis at 50 mA for 2 hours in 0.5 × TBE buffer stained with ethidium bromide. The amplified PCR products were purified by ethanol precipitation by mixing 50 µL PCR, 125 µL ethanol, and 5 µL sodium acetate (3 M, Sigma) and incubating at –20 °C for 6 h. The PCR products were collected by centrifugation at 20,000 rpm.

**Table 3.4.** Amplification primers.

Name	Sequence	Modification
<b>RR-125</b>	5'-CAT TTC ATT TGG AGA GGA CAC G -3' 5'-TGG GGT TTA TGG AAA TTG GAA -3'	5'-Cy5
<b>RR-169</b>	5'-TGG GGT TTA TGG AAA TTG GAA -3' 5'-ATC CCA CTA TCC TTC GCA AGA -3'	5'-Cy5
<b>SL-157</b>	5'-ATG GGC TTG CCT TCT TTC T -3' 5'-CCG ATG TGT GGA TTT GGT G -3'	5'-Cy5
<b>Mu-159</b>	5'-GTA CCG AGC TCG GAT CCA CTA GTA ACG GCC-3' 5'-GCC GCC AGT GTG ATG GAT ATC TGC AGA ATT-3'	

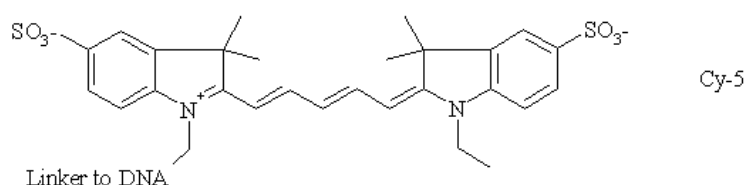


**Figure 3.9.** Chemical structure of Cy5.

### 3.4.2 Amplification for Mu –159

Reagents for each 50 µl reaction include: 5 units of *Taq* polymerase (Amersham Biosciences), 1×PCR buffer (Amersham Biosciences), 60 pmol of the forward primer and 80 pmol of reverse primer (MWG-Biotech), 0.2 mM dNTPs (Fermentas) and 100 ng of the plasmid DNA. Amplification was accomplished on a thermocycler. After the first step of denaturation at 96°C for 1 min, each of the 30 cycles of amplification consists of 30 s of template denaturation at 96°C, 30 s of primer annealing at 50°C and 30 s of primer extension at 72°C.



### **3.4.3 Agarose gel Electrophoresis**

DNAs in solution generally have a negative charge because their phosphate groups are ionized; thus they migrate toward the positive electrode. However, nucleic acids molecules consisting of long chains have almost identical charge-to-mass ratios, whatever their length, because each residue contributes about the same charge and mass. Therefore, if the electrophoresis of nucleic acids were simply carried out in solution, little or no separation of molecules of varying lengths would occur.

Molecules are now most commonly subjected to electrophoresis in a gel, rather than a liquid solution. The size of the pores in such gels limits the rate at which molecules can move through them. Migration in gels is inversely proportional to the size of the nucleic acids. The structure of the nucleic acids (e.g., linear, circular, double-stranded, or single-stranded) will also affect migration in gels. It is possible to distinguish DNA fragments that differ by as little as 1%. A wide range of sizes (10 bp to 20 kb) can be analyzed by gel electrophoresis.

The agarose gel electrophoresis is run to identify the DNA fragments for our purpose. Agarose is purchased from Sigma. Prior to gel casting, 2% of dried agarose is dissolved in 0.5 × TBE buffer by heating with a microwave or heater, until a clear and transparent solution is achieved. The gel mold is assembled beforehand on a level surface, which is a simple container fitted with a well-forming comb. Once the melted solution is poured into the mold, and the mold is allowed to stand undisturbed until the agarose gel solidifies, wells will spontaneously form with the gel hardening, according to the shape of the comb teeth. These wells represent the spaces in the gel that will hold the sample once the gel is loaded.

The DNA sample is mixed with the loading buffer (Fermentas) with a ratio of 1:5, and loaded into the gel wells. Electrophoresis is usually run at 50 mA for around 1.5 hours at room temperature. O'Range Ruler™ 50bp DNA ladder (Fermentas) is co-electrophoresed with DNA samples, identifying fragments from 50bp to 1000bp at 50bp increments. After electrophoresis, the gel is stained by 0.5 µg / ml ethidium bromide (EtBr, Sigma) solution for 30~45 min. The gel is then placed on a UV light box, and a picture of the fluorescent EtBr-stained DNA separation pattern is achieved. All PCR (Table 3.5) were identified by the agarose electrophoresis, as shown in Figure 3.10.

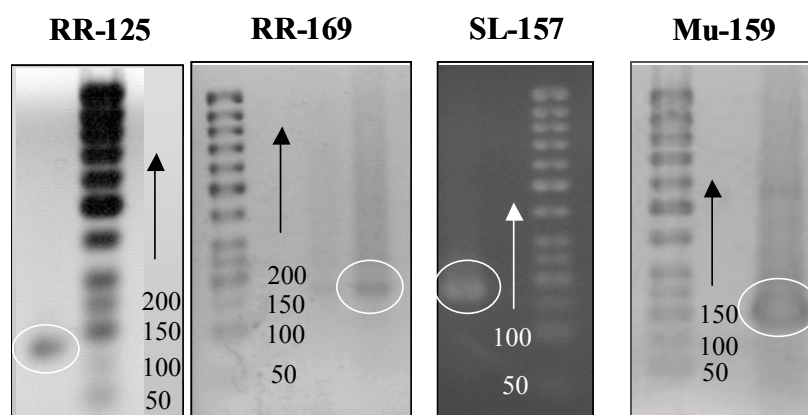


**Figure 3.10.** Electrophoresis patterns of PCR products in 2% agarose gel.

**Table 3.5.** The sequences of PCRs.

Name	Sequence
<b>RR-125</b>	Cy5-5'- CATTTCATTTGGAGAGGACACGCTGACAAGCTGACTCTAG CAGATCTTTCAAGAATGGCACAATTAAACAACATGGCACAAGGGA TACAAACCCTTAATCCCAATTCCAATTTCCATAAACCCCA-3'
<b>RR-169</b>	Cy5-5'- ATCCCACTATCCTTCGCAAGACCCTTCTCTATATAAGGAA GTTTCATTTTCATTTGGAGAGGACACGCTGACAAGCTGACTCTAGCAG ATCTTTCAAGAATGGCACAATTAAACAACATGGCTCAAGGGATAC AAACCCTTAATCCCAATTCCAATTTCCATAAACCCCA-3'
<b>SL-157</b>	Cy5-5'- CCGATGTGTGGATTTGGTGGATCCCAAGAGTTCCGGAAAG TGTCAAACTCAACAGCGACGACTTGATCACCAGACTCGTTTTCGTT GAAAAGACCAAGATAACCTGCATGTGTTTGTGGCTTAGTGTCAATT GGTGCGAGAAAGAAGGCAAGCCCAT-3'
<b>Mu-159</b>	CGGCGGTCACACTACCTATAGACGTCTTAAGCGGGAATGGTGCGCC TAGGTCCGTGCATCTTCAACATGCAGTGTTGATCCGGGAGCCAGGG GAGCTCACAAAGTATTCCCGCTTAAGGTCGTGTGACCGCCGGCAATG ATCACCTAGGCTCGAGCCATG-3'

#### 3.4.4 UV-Vis. Spectrum

The concentration of the PCR product was calculated by the UV- vis. absorbance at  $\lambda = 650$  nm using an extinction coefficient of Cy5 of  $\epsilon = 250,000 \text{ cm}^{-1}\text{M}^{-1}$ . Figure 3.11 shows typical UV- vis. absorbance spectrum of RR-125 (10 times diluted from original product). The calculated concentration of RR-125 was  $0.98 \mu\text{M}$ .

$$A = \epsilon \cdot b \cdot c; \quad c = \frac{0.244}{2.5 \cdot 10^5} = 0.98 \cdot 10^{-6} \text{ M.} \quad (2)$$

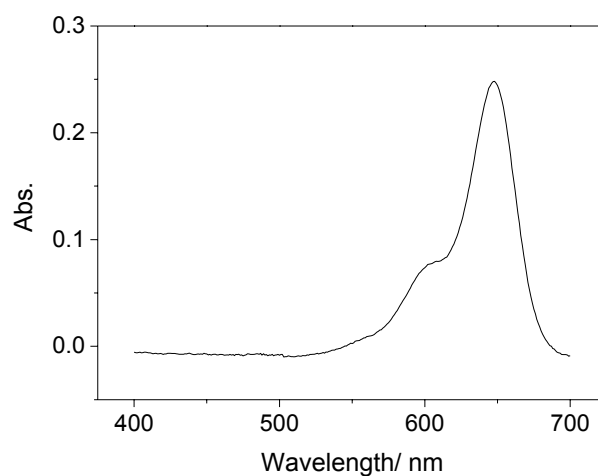


**Figure 3.11.** UV- vis. absorbance of RR-125

### 3.4.5 How to get single-stranded PCR?

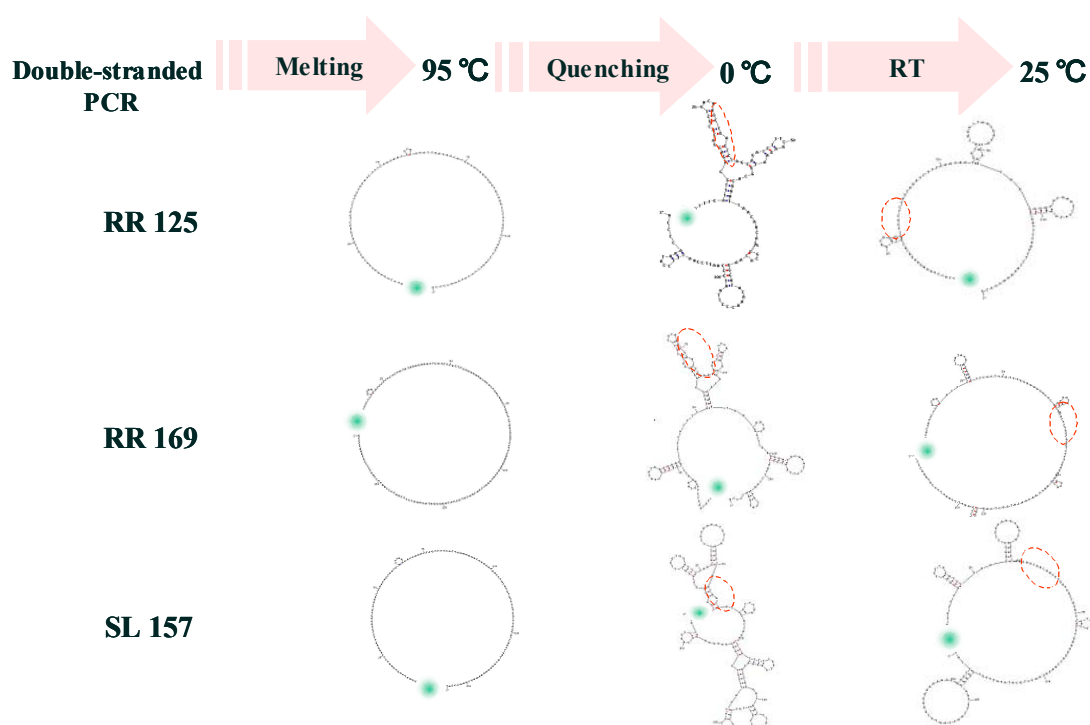


**Figure 3.12.** A melt-quench protocol to separate double stranded PCR products and structures of single stranded nucleic acids using mfold web server. Dashed marks are binding sites to probes

Purified PCRs originally are double-stranded DNAs. In order to hybridize with PNA, a melt-quench protocol was developed [5]: The PCR products are heated to  $T = 95\text{ }^{\circ}\text{C}$  and then

quickly quenched into a low ionic strength buffer containing only 10 mM phosphate buffer solution at 0 °C (Figure 3.12). This results in a Coulombic repulsion in solution between the individual single strands sufficiently strong to prevent (rapid) re-hybridization of the complementary strands. The structures of PCR products were simulated by mfold web server (describes a number of closely related software applications available on the World Wide Web) for the prediction of the secondary structure of single stranded nucleic acids [6,7] under conditions as  $[Na^+]=10\text{mM}$  and  $[Mg^{2+}]=3.5\text{mM}$ .

### 3.5 Kinetic Measurement

In order to monitor the molecular binding on the surface the incidence angle is fixed at a position where the measured scan curve exhibits a linear slope (e.g. at 30% reflectivity) and the detected reflectivity is recorded with time. The reflectivity at this fixed incidence angle is increased if the resonance is shifted towards higher angles and the detected shift represents a linear time dependence of the optical properties of the investigated system.

Usually, the angle of incidence was fixed at  $\theta = 55.5^\circ$  for monitoring the PNA/DNA hybridization. Kinetics curves were recorded in both the reflectivity and fluorescence mode, starting with a measurement of the fluorescence background for a few minutes as a function of time. All the experiments were performed with 1 mL for each target concentration using the same flow cell with an inlet and outlet and a closed loop circulation at room temperature ( $24 \pm 1^\circ\text{C}$ ) and at a flow rate of 10  $\mu\text{L}/\text{sec}$ .

For the global analysis, Cy-5 labeled DNA target solutions (varying in concentration from 1 nM up to 200 nM) were introduced into the flow cell for the association, and allowed to interact with the PNA functionalized sensor surface for 10 min. After that the dissociation was followed by rinsing with fresh buffer solution (10 mM phosphate buffer solution) for each measurement for 10 min. The surfaces could be fully regenerated by treatment with 10 mM NaOH in order to remove remaining bound target DNA for another analysis cycle at the same sensor surface.

For the titration experiment, a 1 nM solution in 10 mM phosphate buffer of target was injected after recording the background fluorescence and the increase in fluorescence intensity was measured as a function of time until the equilibrium surface coverage was reached. Next, target DNA solutions of high concentration until full surface coverage respectively, were applied consecutively.

Each single-exponential analysis was completed by applying a 50 nM target solution until equilibrium was reached, followed by an extended rinsing step.

### 3.6 References

- [1] Neumann, T. *dissertation*, Univ. Mainz, Germany, **2001**.
- [2] Lesignoli, F.; Germini, A.; Corradini, R.; Sforza, S.; et al. *J. Chromatogr. A.* **2001**, 922, 177-185.
- [3] Germini, A.; Mezzelani, A.; Lesignoli, F.; Corradini, R.; et al. *J. Agric. Food Chem.*, **2004**, 52, 4535-4540.
- [4] Germini, A.; Rossi, S.; Zanetti, A.; Corradini, R.; et al. *J. Agric. Food Chem.*, **2005**, 53, 3958-3962.
- [5] Yao, D.; Kim, J.; Yu, F.; Nielsen, P. -E.; Sinner, E. -K.; Knoll, W. *Biophys. J.* **2005**, 88, 2745-2751.
- [6] Zuker, M. *Nucleic Acids Res.* 2003, 31, 3406–3415.
- [7] <http://www.bioinfo.rpi.edu/applications/mfold/old/dna>.

# CHAPTER 4

## PNA/DNA HYBRIDIZATION

---

### 4.1 Motivation

Due to the increasing amount of genetic information in medical diagnostics, environmental monitoring, and food safety, the simultaneous detection method has become important. Biosensors are self-contained, integrated devices using a biological recognition element, which is retained in direct spatial contact with the transduction element [1]. The demands for biosensor techniques are fast, simple, having enough sensitivity and high selectivity to detect of target molecules. For this purpose a stable biosensor surface is required. This demand is realized in optical evanescent wave biosensors [2-7] as a versatile tool for the detection and characterization of biological molecules. In this technique, catcher molecule is immobilized to a sensor surface and the binding process after injection of a target analyte is monitored in real time, detecting small local changes in refractive index at the sensor surface upon biomolecular interaction. The most commonly employed biosensors are a surface plasmon resonance (SPR) biosensor [8-14] with micro- fluidic sample. However for detection of short oligonucleotides having several tens base pairs, the insignificant change of refractive index is not sufficient to analysis in detail. Recently, surface plasmon field-enhanced fluorescence spectroscopy (SPFS), which is a combination of SPR and fluorescence detection, has been introduced [15].

During the binding between catcher probe and target analyte labelled by chromophore, the analyte bounded at the interface of metal/ solution is under evanescent field then the chromophore can be excited giving rise to significant enhanced fluorescence intensity. To get high fluorescence yield, the distance between analyte and metal surface is optimised by employing functional self-assembled architecture avoiding quenching effect [16-19]. This fluorescence intensity shows enough sensitivity to analysis the rate constants for the biomolecular interaction quantitatively even at pM concentration of target. As a catcher probe, peptide nucleic acids (PNAs) has encouraged due to the great potential for the biosensor application as mimics of DNA. PNA is an oligonucleotides mimic having neutral N- (2-aminoethyl) glycine backbone to which the nucleobases are attached instead of the

sugar-phosphate one [20]. Several advantages are investigated for using PNA rather than DNA probes for sensor-based hybridization. Firstly, the hybrid stability expressed as the thermal stability ( $T_m$ ) of PNA/DNA duplexes, displays in general a slightly higher value than the corresponding DNA/DNA duplexes at physiological ionic strength. Secondly, given the fact that PNA has a non-charged pseudopeptide backbone, its physico-chemical properties differ significantly from polyanionic oligonucleotides.

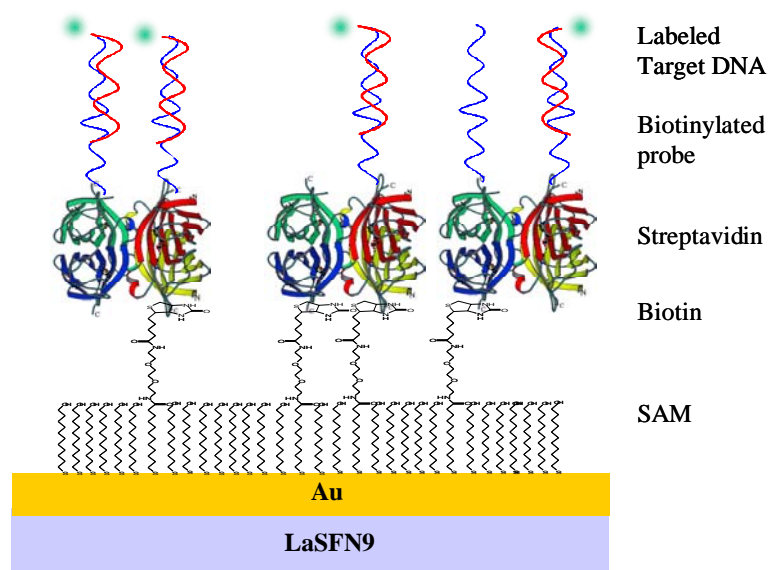


**Figure 4.1.** Illustration of the self-assembled sensor matrix

In this chapter, the hybridization between PNA and DNA (3 different lengths of oligonucleotides probes and complementary matched (MM0) and one base mismatch (MM1) targets) was analyzed quantitatively on the sensor surface and in the solution. Based on SPFS technique, the rate constants for association ( $k_{on}$ ), dissociation ( $k_{off}$ ) and the affinity constant ( $K_A$ ) of the hybridization were determined by fitting the data with simple Langmuir model on the PNA immobilized sensor surface. Alternatively, the thermodynamic parameters of PNA/DNA duplex were carried out from melting curve in solution. DNA is a highly polyelectrolytic species. Its phosphate negative charges have to be neutralized by counterions, which may be metal ions, organic amines, positively charged proteins or, in therapeutic situations, positively charged drugs [21-27]. Thereby the metal counterions are essential for stabilization of DNA/DNA duplex. However, PNA has the non-ionic backbone therefore the stability of PNA/DNA complexes is insensitive to the ionic strength, in principle. To study the effect of ionic strength for MM0 and MM1 PNA/DNA (11mer, 13mer, and 15mer)



hybridizations were performed in high ionic ( $\text{NaCl} = 137 \text{ mM}$ ) and low ionic ( $\text{NaCl} = 20 \text{ mM}$ ) buffer solutions on the surface as well as in the solutions. Additionally, the limit of ionic strength for PNA/DNA hybridization was investigated in various phosphate buffer solutions (without adding salt) and water. Furthermore, the length effect and discrimination of one base mismatched PNA/DNA duplex was achieved with apparent rate constants. Finally the best conditions were proposed for detection of DNA target.

The effect of temperature on hybridization is important to the stability of duplex. Usually, the stability of duplex is expressed by its melting temperature measured by UV-Vis. Spectrophotometer or by calorimeter in solution [28-30]. For the application to biochip technology, the information from solution is not sufficient. Thereby, the kinetics and thermodynamic studies for the PNA/DNA hybridization on the sensor at equilibrium based on Langmuir adsorption isotherm were investigated by SPFS.

## 4.2 Immobilization of PNA Probes

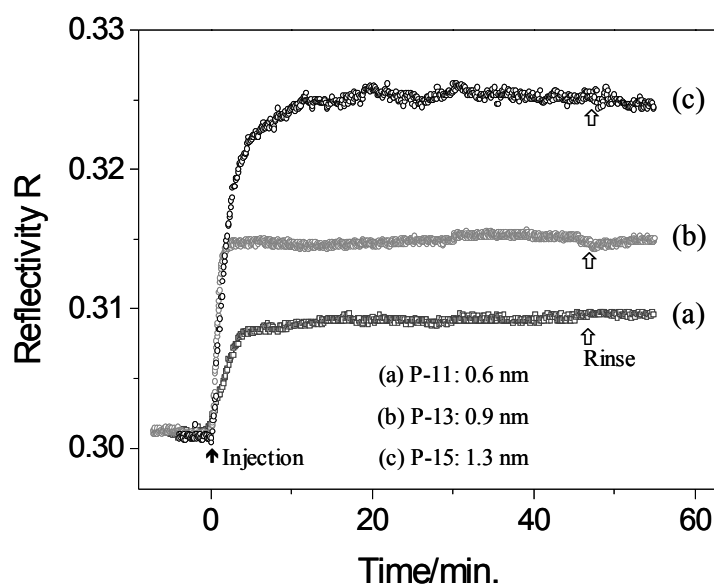
A probe is defined as a short sequence of nucleic bases that can bind to a specific region of a target sequence [31]. The length of the probes can range from 10 to several hundred bases, but the common size is 14-40 bases [32]. From statistical considerations the minimum size of a probe that is unique, is 20 bases. The length of the probe influences the specificity and sensitivity of the assay. Short probes hybridize faster than long ones, but are limited in specificity. In Table 4.1 the sequences of probe and target oligonucleotides that were studied experimentally are summarized. The probe sequences are all biotinylated on the 5' end in order to permit immobilization onto the streptavidin matrix.

Figure 4.1 shows the supramolecular architecture at the metal/ solution interface composed of a mixed biotinylated thiol SAM, a streptavidin monolayers, and the layer of probe PNA coupled to the streptavidin binding matrix via the specific recognition of its biotin moieties [15-19]. The binding of each layer was characterized by SPR. The calculated optical thickness of gold, the mixed thiols, and the streptavidin were 57.5 nm, 1.5 nm, and 3.3 nm, respectively. The immobilization processes of 3 different length PNAs were monitored individually as shown in Figure 4.2. A rapid increase of the reflected intensity by introduction of 0.5  $\mu\text{M}$  probe PNAs indicates the fast binding on biotinylated PNA to the streptavidin (binding affinity for streptavidin/biotin,  $K_A = 10^{14} \text{ M}^{-1}$ ) matrix. An apparent length effect was found resulting increasing the thickness of PNA probe layers with 0.6 nm (11mer), 0.9 nm

(13mer), and 1.3 nm (15mer). This robust sensor architecture ensures a moderate catcher probe density in range of one probe per 40 nm ( $2.5 \times 10^{12}$  probes/ cm<sup>2</sup>) reducing any potential cross-talk between catcher probe and target DNA during hybridization.

**Table 4.1.** The chemical structures of thiols and the sequences of the PNA probes and DNA targets. <sup>a</sup> Mismatched base is underlined in the sequences of target DNA.

<b>Probe</b>	<b>P-11</b>	Biotin- AEEA- AEEA-	AGAGTCAGCTT- NH2
	<b>P-13</b>	Biotin- AEEA- AEEA-	CAGAGTCAGCTTG- NH2
	<b>P-15</b>	Biotin- AEEA- AEEA-	GCAGAGTCAGCTTGT- NH2
<b>Targets</b>	<b>T-11</b>	Cy5- 5'-	AAGCTGACTCT- 3'
	<b>T-13</b>	Cy5- 5'-	CAAGCTGACTCTG- 3'
	<b>T-15</b>	Cy5- 5'-	ACAAGCTGACTCTGC- 3'
	<b>T-mis-11</b> <sup>a</sup>	Cy5- 5'-	AAGCT <u>A</u> ACTCT- 3'
	<b>T-mis-13</b> <sup>a</sup>	Cy5- 5'-	CAAGCT <u>A</u> ACTCTG- 3'
	<b>T-mis-15</b> <sup>a</sup>	Cy5- 5'-	ACAAGCT <u>A</u> ACTCTGC- 3'



**Figure 4.2.** Kinetics curves for 3 different PNA immobilizations during injection (black arrow) of biotinylated PNA to streptavidin in phosphate buffer solution. After stable binding of PNA pure buffer solution was applied into the flow cell for rinsing. The calculated thickness of PNA 11mer (a), 13mer (b), and 15mer (c) were 0.6 nm, 0.9 nm, and 1.3 nm, respectively.

### 4.3 Kinetic Analysis of Binding Data

If a target solution is applied to a probe-modified sensor surface, it is difficult to observe a response effectively by SPR because duplex formation with oligomeric DNA does not generate a significant change in the optical thickness. However, SPFS measurements demonstrated a high sensitivity for monitoring a binding event between immobilized PNA and chromophor-labeled target DNA even at concentrations in the fM range. This fluorescence intensity carries kinetic information of hybridization and can be analyzed in terms of the corresponding rate constants for association ( $k_{on}$ ), dissociation ( $k_{off}$ ), and the affinity constant ( $K_A$ ).

The evaluation of association ( $k_a$ ) and dissociation ( $k_{off}$ ) rate constants was performed by fitting to the binding data using the 1:1 Langmuir model [33,34]. All kinetic experiment data was taken at  $\theta = 55.7^\circ$  at different concentrations of the target DNA with PNA probe in 2 different ionic strength buffer solutions on the same sensor surface. Starting for a short time with the base line measurement (the intensity of the baseline gives  $I_0$  in equation (1)), solutions of varying concentrations of DNA targets were injected and circulated for 10 min approximately for the association process seen by the increasing fluorescence intensity. Then the cell was rinsed with fresh buffer solution for the dissociation process again for 10 min. Based on the Langmuir model the increase of the fluorescence intensity as a function of time is described by a simple biomolecular reaction:

$$I_{fl}(t) = (I_{max} - I_0)(1 - \exp(-(k_a)t)), \quad k_a = k_{on} \cdot c_0 + k_{off} \quad (1)$$

with  $I_{max}$  being the maximum fluorescence intensity from surface-bound duplexes at  $c_0$ ,  $I_0$  is the initial background fluorescence, and  $c_0$  the bulk solution concentration in the global analysis.

The association kinetics is quantified with respect to the concentration dependence. Fitting the association phase data recorded from starting the injection of target to changing the pure buffer with equation (1) the rate constants  $k_a = k_{on} \cdot c_0 + k_{off}$  were obtained individually at different target concentrations. The time-dependent dissociation is described by equation (2): The dissociation is sufficiently enhanced and leads to a measurable loss of fluorescence intensity even within the 10 min of the rinsing phase of the analysis.

$$I_{fl}(t) = (I_{max} - I_0) \exp(-k_{off} \cdot t) \quad (2)$$

The affinity constant ( $K_A$ ) was obtained from the ratio of the rate constant ( $K_A = k_{on}/k_{off}$ ). For each set of hybridizations, a series of independent experiments was performed over the target concentrations of 1-200 nM.

#### **4.4 Dependence of Ionic Strength for PNA/DNA hybridization**

Here, the hybridization between PNA and DNA (3 different lengths of oligonucleotides probes and complementary matched (MM0) and one base mismatch (MM1) targets) was analyzed quantitatively on the sensor surface and in the solution. Based on SPFS technique, the rate constants for association ( $k_{on}$ ), dissociation ( $k_{off}$ ) and the affinity constant ( $K_A$ ) of the hybridization were determined by fitting the data with simple Langmuir model on the PNA immobilized sensor surface. Alternatively, the thermodynamic parameters of PNA/DNA duplex were carried out from melting curve in solution.

DNA is a highly poly-electrolytic species. Its phosphate negative charges have to be neutralized by counterions, which may be metal ions, organic amines, positively charged proteins or, in therapeutic situations, positively charged drugs [21-27]. Thereby the metal counterions are essential for stabilization of DNA/DNA duplex. However, PNA has the non-ionic backbone therefore the stability of PNA/DNA complexes is insensitive to the ionic strength, in principle.

To study the effect of ionic strength for MM0 and MM1 PNA/DNA (11mer, 13mer, and 15mer) hybridizations were performed in high ionic (NaCl = 137 mM) and low ionic (NaCl = 20 mM) buffer solutions on the surface as well as in the solutions. Additionally, the limit of ionic strength for PNA/DNA hybridization was investigated in various phosphate buffer solutions (without adding salt) and water. Furthermore, the length effect and discrimination of one base mismatched PNA/DNA duplex was achieved with apparent rate constants.

##### **4.4.1 PNA/DNA hybridization (MM0)**

Figure 4.3 shows sets of hybridization data between MM0 DNA (11mer) targets and surface attached PNA (11mer) probes at 2 different ionic strengths (NaCl = 20 mM and 137 mM in 10 mM phosphate buffer solutions). For each kinetic measurement the association phase was carried out by injection of 1 nM target solution after short time background

measurement. The fluorescence intensity increased during hybridization event. Then the pure buffer solution applied into the flow cell for dissociation kinetics.

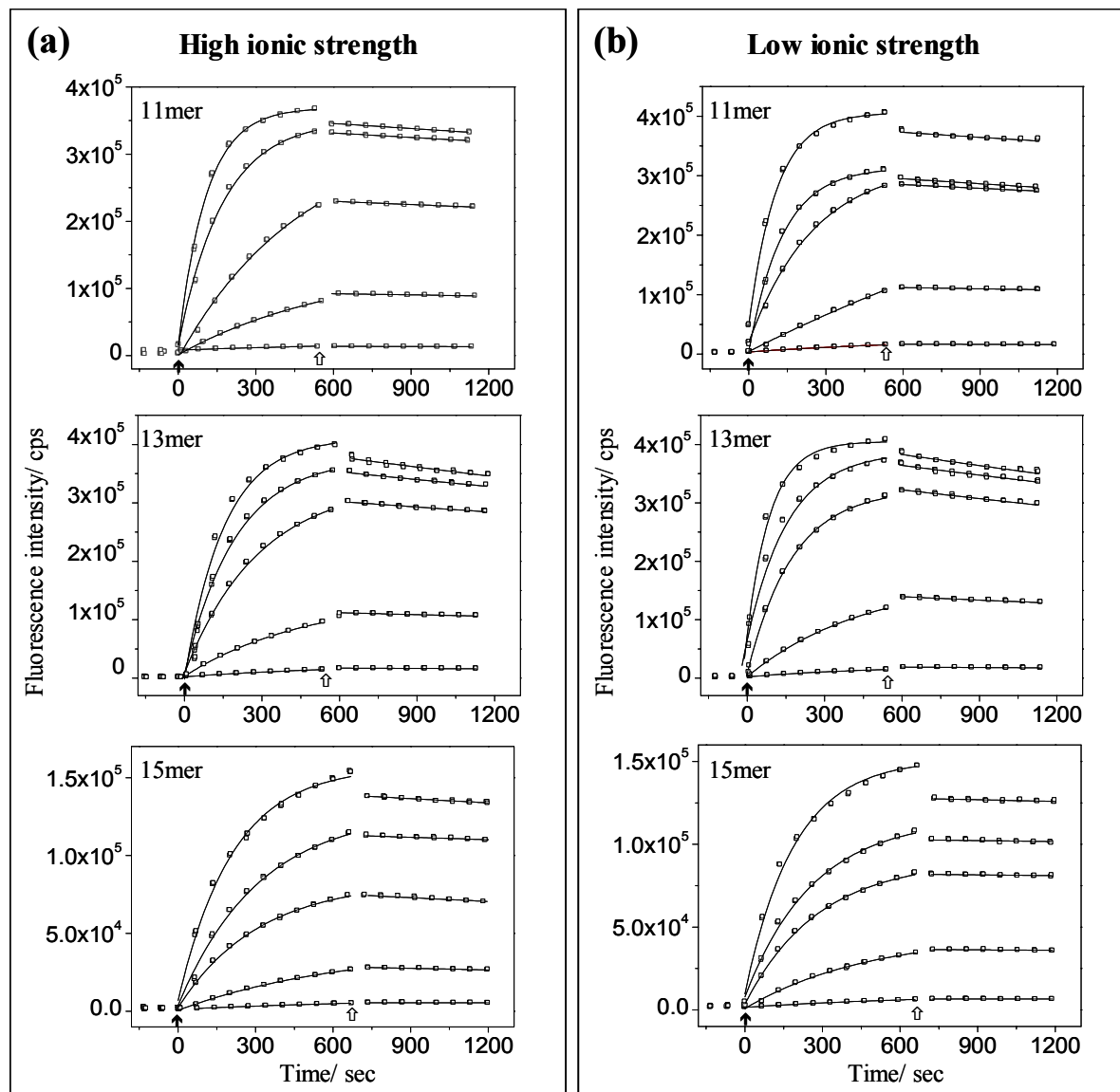


**Figure 4.3** SPFS measurements for kinetic analysis of the association and dissociation phase (taken at  $\theta = 55.7^\circ$ ) at the surface. Open squares are data points collected every 1 min. The solid arrow ( $\uparrow$ ) at  $t = 0$  indicates the injection of the target solutions of different concentrations for the recording of the association phase. The open arrows ( $\Uparrow$ ) point to the beginning of the rinsing step for the dissociation phase. The solid lines are the best fit to a Langmuir model. Typical  $R^2$  after fitting is 0.999. The target concentrations are 1, 10, 50, 100, and 200 nM, respectively. (a) Hybridization between MM0 DNA targets and their PNA probes in high ionic strength buffer solution. (b) Hybridization between MM0 DNA targets and their PNA probes in low ionic strength buffer solution. The sensor surface was regenerated with 10 mM NaOH after rinsing for next experiment.

In the first 10 min, one can observe the distinct kinetic steps by increasing the target DNA as a function of time. The association rate increased with increasing the concentration of target DNA. By fitting of each association phase using equation 1, an approximately linear correlation of the measured rate constants with concentration of target was found. The association constant  $k_{on}$  is obtained as the slope of a  $k_a$  versus concentration plot.

During rinsing process, dissociation starts with decreasing fluorescence intensity. As expected, the dissociation kinetics showed no significant dependence of target concentration. The dissociation constant was determined as the average of  $k_{off}$  values determined at the different concentrations of target by fitting of dissociations phases using equation 2.

The collected results for the hybridization of PNA/DNA on the sensor surface are presented in Figure 4.3 and Table 4.2. One can notify that there are no significant differences in rate constants and fluorescence intensities for each set of PNA/ DNA hybridization at 2 different ionic strengths.

**Table 4.2** Apparent kinetic rate constants and equilibrium constants for MM0 PNA/DNA hybridizations. The rate constants,  $k_{on}$ ,  $k_{off}$ , and the affinity constant,  $K_A$  were determined for each data set at the different ionic strength from the fitting Langmuir model in Figure 4.3.

	High ionic strength			Low ionic strength		
	P-11/T-11	P-13/T-13	P-15/T-15	P-11/T-11	P-13/T-13	P-15/T-15
$k_{on} / \text{M}^{-1} \text{s}^{-1}$	$4.2 \times 10^4$	$3.2 \times 10^4$	$1.6 \times 10^4$	$4.5 \times 10^4$	$3.9 \times 10^4$	$1.7 \times 10^4$
$k_{off} / \text{s}^{-1}$	$7.0 \times 10^{-5}$	$4.1 \times 10^{-5}$	$2.0 \times 10^{-5}$	$7.6 \times 10^{-5}$	$4.5 \times 10^{-5}$	$2.0 \times 10^{-5}$
$K_A / \text{M}^{-1}$	$5.9 \times 10^8$	$7.8 \times 10^8$	$8.0 \times 10^8$	$6.0 \times 10^8$	$9.1 \times 10^8$	$8.5 \times 10^8$
$T_m / ^\circ\text{C}$	64.1	69.5	75.5	67.5	70.7	76.6

Indeed, the ionic strength does not play a dominant role on PNA/DNA hybridization kinetics due to the PNA having neutral backbone in both MM1 and MM0 case using different lengths of oligonucleotides.

#### 4.4.2 PNA-11mer/DNA-11mer (MM1)

Similar sets of kinetic curves were obtained for one base mismatched DNA targets to PNA probes at the same sensor surface in 2 different buffer solutions as shown in Figure 4.4. And calculated rate constants were summarized in Table 4.3. These values were virtually identical to each set of PNA/DNA hybridizations at high and low ionic strength buffer solutions.

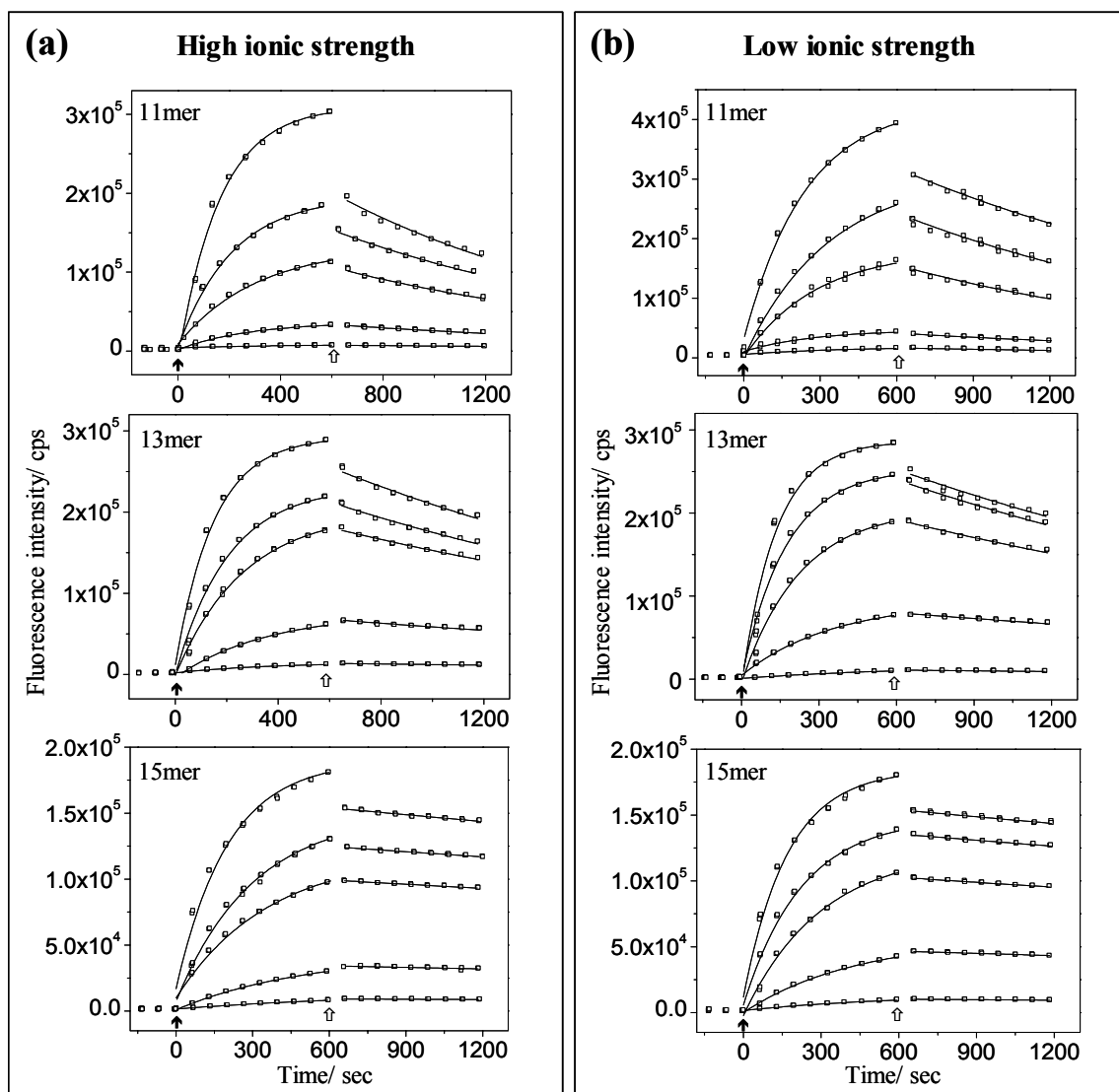


**Figure 4.4** SPFS measurements for kinetic analysis of the association and dissociation phase (taken at  $\theta = 55.7^\circ$ ) at the surface. Open squares are data points collected every 1 min. The solid lines are the best fit to a Langmuir model. Typical  $R^2$  after fitting is 0.999. The target concentrations are 1, 10, 50, 100, and 200 nM, respectively. (a) Hybridization between MM1 DNA targets and their PNA probes in high ionic strength buffer solution. (b) Hybridization between MM1 DNA targets and their PNA probes in low ionic strength buffer solution. The sensor surface was regenerated with 10 mM NaOH after rinsing for next experiment.

The collected results for the hybridization of PNA/DNA on the sensor surface are presented in Figure 4.4 and Table 4.3. One can notify that there are no significant differences in rate constants and fluorescence intensities for each set of PNA/ DNA hybridization at 2 different ionic strengths.

**Table 4.3** Apparent kinetic rate constants and equilibrium constants for MM1 PNA/DNA hybridizations. The rate constants,  $k_{on}$ ,  $k_{off}$ , and the affinity constant,  $K_A$  were determined for each data set at the different ionic strength from the fitting Langmuir model in Figure 4.4.

	High ionic strength			Low ionic strength		
	P-11/ T-mis-11	P-13/ T-mis-13	P-15/ T-mis-15	P-11/ T-mis-11	P-13/ T-mis-13	P-15/ T-mis-15
$k_{on} / \text{M}^{-1} \text{s}^{-1}$	$1.0 \times 10^4$	$2.1 \times 10^4$	$1.5 \times 10^4$	$1.6 \times 10^4$	$2.5 \times 10^4$	$1.8 \times 10^4$
$k_{off} / \text{s}^{-1}$	$6.6 \times 10^{-4}$	$4.5 \times 10^{-4}$	$1.1 \times 10^{-4}$	$7.9 \times 10^{-4}$	$4.5 \times 10^{-4}$	$1.3 \times 10^{-4}$
$K_A / \text{M}^{-1}$	$1.5 \times 10^7$	$4.7 \times 10^7$	$1.4 \times 10^8$	$2.0 \times 10^7$	$5.5 \times 10^7$	$1.4 \times 10^8$
$T_m / ^\circ\text{C}$	42.5	51.3	60.0	43.6	53.0	62.1

## 4.5 Influence of Ionic Strength for Fluorescence Intensity

### 4.5.1 PNA-11mer/DNA-11mer (MM0)

To investigate the limit of ionic strength for MM0 11mer PNA/DNA hybridization, 7 different concentrations of phosphate buffer solutions were prepared without adding salt. Figure 4.5 shows experimental data for individual hybridization of MM0 DNA 11mer target (50 nM) to surface attached PNA 11mer probe at different ionic strength. Once the hybridization reached equilibrium, the subsequent rinsing step followed by changing same buffer solution. Based on the Langmuir model, the rate constants,  $k_{on}$  and  $k_{off}$  and affinity constant,  $K_A$  for individual interaction were calculated and summarized in Table 4.4.



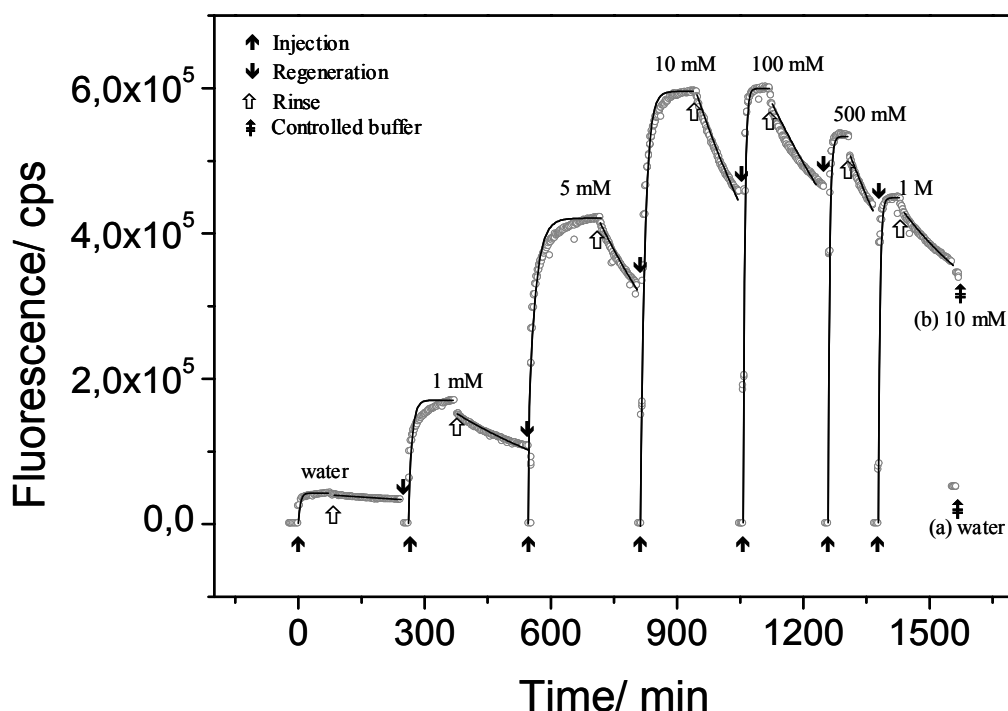


**Figure 4.5** Hybridization kinetics for PNA 11mer (P-11) and DNA 11mer (T-11) at 7 different phosphate buffer solutions. Kinetic curves were recorded by SPFS as a function of time (open circle). The solid arrows ( $\uparrow$ ) indicate the injections of the target (50 nM) DNA for  $k_{on}$  and the open arrows ( $\uparrow$ ) are rinsing for  $k_{off}$  with fresh buffer solution. The sensor surface was regenerated ( $\downarrow$ ) with 10 mM NaOH for the next experiment. After kinetic experiment of PNA/DNA hybridization at 1 M phosphate buffer solution, the buffer solution was switched ( $\downarrow$ ) with water (a) and 1 M (b). To analysis the rate constants for PNA/DNA hybridization in different buffer solutions, the kinetic data was fitted by Langmuir model (solid lines).

**Table 4.4** Rate constants and affinity constant for PNA 11mer (P-11) and DNA 11mer (T-11) hybridizations in different phosphate buffer solutions.

Hybridizations for P-11/T-11						
Buffer concentration $c_0$ / mM	1	5	10	100	500	1000
$k_{on} / (M^{-1} s^{-1})$	$4.4 \times 10^4$	$4.1 \times 10^4$	$4.2 \times 10^4$	$4.8 \times 10^4$	$5.1 \times 10^4$	$5.5 \times 10^4$
$k_{off} / (s^{-1})$	$4.0 \times 10^{-5}$	$4.8 \times 10^{-5}$	$5.8 \times 10^{-5}$	$5.9 \times 10^{-5}$	$6.0 \times 10^{-5}$	$5.6 \times 10^{-5}$
$K_A / (M)$	$1.1 \times 10^9$	$8.5 \times 10^8$	$7.2 \times 10^8$	$8.1 \times 10^8$	$8.5 \times 10^8$	$9.8 \times 10^8$

DNA/DNA hybridization reactions, in general, are very ionic strength dependent. Various contributions to the observed effects have been identified: (1) first of all, DNA shows a limited solubility at low ionic strength, (2) at the single strand level, changing the ionic strength results in a change of the degree of stretching of these oligo-electrolytes, (3) the hybridization reaction at a single site on the sensor surface strongly responds to any change in ionic strength of the bulk solution simply because the charges along the probes repel the co-charges along the target strands that are approaching from solution in low ionic strength buffer much more than at high ionic strength, and (4) single or double strands on individual sites on the sensor surface talk to their neighbors via their electrostatic interaction unless they are sufficiently (laterally) separated. For the employed PNA catcher probe matrix only at the very beginning of the hybridization reaction, i.e., at a negligible DNA target surface coverage, the ionic strength does not play a role for the hybridization reaction. As soon as a significant fraction of the probe binding sites are occupied electrostatic cross talk sets in. This can be clearly identified in Figure 4.5 by at least 2 observations: for the experiments in very low ionic strength buffer the level of fluorescence intensity that is reached at saturation constantly increased with increasing ionic strength up to 10 mM. We interpret this dependence as a direct consequence of the electrostatic repulsion between neighboring DNA (target) strands leading to an effective reduction of the affinity constant and, hence, a reduced coverage for the lower ionic strength buffers at otherwise identical conditions, in particular, at identical bulk target concentrations. Nevertheless, it is remarkable that a significant hybridization could be observed even in pure water. This is impossible for DNA/DNA hybridization experiments given the solubility limits for DNA.

The other clear indication for an ionic strength dependent cross talk between individual sites are the deviations in the kinetics with increasing coverage, again much more pronounced for the low ionic strength, e.g., 1 mM and 5 mM, than at high ionic strength, e.g., for a 1 M buffer (Figure 4.5).

Due to these deviations in the Langmuir fits the obtained rate constants are only approximate. Nevertheless, it can be clearly seen that the ionic strength effect for PNA/DNA interactions does not result in any drastic changes of the rate constants compared with the situation for DNA/DNA hybridization. Because of the neutral nature of the PNA, the charge density accumulating at the interface during the hybridization with DNA is considerably lower than that of DNA/DNA hybridization minimizing repulsion effects.

For the hybridization in 10 mM phosphate buffer solution (NaCl=0 mM), the affinity constant was determined to be  $K_A = 7.2 \times 10^8 M^{-1}$ . This is comparable with the hybridizations performed in the 10 mM phosphate buffer solutions adding 20 mM ( $K_A = 6.0 \times 10^8 M^{-1}$ ) and 137 mM ( $K_A = 5.9 \times 10^8 M^{-1}$ ) NaCl presented in Figure 4.3 and Table 4.2. The  $K_A$  value from the hybridization in NaCl=0 mM is little higher than those of hybridizations in phosphate buffer solutions with adding salt (NaCl=20 mM, and 137 mM). Indeed, the ionic strength shows little influence on the PNA/DNA hybridization kinetics.

Although the effect of ionic strength is negligible for the binding kinetics, the fluorescence intensity for PNA/DNA hybridization was influenced by the ionic strength as shown in Figure 4.5. That phenomenon could be understood in respect of surface plasmon optics. In principle, the chromophors near the metal/solution interface can be excited by evanescence field generated from surface plasmon. The emitted fluorescence photons are monitored during hybridization event in real time. In order to achieve an optimized fluorescence signal and not to lose too much intensity by energy transfer to the metal substrate, the chromophors have to be separated sufficiently from the metal surface. Chromophors close to the metal is quenched easily leading low fluorescence yield. The PNA/DNA duplex in water (low ionic strength) can be precipitated easily due to the PNA solubility so the chromophors sit very close to the metal surface. Thereby the fluorescence intensity for hybridizations done in low ionic strength (1 mM and 5 mM) is much less than hybridizations in high ionic strength. The PNA/DNA duplex at high ionic strength (500 mM and 1 M) are collapsed because negatively charged DNA is aggregated by positive metal ions.

As a result the chromophors are close to the metal surface losing fluorescence intensity. The maximum hybridization signal was achieved at 10 mM and 100 mM phosphate buffer solution. Subsequently, buffer solution was switched sequentially after the kinetic experiment for PNA/DNA hybridization done at 1 M phosphate buffer solution. By changing with water, the fluorescence intensity dropped down immediately to the intensity of PNA/DNA hybridization done at water (Figure 4.5 (a)). As one can see in Figure 4.5 (b), the fluorescence intensity was almost recovered and visually appeared on the prolongation of the dissociation curve. Actually, the fluorescence changes are not due to the amount of bound DNA target but due to the distance of dye and metal surface.

By varying the ionic strength, the geometric rearrangement of PNA/DNA duplex might be changed, that means different distance from surface to chromophors can influence the

fluorescence intensity. SPFS provides enough sensitivity for small configuration change of PNA/DNA duplex on the sensor surface.

#### 4.5.2 PNA-11mer/DNA-11mer hybridization in water (MM0)

Figure 4.6 shows typical global analysis of 11mer PNA/DNA hybridization in deionized water (MilliQ-water, 18 M $\Omega$ /cm). In the first 10 min, one can observe the distinct kinetic steps by increasing the target DNA as a function of time. The association rate increased with increasing the concentration of target DNA. By fitting of each association phase using equation 1, an approximately linear correlation of the measured rate constants with concentration of target was found. The association constant  $k_{on} = 4.6 \times 10^5 \text{ M}^{-1}$  is obtained as the slope of a  $k_a$  versus concentration plot. It was surprising that the association rate in deionized water observed faster one order of magnitude than water containing salt. The DNA target could be stretched in water without salt. These stretched target DNAs can bind to PNA easily resulting fast association.

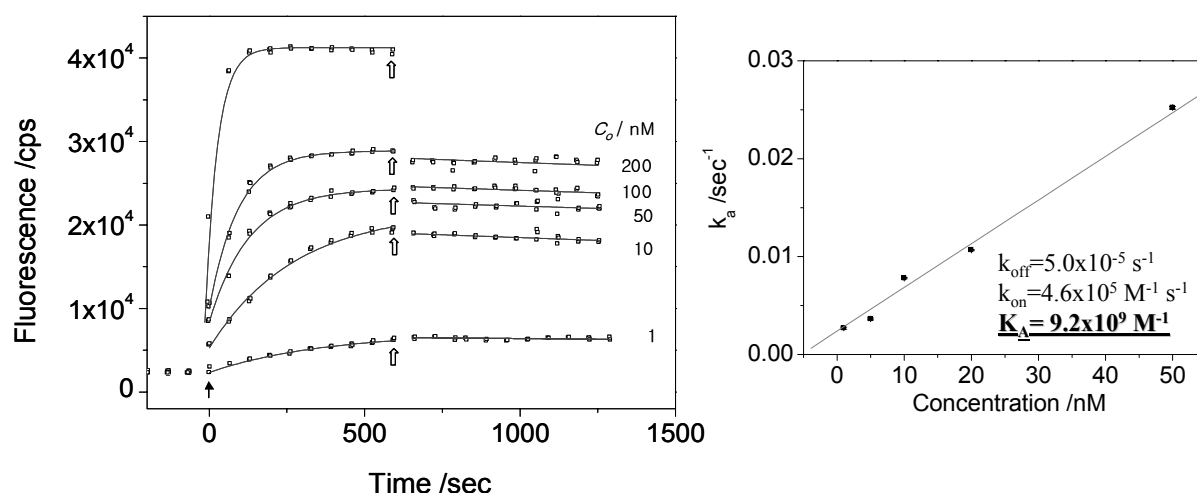


**Figure 4.6.** (a) Global analysis of 11mer PNA/DNA hybridization at 55.7° in deionized water. Open squares are data points collected every 1 min. The solid lines are the best fitting to Langmuir model. (b)  $k_a$  obtained from fitting data (open squares) of (a) versus concentration as a function of target concentration  $c_0$ . The solid line is a linear fit.

During rinsing process, dissociation starts with decreasing fluorescence intensity. As expected, the dissociation kinetics showed no significant dependence of target concentration. The dissociation constant was determined as the average of  $k_{off} = 5.0 \times 10^{-5} \text{ M}^{-1}$  values

determined at the different concentrations of target by fitting of dissociations phases using equation 2. As a result, the affinity constant  $K_A = 9.2 \times 10^9 M^{-1}$  was determined.

It is remarkable that the hybridization was analyzed in water with reliable rate constants. The affinity of PNA/DNA hybridization in water was higher about one order of magnitude than that measured in salt containing water.

#### 4.5.3 Fluorescence intensity at different ionic strength

The effect of ionic strength in bulk solution was evaluated by fluorescence spectroscopy. Figure 4.7 shows the fluorescence intensities according to the ionic strength using the Cy5-labelled DNA 11mer in a range of  $Na^+$  concentration. The fluorescence emission is nearly invariant to the variation of the sodium concentration in a rather wide concentration range from 0 mM to 1000 mM.

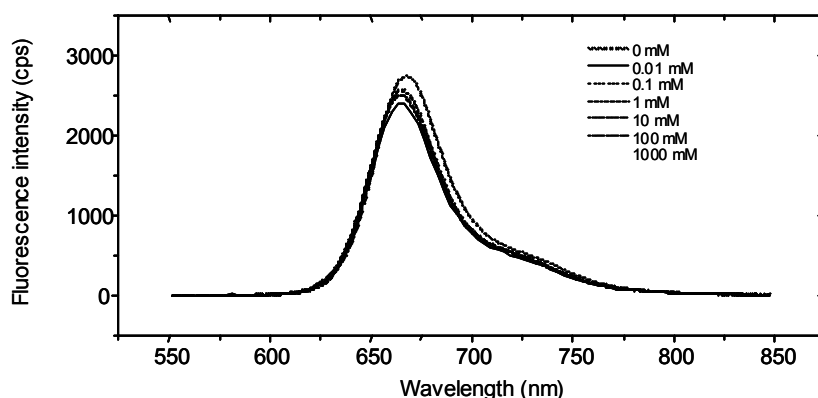


**Figure 4.7.** Fluorescence intensity of Cy5 labelled DNA in a range of ionic strength.

In order investigate the fluorescence intensity at the metal surface, controlled experiments were performed (Figure 4.8) by changing the ionic strength after 11mer PNA/DNA hybridization.

First, the hybridization of 11mer PNA/DNA was performed at different ionic strength as discussed in chapter 4.5.1. The each fluorescence intensities were collected (Figure 4.8(a)) in angular scan after hybridization (Figure 4.5). The window of maximum fluorescence yield

was observed between the hybridization in 10 and 100 nM PB. The difference of fluorescence intensity is not due to the chromophore. The emission of chromophore does not influenced by the ionic strength as shown in the fluorescence spectroscopy.

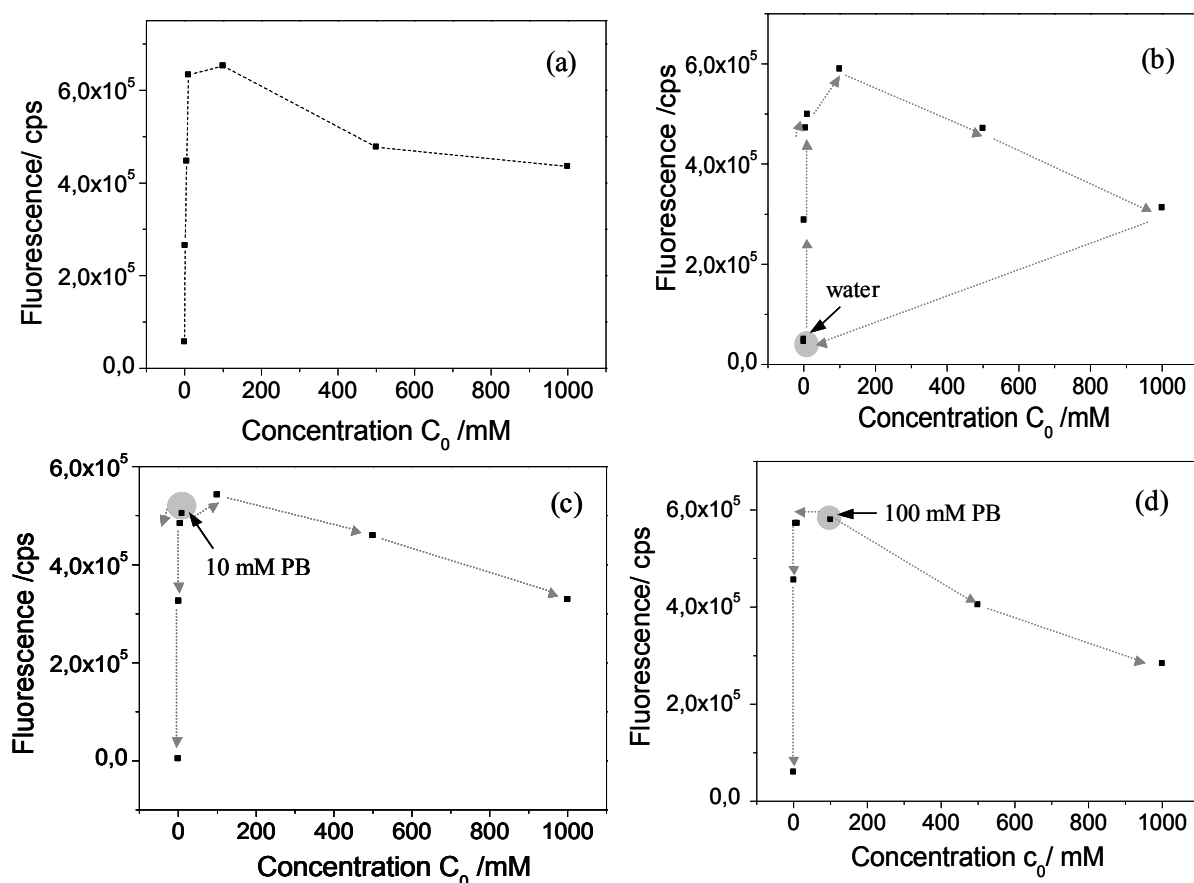


**Figure 4.8.** Fluorescence intensity vs. PB buffer concentration  $c_0$  at different ionic strength. (a) The data points (black squares) were taken from the maximum fluorescence intensities of angular scan after PNA (11mer)/ DNA (11mer) hybridization at different ionic strength. (b) The data points were taken from the maximum fluorescence intensities of angular scan after PNA (11mer)/ DNA (11mer) hybridization in deionized water. Then the buffer solution was changed to 1, 5, 10, 100, 500, 1000 mM of PB, and deionized water, respectively. (c) The data points were taken from the maximum fluorescence intensities of angular scan after PNA (11mer)/ DNA (11mer) hybridization in 10 mM. Then the buffer solution was changed to 100, 500, 1000, 10, 5, 1 mM of PB, and water, respectively. (d) The data points were taken from the maximum fluorescence intensities of angular scan after PNA (11mer)/ DNA (11mer) hybridization in 100 mM. Then the buffer solution was changed to 500, 1000, 100, 10, 5, 1 mM of PB, and water, respectively.

Next, the PNA (11mer)/ DNA (11mer) hybridization was performed in deionized water. Then the buffer solution was changed to 1, 5, 10, 100, 500, 1000 mM of PB, and deionized

water, respectively (Figure 4.8 (b)). In water, the fluorescence intensity was recorded extremely low. This is not due to the amount of bound target DNA. Because the fluorescence was recovered if the buffer was changed to 10 mM PB. The fluorescence loss could be considered that the PNA/DNA duplex in water is collapsed to the metal surface resulting quenching effect of the metal substrate.

In order to investigate the trend of ionic strength the PNA /DNA hybridizations was done in 10 mM PB. Then the buffer solution was changed to 100, 500, 1000, 10, 5, 1 mM of PB, and water, respectively (Figure 4.8 (c)). Also the PNA/DNA hybridizations was done in 100 mM PB. Then the buffer solution was changed to 100, 500, 1000, 10, 5, 1 mM of PB, and water, respectively (Figure 4.8 (d)). All fluorescence intensities showed reversibility according to the ionic strength. In 10 and 100 mM PB the fluorescence intensity observed high emission yield.

## 4.6 Effect of Length

3 different lengths of oligonucleotides (11mer, 13mer, and 15mer) were employed in order to investigate the length dependence for PNA/ DNA hybridization kinetics (for MM0 and MM1 in 2 different ionic strengths) on the surface and in the solution.

PNA 13mer and 15mer have additional 2 base pairs prorogated from the end of PNA 11mer. The association rate of 11mer PNA/DNA hybridization was faster than those of 13mer and 15mer in MM0 situation as shown in Figure 4.3 and summarized in Table 4.2. A short length of oligonucleotides is easier to hybridize than long one. Once DNA binds PNA forming duplex, the duplex for 15mer having 4 more base pairs is more stabile than 11 mer because long one has more hydrogen bonds. Thereby the dissociation rate of long PNA/DNA is much slower than short one. Thus the affinity constant of 15 mer PNA/DNA is higher than those of 13mer and 11mer.

The length dependence is much clearer in MM1 case as shown in Figure 4.4 and summarized in Table 4.3. The length effect of PNA/DNA hybridization is not significant for MM0 case providing similar affinity constant. On the other hand, the length effect for MM1 case is more dominant due to the mismatched base pare in the middle of the sequence. The dissociation rate for 11mer was much faster than those of 13mer and 15mer. The one base mismatched duplex is unstable than fully matched duplex (40 times difference of affinity

constant for 11mer). This mismatched one base could enhance the rate for dissociation much faster than MM0. The difference of affinity between 11mer and 15mer is almost 10 times.

This tendency of length effect for PNA/DNA hybridization is also observed in the solution with comparable  $T_m$  values as summarized in Table 4.2 and 4.3. Increasing the number of base pairs leads the duplex to increase thermal stability. The  $T_m$  of 15mer PNA/DNA is higher than those of 13mer and 11mer. And the difference (20 times) of  $T_m$  between 11mer and 15mer for MM1 case is higher than that (10 times) of  $T_m$  for MM0 case.

Once more, the ionic strength does not influence for short length of oligonucleotides hybridization kinetics.

## 4.7 Mismatch Discrimination

To detect point mutation, one base mismatched DNA target was introduced to the PNA probes at 2 different ionic strengths (NaCl= 20 mM and 137 mM in 10 mM phosphate buffer solution). Figure 4.4 shows the kinetic curves for 11mer 13mer, and 15mer PNA/DNA hybridizations on the sensor surface. The association phase was carried out by injection of 1 nM target solution after short time background measurement. Then the pure buffer solution applied into the flow cell for dissociation kinetics. The hybridization experiments were carried out varying concentration of targets from 1 nM to 200 nM for systematic analysis. The association rate increased with increasing the concentration of target DNA. The analysis of this experiment is also based on the simple Langmuir model. By fitting of each association phase using equation 1, an approximately linear correlation of the measured rate constants with concentration of target was found. The association constant,  $k_{on}$  is obtained as the slope of a  $k_a$  versus concentration plot.

The dissociation starts with decreasing fluorescence intensity during rinsing steps. The dissociation kinetics is distinguished between MM0 and MM1 (Figure 4.3 and 4.4). The dissociation constant was determined as the average of  $k_d$  values at the different concentrations of target by fitting of dissociations phases using equation 2.

The association rate constant is considerably slower than that of the fully complementary hybrid in both low and high ionic strength for all 3 lengths of PNA/DNA duplexes. In addition, the dissociation rate is much faster compared to the fully matched duplex. As a consequence, the affinity constant of MM1 case is lower than that of MM0. This indicates



that good discrimination is possible for a point mutation using the sensor matrix. Especially, the difference between MM0 and MM1 is about 40 times in 11mer case.

## 4.8 Effect of Temperature

The stability of duplex (DNA or PNA) is influenced on temperature, pH, ionic strength or chemical agents that disrupt the hydrogen bonds or the hydrophobic interactions [35]. Among them, temperature is an important physical parameter that can be used to discriminate a point mutation easily. As a duplex can be denatured either chemically (by sodium hydroxide) or by heat a measure of the stability can be obtained by measuring a value known as the melting temperature,  $T_m$ . The melting temperature is defined as the temperature at which 50% of the DNA exists as a duplex and 50% is single stranded. According to the melting temperature, a fully complementary hybrid has a higher melting temperature than hybrids containing mismatches [36,37]. This result is based on the stability of the duplex. However, the melting temperature is usually measured in solution. For the application of biochip technology, it is worth to investigate the temperature dependence of surface hybridization [38,39]. In this section, the kinetics and thermodynamics of the PNA (11mer)/DNA (11mer) hybrids on surface have been studied using the self-assembled sensor matrix (Figure 4.1).

### 4.8.1 Titration analysis for PNA-11mer/DNA-11mer (MM0)

According to the Langmuir model the amount of analyte adsorbed at a given temperature to the binding sites is determined by the equilibrium between free and bound analyte molecules, i.e., by the surface coverage  $\Theta$ , corresponding to the fluorescence intensity,  $I_{max}$ . This surface coverage depends on the affinity constant  $K_A$  and on the bulk concentration  $c_0$ . It is possible to monitor the Langmuir adsorption isotherm by performing experiments in which surface saturation is reached by a stepwise increase (or decrease) of the bulk concentration. The general procedure involves the injection of the analyte solution at low concentration and allowing for the adsorption process to reach equilibrium. This process is repeated with target solutions of higher concentrations until the surface is fully covered by analyte. In practice, the surface coverage  $\Theta(c_0)$  is determined by scaling the detected signal intensity  $I_{fl}(c_0)$  to that of a fully saturated surface. The Langmuir isotherm curve was constructed from the data taken at

the angle of maximum intensity of the angular scans (after rinsing for a short time) as a function of target concentration.

An alternative measurement for the quantitative study of the hybridization process is a titration experiment. According to the Langmuir model the amount of analyte adsorbed at a given temperature to the binding sites is determined by the equilibrium between free and bound analyte molecules, i.e., by the surface coverage  $\Theta$ , corresponding to the fluorescence intensity. This surface coverage depends on the affinity constant  $K_A$  and on the bulk concentration  $c_0$ . It is possible to monitor the Langmuir adsorption isotherm by performing experiments in which surface saturation is reached by a stepwise increase (or decrease) of the bulk concentration. The general procedure involves the injection of the analyte solution at low concentration and allowing for the adsorption process to reach equilibrium. This process is repeated with target solutions of higher concentrations until the surface is fully covered by analyte. The surface coverage is described by equation (3):

$$I_f(c_0) \propto \Theta(c_0) = \frac{c_0 \cdot K_A}{1 + c_0 \cdot K_A} \quad (3)$$

In practice, the surface coverage  $\Theta(c_0)$  is determined by scaling the detected signal intensity  $I_f(c_0)$  to that of a fully saturated surface.

Figure 4.9 (a) shows the titration experiment for PNA (P-RR-11)/DNA (T-RR-11) hybridization monitored at  $20 \pm 0.5$  °C (using the preheating method mentioned in chapter 3.1.3, incidence angle  $\theta = 55.7^\circ$ ).

After the background fluorescence was recorded for a few minutes, a 0.63 nM solution of T-RR-11 was injected and the increase in fluorescence intensity was measured as a function of time until the equilibrium between the bulk concentration and the corresponding surface coverage was reached. Next, the injection of 3.35 nM, 7.5 nM, 15 nM, 37 nM, 76 nM, and 154 nM target in PBS, respectively, resulted in correspondingly higher equilibrium surface coverages with the higher equivalent fluorescence intensities (Figure 4.9 (a)).

The Langmuir isotherm curve (Figure 4.9 (b)) was constructed from the data taken at saturated fluorescence intensity as a function of target concentration. The fitting to the curve gives the affinity constant as  $K_A = 1.1 \times 10^8 \text{ M}^{-1}$  for PNA/DNA hybridization at 20 °C.

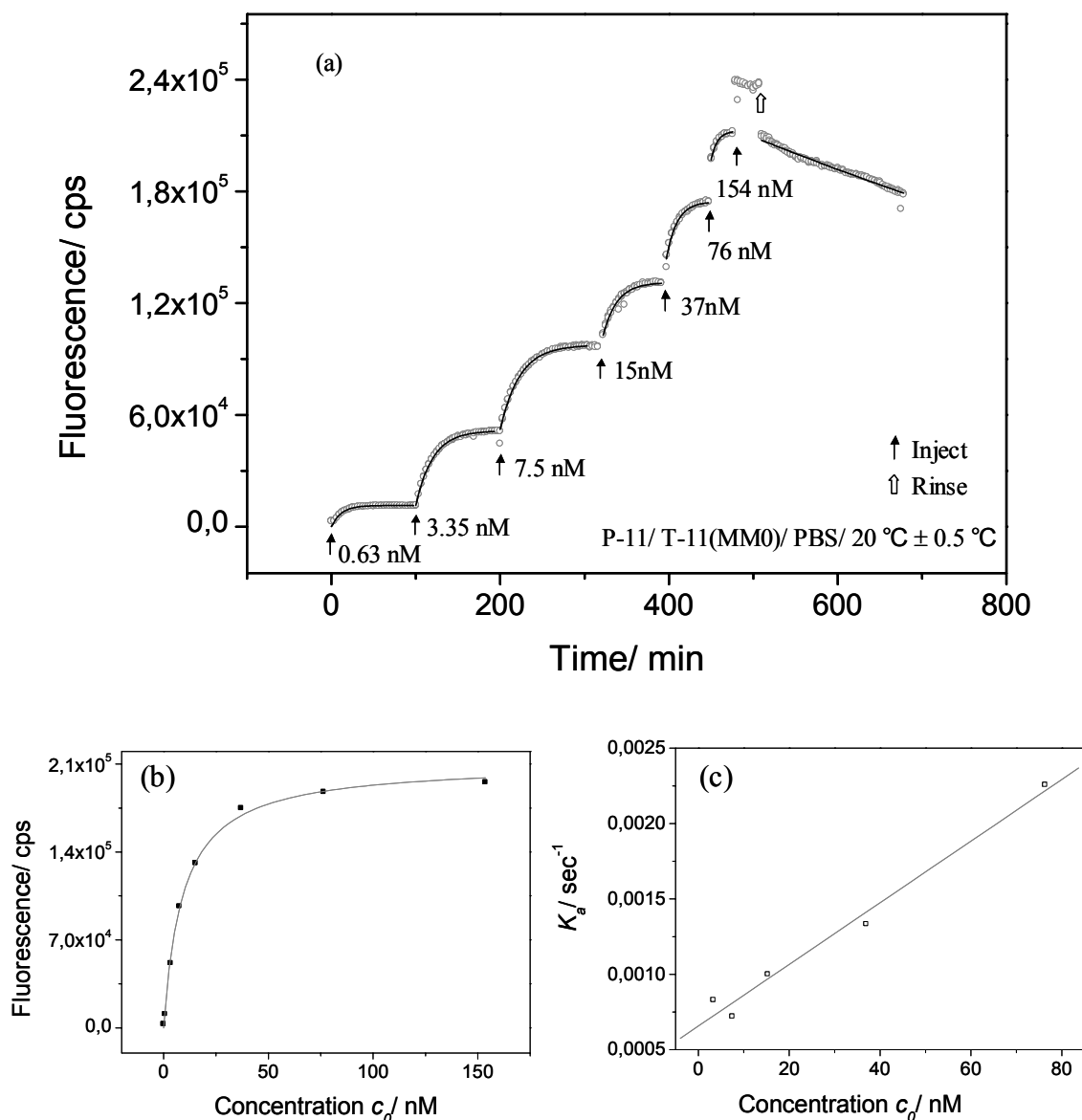


**Figure 4.9.** (a) Titration curves for PNA (P-RR-11)/DNA (T-RR-11) hybridization at  $20 \pm 0.5 \text{ }^\circ\text{C}$ . Open circles are data points collected every 3 min. The solid arrows indicate the injection of the target solution. The fluorescence was recorded until the saturation intensity was reached. After the recording of the 154 nM sample the dissociation process was started by rinsing with pure buffer (open arrow). Insert figure is a Langmuir isotherm curve from data points (black squares) of the saturated fluorescence intensity in titration exp. *versus* target concentration  $c_0$ . (b) Plots (open squares) of the saturated fluorescence intensity taken from (a) *versus* target concentration  $c_0$ . The gray curve corresponds to the fit by the Langmuir isotherm. (c)  $k_a$  obtained from fitting the data (open squares) of (a) as a function of target concentration  $c_0$ . The solid straight line is a linear fit.

Based on the Langmuir model the increase of the fluorescence intensity as a function of time is described by a simple bimolecular reaction:

$$I_{fl}(t) = (I_{\max} - I_0)(1 - \exp(-(k_a)t)), \quad k_a = k_{on} \cdot c_0 + k_{off} \quad (4)$$

with  $I_{\max}$  being the maximum fluorescence intensity from surface-bound duplexes at  $c_0$ .  $I_0$  is the initial background fluorescence, and  $c_0$  the bulk solution concentration in the measurement.

The association kinetics is quantified with respect to the concentration dependence. Fitting the association phase data individually at different target concentrations. The  $k_a$  values increased as the concentration increased as shown in Figure 4.9 (c). The  $k_{on}$ -value was thus obtained by the slope of the  $k_a$  versus target concentration plot and calculated to be  $k_{on} = 2.0 \times 10^4 \text{ M}^{-1} \text{ s}^{-1}$ . By analyzing the dissociation phase of Figure 4.9 (a) a dissociation rate constant of  $k_{off} = 1.5 \times 10^{-5} \text{ s}^{-1}$  can be calculated. Together with the  $k_{on}$  value affinity constant was determined to be  $K_A = 1.3 \times 10^9 \text{ M}^{-1}$ .

The  $K_A$  value obtained from the individual kinetic rates is ca. 10 times higher than that calculated from the Langmuir adsorption isotherm. We attribute this effect to the increasing surface charge density upon hybridization of DNA targets: starting with an (empty) uncharged PNA probe matrix at the sensor surface, each bound target oligonucleotide adds 11 charges to the interface. As the coverage increases, this surface charge density generates a successively repulsive Coulomb barrier for further target binding to the still free binding sites which are, however, cross-talking with the neighboring (charged) hybrids. The target binding-induced generation of a repulsive Coulomb barrier also reduces the apparent affinity  $K_A$  measured in a titration experiment. The same phenomenon will be even more pronounced for the binding of PCR amplicons (chapter 5), for which 125 charges are added to the interface for every bound analyte molecule.

On the other hand, the individual fittings at each concentration are not influenced on the surface effect. Therefore, the affinity constant is high.

Figure 4.10 (a) shows the titration experiment for PNA (P-RR-11)/DNA (T-RR-11) hybridization monitored at 24 °C (incidence angle  $\theta = 55.7^\circ$ ). And The Langmuir isotherm curve (Figure 4.10 (b)) was constructed from the data taken at saturated fluorescence intensity as a function of target concentration. The fitting to the curve gives the affinity constant as  $K_A = 7.2 \times 10^7 \text{ M}^{-1}$  for PNA/DNA hybridization at room temperature. This value based on surface coverage becomes small by increasing the temperature. This means that the bulk

concentration needed to cover the PNA surface with DNA target is higher if the temperature is raised to a higher value.

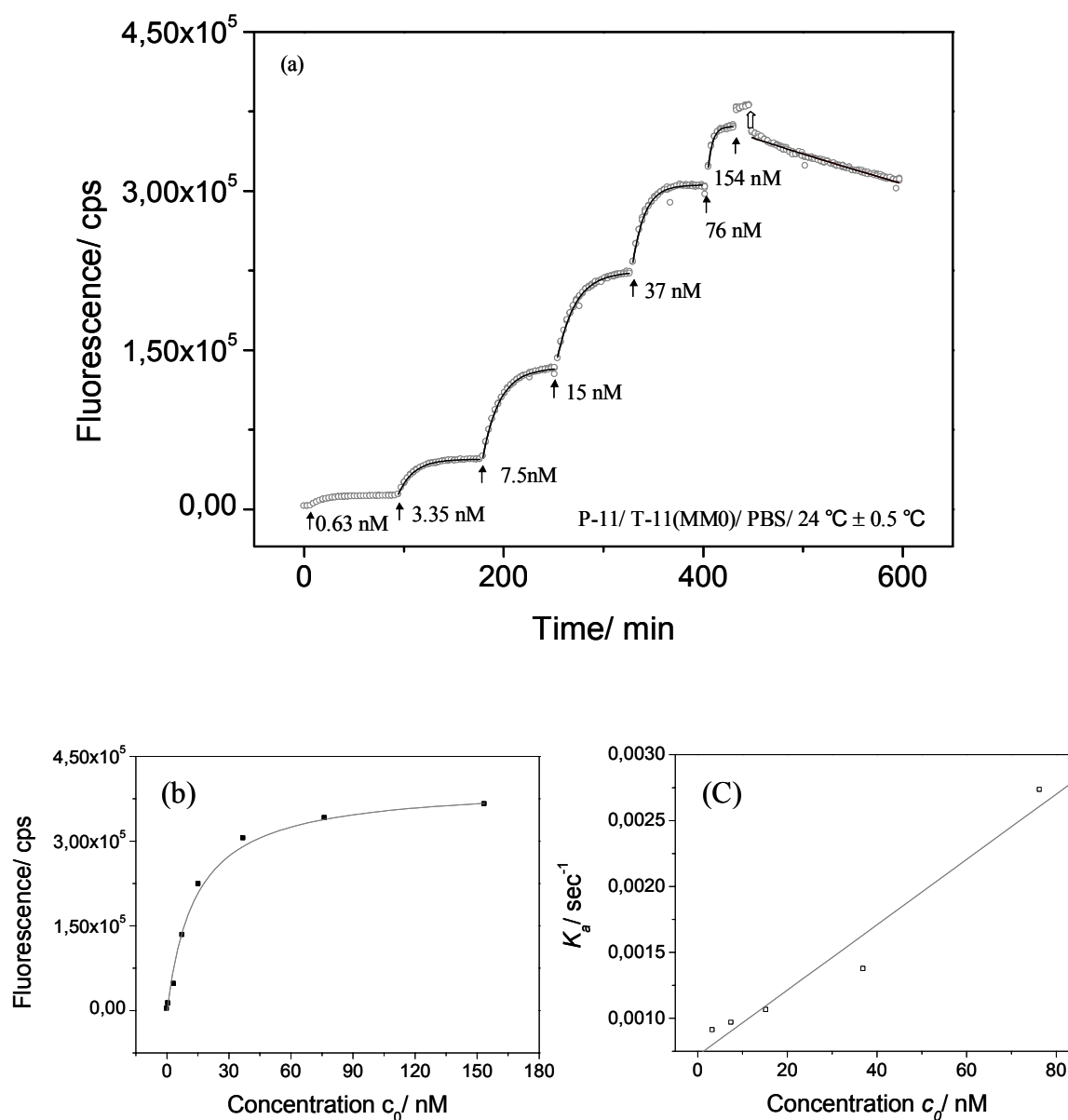
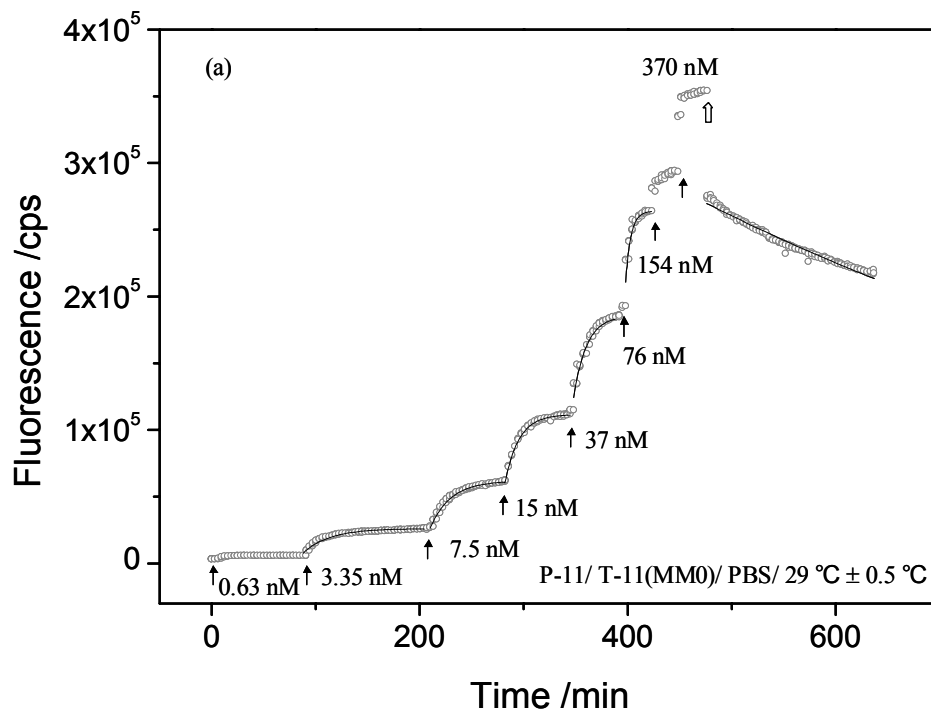


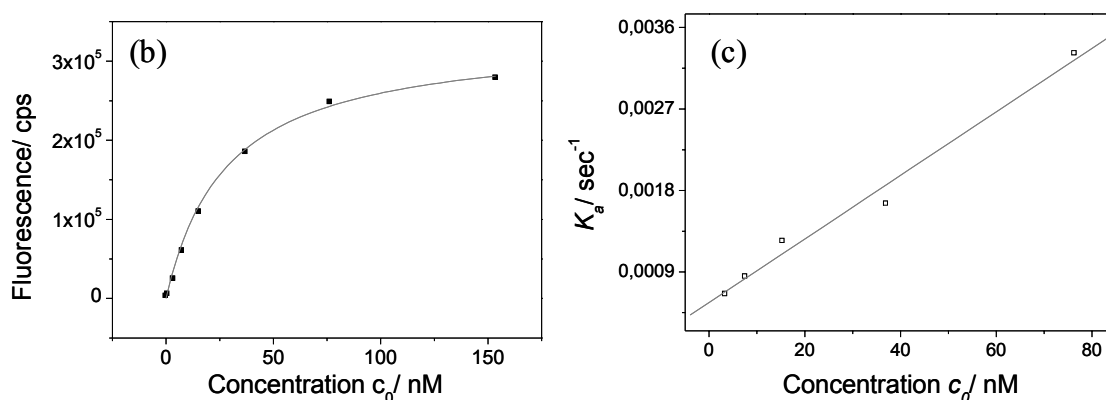
**Figure 4.10.** Titration curves for PNA (P-RR-11)/DNA (T-RR-11) hybridization at  $24 \pm 0.5$  °C. The fluorescence was recorded until the saturation intensity was reached. After the recording of the 154 nM sample the dissociation process was started by rinsing with pure buffer (open arrow). Insert figure is a Langmuir isotherm curve from data points (black squares) of the saturated fluorescence intensity in titration exp. *versus* target concentration  $c_0$ . (b) Plots (open squares) of the saturated fluorescence intensity taken from (a) *versus* target concentration  $c_0$ . The gray curve corresponds to the fit by the Langmuir isotherm. (c)  $k_a$  obtained from fitting the data (open squares) of (a) as a function of target concentration  $c_0$ . The solid straight line is a linear fit.

The  $k_a$  values increased as the concentration increased as shown in Figure 4.10 (c). The  $k_{on}$ -value was thus obtained by the slope of the  $k_a$  *versus* target concentration plot and calculated to be  $k_{on} = 2.5 \times 10^4 \text{ M}^{-1} \text{ s}^{-1}$ . As increasing the temperature, the association rate increased. This temperature effect for association and dissociation rate is more dramatic at high temperature. By analyzing the dissociation phase of Figure 4.10 (a) a dissociation rate constant of  $k_{off} = 1.6 \times 10^{-5} \text{ s}^{-1}$  can be calculated. Together with the  $k_{on}$  value affinity constant was determined to be  $K_A = 1.6 \times 10^9 \text{ M}^{-1}$ .

Figure 4.11 (a) shows the titration experiment for PNA (P-RR-11)/DNA (T-RR-11) hybridization monitored at 29 °C (incidence angle  $\theta = 55.7^\circ$ ). Fitting to the curve gives the affinity constant as  $K_A = 3.5 \times 10^7 \text{ M}^{-1}$  (Figure 4.11 (b)) for PNA/DNA hybridization at 29 °C.

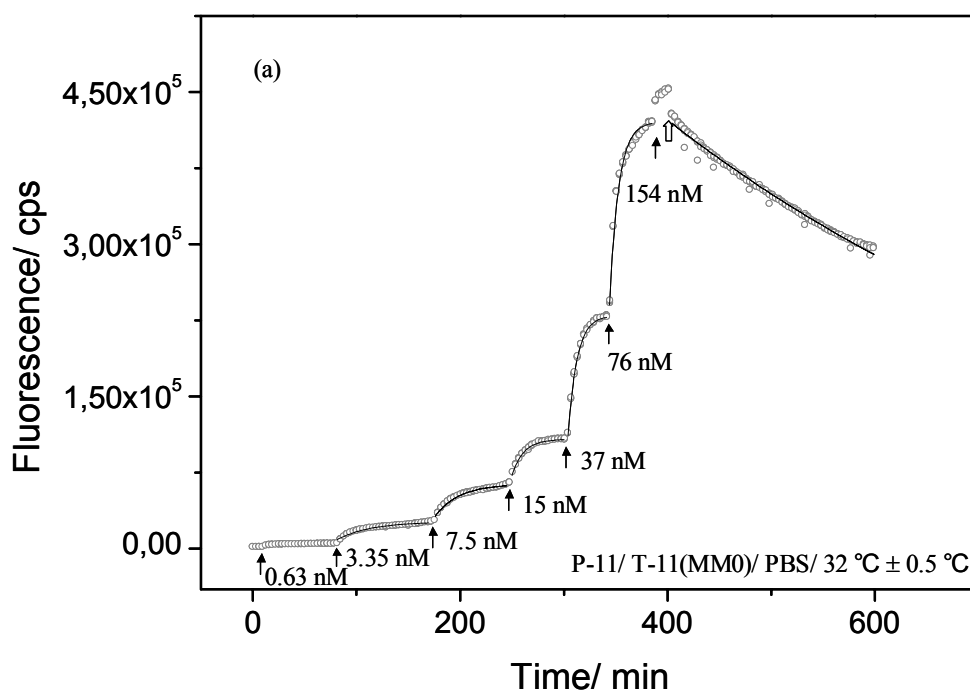
The  $k_a$  values increased as the concentration increased as shown in Figure 4.11 (c). The  $k_{on}$ -value was thus obtained by the slope of the  $k_a$  *versus* target concentration plot and calculated to be  $k_{on} = 3.5 \times 10^4 \text{ M}^{-1} \text{ s}^{-1}$ . By analyzing the dissociation phase of Figure 4.11 (a) a dissociation rate constant of  $k_{off} = 2.4 \times 10^{-5} \text{ s}^{-1}$  can be calculated. Together with the  $k_{on}$  value affinity constant was determined to be  $K_A = 1.5 \times 10^9 \text{ M}^{-1}$ .





**Figure 4.11.** Titration curves for PNA (P-RR-11)/DNA (T-RR-11) hybridization at  $29 \pm 0.5$  °C. After the recording of the 370 nM sample the dissociation process was started by rinsing with pure buffer (open arrow). Insert figure is a Langmuir isotherm curve from data points (black squares) of the saturated fluorescence intensity in titration exp. *versus* target concentration  $c_0$ . (b) Plots (open squares) of the saturated fluorescence intensity taken from (a) *versus* target concentration  $c_0$ . The gray curve corresponds to the fit by the Langmuir isotherm. (c)  $k_a$  obtained from fitting the data (open squares) of (a) as a function of target concentration  $c_0$ . The solid straight line is a linear fit.

Figure 4.12 (a) shows the titration experiment for PNA (P-RR-11)/DNA (T-RR-11) hybridization monitored at 32 °C (incidence angle  $\theta = 55.7^\circ$ ). Fitting to the curve gives the affinity constant as  $K_A = 2.0 \times 10^7 M^{-1}$  (Figure 4.12 (a)) for PNA/DNA hybridization at 32 °C.



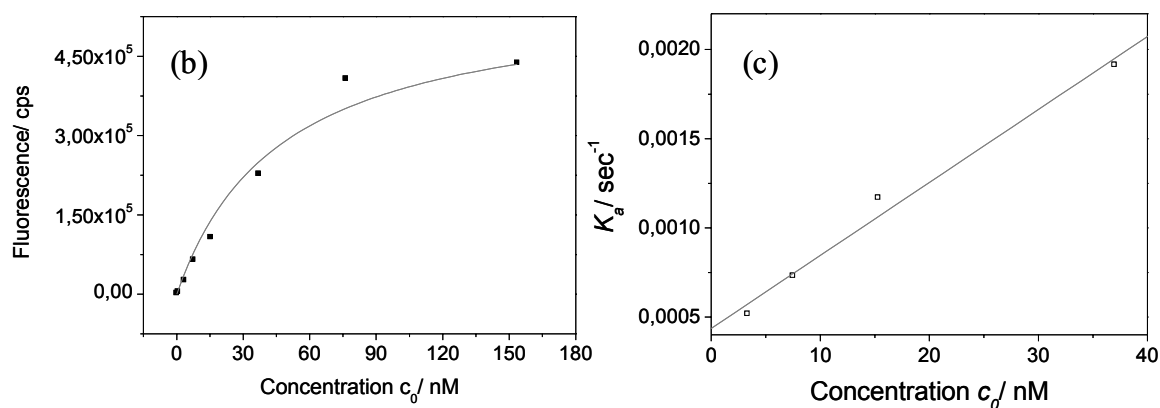


**Figure 4.12.** (a) Titration curves for PNA (P-RR-11)/DNA (T-RR-11) hybridization at  $32 \pm 0.5$  °C. Insert figure is a Langmuir isotherm curve from data points (black squares) of the saturated fluorescence intensity in titration exp. *versus* target concentration  $c_0$ . (b) Plots (open squares) of the saturated fluorescence intensity taken from (a) *versus* target concentration  $c_0$ . The gray curve corresponds to the fit by the Langmuir isotherm. (c)  $k_a$  obtained from fitting the data (open squares) of (a) as a function of target concentration  $c_0$ . The solid straight line is a linear fit.

The  $k_a$  values increased as the concentration increased as shown in Figure 4.12 (c). The  $k_{on}$ -value was thus obtained by the slope of the  $k_a$  *versus* target concentration plot and calculated to be  $k_{on} = 4.1 \times 10^4 \text{ M}^{-1} \text{ s}^{-1}$ . By analysing the dissociation phase of Figure 4.12 (a) a dissociation rate constant of  $k_{off} = 3.2 \times 10^{-5} \text{ s}^{-1}$  can be calculated. Together with the  $k_{on}$  value affinity constant was determined to be  $K_A = 1.3 \times 10^9 \text{ M}^{-1}$ .

In conclusion, the rate constants (both  $k_{on}$  and  $k_{off}$ ) were increased as the temperature increased (Figure 4.13).

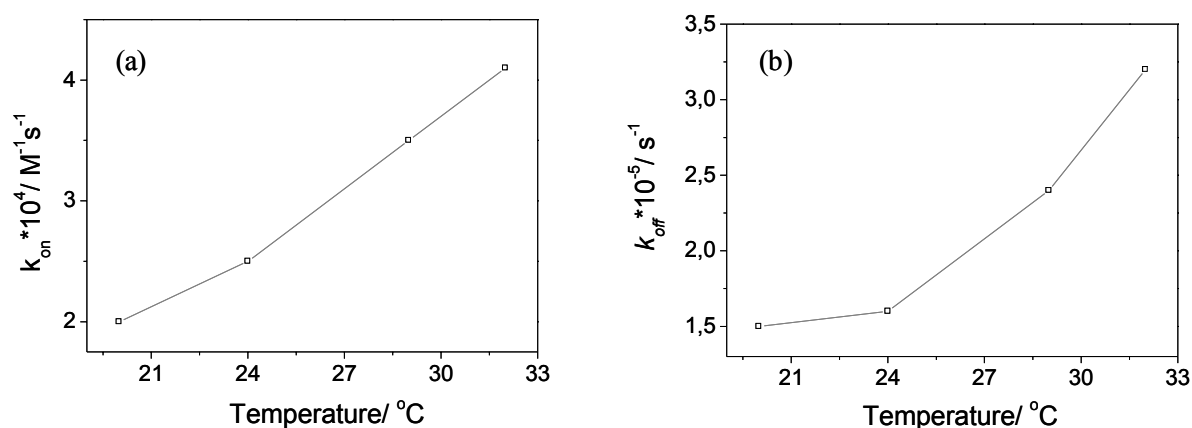


**Figure 4.13.** Temperature effect on the kinetic rate constants. Both association (a) and dissociation (b) rates were increased with increasing of temperature.



### 4.8.2 Langmuir adsorption isotherm

The Langmuir adsorption isotherm is shown in Figure 4.14 by plotting the surface coverage (data from chapter 4.8.1) as a function of concentration at different temperature. By increasing the temperature (from 20 °C to 30 °C) the decrease of surface coverage were observed at certain concentration,  $c_n$ . This means that the bulk concentration needed to cover the PNA surface with DNA target is higher if the temperature is raised to a higher value. When the temperature is cooled down from 32 °C to 20 °C, a gain in surface coverage was observed in presence of target (Figure 4.15).

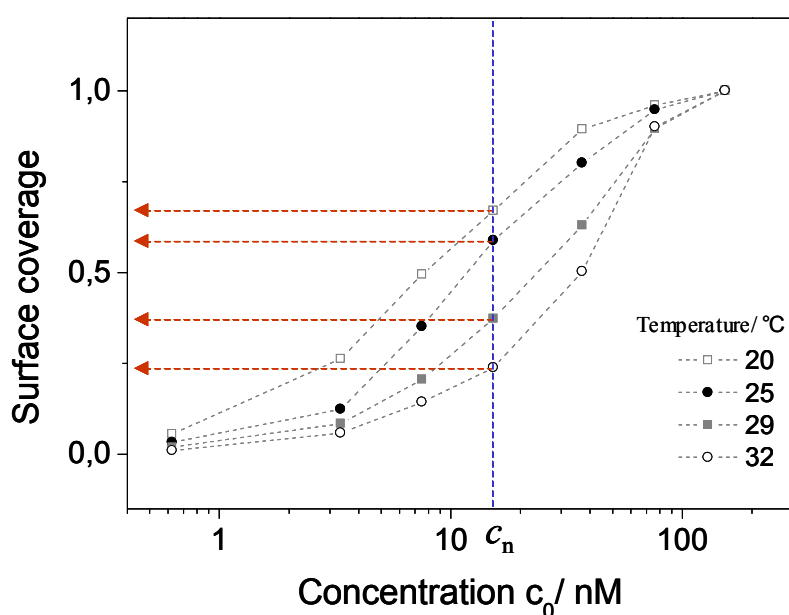


**Figure 4.14.** Normalized semi-logarithmic Langmuir adsorption isotherm curves, surface coverage *versus* concentration,  $c_0$  for PNA (11mer)/DNA (11mer) hybridization at different temperatures. Note the shifts in Langmuir isotherm curves due to the changes of the affinity constants.

This reversibility test of hybridization between PNA and DNA was performed at 26 °C. According to the change of temperature the fluorescence changed. If there is no hysteresis in Langmuir adsorption isotherm curve, the fluorescence intensity should be identical to the initial value ( $4.6 \times 10^5$  cps). However, a complete recovery of fluorescence was not observed (less than 10% loss). However this influence of temperature to the sensor matrix is negligible for kinetic measurement.

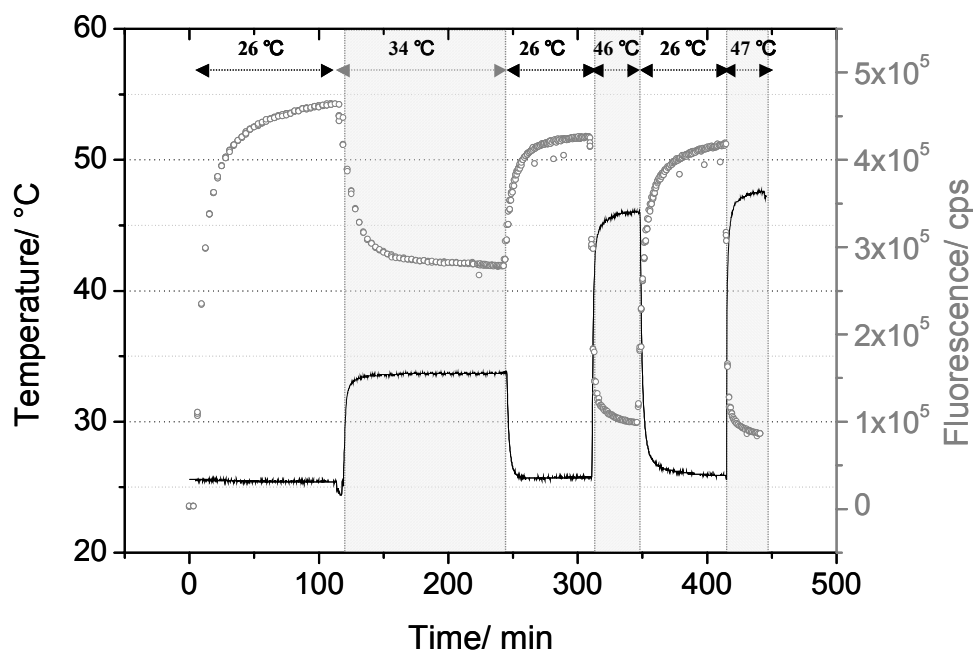


**Figure 4.15.** Reversible hybridization event for PNA (11mer)/DNA (11mer) hybridization at different temperatures.

#### 4.8.3 Gibbs free energy

The kinetic measurements for the PNA/DNA hybridization (chapter 4.8.1) performed at different temperature provide thermal parameters by using the Gibbs free energy [40-43]:

$$\Delta G^0 = \Delta H^0 - T\Delta S^0 = -RT \ln K_A = RT \ln K_D \quad (5)$$

The equation (5) corresponds to a modification of equation (6):

$$\ln K_D = \Delta H / RT - \Delta S / R \quad (6)$$

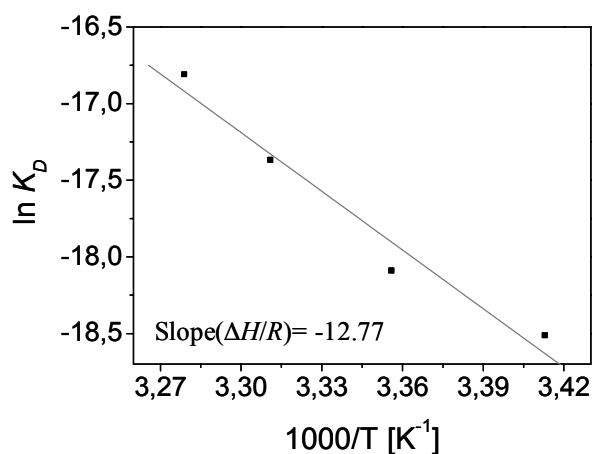


**Figure 4.16.** The van't Hoff plot from the titration experiment of the PNA (11mer)/DNA (11mer) hybridization in a range of temperature.

By plotting  $\ln K_D$  versus temperature the thermodynamic parameters of enthalpy ( $\Delta H = -106 \text{ kJ/mol}$ ) and entropy ( $\Delta S = 207 \text{ J/mol}\cdot\text{K}$ ) for the fully matched 11mer PNA/DNA hybridization were calculated on the surface (Figure 4.16).

## 4.9 Conclusion

The noncharged nature of the PNA backbone is an important feature with many interesting biophysical consequences with a promising probe for detecting the DNA targets. Major benefits of using PNA as a probe are to overcome the limit of ionic strength (even hybridization in water) and to detect a point mutant efficiently with high thermal stability. These advantages were accomplished in this chapter and the application of PNA as a probe for detection of DNA promise for development of DNA sensors.

The presented study has clearly demonstrated the influence of the ionic strength for PNA/DNA hybridization on the well-established sensor surface employing self-assembly strategy and in the solution. SPFS provides enough sensitivity for kinetic analysis in real time on the sensor surface. Indeed, the ionic strength does not play a dominant role on PNA/DNA hybridization kinetics due to the PNA having neutral backbone in both MM1 and MM0 case using different lengths of oligonucleotides. However the fluorescence intensity could be affected according to the change of distance between surface and PNA/DNA duplex generated by the ionic strength. And the limit of ionic strength for detection of DNA target was qualified by varying the concentration of ionic strength from water to 1 M phosphate buffer solution with providing maximum fluorescence window (10~100 mM). Furthermore the discrimination between fully matched and single base mismatched hybridization was accomplished with significant difference of affinity constant. The best discrimination was achieved using 11mer PNA.

And the kinetics and thermodynamics of the fully matching 11mer PNA/DNA hybrids on surface has been studied at a range of temperature based on the Langmuir adsorption isotherm at equilibrium using the self-assembled sensor matrix. By increasing the temperature the shifts of Langmuir adsorption isotherm was observed resulting the increasing of target concentration at certain surface coverage. This affinity shift could provide the information for the concentration of target DNA for further application on biochip to get better performance. Finally, the reliable thermodynamic parameters of enthalpy and entropy for PNA/DNA hybridization were calculated on the surface.

## 4.10 References

- [1] Thévenot, D. R.; Toth, K.; Dust, R. A.; Wilson G. S. *Pure Appl. Chem.*, 1999, 71, 2333-2348.
- [2] Löfås, S.; Malmqvist, M.; Rönnberg, I.; Stenberg, E.; Liedberg, B.; Lundström, I. *Sensors*
- [3] Cush, R.; Cronin, J. M.; Steward, W. J.; Maule, C. H.; Molloy, J.; Goddard, N. J. *Biosens. Bioelectron.*, 1993, 8, 347–353
- [4] Bernard, A.; Bosshard, H. R. *Eur. J. Biochem.*, 1995, 230, 416–423.
- [5] van den Heuvel, D. J.; Kooyman, R. P.; Drijfhout, H. J. W.; Welling, G. W. *Anal. Biochem.*, 1993, 215, 223–230.
- [6] Schuck, P. *Annu. Rev. Biophys. Biomol. Struct.*, 1997, 26, 541–566.
- [7] Lakey, J. H.; Raggett, E. M. *Curr. Opin. Struct. Biol.*, 1998, 8, 119–123.
- [8] Wood S. J. *Microchem. J.*, 1993, 47, 330-337
- [9] Nilsson, P.; Persson, B.; Uhlen, M.; Nygren, P.A. *Anal. Biochem.*, 1995, 224, 400–408.
- [10] Gotoh, M.; Hasegawa, Y.; Shinohara, Y.; Shimizu, M.; Tosu, M. *DNA Res.*, 1995, 2, 285–293.
- [11] Herne, T.; Tarlov, M. J. *Am. Chem. Soc.*, 1997, 119, 8916-8920.
- [12] Jensen, K.K.; Ørum, H.; Nielsen, P.E.; Nordén, B. *Bioche.*, 1997, 36, 5072–5077.
- [13] Kai, E.; Sawata, S.; Ikebukuro, K.; Iida, T.; Houda, T.; Karube, I. *Anal. Chem.*, 1999, 71, 796–800.
- [14] Piscevic, D.; Lawall, R.; Veith, M.; Liley, M.; Okahata, Y.; Knoll, W. *Appl. Surf. Sci.*, 1995, 90, 425–436.
- [15] Liebermann, T.; Knoll, W. *Colloids Surf. A*, 2000, 171, 115-130.
- [16] Neumann, T.; Johansson, M. -L.; Kambhampati, D.; Knoll, W. *Adv. Funct. Mater.*, 2002, 12, 575-586.
- [17] Knoll, W.; Liley, M.; Piscevic, D.; Spinke, J.; Tarlov, M. -J. *Adv. Biophys.*, 1996, 34, 231-251.
- [18] Kambhampati, D.; Nielsen P. -E.; Knoll, W. *Biosens. Bioelectron.*, 2001, 16, 1109-1118.
- [19] Knoll, W.; Park, H.; Sinner, E. -K.; Yao, D.; Yu, F. *Surf. Sci.*, 2004, 570, 30-42.
- [20] Nielsen, P. -E.; Egholm, M.; Berg, R. -H.; Buchardt, O. *Science*, 1991, 254, 1497-1500.
- [21] Anastassopoulou, J. J. *Mol. Struct.*, 2003, 651, 19-26.
- [22] Luscombe, N. M.; Laskowski, R. A.; Thornton, J. M. *Nucl. Acids Res.*, 2001, 29, 2860–2874.

- [23] Todd, A. K.; Adams, A.; Thorpe, J. H.; Denny, W. A.; Wakelin, L. P.; Cardin, C. J. J. *Med. Chem.*, 1999, 25, 536–540.
- [24] Liu, J.; Malinina, L.; Huynh-Dinh, T.; Subirana, J. A. *FEBS Letters*, 1998, 438, 211–214.
- [25] Gao, Y.; Sriram, M.; Wang, A. H. -J. *Nucl. Acids Res.*, 1993, 21, 4093–4101.
- [26] Rulisek, L.; Havlas, Z. *J. Am. Chem. Soc.*, 2000, 122, 10428–10439.
- [27] Tereshko, V.; Wilds, C. J.; Minasov, G.; Prakash, T. P.; Maier, M. A.; Howard, A.; et al. *Nucl. Acids Res.*, 2001, 29, 1208–1215.
- [28] Bains, S. & Smith, C. G. J. *Theor. Biol* 135, 303-307 (1988).
- [29] Freier, S. M. (ed. Crooke, S. T., Lebleu, B.) 67-82 (CRC Press, Boca Raton, FL., 1993).
- [30] Mathews, D. H., Sabina, J., Zuker, M. & Turner, D. H. *J. Mol. Biol.* 288, 911-940 (1999).
- [31] Tenover, F. C. in *Manual of Clinical Microbiology* 119-127 (, Washington, 1991).
- [32] Wolcott, M. J. *Clinical Microbiology Reviews* 5, 370-386 (1992).
- [33] Langmuir, I. *J. Am. Chem. Soc.*, 1918, 40, 1361-1403.
- [34] Karlsson, R.; Michaelsson, A.; Mattsson, L. *J. Immunol. Methods*, 1991, 145, 229-240.
- [35] Tenover, F. C. in *Manual of Clinical Microbiology* Washington, 1991, 119-127.
- [36] Kosaganov, Y. N.; Stetsenko, D. A.; Lubyako, E. N. et al. *Biochemistry* 2000, 39, 11742-11747.
- [37] Tenover, F. C. in *Manual of Clinical Microbiology* Washington, 1991, 119-127.
- [38] Peterson, A. W.; Heaton, R. J.; Georgiadis, R. J. *Am. Chem. Soc.* 2000, 122, 7837-7838.
- [39] Peterlinz, K. A.; Georgiadis, R. *Opt. Commun.* 1996, 130, 260-266.
- [40] Puglisi, J. D., and Tinoco, J. I. (1989) *Methods Enzymol.* 180, 304-325.
- [41] Ratilainen, T.; Holmén, A.; Tuite, E.; Nielsen, P. E. *Biochemistry* 2000, 39, 7781-7791.
- [42] Marky, L. A., and Breslauer, K. J. (1987) *Biopolymers* 26, 1601-1620.
- [43] Draper, D. E., and Gluick, T. C. (1995) *Methods Enzymol.* 259, 281-351.

## CHAPTER 5

# DETECTION OF OLIGONUCLEOTIDES AND GENETICALLY MODIFIED AMPLICONS

---

### 5.1 Motivation

Recently, genetically modified organisms (GMOs) have raised a high interest and many political debates due to their influence on the environment and concerning their safety as food and feed. Strict regulations have been enforced during the 1990s in the European Union, and even more stringent rules for food and feed labeling and traceability have recently been approved [1]; whereas, other countries do not require specific labeling. The need for rapid, simple, and sensitive methods for the detection and quantification of GMOs in food is increasingly important [2].

Two primary techniques have been developed thus far for the detection of GMOs: DNA analysis by Polymerase Chain Reaction (PCR) and protein analysis [3]. Molecular biological methods routinely used in the food industry, mostly PCR, sometimes lead to ambiguous interpretations due to the low specificity of the primer sequences or the “carry-over” contaminations that can produce false positives. A recent example of controversial assignment made on the basis of PCR results is the suspect evidence of transgenic contamination of maize in Mexico, which raised a great debate among scientists [4-7]. Nested PCR [8], real-time quantitative PCR [9], and biosensor technology [10] are suitable methods for increasing the specificity of GMO analysis.

Peptide nucleic acids (PNAs) will play an important role in improving existing and developing novel techniques for DNA hybridization-based sensing with better sequence discrimination in genetic diagnostics and molecular biology [11]. Several key issues suggest the use of PNA rather than DNA probes for sensor-based hybridization. First, the hybrid stability, as measured by the melting temperature ( $T_m$ ) of PNA / DNA duplexes, displays in general a slightly higher value than the corresponding DNA / DNA duplexes at physiological ionic strength [12]. Second, given that PNA has a non-charged peptide backbone, its physico-chemical properties differ significantly from polyanionic oligonucleotides. The stability of

PNA/DNA complexes (which is, in part, due to the non-charged PNA backbone) is therefore almost insensitive to the ionic strength [13].

Biomolecular interactions have been analyzed based on electrochemical data [14], AFM studies [15], quartz crystal microbalance measurements (QCM) [16], and by other techniques. Among the optical methods, surface plasmon resonance (SPR) [17-19] has been used to monitor in real time the interaction between molecules at the surface of a thin metal film, typically gold. The surface plasmon resonance occurs if polarized light reaches the interface between a thin metal film and a dielectric medium, e.g., in the Kretschmann geometry [20]. The alternating electro-magnetic field of the light causes oscillations of the nearly free electrons in the metal. These oscillations produce an evanescent wave that is spatially confined and decays normal to the interface exponentially. In surface plasmon field-enhanced fluorescence spectroscopy (SPFS), such surface plasmon waves are used to excite chromophore-labeled analyte target molecules and monitor their fluorescence intensity during hybridization [21]. The nature of the evanescent field of the surface plasmon mode leads to an excitation probability that also exponentially decays away from the interface [22]. However, should the chromophore be placed too close to the metal substrate, Förster energy transfer would result in an undesired loss of emission probability. Considering both effects, the chromophore-labeled analyte should be placed within a matrix layer of ca. 30 to 100 nm away from the Au sensor surface [23]. In order to achieve an optimized fluorescence signal, a well-established architecture was used for the sensor surface (Figure 5.1.) [24]. This architecture is a stable, specific sensor surface employing covalently immobilized PNAs on a streptavidin layer prepared *via* a self-assembly process.

In order to evaluate the kinetics for biomolecular interaction, especially PNA/DNA hybridization on a sensor surface the probe PNAs were designed carefully to be complementary to a recognition sequence of GMOs in food [25-27]. As target GMOs, DNA amplicons were amplified by polymerase chain reaction (PCR) using a template gene extracted from Monsanto's Round-up Ready<sup>TM</sup> soybean. By a heating-quenching process, the prepared double stranded PCR targets were separated, and used as a target at low ionic strength [28]. Many examples for the kinetic analysis of biomolecular interaction processes on a sensor surface using SPFS have been reported [29-35]. The rate constants for hybridization could be determined by several different experiments. As a model system for the understanding of long PCR products, the kinetics for oligonucleotides PNA/DNA

hybridization was demonstrated on a sensor surface with a complementarily matched sequence as well as a partly mismatched sequence.

Popular methods for DNA diagnostics are denaturing HPLC (dHPLC) [36,37], temperature gradient capillary electrophoresis [38], matrix assisted laser desorption/ionization (MALDI) resequencing [39], and gel electrophoresis. However, problems arise due to the long associated with the consuming of analyzing time, high cost of the preparation, and difficulty in detection of single nucleotide polymorphisms (SNPs). The SPFS technique based on specific DNA sequences is suitable for rapid and sensitive detection to identify GMOs on the surface. This optical technique detects and quantifies changes in response signal in the vicinity of sensor chip surfaces to which probes are immobilized, allowing detection of analytes interacting with the probes. The investigation of the effect of probe PNAs immobilized on the surface is required for better sensing properties. Furthermore, it is possible to measure the reliable detection limit of the PCR target on the surface using SPFS as well as the quantitative kinetic analysis on account of the high sequence specificity of PNA and stability of duplex [40,41],

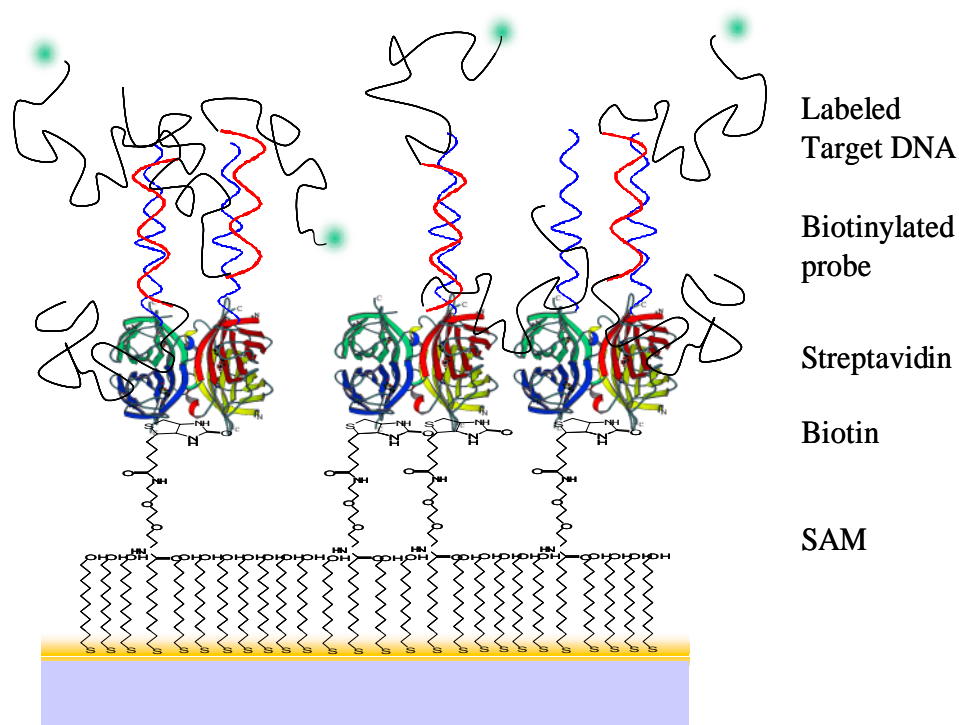


**Figure 5.1.** Illustration of the sensor matrix used in this study. See chapter 3 for more detail on the architecture assembly.



**Table 5.1.** The sequences of the probes and targets used in this study.

<sup>a</sup> Bold-underlined letter is the mismatched base to their probe and target. <sup>b</sup> Italic-underlined base pairs are complementary to the PNA probe. <sup>c</sup> Selected PCR as an impurity for limit of detection.

Probes	PNA	P-RR-11	Biotin-AEEA-AEEA - AGAGTCAGCTT -NH <sub>2</sub>
		P-RR-13	Biotin-AEEA-AEEA - CTAGAGTCAGCTT -NH <sub>2</sub>
		P-RR-15	Biotin-AEEA-AEEA -TGCTAGAGTCAGCTT -NH <sub>2</sub>
	P-RR-mis-11 <sup>a</sup>	Biotin-AEEA-AEEA - AGAG <b>CC</b> AGCTT -NH <sub>2</sub>	
		P-RR-mis-13 <sup>a</sup>	Biotin-AEEA-AEEA - CTAGAG <b>CC</b> AGCTT -NH <sub>2</sub>
		P-RR-mis-15 <sup>a</sup>	Biotin-AEEA-AEEA -TGCTAGAG <b>CC</b> AGCTT -NH <sub>2</sub>
	DNA	D-RR-15	Biotin- 5'-TTT-TTT-TTT-TGCTAGAGTCAGCTT-3'
	DNA	T-RR-11	Cy5-5'- AAGCTGACTCT-3'
		T-RR-13	Cy5-5'- AAGCTGACTCTAG-3'
		T-RR-15	Cy5-5'- AAGCTGACTCTAGCA-3'
T-RR-mis-11 <sup>a</sup>		Cy5-5'- AAGCTG <b>G</b> CTCT-3'	
T-RR-mis-13 <sup>a</sup>		Cy5-5'- AAGCTG <b>G</b> CTCTAG-3'	
T-RR-mis-15 <sup>a</sup>		Cy5-5'- AAGCTG <b>G</b> CTCTAGCA-3'	
Targets	T-RR-125 <sup>b</sup>	Cy5-5'- CATTTCATTTGGAGAGGACACGCTGAC <b>AAGCTGACTC</b>	
		<b>TAGCA</b> GATCTTTCAAGAATGGCACAATAAACAACATGGCAC	
		AAGGGATACAAACCCCTTAATCCCAATTCCAA TTTCATAAACC CCA	
	T-RR-169 <sup>b</sup>	Cy5-5'- ATCCCACTATCCTTCGCAAGACCCCTTCCTCTATAAG	
		GAAGTTCAATTCATTTGGAGAGGACACGCTGAC <b>AAGCTGACTC</b>	
		<b>TAGCA</b> GATCTTTCAAGAATGGCACAATAAACAACATGGCTCA AGGGATACAAACCCCTTAATCCCAATTCCCAATTTCATAAACC CA	
	T-Mu-159 <sup>c</sup>	CGGCGGTCACTACCTATAGACGTCTTTAAGCGGGAATGGTG	
		CGCCTAGGTCCTGCATCTTCAACATGCAGTGTGATCCGGGA	
		GCCAGGGGAGCTCACAAAGTATCCCGCTTAAGGTCGTGTGAC CGCCGGCAAATGATCACCTAGGCTCGAGCCCATG	

## 5.2 Kinetic Experiments for PNA/DNA Hybridization

If the target solution is applied to a probe-modified sensor surface, it is difficult to observe a reasonably strong response by SPR because duplex formation with oligomeric DNA does not generate a significant change in the optical thickness. However, SPFS measurements demonstrated a high sensitivity for monitoring binding events between immobilized PNA and chromophor-labeled target DNA even at concentrations in the fM range [42]. This fluorescence intensity carries kinetic information of hybridization and can be analyzed in terms of the corresponding rate constants for association ( $k_{on}$ ), dissociation ( $k_{off}$ ), and the affinity constant ( $K_A$ ) for PNA/DNA hybridization.

The angle of incidence was fixed at  $\theta = 55.5^\circ$  for monitoring the PNA/DNA hybridization. Kinetics curves were recorded in both the reflectivity and fluorescence mode, starting with a measurement of the fluorescence background for a few minutes as a function of time. All the experiments were performed with 1 mL for each target concentration using the same flow cell with an inlet and outlet and a closed loop circulation at room temperature ( $24 \pm 1^\circ\text{C}$ ) and at a flow rate of 10  $\mu\text{L}/\text{sec}$ .

For the global analysis, Cy-5 labeled DNA target (T-RR-15) solutions (varying in concentration from 1 nM up to 200 nM) were introduced into the flow cell for the association process, and allowed to interact with the PNA functionalized sensor surface for 10 min. After that the dissociation was followed by rinsing with fresh buffer solution (10 mM phosphate buffer solution) for each measurement for 10 min. The surfaces could be fully regenerated by treatment with 10 mM NaOH in order to remove remaining bound target DNA for another analysis cycle at the same sensor surface.

For the titration experiment, a 1 nM solution in 10 mM phosphate buffer of target (T-RR-15) was injected after recording the background fluorescence and the increase in fluorescence intensity was measured as a function of time until the equilibrium surface coverage was reached. Next, target DNA solutions of 5, 10, 20, 50, and 100 nM, respectively, were applied consecutively.

The kinetic-titration experiment was performed as follows: a 1 nM solution of target (T-RR-125 and T-RR-169) was injected, and the increase in fluorescence intensity measured as a function of time until the surface coverage reached equilibrium. Then, the injection of 5 nM to 10 nM target solutions resulted in correspondingly higher equilibrium coverages. After equilibrium with the 10 nM target solution was reached the surface was rinsed with pure 10 mM phosphate buffer solution for typically 1 hour. Next the 20, 50, and 100 nM target

concentrations, respectively, were applied with rinsing steps with phosphate buffer in between. An angular scan was taken at each equilibrium state with the bulk solution in the flow cell and shortly after rinsing the cell with pure buffer.

Each single-exponential analysis was completed by applying a 50 nM target solution until equilibrium was reached, followed by an extended rinsing step.

### **5.3 Hybridization of PNA/ oligomer DNA**

The hybridization between oligomer DNA targets and PNA probes immobilized on the sensor surface was studied as a model system for comparison to elongated PCR targets. The kinetics and affinities for the hybridization of 15mer PNA probes and 15mer DNA targets were analyzed quantitatively with different measurements in order to obtain reliable kinetics and affinity constants.

In the global analysis measurement, hybridization is performed for very short time (almost for 10 min) over a wide range of varied target concentrations from starting an empty catcher PNA probe layer. In order to evaluate the effect of high ionic strength 10 mM phosphate buffer solution with 137 mM NaCl was prepared. The hybridization kinetics of T-RR-15 DNA to the surface-attached PNA probes on the sensor surface was compared at different ionic strengths by global analysis.

The affinity constants were determined by titration experiment, which depends on the surface coverage by increasing the target DNA onto the occupied PNA probe by performing titration experiment.

The single kinetic experiment allowed for the determination of rate constants for MM0 and MM1 (in the middle of the sequence) hybridization and the discrimination between them. Different lengths of PNA probes were used for the hybridization kinetics.

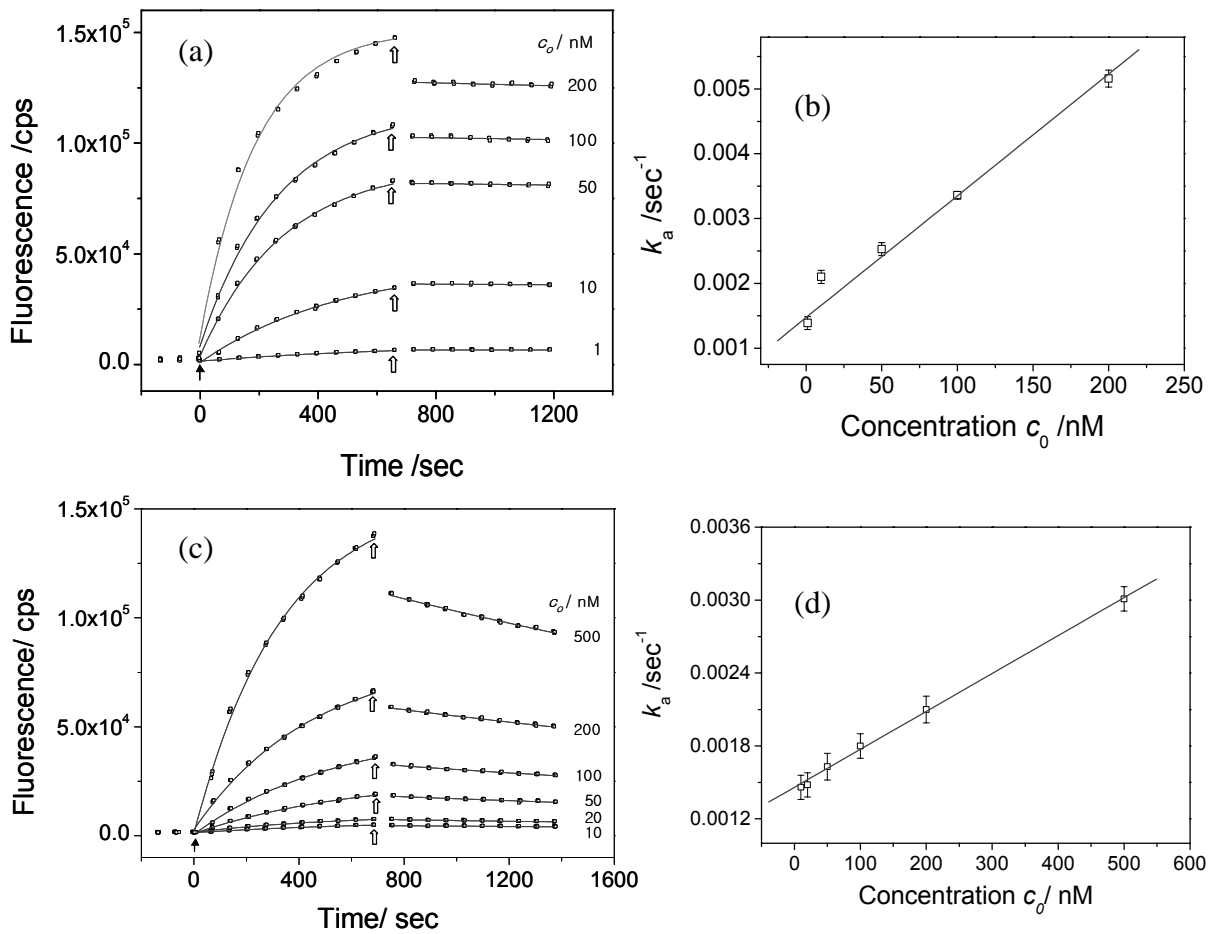
#### **5.3.1 Global analysis**

Figure 5.2 (a) shows experimental data of the global analysis at different concentrations of the complementary DNA (T-RR-15) with PNA (P-RR-15) at low ionic strength (10 mM phosphate) buffer solution using each time the same (regenerated) sensor surface. Starting for a short time with a base line measurement (the intensity of the baseline gives  $I_0$  in equation (1)), solutions of varying concentrations of DNA targets were injected and circulated for 10 min approximately in order to follow the association process as measured by the increase in

fluorescence intensity. Then the cell was rinsed with fresh buffer solution for 10 min in order to measure the dissociation process. Based on the Langmuir model the increase of the fluorescence intensity as a function of time is described by a simple bimolecular reaction:

$$I_{fl}(t) = (I_{\max} - I_0)(1 - \exp(-(k_{on} \cdot c_0 + k_{off})t)) \quad (1)$$

with  $I_{\max}$  being the maximum fluorescence intensity from surface-bound duplexes at  $c_0$ .  $I_0$  is the initial background fluorescence, and  $c_0$  the bulk solution concentration in the global analysis.



**Figure 5.2.** (a) Global analysis of the association and dissociation phase (taken at  $\theta=55.7^\circ$ ) of PNA (P-RR-15)/DNA (T-RR-15) hybridization in a solution containing 10 mM phosphate buffer solution. Open squares are data points collected every 1 min. The solid arrow at  $t=0$  indicates the injection of the target solutions of different concentrations for the recording of the association phase. The open arrows point to the beginning of the rinsing step for the dissociation phase. (b)  $k_a$  obtained from fitting the data (open squares) of (a) as a function of target concentration  $c_0$ . The solid straight line is a linear fit. (c) Global analysis of the association and dissociation phase (taken at  $\theta=55.7^\circ$ ) of PNA (P-RR-15)/DNA (T-RR-mis-15) hybridization in a solution containing 10 mM phosphate buffer solution. (d)  $k_a$  obtained from fitting the data (open squares) of (c) as a function of target concentration  $c_0$ . The solid lines are the best fit to the Langmuir model.

The association kinetics is quantified with respect to the concentration dependence. Fitting the association phase data recorded from 0 sec to 670 sec with equation (1) the rate constants  $k_a = k_{on} \cdot c_0 + k_{off}$  were obtained individually at different target concentrations. The  $k_a$  values increased as the concentration increased as shown in Figure 5.2 (b). The  $k_{on}$ -value was thus obtained by the slope of the  $k_a$  versus target concentration plot and calculated to be  $k_{on} = 1.7 \times 10^4 \text{ M}^{-1} \text{ s}^{-1}$ .

For a hybrid as stable as the fully matched double strand between the PNA probe and the 15mer DNA target (T-RR-15) only a very small decrease of the fluorescence intensity by the dissociating target can be found during the 10 min rinsing phase of the global analysis. This clearly limits the quantification of the full set of kinetic parameters by this approach for very stable hybrids. However, by introducing a single mismatch in the base sequence of the target (T-RR-mis-15) the duplex is largely destabilized and, hence, the dissociation sufficiently enhanced, thus, leading to a measurable loss of fluorescence intensity even within the 10 min of the rinsing phase of the global analysis. This is shown in Figure 5.2 (c). The rate constant  $k_a$  for the T-RR-mis-15 target is plotted in Figure 5.2 (d). From the slope,  $k_{on}$  is obtained to be  $k_{on} = 3.1 \times 10^3 \text{ M}^{-1} \text{ s}^{-1}$ , significantly lower than for the full match RR-15 case.

The time-dependent dissociation is described by equation (2):

$$I_{fl}(t) = (I_{\max} - I_0) \exp(-k_{off} \cdot t) \quad (2)$$

Note that after exchanging the buffer solution a drop in the fluorescence intensity can be observed at the starting point of the dissociation phase, which accounts for 5.2, 13.4, and 19.7 % of the fluorescence intensity at  $c_0 = 100, 200$ , and  $500 \text{ nM}$ , respectively. This contribution originates from free fluorophores (targets) in the solution near the surface that are rinsed out during the exchange with pure buffer solution.

From the decrease of the fluorescence intensity during the following rinsing process the dissociation rate was determined to be  $k_{off} = 2.5 \times 10^{-4} \text{ s}^{-1}$ , which is the average value of each  $k_{off}$ -value by fitting each dissociation part of the measurement (during rinsing) using equation (2) as shown in Figure 5.2(c). Thus the affinity constant,  $K_A$  ( $K_A = k_{on}/k_{off}$ ), is found to be  $K_A = 1.2 \times 10^7 \text{ M}^{-1}$  for the T-RR-mis-15 target.

### 5.3.2 Ionic strength dependence

A major benefit of using PNA as a probe is the fact that the PNA/DNA duplex formation is not (so strongly) influenced by the ionic strength of the bulk solution [43,44]. In addition to the study of PNA/DNA hybridization in low ionic strength discussed so far, we also investigated the dependence of hybridization for T-RR-15 at high ionic strength, i.e. in bulk solutions containing 137 mM NaCl in addition to the 10 mM phosphate. The data obtained by the global analysis with 1, 10, 50, 100, and 200 nM DNA target solutions are presented in Figure 5.3 (a). The  $k_{on}$  value is obtained from the slope (solid line,  $k_{on} = 1.7 \times 10^4 M^{-1} \text{sec}^{-1}$ ) of the  $k_a$  (opened squares) versus concentration plot as shown in Figure 5.3(b).

This value is virtually identical to the one obtained at low ionic strength (cf. Figure 5.2 (a)) in sharp contrast to DNA target hybridization to a DNA probe matrix.

The dissociation rate constant,  $k_{off} = 1.0 \times 10^{-5} \text{sec}^{-1}$ , was used to fit all 5 dissociation phases.

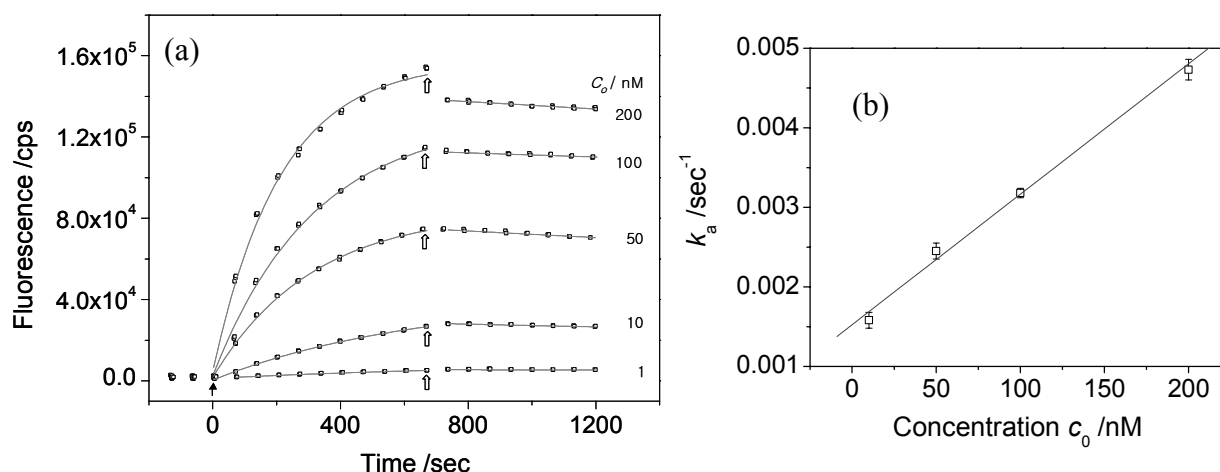


**Figure 5.3.** (a) Global analysis of PNA (P-RR-15)/DNA (T-RR-15) hybridization at 55.7° at high ionic strength, 137 mM NaCl added 10 mM phosphate buffer solution. Open squares are data points collected every 1 min. The solid lines are the best fitting to the Langmuir model. (b)  $k_a$  obtained from fitting data (open squares) of (a) versus concentration as a function of target concentration  $c_0$ . The solid line is a linear fit.

Finally the affinity constant was determined to be  $K_A = 4.0 \times 10^8 M^{-1}$ . These constants of the PNA/DNA hybridization at high ionic strength bulks are almost identical to the values obtained for hybridization at low ionic strength. Indeed, the ionic strength shows little influence on the PNA/DNA hybridization kinetics.

### 5.3.3 Titration measurement

An alternative measurement for the quantitative study of the hybridization process is a titration experiment. According to the Langmuir model the amount of analyte adsorbed at a given temperature to the binding sites is determined by the equilibrium between free and bound analyte molecules, i.e., by the surface coverage  $\Theta$ , corresponding to the fluorescence intensity,  $I_{fl}$ . This surface coverage depends on the affinity constant  $K_A$  and on the bulk concentration  $c_0$ . It is possible to monitor the Langmuir adsorption isotherm by performing experiments in which surface saturation is reached by a stepwise increase (or decrease) of the bulk concentration. The general procedure involves the injection of the analyte solution at low concentration and allowing for the adsorption process to reach equilibrium. This process is repeated with target solutions of higher concentrations until the surface is fully covered by analyte. The surface coverage is described by equation (3):

$$I_{fl}(c_0) \propto \Theta(c_0) = \frac{c_0 \cdot K_A}{1 + c_0 \cdot K_A} \quad (3)$$

In practice, the surface coverage  $\Theta(c_0)$  is determined by scaling the detected signal intensity  $I_{fl}(c_0)$  to that of a fully saturated surface. Figure 5.4 shows the titration experiment for PNA (P-RR-15)/DNA (T-RR-15) hybridization monitored at a fixed angle of incidence of  $\theta = 55.7^\circ$ . After the background fluorescence was recorded for a few minutes, a 1 nM solution of T-RR-15 was injected and the increase in fluorescence intensity was measured as a function of time until the equilibrium between the bulk concentration and the corresponding surface coverage was reached. Next, the injection of 5 nM, 10 nM, 20 nM, 50 nM, and 100 nM target solutions, respectively, resulted in correspondingly higher equilibrium surface coverages with the higher equivalent fluorescence intensities as shown in Figure 5.4 (a). In addition, a series of angular scans was taken after the surface coverage reached a new equilibrium for each new bulk concentration as shown in Figure 5.4 (b). Several features are noteworthy: (1) No significant shift of the surface plasmon minimum angle was observed (the various reflectivity curves are virtually superimposed) indicating the negligible increase in the optical thickness upon forming the PNA/DNA duplex. (2) The fluorescence from the bulk solution excited by light transmitted through the 50 nm Au substrate at  $45^\circ$ , below the critical angle ( $\theta_c = 47.3^\circ$ ) was measured at each concentration. As demonstrated in Figure 5.5 (a) this intensity is a linear function of the target concentration (from 1 nM to 100 nM), due to the direct excitation of the fluorophores in the bulk solution.

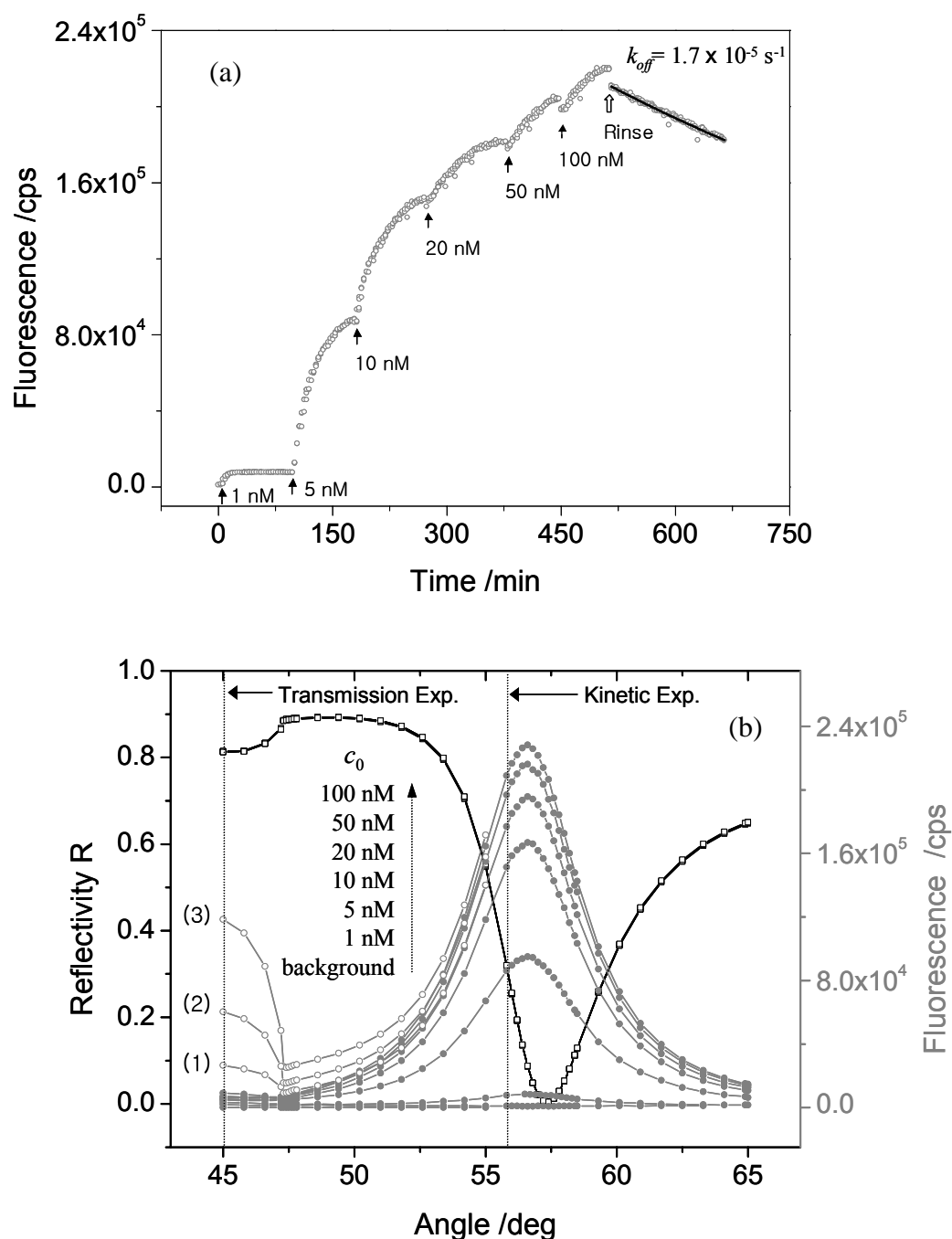


**Figure 5.4.** (a) Titration curves for PNA (P-RR-15)/DNA (T-RR-15) hybridization at  $\theta = 55.7^\circ$ . The concentration of the target DNA, T-RR-15 was stepwise increased from 1 to 5, 10, 20, 50, and 100 nM, respectively, in 10 mM phosphate buffer solution. Open circles are data points collected every 3 min. The solid arrows indicate the injection of the target solution. The fluorescence was recorded until the saturation intensity was reached. After the recording of the 100 nM sample the dissociation process was started by rinsing with pure buffer (open arrow). The solid line is the Langmuir fit to the dissociation data. (b) Angular scans taken after saturation was reached for the 1, 5, 10, 20, 50, and 100 nM target solutions, respectively, together with the background fluorescence intensity. Open squares are reflectivities. Note that there is no significant plasmon minimum angle shift by forming a PNA/DNA duplex. Angular fluorescence curves were taken before (open symbols) and after rinsing (full symbols) the flow cell with pure buffer following the equilibrium binding of targets from solutions. (1) 20 nM, (2) 50 nM, (1) 100 nM.



The Langmuir isotherm curve was constructed from the data taken at the angle of maximum intensity of the angular scans (after rinsing for a short time) as a function of target concentration. In Figure 5.5 (b) and (c) the open squares are the data from angular scans (Figure 5.4 (b)) and the solid line is a simulated Langmuir fit using equation (3). Figure 5.5 (c) corresponds to a linearized Langmuir isotherm (equation (4)) according to a modification of equation (3) with a slope giving the affinity constant as  $K_A = 1.7 \times 10^8 M^{-1}$ .

$$\frac{c_0}{I_{fl}} \propto \frac{1}{K_A} + c_0 \quad (4)$$

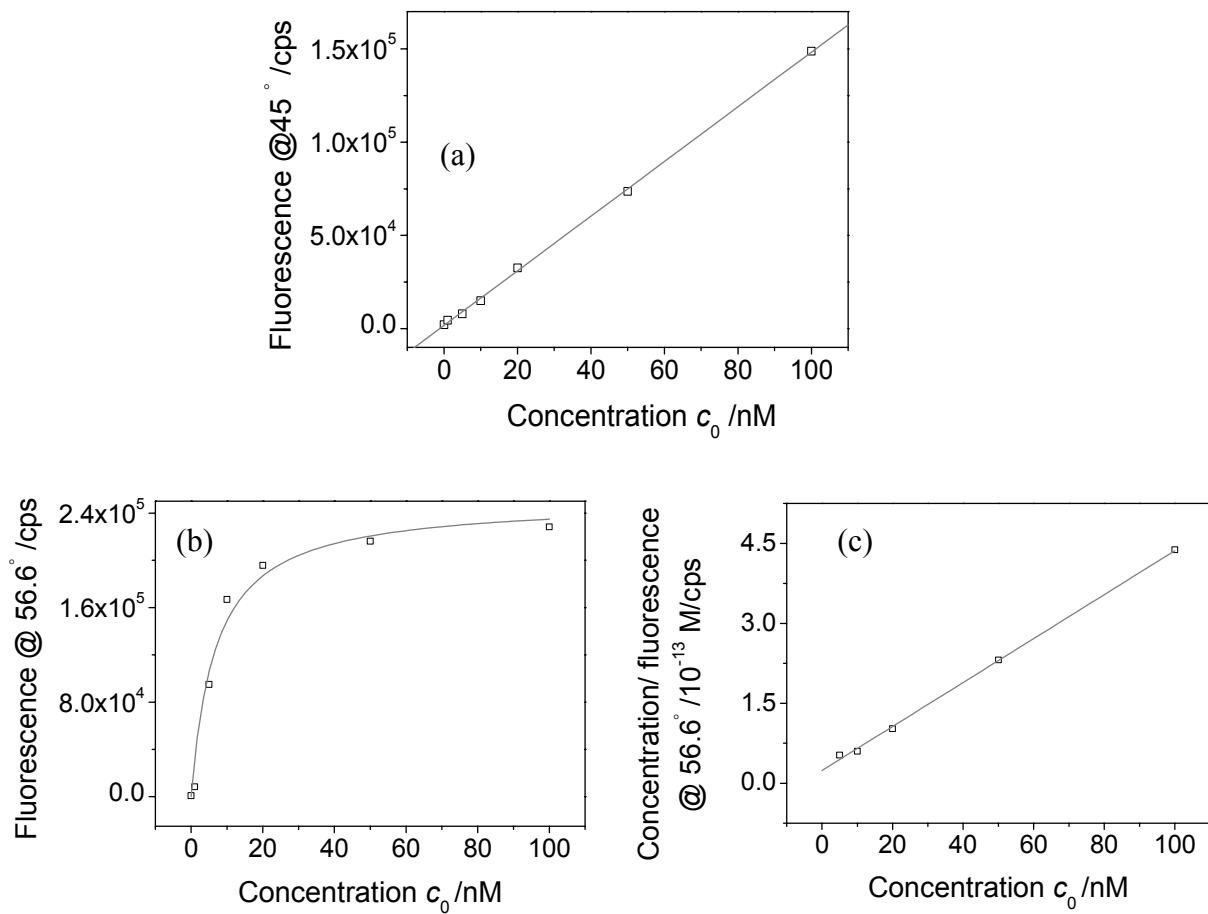


**Figure 5.5.** (a) Fluorescence intensity measured at  $\theta = 45^\circ$ , i.e., below the critical angle, giving information of the bulk concentration  $c_0$ . (b) Plots (open squares) of the maximum fluorescence intensity ( $\theta = 56.6^\circ$ ) taken from Figure 5.4 (b) versus target concentration  $c_0$ . The gray curve corresponds to the fit by the Langmuir isotherm. (c) Linearized Langmuir isotherm of the data of (b). From the slope, the affinity constant  $K_A$  can be determined,  $K_A = 1.7 \times 10^8 M^{-1}$ .

At the end of the stepwise increase of the bulk concentration a rinsing step for about 150 min resulted in a measurable loss of fluorescence intensity even for this fully match hybrid

(see also the kinetic measurement presented in Figure 5.6 with a rinsing phase of more than 700 min). This confirms that 10 min rinsing for hybridization with RR-15 in the global analysis was not enough to detect  $k_{off}$  reliably.

However, by analysing the dissociation phase of Figure 5.4 (a) (and of Figure 5.6) a dissociation rate constant of  $k_{off} = 1.7 \times 10^{-5} \text{ s}^{-1}$  can be calculated. Together with the  $k_{on}$  value derived from the association phase of the global analysis this leads to an affinity constant of  $K_A = 1 \times 10^9 \text{ M}^{-1}$ .

It is interesting to compare this affinity constant with that determined from the titration analysis. The  $K_A$  value obtained from the global analysis is ca. 6 times higher than that of the titration analysis. We attribute this effect to the increasing surface charge density upon hybridization of DNA targets: starting with an (empty) un-charged PNA probe matrix at the sensor surface, each bound target oligonucleotide adds 15 charges to the interface. As the coverage increases, this surface charge density generates a successively repulsive Coulomb barrier for further target binding to the still free binding sites which are, however, cross-talking with the neighboring (charged) hybrids. In earlier studies, we demonstrated that this effect could be reduced when working at high ionic strength or by diluting the probe density of the sensor matrix thus increasing the average distance between individual hybridization sites.<sup>27</sup> The target binding-induced generation of a repulsive Coulomb barrier also reduces the apparent affinity  $K_A$  measured in a titration experiment (cf. Figure 5.4 (a) and the accompanying discussion). The same phenomenon will be even more pronounced for the binding of PCR amplicons (cf. Figure 5.7 and Table 5.1), for which 125 charges are added to the interface for every bound analyte molecule.

In the global analysis, on the other hand, the catcher probe matrix is regenerated for each separate run starting each time with an empty uncharged matrix. Only the first minutes are observed during hybridization reaching a surface coverage that doesn't exceed typically 30 % of the full monolayer capacity, hence is less influenced by the build-up of a Coulombic barrier. Thus, the global analysis measures a more reliable affinity constant with less cross-talk between the bound targets at the interface.

#### 5.3.4 *Single Kinetic analysis*

The SPFS technique is sensitive and reproducible enough to not only obtain kinetic and affinity data discussed above but also to detect the effect of one base mismatch of a nucleic

acid target on the PNA/ DNA hybridization process. For this purpose, and to demonstrate the potential (and difficulties) of a single kinetic experiment the binding kinetics between PNA (P-RR-15) and DNA (T-RR-15) were measured at a target concentration of  $c_0 = 50$  nM. The analysis of this experiment is also based on the simple Langmuir model. By introducing the T-RR-15 target DNA solution into the cell and recirculating it until saturation of the fluorescence signal from the PNA sensor surface was reached, the association kinetic was measured. Then the dissociation process was triggered by switching to a 10 mM phosphate buffer solution (Figure 5.6). By using a single exponential Langmuir fit, the obtained rate constants are  $k_{on} = 1.7 \times 10^4 \text{ M}^{-1} \text{ s}^{-1}$ ,  $k_{off} = 1.7 \times 10^{-5} \text{ s}^{-1}$ , and the resulting affinity constant is  $K_A = 1.0 \times 10^9 \text{ M}^{-1}$ . As one can see from Figure 5.6 (1) the high  $k_{on}$  value is obtained by fitting only the early stage (dash curve, first 10 min) of the association process. The  $k_{on}$  and the  $K_A$  values thus obtained are in good agreement with the  $K_A$  value derived from the association phase in the global analysis (Figure 5.2 (b)).

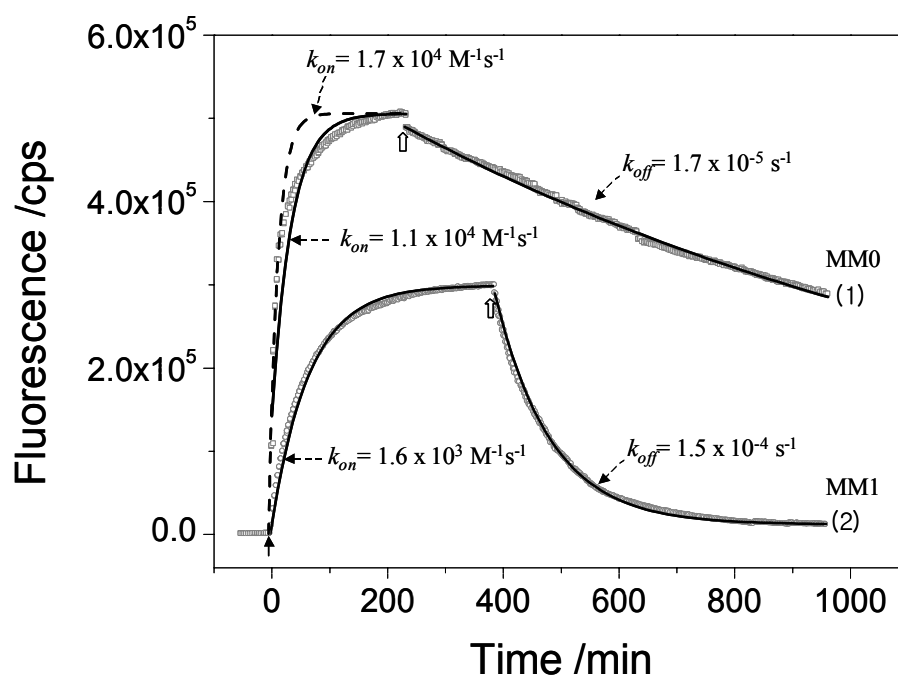


**Figure 5.6.** Hybridization kinetics for (1) PNA (P-RR-15)/DNA (T-RR-15) (MM0, 50 nM, open squares). (2) Kinetic run for the discrimination of a single mismatch hybridization: PNA (P-RR-15)/DNA (T-RR-mis-15). Open symbols are data points collected every 3 min. The solid arrow at  $t = 0$  indicates the injection of the target solutions (50 nM) for the recording of the association phase. Solid curves are Langmuir fits. Dash curve is the fitting only the first 10 min.

One can see from the association phase in Figure 5.6 (1) that for high coverages the build-up of the Coulomb barriers leads to a slowing down of the hybridization reaction thus resulting in an increasing deviation from the single-exponential behavior expected for a Langmuir adsorption.

However, the best fitting (solid curve, Figure 5.6 (1)) of the association phase fully gives the rate constant to be  $k_{on} = 1.1 \times 10^4 \text{ M}^{-1} \text{ s}^{-1}$ . Compared with the global analysis, the determined  $k_{on}$  value is slightly lower. We attribute this effect to the increasing surface charge density upon hybridization of DNA targets: starting with an (empty) un-charged PNA probe matrix at the sensor surface, every target oligonucleotide adds 15 charges to the interface. As the coverage increases, this surface charge density generates a successively repulsive Coulomb barrier for further target binding to the still unoccupied binding sites which are, however, cross-talking with the neighboring (charged) hybrids. In earlier studies, we demonstrated that this effect could be reduced when working only at high ionic strength or by diluting the probe density of the sensor matrix thus increasing the average distance between individual hybridization sites.

For the detection of a point mutation, DNA (T-RR-mis-15, 50 nM) was hybridized to the PNA using the same conditions. As plotted in Figure 5.6 (2), the rate constant of the association phase is considerably lower than that of the fully complementary hybrid with  $k_{on} = 1.6 \times 10^3 \text{ M}^{-1} \text{ s}^{-1}$ . In addition, the dissociation rate ( $k_{off} = 1.5 \times 10^{-4} \text{ s}^{-1}$ ) is faster compared to the fully matched duplex. As a consequence, the affinity constant is determined to be  $K_A = 1.1 \times 10^7 \text{ M}^{-1}$  i.e. about 2 orders of magnitude lower. This indicates that good discrimination is possible for a point mutation using this sensor matrix. Since in this experiment the equilibrium coverage is still significantly below a full monolayer the Coulomb barrier is not so strong yet and, hence, the kinetics of association and dissociation are well described by a single exponential fit. The obtained kinetic rate constants for the association  $k_{on} = 1.6 \times 10^3 \text{ M}^{-1} \text{ s}^{-1}$  and dissociation  $k_{off} = 1.5 \times 10^{-4} \text{ s}^{-1}$  are also reasonable close to the values obtained from the global analysis ( $k_{on} = 3.1 \times 10^3 \text{ M}^{-1} \text{ s}^{-1}$  and  $k_{off} = 2.5 \times 10^{-4} \text{ s}^{-1}$ , respectively) with the latter being however, a much faster approach.

### 5.3.5 Effect of PNA probes

Probe selection is important since it is critical for determining hybridization efficiency and mismatch discrimination [45]. In chapter 4, the length effects were investigated on

hybridization between 11, 13, and 15mer probe PNA and 11, 13, and 15mer target DNA at different ionic strength. The short oligonucleotides hybridize faster than long one, but the long oligonucleotides duplex is more stable so the dissociation observed slower than for short ones.

Here the same target DNA (T-RR-15, MM0) was introduced to 3 different PNA probes (11, 13, and 15mer of different length) in 10 mM PB as shown in Figure 5.7. The immobilization processes of the 3 different PNAs were monitored by SPR individually. The length effect found was the increase of the thickness of the PNA probe layers with 0.6 nm (11mer), 0.9 nm (13mer), and 1.3 nm (15mer). This robust sensor architecture ensures a moderate catcher probe density in the range of one probe per 40 nm ( $2.5 \times 10^{12}$  probes/ cm<sup>2</sup>) reducing any potential cross-talk between the catcher probes and the target DNAs during hybridization.

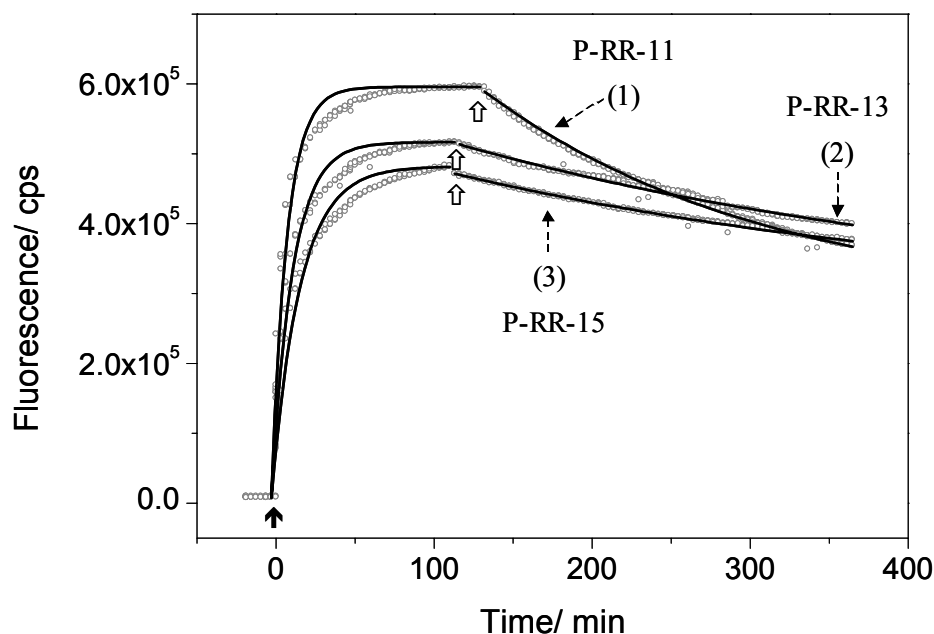


**Figure 5.7.** Hybridization kinetics for (1) P-RR-11/T-RR-15, (2) P-RR-13/T-RR-15, and (3) P-RR-15/T-RR-15. Open symbols are data points collected every 3 min. The solid arrow at  $t = 0$  indicates the injection of the target solutions (50 nM) for the recording of the association phase. The solid curves are fits to the data by the Langmuir model with association and dissociation phase.

**Table 5.2.** Rate constants obtained by the single kinetic analysis (Figure 5.7) for 3 different lengths of PNA probes and one DNA target hybridizations.

	P-RR-11/T-RR-15	P-RR-13/T-RR-15	P-RR-15/ T-RR-15
$k_{on} / \text{M}^{-1} \text{s}^{-1}$	$3.4 \times 10^4$	$1.5 \times 10^4$	$1.1 \times 10^4$
$k_{off} / \text{s}^{-1}$	$9.2 \times 10^{-5}$	$3.5 \times 10^{-5}$	$1.7 \times 10^{-5}$
$K_A / \text{M}^{-1}$	$3.7 \times 10^8$	$4.3 \times 10^8$	$6.5 \times 10^8$

The association rate of the 11mer PNA/ 15mer DNA hybridization was found to be faster than those of the 13mer and the 15mer for the MM0 situation as shown in Figure 5.7. All rate constants are summarized in Table 5.2.

The recognition sequence is increasing by increasing the length of PNA probe. A short length of oligonucleotides is easier to hybridize than long one due to less base pair. Once DNA binds to PNA, forming a duplex, the duplex for 15mer having 4 more base pairs is more stable than 11 mer because the long one has more hydrogen bonds. Thereby the dissociation rate of long PNA/DNA is much slower than that of the short one. Thus the affinity constant of 15 mer PNA/DNA is higher than those of the 13mer and the 11mer. Probe selection is important since it is critical for determining hybridization efficiency and performance [45].

### 5.3.6 Sequence dependence

In order to evaluate the sequence dependence, two different 15mer PNA probes and two different 15mer DNA targets were selected. Using P-RR-15 as a probe, single kinetic experiments were performed with T-RR-15 (MM0) and T-RR-mis-15 (MM1, T-G mismatch) (cf. chapter 5.3.4). The probe P-RR-mis-15 has one different base in the middle of sequence to P-RR-15 thus being complementary (MM0) to the target T-RR-mis-15, and has one base mismatch (MM1) with the target T-RR-15 (C-A mismatch).

All hybridizations were recorded by the single kinetic runs as shown in Figure 5.8. with the corresponding rate constants being summarized in Table 5.3.

The stability of the duplex is governed by its identity (G-C, A-T, hydrogen bonds), the condition (MM0, MM1), and neighbored base pairs (stacking energy). Additional factors that have to be considered are the salt concentration, helix nucleation energy, and the formation of secondary structures in the duplex [46-51].

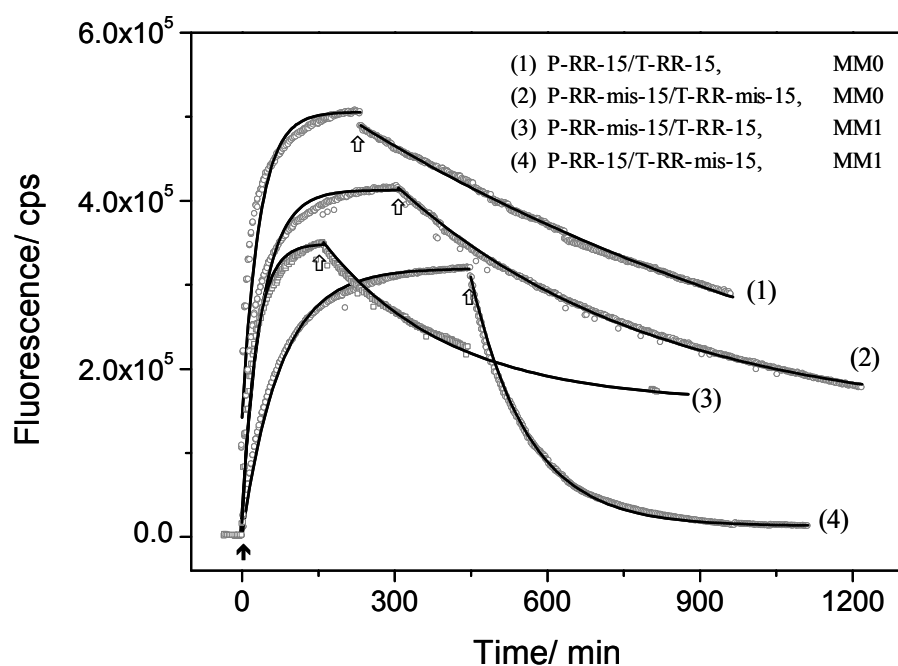


**Figure 5.8.** Hybridization kinetics for (1) P-RR-15/T-RR-15 (MM0), (2) P-RR-mis-15/T-RR-mis-15 (MM0), (3) P-RR-mis-15/T-RR-15 (MM1) and (4) P-RR-15/T-RR-mis-15 (MM1). Open symbols are data points collected every 3 min. The solid arrow at  $t = 0$  indicates the injection of the target solutions (50 nM) for the recording of the association phase. The solid curves are fits to the data by the Langmuir model with association and dissociation phase.

**Table 5.3.** Rate constants obtained by the single kinetic analysis (Figure 5.8) for PNA probes and one DNA targets hybridizations.

	P-RR-15/ T-RR-15 (MM0)	P-RR-mis-15/ T-RR-mis-15 (MM0)	P-RR-mis-15/ T-RR-15 (MM1)	P-RR-15/ T-RR-mis-15 (MM1)
$k_{on} / M^{-1} s^{-1}$	$1.1 \times 10^4$	$1.0 \times 10^4$	$9.0 \times 10^3$	$1.6 \times 10^3$
$k_{off} / s^{-1}$	$1.7 \times 10^{-5}$	$1.9 \times 10^{-5}$	$2.0 \times 10^{-5}$	$1.5 \times 10^{-4}$
$K_A / M^{-1}$	$6.5 \times 10^8$	$5.3 \times 10^8$	$4.5 \times 10^8$	$1.1 \times 10^7$

In the MM0 situation, the rate constants were not influenced by one more C-G base pair (Table 5.3). However, the C-A mismatching base pair (Table 5.3) produced a duplex much more stable than the T-G pair (Figure 5.8 (4)). The affinity constant of the P-RR-mis-15/T-RR-15 is  $K_A = 1.4 \times 10^8 M^{-1}$  and it is hard to discriminate between MM0 and MM1.

Obviously, this indicates that the T-G mismatch showed much less stability than the C-A mismatch leading to good discrimination. This sequence dependence on the sensor surface will give useful information for the development of sensors not only for mutation detection but also for a wider range of molecular recognition studies.

#### 5.4 Ionic Strength Influence for DNA/DNA Hybridization

DNA is a highly poly-electrolytic species. The negative charges of its phosphate groups have to be neutralized by counteractions, which may be small counterions, organic amines, positively charged proteins (notably lysine and arginine residues [52] or, in therapeutic situations, positively charged drugs [53]. Metal ions bind to poly-nucleotides in several ways [54-57]. Therefore, the moderate salt condition for DNA/DNA hybridization is essential to stabilize the duplex.

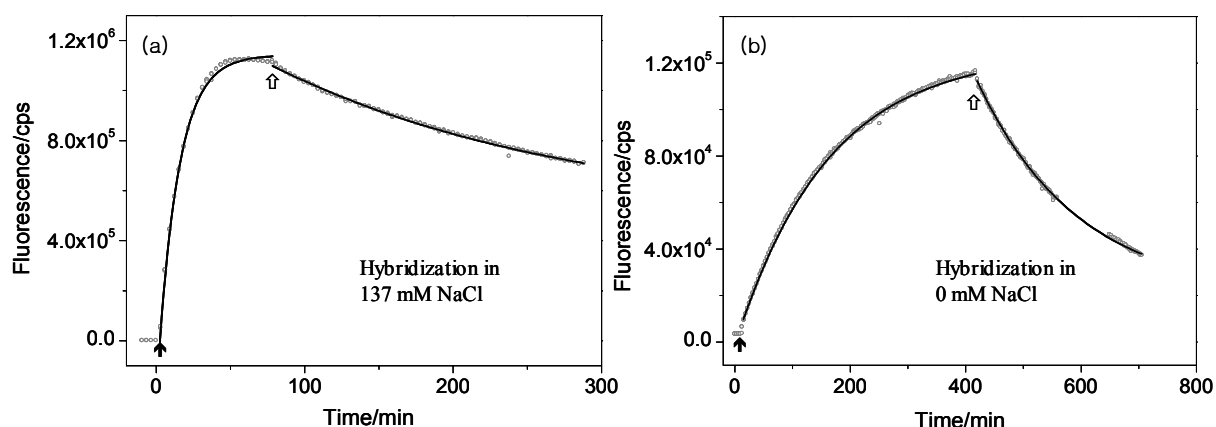


**Figure 5.9.** Hybridization kinetics for (a) DNA (D-RR-15)/DNA (T-RR-15) hybridization in 10 mM PB with 137 mM NaCl and (b) DNA (D-RR-15)/DNA (T-RR-15) hybridization in 10 mM PB without NaCl. Open squares are data points collected every 3 min. The solid arrow at  $t=0$  indicates the injection of the target solutions (50 nM) for the recording of the association phase. The open arrows point to the beginning of the rinsing step for the dissociation phase. The solid curves are fits to the data by the Langmuir model.

As mentioned in the previous chapter, the stability of the PNA/DNA hybrid is higher than that of DNA/DNA hybrids. Nevertheless, it is interesting to investigate the ionic strength effect for DNA/DNA hybridization on the sensor surface. The DNA/DNA duplex is highly sensitive to environmental effects of the counterions to achieve electroneutrality for anionic DNA.



The effects of salt on the DNA/DNA duplex have been investigated in 10 mM PB buffer solution with and without the addition of 137 mM NaCl and compared to the effects on a PNA/PNA duplex having the completely analogous base sequence. For DNA/DNA hybridization, the biotinylated DNA probe (D-RR-15) was immobilized on the streptavidin *via* self-assembled sensor architecture (Figure 5.1).

The immobilization of the DNA probe was monitored by SPR and found to result in a layer of 1.7 nm in thickness. On the DNA probe complementary matching DNA target (T-RR-15) was introduced for association, then the rinsing step was followed for dissociation. In the presence of 137 mM NaCl (Figure 5.9 (a)), the binding process was observed to be faster than the hybridization in the absence of NaCl. By fitting the association parts by the Langmuir model, the association rate constants were determined to be  $k_{on} = 1.4 \times 10^3 \text{ M}^{-1} \text{ s}^{-1}$  for the hybridization in 137 mM NaCl and  $k_{on} = 1.5 \times 10^2 \text{ M}^{-1} \text{ s}^{-1}$  for the NaCl free case. As expected, the association rate for DNA/DNA hybridization at high ionic strength is an order of magnitude higher than that for hybridization at low ionic strength. Due to the repulsive force between the DNA probe and the DNA target, counterions are necessary to screen the charge density. After hybridization of the DNA target to PNA probe, pure buffer solution was injected for dissociation. In the dissociation phase, the DNA/DNA duplex is less stable at low ionic strength, leading to a faster dissociation rate ( $k_{off} = 8.2 \times 10^{-5} \text{ s}^{-1}$ ) than at high ionic strength ( $k_{off} = 9.7 \times 10^{-4} \text{ s}^{-1}$ ). As a result, the affinity constant difference was two orders of magnitude. Actually the cations play an important role for DNA/DNA hybridization.

In order to investigate the ionic strength effect for the PCR target (T-RR-125) having more charges, the hybridization was performed on the 15mer DNA probe bound sensor surface at 2 different ionic strengths. As shown in Figure 5.10 (1) hybridization could not be observed in 0 mM NaCl due to the charge screening effect between probe DNA and target DNA. This effect was enhanced by increasing the charges at the surface. However, hybridization in the presence of 137 mM NaCl (Figure 5.10. (2)) was detected, but the signal was too weak to be analysed the.

As a consequence, DNA probes are not suitable to detect long DNA targets, especially at low ionic strength. In chapter 4, the limit of ionic strength was further studied for detection of DNA targets using a PNA immobilized sensor surface. Through the use of a neutral PNA probe, the ionic strength influence could be circumvented resulting in stable PNA/DNA hybridization.

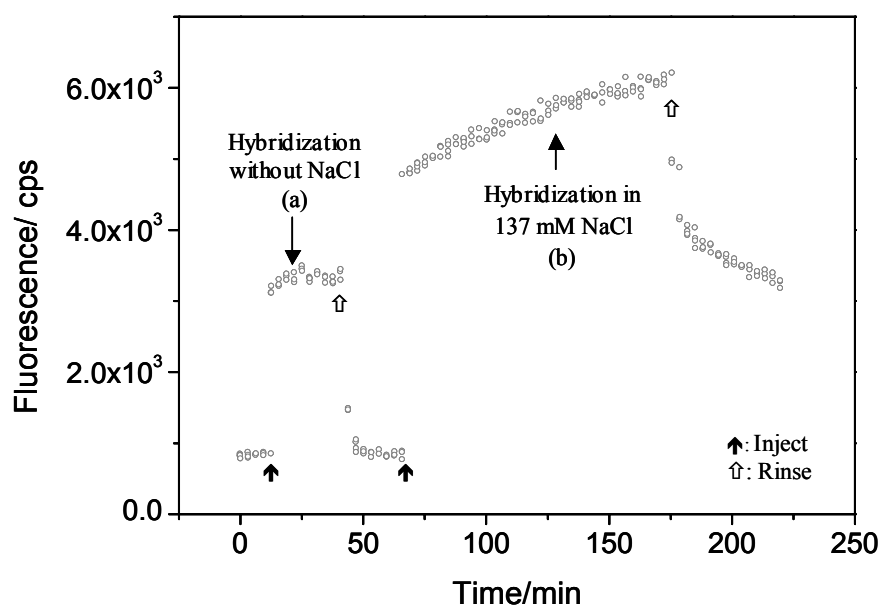


**Figure 5.10.** Hybridization kinetics for (a) DNA (D-RR-15)/DNA (T-RR-125) hybridization in 10 mM PB with 137 mM NaCl and (b) DNA (D-RR-15)/DNA (T-RR-125) hybridization in 10 mM PB without NaCl. Open squares are data points collected every 3 min. The solid arrow at  $t=0$  indicates the injection of the target solutions (50 nM) for the recording of the association phase. The solid curves are fits to the data by the Langmuir model.

## 5.5 Detection of PCR Amplicons from Roundup Ready<sup>TM</sup> Soybean

Identification of genetically modified organisms (GMO) in foods is becoming an issue of great interest, because of the increasing number of GMO-derived products launched into the food market [58,59] and the increased customer demand for strict regulations and labeling of such foods [60,61]. Accordingly, a variety of methods for the detection of GMO were developed that can be used for screening purposes. For instance, the fast and simple polymerase-chain reaction (PCR) procedure was recently applied for the detection of FLAVR SAVR tomato [62], Roundup Ready<sup>TM</sup> soybean [63], Bt-maize [64], and gbss-antisense transgene potatoes [65]. The recent development of surface plasmon field-enhanced fluorescence spectroscopy (SPFS) based biosensors [22-27, 31-33, 36,37] enables one to perform biospecific interaction analysis for monitoring a variety of molecular reactions in real time.

In chapter 5.3, the model hybridization kinetics between PNA probes and oligomer DNA targets were studied on the sensor surface by different kinetic measurements using SPFS.

The global analysis turned out to be the fastest and most reliable method to determine association rate constants because it analyses only early stages of the binding. For rather stable complexes like a hybrid of two 15mer oligonucleotides with zero mismatch a 10 min rinsing phase is not sufficient to see a significant dissociation that can be analyzed quantitatively. However, it is very well suited to obtain the dissociation rate in the case of a single base mismatched double strand during the rinsing step resulting in a visible loss of fluorescence intensity that allows for a quantitative determination of  $k_{off}$  in addition to  $k_{on}$ , and hence can also give the affinity constant  $K_A$ .

The typical titration experiment allows for the determination of the Langmuir adsorption isotherm and, hence, the affinity constant  $K_A$  based on the evaluation of surface coverages. However, by increasing the concentration and, hence, the occupancy of the probe binding sites, the interface is more and more charged resulting (at the low ionic strength used in these experiments) in an increasingly significant Coulombic barrier for the hybridization at the sensor surface. As a consequence the (averaged) affinity constant can be significantly lower than that found by the global analysis or by kinetic-titration experiments at low bulk concentrations (relative to  $K_D = K_A^{-1}$ ), i.e., low surface coverages.

Here, the kinetic and equilibrium coverage measurements that are done in the kinetic-titration experiment clearly revealed the influence of the interfacial charging effect using PCR targets amplified from Roundup Ready<sup>TM</sup> soybean and having more charges. For each concentration  $c_0$  of the bulk solution the association and dissociation of the target to and from the sensor surface can be quantified and then also an apparent (concentration dependent) affinity constant can be determined. The evaluation for the discrimination of MM0 and MM1 hybridization and the probe length effect were investigated by single kinetic experiment. Furthermore, the limit of detection for PCR target was carried by down the target concentration on the sensor surface.

### 5.5.1 Kinetic-titration analysis for P-RR-15/T-RR-125

The detection of long DNA fragments obtained by PCR amplification from genetically modified soybean is also possible using SPFS both in the kinetic or the titration mode. PCR is based on a sequence-specific hybridization of two primers to the template DNA. One primer was modified with Cy5 for fluorescence detection of the target strand. Purified PCRs originally are double-stranded DNAs. In order to hybridize with PNA, a melt-quench protocol was developed [67]: The PCR products are heated to  $T = 95\text{ }^{\circ}\text{C}$  and then quickly quenched into a low ionic strength buffer containing only 10 mM phosphate at  $0\text{ }^{\circ}\text{C}$  (chapter 3.4.7). This results in a Coulombic repulsion in solution between the individual single strands sufficiently strong to prevent (rapid) re-hybridization of the complementary strands.

With the target strands being fluorescently-labeled, one can perform a hybridization experiment at a fixed angle of observation in the SPFS set-up (at  $\theta = 55.7^{\circ}$ ). The kinetic-titration experiment with supplementary rinsing steps provides both kinetic information at each concentration and the affinity constant from a Langmuir adsorption isotherm curve. The basic concept is a combination of the kinetic analysis that gives a series of rate constants at different concentrations and a titration experiment providing information of surface coverage and, hence, the affinity constant  $K_A$ . Figure 5.11 shows the kinetic-titration experiment in detail.

Once the background fluorescence was recorded for a few minutes, a 1 nM solution of T-RR-125 was injected and the increase in fluorescence intensity measured as a function of time until the equilibrium between the bulk concentration and the corresponding surface coverage was reached (Figure 5.11 (a)). Next, the injection of 5 nM and 10 nM target solutions resulted in correspondingly higher equilibrium surface coverages with the equivalent higher fluorescence intensities. After the equilibrium of the 10 nM target solution was reached the flow cell was filled with pure buffer. A small immediate decrease of the fluorescence intensity (by the exchange of the target solution by pure bulk solution, cf. above) was followed by a gradual decrease in intensity corresponding to the dissociation of target strands from the surface bound probe PNAs. Each of the kinetic experiments was analyzed on the basis of the Langmuir model as also shown in Figure 5.11 (a): the corresponding association and dissociation phases are fitted by equations (1) and (2), respectively (solid lines).

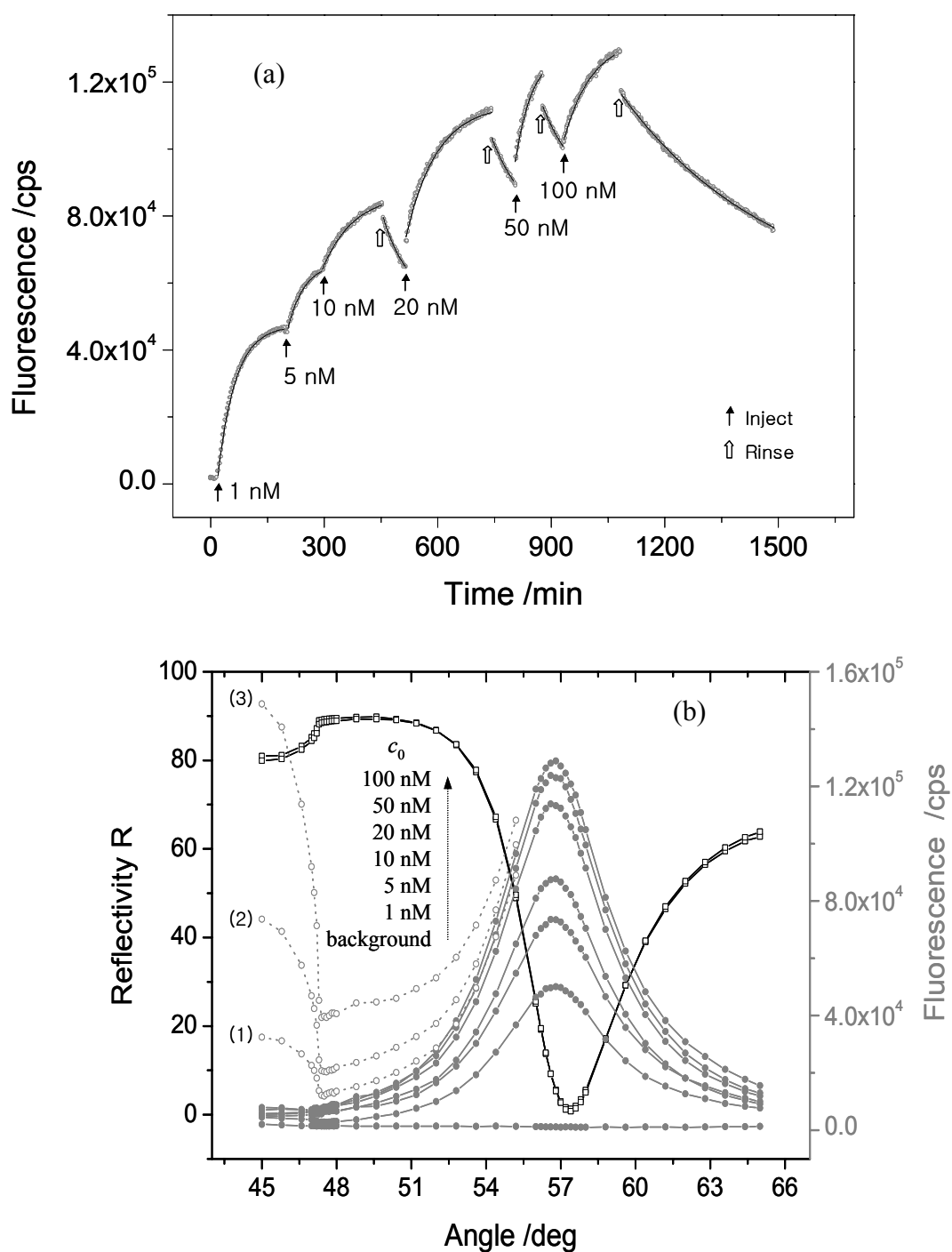


**Figure 5.11.** (a) Kinetic-titration curves for P-RR-15/T-RR-125 hybridization at  $\theta = 55.7^\circ$ . The concentration of target T-RR-125 was increased from 1 to 5, 10, 20, 50, and 100 nM, respectively, in 10 mM phosphate buffer. Open circles are data points collected every 3 min. The full curves are Langmuir fit to the experimental data. (b) Angular scans taken after saturation of the fluorescence was reached for 1, 5, 10, 20, 50, and 100 nM target solutions, respectively, together with background fluorescence intensity recorded after rinsing (full symbols) and for (1) 20 nM, (2) 50 nM, (1) 100 nM samples also before rinsing (open symbols).

**Table 5.4.** Rate constants obtained by the kinetic-titration analysis for P-RR-15/T-RR-125 hybridization at different target concentrations.

<sup>a</sup>  $K_A$  determined from  $k_{on}$  ( $c_0$ ) and a  $k_{off}$  value, that was averaged over the measurements taken at 10, 20, 50, and 100 nM target solutions, respectively, i.e.,  $k_{off} = 2.35 \times 10^{-5} \text{ s}^{-1}$

$c_0$ nM	$k_{on}$ $M^{-1} \text{ s}^{-1}$	$k_{off}$ $\text{s}^{-1}$	$K_A$ $M^{-1}$
1	$3.5 \times 10^4$		$(14.9 \times 10^8)^a$
5	$2.3 \times 10^4$		$(9.8 \times 10^8)^a$
10	$8.2 \times 10^3$	$2.5 \times 10^{-5}$	$3.3 \times 10^8$
20	$5.2 \times 10^3$	$1.7 \times 10^{-5}$	$3.1 \times 10^8$
50	$5.0 \times 10^3$	$1.7 \times 10^{-5}$	$2.9 \times 10^8$
100	$4.0 \times 10^3$	$3.5 \times 10^{-5}$	$1.1 \times 10^8$

The calculated rate constants are listed in Table 5.4. With increasing target concentration, the association rate constant,  $k_{on}$ , decreased gradually. On the other hand the dissociation constant,  $k_{off} \approx 2.35 \times 10^{-5} \text{ s}^{-1}$  turns out to be almost identical for all concentrations (surface coverages). As a result, the affinity constant gradually decreased with increasing target concentration. As can be seen from Table 5.4 the increasing coverage of the PNA catcher matrix by T-RR-125 amplicons leads to a rather dramatic effect on the association rate, slowing the hybridization process down by about an order of magnitude (from  $3.5 \times 10^4 \text{ M}^{-1} \text{ s}^{-1}$  to  $4.0 \times 10^3 \text{ M}^{-1} \text{ s}^{-1}$ ). The resulting (coverage dependent) affinity “constant” thus determined decreased from ca.  $1.5 \times 10^9 \text{ M}^{-1}$  to  $1.1 \times 10^8 \text{ M}^{-1}$ .

The affinity constant determined from the equilibrium coverages at different concentration, i.e., from the titration experiment (Figure 5.11) evaluated in Figure 5.12 (a) and (b) again can be seen as an average over different coverages.

It is interesting to compare the rate constants and affinity constants for the T-RR-15 oligonucleotide and the T-RR-125 amplicons which contain the identical recognition sequence fully complementary to the PNA catcher at the sensor surface somewhere in the middle of the single strand (cf. Table 5.1). This is somewhat surprising given the fact that upon the binding of a single T-RR-125 amplicon 125 charges are added to the interface, significantly higher than the 15 charges of an oligonucleotide T-RR-15. However, the stretching of the target at the low ionic strength used in these experiments (10 mM PB) lead to a thicker oligoelectrolyte layer but not necessarily to a higher (spatial) charge density.

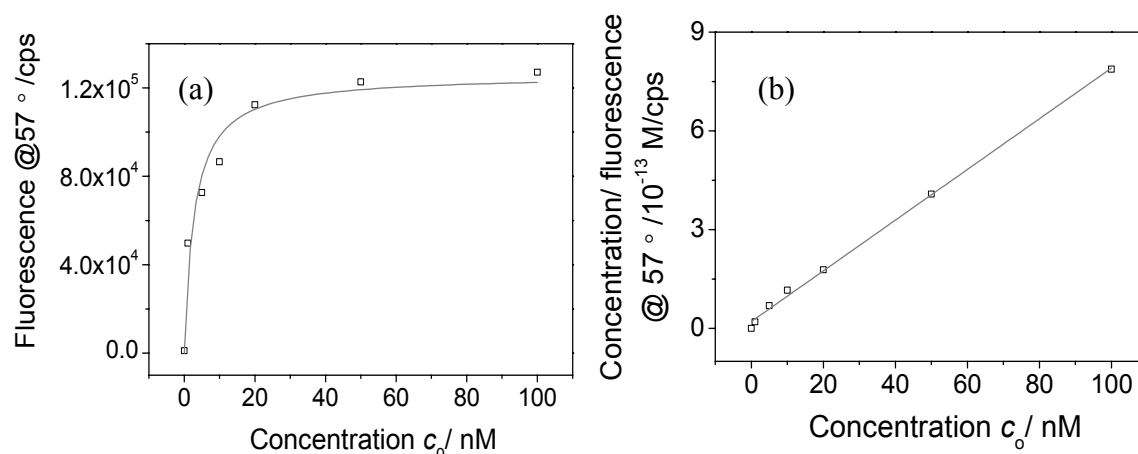


**Figure 5.12.** (a) shows the data taken by analyzing the intensities at equilibrium surface coverages from Figure 5.11 (b). Figure 5.11 (b) gives the linearized form according to equation (4). The fit gives the affinity constant,  $K_A = 3.7 \times 10^8 M^{-1}$ , average over all concentrations.

### 5.5.2 Kinetic-titration analysis for P-RR-15/T-RR 169

To detect longer DNA amplicons (45 bases more) target PCR, T-RR-169 (Table 5.1) was obtained by PCR amplification from genetically modified soybean. After amplification the double stranded PCR product was separated by a melting-quench protocol. The PCR products are heated to  $T = 95^\circ\text{C}$  and then quickly quenched into a low ionic strength buffer containing only 10 mM phosphate at  $0^\circ\text{C}$ . The recognition sequence of T-RR-169 is 15 bases complimentary to the PNA probe, P-RR-15. Figure 5.13 shows the kinetic-titration experiment in detail.

Once the background fluorescence was recorded for a few minutes, a 1 nM solution of T-RR-169 was injected and the increase in fluorescence intensity measured as a function of time until the equilibrium between the bulk concentration and the corresponding surface coverage was reached (Figure 5.13 (a)). It took much more time to reach equilibrium state with 1 nM of target to PNA sensor surface. By fitting the association phase for 500 min, the association rate was determined to be  $k_{on} = 1.8 \times 10^3 M^{-1}s^{-1}$ . This value is lower than that of T-RR-125 ( $k_{on} = 3.5 \times 10^4 M^{-1}s^{-1}$ ) about 20 times. Next, the injection of 5 nM and 10 nM target solutions resulted in correspondingly higher equilibrium surface coverages with the equivalent higher fluorescence intensities. At equilibrium state for each association the flow cell was filled with pure buffer subsequently. Each of the kinetic experiments was analyzed on the basis of the Langmuir model as also shown in Figure 5.13 (a): the corresponding

association and dissociation phases are fitted by equations (1) and (2), respectively (solid lines). The calculated rate constants are listed in Table 5.5.

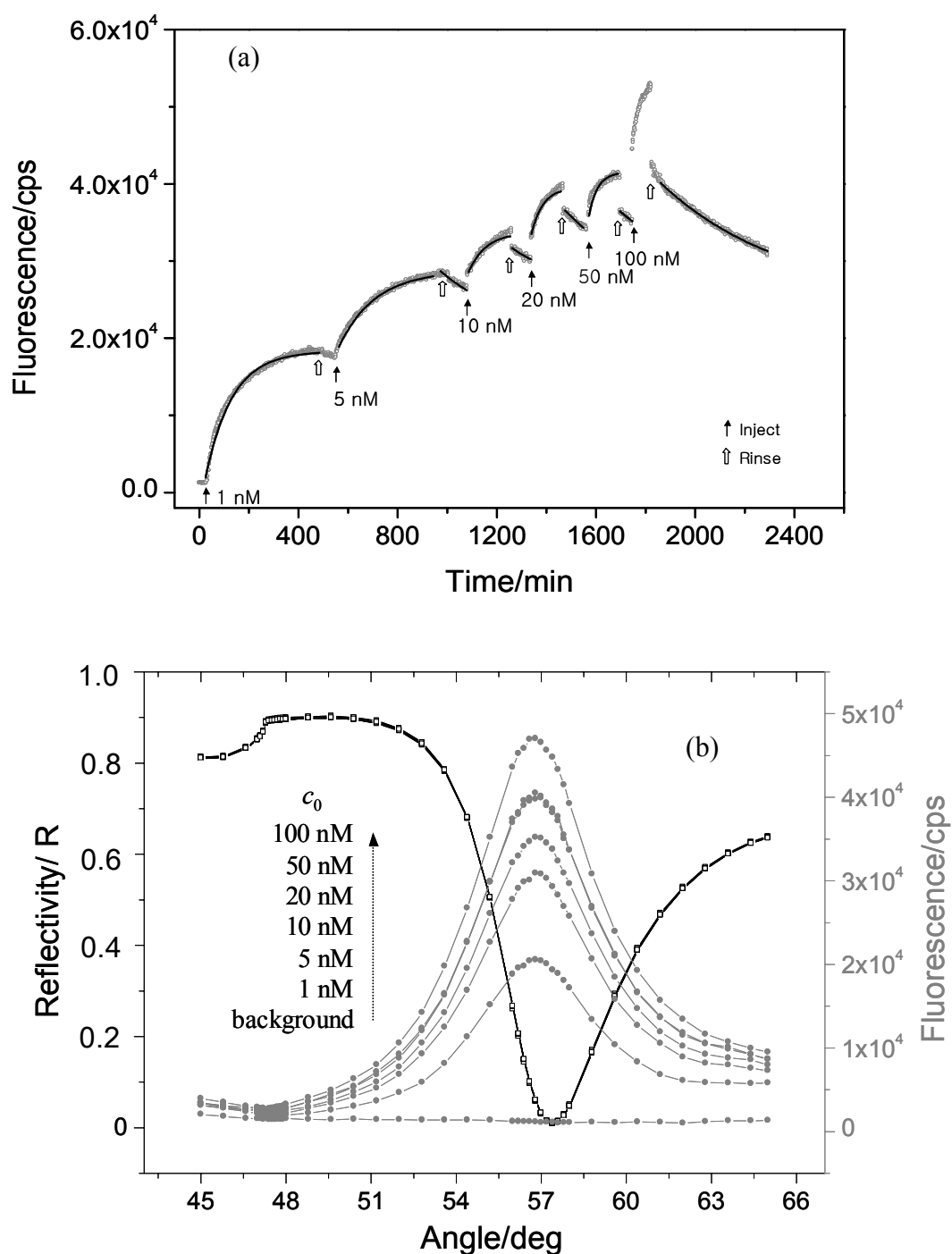


**Figure 5.13.** (a) Kinetic-titration curves for P-RR-15/T-RR-169 hybridization at  $\theta = 55.7^\circ$ . The concentration of target DNA RR-125 was increased from 1 to 5, 10, 20, 50, and 100 nM, respectively, in 10 mM phosphate buffer. Open circles are data points collected every 3 min. The full curves are Langmuir fit to the experimental data. (b) Angular scans taken after saturation of the fluorescence was reached for 1, 5, 10, 20, 50, and 100 nM target solutions, respectively, together with background fluorescence intensity recorded after rinsing (full symbols) and for (1) 20 nM, (2) 50 nM, (1) 100 nM samples also before rinsing (open symbols).



However, by increasing the concentration of T-RR-169 the surface has more charges therefore the Coulombic repulsion could be significantly higher during hybridization. Furthermore the huge (resulting in steric influence) and highly poly-electrolytic DNA target occupied on the surface does not allow hybridizing with next high concentration of target. As a result, the saturation of surface coverage was done at low target concentration ( $K_A = 3.8 \times 10^8 \text{ M}^{-1}$ , Figure 5.14). This value does not mean high affinity constant just due to the low surface density of target DNA.

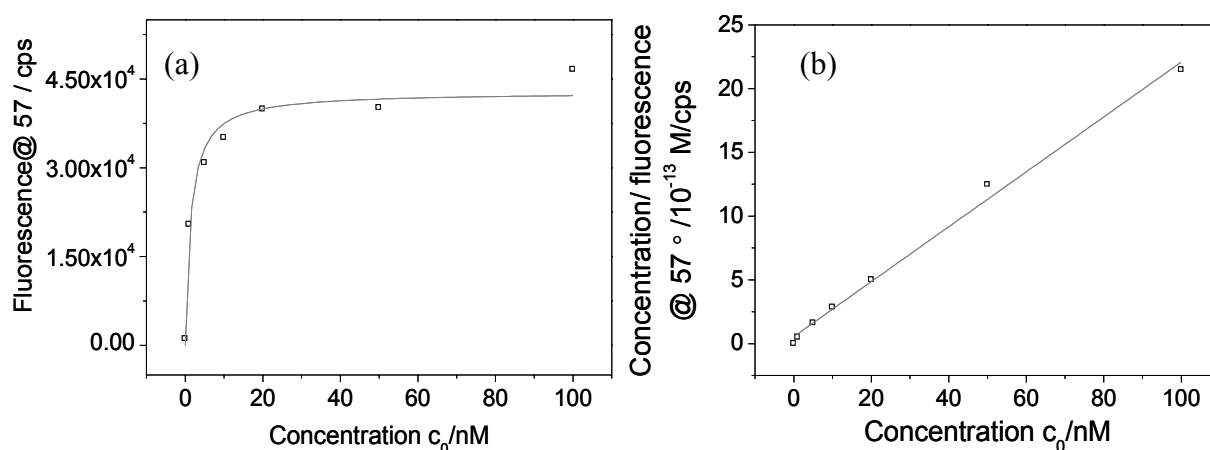


**Figure 5.14.** (a) shows the data taken by analyzing the intensities at equilibrium surface coverages from Figure 5.13 (b). (b) gives the linearized form according to equation (4). The fit gives the affinity constant,  $K_A = 3.8 \times 10^8 \text{ M}^{-1}$ .

### 5.5.3 Mismatch discrimination

Mismatch discrimination of PCR products is also important for biological application. With more fast and reliable single kinetic experiment the mismatch discrimination was accomplished for long PCR targets. The single kinetic experiments were measured with a target concentration of  $c_0 = 50 \text{ nM}$  (T-RR-125) in 10 mM PB. For MM0 situation the PNA, P-RR-15 was immobilized on the sensor surface and P-RR-mis-15 was used for the MM1 case (C-A mismatch).

By introducing the T-RR-125 target DNA solution into the cell and recirculating it until saturation of the fluorescence signal from the PNA sensor surface was reached, the association kinetic was measured. Then the dissociation process was triggered by switching to a 10 mM phosphate buffer solution (Figure 5.15). The analysis of this experiment is also based on the simple Langmuir model.

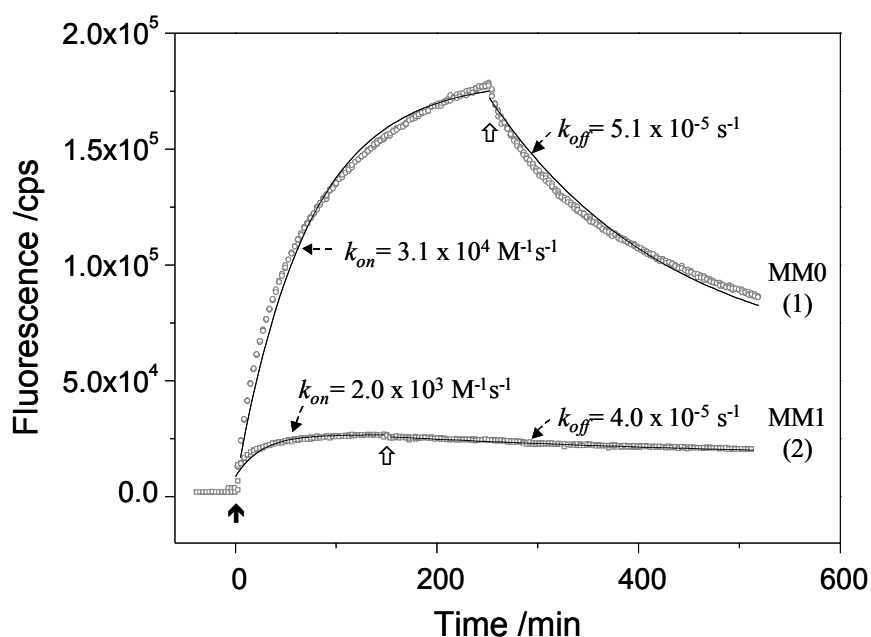


**Figure 5.15.** Hybridization kinetics for (1) P-RR-15/T-RR-125 (50 nM, open circles). (2) Kinetic run for the discrimination of a single mismatch hybridization: P-RR-mis-15/T-RR-125. Open squares are data points collected every 3 min. The solid arrow at  $t=0$  indicates the injection of the target solutions (50 nM) for the recording of the association phase. The solid curves are fits to the data by the Langmuir model.

By using a single exponential Langmuir fit, the obtained rate constants for MM0 are  $k_{on} = 3.1 \times 10^4 \text{ M}^{-1} \text{ s}^{-1}$ ,  $k_{off} = 5.1 \times 10^{-5} \text{ s}^{-1}$ , and the resulting affinity constant is  $K_A = 6.1 \times 10^8 \text{ M}^{-1}$ . As plotted in Figure 5.15 (2), the rate constant of the association phase for MM1 is considerably lower than that of the fully complementary hybrid with  $k_{on} = 2.0 \times 10^3 \text{ M}^{-1} \text{ s}^{-1}$ . However, the dissociation rate ( $k_{off} = 4.0 \times 10^{-5} \text{ s}^{-1}$ ) is not changed significantly compared to the fully matched duplex. As a consequence, the affinity constant is determined to be  $K_A = 5.0 \times 10^7 \text{ M}^{-1}$  i.e. about an order of magnitude lower. This indicates that the one base substitution can be distinctly distinguished by the kinetic responses.

#### 5.5.4 Effect of PNA probe

As mentioned in 5.3.5~6, the probe selection is important for hybridization efficiency and performance. By varying the catcher probe (P-RR-11, 13 and 15, all MM0) the hybridization was studied using the T-RR-169 target on the sensor surface.

Here the same target DNA (T-RR-169, MM0) was introduced to 3 different lengths of PNA probes (11, 13, and 15mer) immobilized on the surface in 10 mM PB as shown in Figure 5.16.

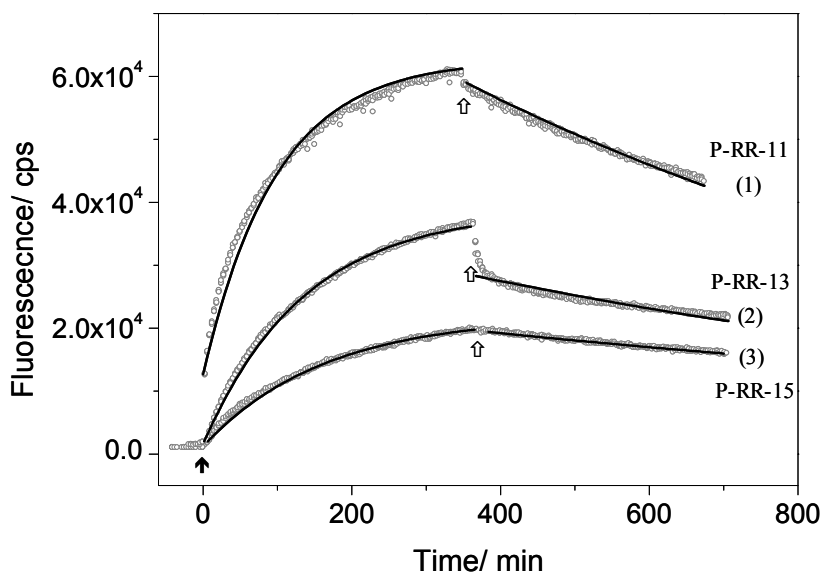


**Figure 5.16.** Hybridization kinetics for MM0 (1) P-RR-11/T-RR-169, (2) P-RR-13/T-RR-169, and (3) P-RR-15/T-RR-169. Open squares are data points collected every 3 min. The solid arrow at  $t=0$  indicates the injection of the target solutions (50 nM) for the recording of the association phase. The solid curves are fits to the data by the Langmuir model with association and dissociation phase.

The association rate of the 11mer PNA/ 169mer PCR hybridization was found to be faster than those of the 13mer and the 15mer in MM0 situation (Figure 5.16); rate constants are summarized in Table 5.6.

**Table 5.6.** Rate constants obtained by the single kinetic analysis (Figure 5.16) for 3 different lengths of PNA probes and one PCR target hybridizations.

	P-RR-11/T-RR-169	P-RR-13/T-RR-169	P-RR-15/ T-RR-169
$k_{on} / \text{M}^{-1} \text{s}^{-1}$	$5.8 \times 10^3$	$3.0 \times 10^3$	$2.0 \times 10^3$
$k_{off} / \text{s}^{-1}$	$3.8 \times 10^{-5}$	$1.8 \times 10^{-5}$	$1.2 \times 10^{-5}$
$K_A / \text{M}^{-1}$	$1.5 \times 10^8$	$1.7 \times 10^8$	$1.7 \times 10^8$

The tendency that the affinity is increased if the recognition sequence of the PNA probe is increased in the length follows the result of oligomer targets (Figure 5.7 and Table 5.2). A short length of oligonucleotides can hybridize more easily than long ones due to fewer base

pair. Once DNA binds with PNA, the duplex for 15mer having 4 more base pairs is more stable than the 11 mer because the long one has more hydrogen bonds. Thereby the dissociation rate of long PNA/DNA is much slower than that for the short one. Thus the affinity constant of 15 mer PNA/DNA is higher than that of 11mer.

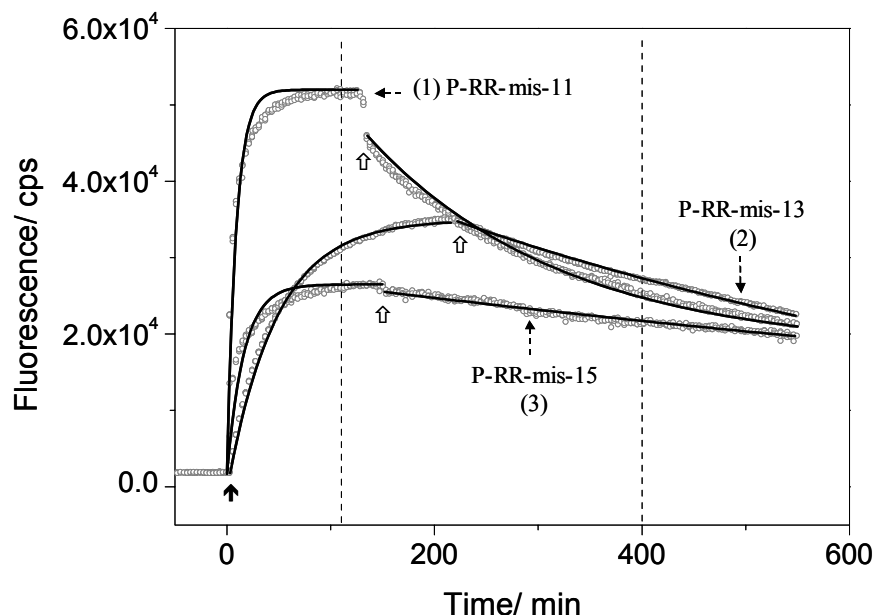


**Figure 5.17.** Hybridization kinetics for MM1 (1) P-RR-mis-11/T-RR-125, (2) P-RR-mis-13/T-RR-125, and (3) P-RR-mis-15/T-RR-125. Open squares are data points collected every 3 min. The solid arrow at  $t=0$  indicates the injection of the target solutions (50 nM) for the recording of the association phase. The solid curves are fits to the data by the Langmuir model with association and dissociation phase. Dash lines are the time (110 and 140 min) for the difference of fluorescence intensity.

**Table 5.7.** Rate constants obtained by the single kinetic analysis (Figure 5.17) for 3 different lengths of PNA probes and one PCR target hybridizations.

	P-RR-mis-11/ T-RR-125	P-RR-mis-13/ T-RR-125	P-RR-mis-15/ T-RR-125
$k_{on} / \text{M}^{-1} \text{s}^{-1}$	$4.4 \times 10^3$	$1.7 \times 10^3$	$2.0 \times 10^3$
$k_{off} / \text{s}^{-1}$	$9.8 \times 10^{-5}$	$5.4 \times 10^{-5}$	$4.0 \times 10^{-5}$
$K_A / \text{M}^{-1}$	$4.5 \times 10^7$	$3.1 \times 10^7$	$1.7 \times 10^7$

Another probe effects were evaluated for MM1 situation by varying the catcher probe (P-RR-mis-11, 13 and 15) using the T-RR-125 target on the sensor surface in 10 mM PB (Figure 5.17 and Table 5.7)

The association and dissociation rates of 11mer PNA/ 125mer PCR hybridization were observed faster than those of 13mer and 15mer in MM1. As a result, the affinity constants were determined with similar values. With respects to the affinity constant, the evaluation of probe PNAs efficiency is not dramatic. However the difference of fluorescence intensity (at 110 and 400 min, Figure 5.17) is significant for PNA 11mer case. The fluorescence intensity of PNA 11mer is the highest (51713 cps). And the difference of fluorescence is 47.5, 22.6, and 19.1 % for 11mer, 13mer, and 15mer, respectively. Thereby the PNA, P-RR-mis-11 could be the best candidate for the application to micro-array biosensor.

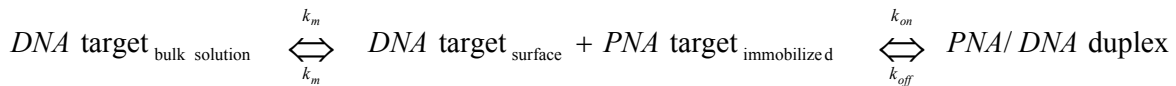
### 5.5.5 Limit of detection for PCR target on the sensor surface

The limit of detection (LOD) is used to decide whether an analyte is present, while the limit of quantification is used to decide whether the concentration of an analyte can be reliably determined [68]. In statistics, LOD is the minimum single result which can be distinguished from a suitable blank value. The LOD is derived from the smallest measure ( $x_L$ ), expressed as the concentration or the quantity. The value of  $x_L$  is given by the equation:

$$x_L = \overline{x_{bi}} + k \cdot s_{bi} \quad (5)$$

where  $\overline{x_{bi}}$  is the mean of the blank measures,  $s_{bi}$  is the standard deviation of the blank measures, and  $k$  is a numerical factor chosen according to the confidence level [69].

The formation of the PNA/DNA duplex can be influenced by the mass-transport rate constant  $k_m$  from the bulk to the interface and from the interface to the bulk as follows:



At such low analyte concentrations, the binding kinetics of PCR target are all controlled by the mass-transport rate from the bulk solution to the interface and can be described by:

$$dR/dt = k_m c_0 \quad (6)$$

indicating that the response  $R$  increases linearly with time  $t$  and the binding slope is proportional to the bulk concentration  $c_0$  of the analyte [70]. The proportionality factor  $k_m$  is known as the mass-transport rate constant. This can be used for the concentration analysis of

analyte *DNA*, since the slope of the initial stage of the binding curve is proportional to the analyte concentration. The mass-transport rate constant,  $k_m$  is dependent on the diffusion coefficient ( $D$ ) of the target, the dimensions of the flow cell (height- $h$ , width- $b$ ), and the flow rate ( $v$ ) described by:

$$k_m = 0.98 \left( \frac{D}{h} \right)^{2/3} \left( \frac{v}{bx} \right)^{1/3} \quad (7)$$

where  $D$  is the diffusion coefficient,  $h$  and  $b$  are the height and the width of the flow cell,  $v$  is the volumetric flow rate, and  $x$  is the distance from the flow cell entrance [71, 72].

The PCR targets (T-RR-125) having a complementary sequence with the probe (P-RR-15) could hybridize to the immobilized probe PNA on the sensor surface (Figure 5.18). As one can see, the initial part of each association phase is a straight line, indicating that those are all mass-transport limited interactions.

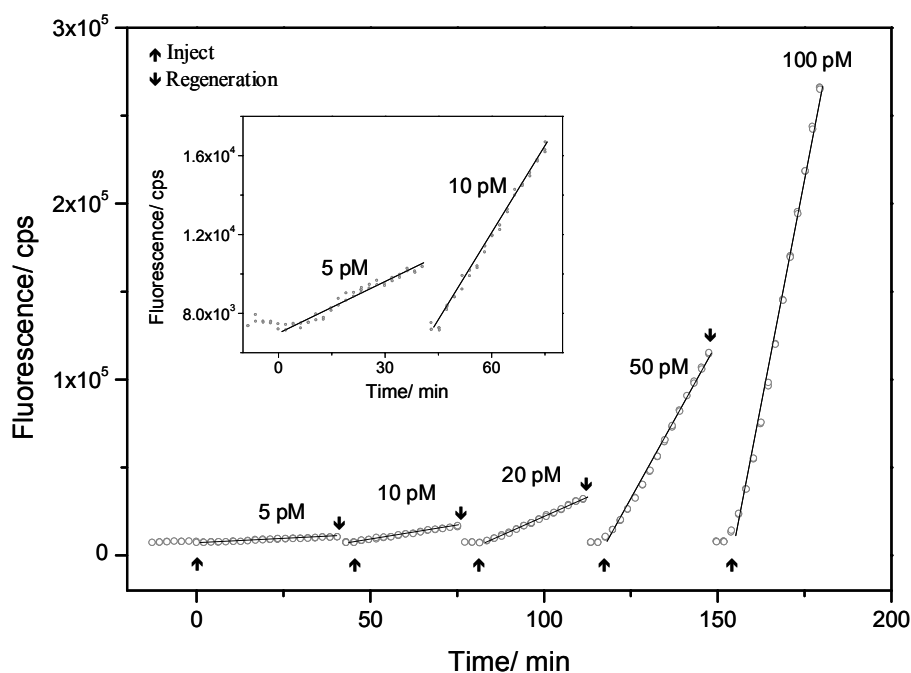


**Figure 5.18.** (A) Fluorescence intensity upon the injection of sample solutions with 5, 10, 20, 50, and 100 pM concentrations of PCR target (T-RR-125) on the PNA probe (P-RR-15) in 10 mM PB. Regenerations were performed after every sample injection to re-set the baseline level. Solid lines are the linear fits to the binding curves (open circles are data points collected every 3 min.) to yield the corresponding binding slopes. The inset shows the binding with 5 and 10 pM of target.

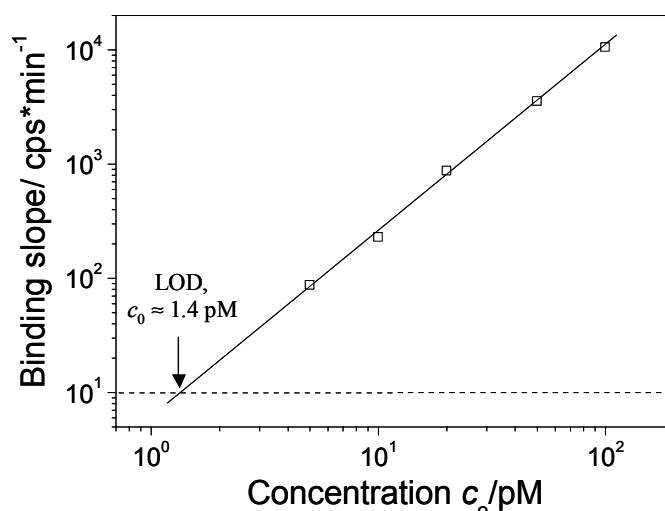


**Figure 5.19.** Double-logarithmic plot of the binding of PCR target (T-RR-125) to the PNA probe (P-RR-15) surface. The solid line is the linear fit. The dashed line represents the baseline fluctuation level (3~5 cps min<sup>-1</sup>). The LOD was indicated to be  $c_0 \approx 1.4$  pM. Error bars are smaller than the data point.

Therefore, plotting the binding slope (from Figure 5.18) *versus* the bulk concentration defines a calibration curve, shown in Figure 5.19. The baseline stability was tested by five repetitive injections of mere buffer solutions and the resulting five slopes were analyzed statistically. The sum of the mean plus 3 times the standard deviation was considered as the baseline signal deviation, which was 3~5 cps min<sup>-1</sup> [73]. From the experimental curves in Figure 5.19, one can see the following: (1) mass-transport-limited binding signals from all applied concentrations could be resolved from the baseline, and (2) the regeneration procedures re-set the fluorescence signal to the background level. The resulting curve intersects with the baseline deviation level, which gives a LOD concentration of 1.4 pM.

### 5.5.6 Detection limit for mixed PCR targets on the sensor surface

A selective detection based on specific DNA hybridization is needed in order to screen for GMOs in food. The SPFS measurement was conducted in order to detect reliably the presence of GMO (T-RR-125) in a mixture with other PCR amplicons selected from the natural material.

First, the unspecific binding using the selected PCR target (Mu-159 labelled with Cy5) having a random sequence (non-complementary) was investigated on the PNA (P-RR-15) sensor surface (Figure 5.20) in 10 mM PB. If the target Mu-159 applied to the PNA probe, the fluorescence intensity was observed to jump a little but then remained constant as a function

of time (Figure 5.20 (1)). This increase is due to the emission from the chromophors in the 50 nM bulk solution. By replacing the target solution with pure 10 mM PB the fluorescence intensity went back to the background level. This result indicates that there is no (specific or unspecific) binding between Mu-159 and P-RR-15.

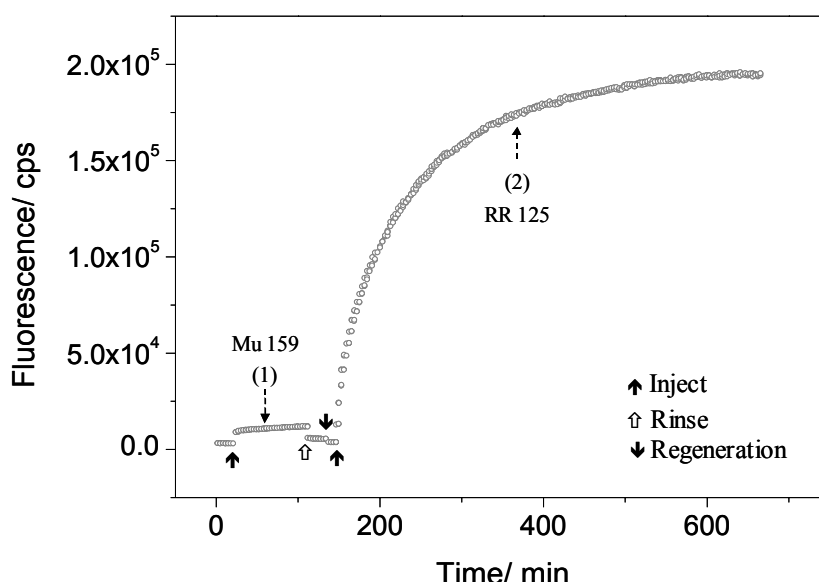


**Figure 5.20.** Hybridization kinetics recorded at  $\theta=55.7^\circ$  for (1) P-RR-15/Mu-159 (50 nM). (2) P-RR-15/RR-125 (50 nM). Regenerations were performed after unspecific binding of Mu 159. Open circles are data points collected every 3 min.

On the other hand, the target T-RR-125 (complementary MM0) binds to the probe P-RR-15, resulting in a gradual increase (above an order of magnitude) of fluorescence intensity emitted by the surface attached chromophors. The 15mer oligomer probe PNA is sufficient to detect long PCR targets with high selectivity and sensitivity.

Next, SPFS measurements were performed using mixture of PCRs (Mu-159 without labeling and T-RR-125) and the PNA probe (P-RR-15) in order to determine the detection limit of GMO PCR. 4 samples of PCR targets were prepared as following:

- (a) 10 pM of T-RR-125; reference
- (b) 10 pM of T-RR-125 + 1 nM of Mu-159; 1% detection
- (c) 10 pM of T-RR-125 + 10 nM of Mu-159; 0.1% detection
- (d) 10 pM of T-RR-125 + 100 nM of Mu-159; 0.01% detection.



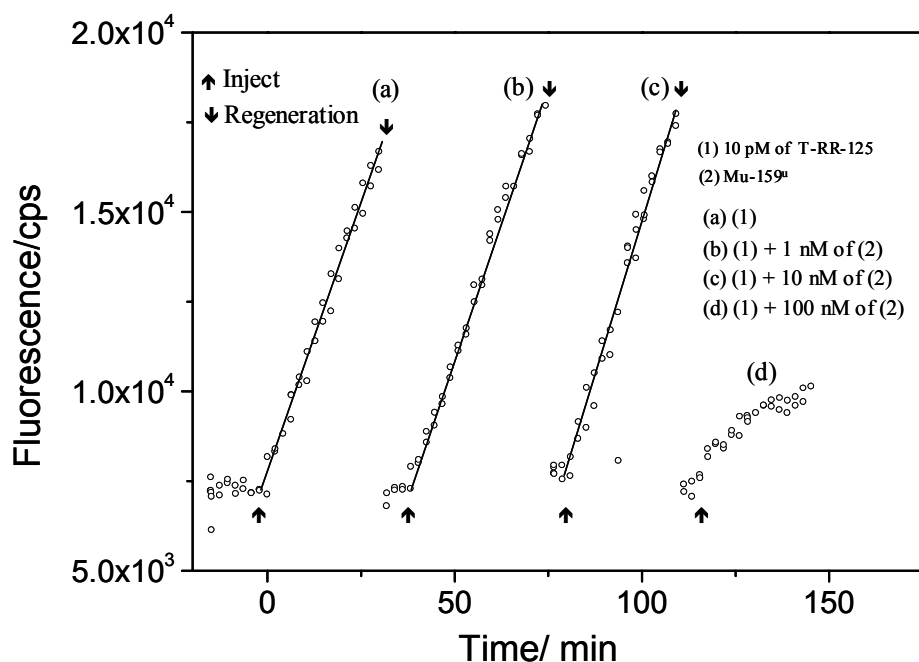


**Figure 5.21.** (A) Fluorescence intensity upon the injection of sample solutions with (a) 10 pM (reference), (b) 10 pM of T-RR-125 + 1 nM of Mu-159 (1 % detection), (c) 10 pM of T-RR-125 + 10 nM of Mu-159 (0.1 % detection), and (d) 10 pM of T-RR-125 + 100 nM of Mu-159 (0.01 % detection) concentrations of mixed PCR targets on the PNA probe (P-RR-15) in 10 mM PB. Regenerations were performed after every sample injection to re-set the baseline level. Solid lines are the linear fits to the binding curves (open circles are data points collected every 3 min.) to yield the corresponding binding slopes.

Figure 5.21 shows experimental data for the detection limit taken at low ionic strength (10 mM phosphate) using each time the same sensor surface. Starting for a short time with the baseline measurement, a 10nM reference sample solution (Figure 5.21(a)) was injected and circulated for 30 min approximately in order to monitor the increase in fluorescence intensity. The binding data was fitted by a linear plot giving the intrinsic slope. The surface was fully regenerated by treatment with 10 mM NaOH in order to remove remaining bound target DNA for another analysis cycle at the same sensor surface. The detection of 1 and 0.1 % GMO PCR (Figure 5.21 (b) and (c)) in mixed PCR solutions was accomplished with same slope of reference target (Figure 5.21 (a)). However, at 0.01% GMO target a different fluorescence increase was observed. The large excess of Mu-159 could play a role like unexpected binding or preventing the specific binding of T-RR-125 onto the probe surface.

SPFS offers a good specificity and sensitivity for the detection of 0.01% GMO PCR from mixed target solutions.

### 5.5.7 Detection of GMO on an array by surface plasmon fluorescence microscopy (SPFM)

The technique of surface plasmon fluorescence microscopy (SPFM) [74] is a combination of surface plasmon microscopy [75-77] with fluorescence detection by using a highly sensitive CCD camera. The principle is based in the detection of light from chromophores located near the metal/dielectric interface, excited by the resonantly coupled surface-plasmon modes propagating along this interface.

The mixed thiols were incubated on gold overnight to immobilize biotinylated PNA probes. In order to detect PCR products from GMO 9 kinds of PNAs (1  $\mu$ M) with different affinities to the same target were spotted in an array using a pin-tool spotter. The SPM image of the array is shown in Figure 5.22 (a).

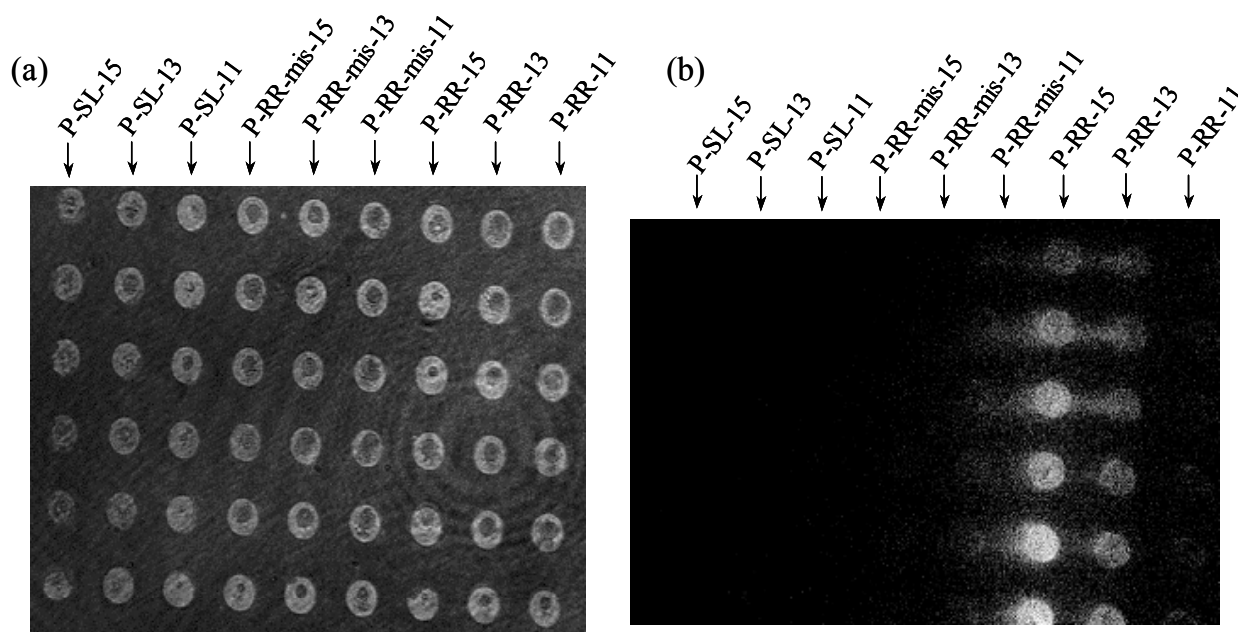


**Figure 5.22.** (a)SPM image of whole PNA probes and (b)SPFM image after hybridization with target PCR (T-RR-125).

After immobilization of the PNA probes, the RR-125 PCR target (50 nM) was applied to the cell for about 40 hr. As can be seen in Figure 5.22 (b), the target PCR bound only to the complementary matching PNA probes according to their affinities (15>13>11mer). Furthermore, there was no unspecific binding with P-SL (complementary matching to the PCR target from natural soybean).

### 5.3.4 Morphology study by AFM

Scanning probe microscopy (SPM), which includes scanning tunneling microscopy (STM) [78], atomic force microscopy (AFM) [79], and related techniques, has been widely applied for the characterization of surface structures and the fabrication of nanostructures at the atomic scale on surfaces. AFM does not require conductivity of the material, and it is therefore the favored technique to study surface. Surfaces modified with DNAs have been investigated for potential applications in biosensing and biochemical imaging [80-83]. It is essential to understand the surface structure of these modified DNAs, since different DNA conformations lead to different interactions with biomolecules. Recently, many attempts to fabricate DNA films, networks, and other patterned constructions as well as other various methods have been used such as DNA molecular deposition, immobilization of DNA on SAMs [84,85]. It is important to evaluate the DNA film for further application.

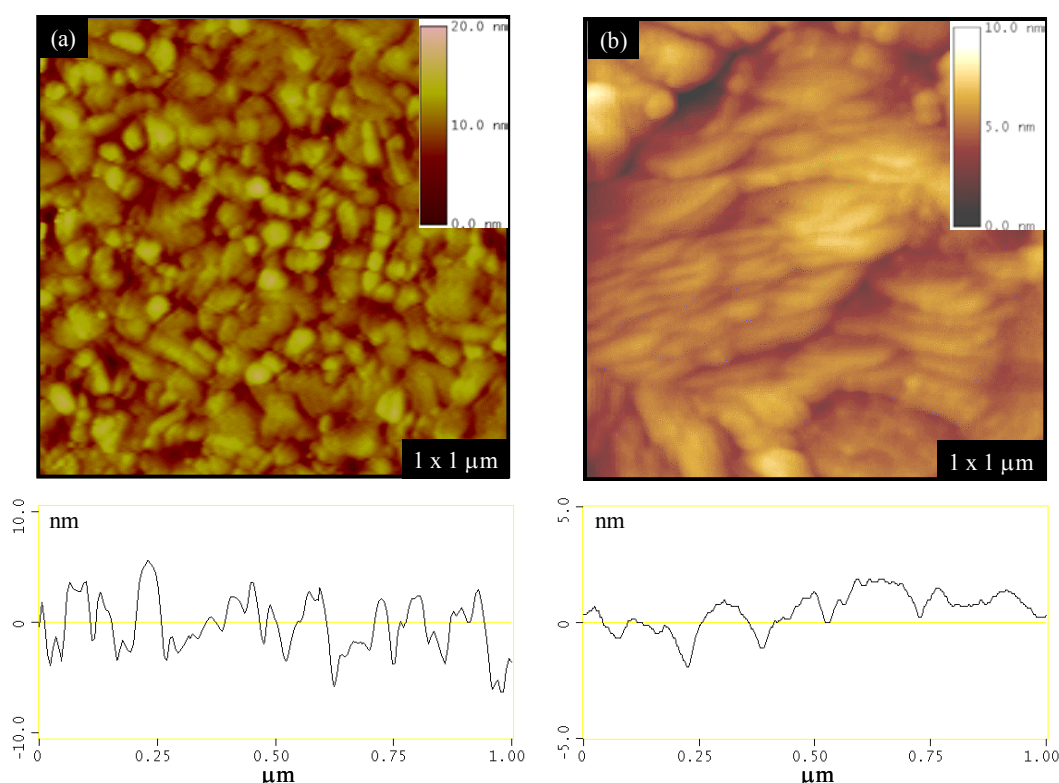


**Figure 5.23.** Tapping-mode AFM images of the gold substrates. (a) The gold substrate with 200 nm thickness after thermal evaporation on the glass. The rms roughness was 2.7 nm. (b) The gold substrate after annealing of (a) at 400 °C for 1 h. The rms roughness was 1.0 nm.

The surfaces of each layer described in chapter 3 were studied using tapping-mode AFM (Nanoscope IIIa, Digital Instruments, USA) with WC<sub>2</sub>-coated Si tips (Mikro Masch, USA) in air. A 200 nm thick gold layer was prepared onto a freshly cleaved mica substrate by thermal evaporation at a rate of 0.1 nm/s under ultra-high vacuum condition ( $5 \times 10^{-6}$  m bar). Then the gold substrate was annealed at 400 °C for 30min to obtain a flat surface. Figure 5.23 (a) is the AFM image of gold substrate with 200 nm thickness after thermal deposition. The gold dots were deposited randomly and the rms roughness ( $1 \times 1 \mu\text{m}^2$  in dimension) was 2.7 nm that is too rough to analyse the surface as a starting substrate. By annealing the gold substrate at a high temperature the surface became smooth with flat terraces (Figure 5.23 (b)). Terraces with orientation as large as  $200 \times 200 \text{ nm}^2$  in dimension were observed in the AFM image. Although this annealed gold substrate has a flat surface, the area of the terrace is still too small to quantify the analyte on the surface.

Many approaches to functionalize surfaces were taken by tailoring biotinylated chain molecules with a reactive endgroup capable of forming SAMs on various substrates [86-88]. In particular, a binary mixed thiol (biotinylated thiol and spacer thiol) was investigated for the fabrication of supramolecular interfacial architectures [89-91]. The binary mixtures of the biotin-derivatized thiols and a suitable diluent thiol had to be used for this SAM formation. The flat gold substrate was used for the self-assembled monolayers of a binary mixed thiol (chapter 3.2.3). For the preparation of the self-assembled monolayers (SAM), the gold surface was incubated overnight in a binary mixed thiol solution of a biotinylated thiol (Biotinamino-capronacid-amidodioctyl-mercaptopropionamide, Table x) and a spacer thiol (11-Mercapto-1-undecanol, Aldrich, Table x) at a molar ratio of 1: 9 and a total concentration of 0.5 mM in absolute ethanol (Aldrich). The thiol mixture is composed of two different kinds of alkanethiols, one terminated with a biotin group for subsequent streptavidin binding (10 mol %), and a shorter thiol (90 mol %) terminated with a hydroxyl group that acts as a spacer to dilute the biotinylated species, in order to control the surface density and to minimize non-specific adsorption of analyte (target) molecules. The thiolated molecules were bound on the gold terrace as shown in Figure 5.24 (a).

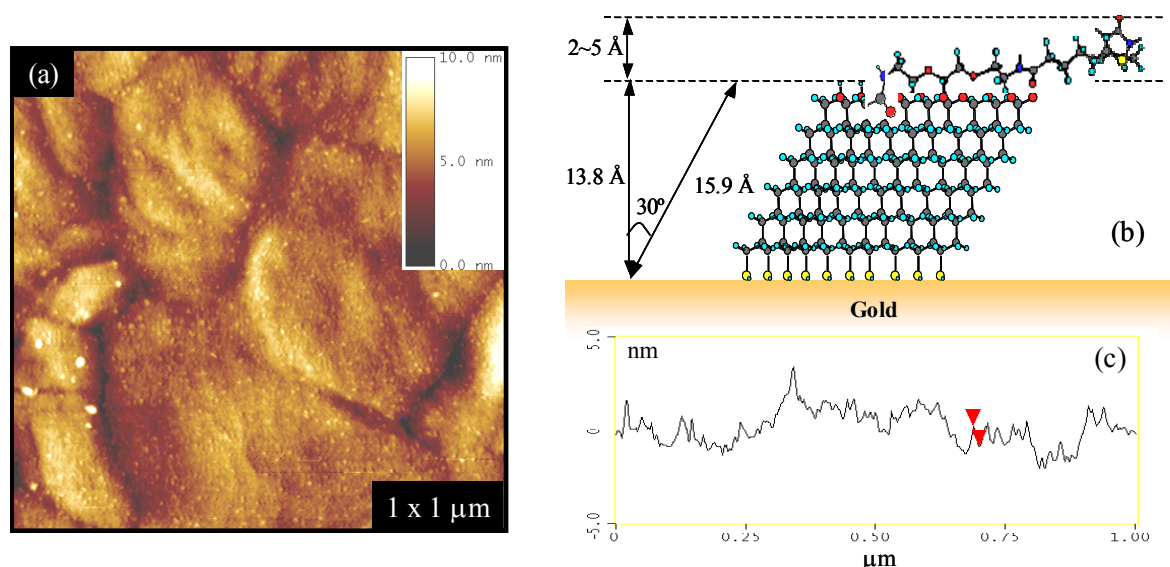


**Figure 5.24.** (a) Tapping mode AFM image of the mixed thiols modified gold substrate. The rms roughness was 1.37 nm. (b) Schematic drawing of the formation of SAMs. (c) Cross section of the image (a).

The height measured from the cross section of the AFM image (Figure 5.24 (a), small dots) is  $1.7 \pm 0.3$  nm, which nearly agreed with the optical thickness calculated from SPR measurement (chapter 3.2.4). The thickness is expected to be 1.4 nm of height (Figure 5.24 (a)) theoretically for self-assembled monolayers of alkanethiol having 12 carbons tilted  $30^\circ$  from the plane [92-95]. The alkanethiol (11 carbons) part of the biotinylated thiol could be self-assembled with spacer thiol (12 carbons) under van der Waals interactions, however the other part containing biotin moiety seemed to lie down due to the flexible C-C bond (rotatable  $\sigma$ -bond) next to the amide group. Therefore formation of the mixed SAM can be drawn schematically as a Figure 5.24 (c).

The streptavidin-biotin system has been frequently used in an effort to generate bio-functional surfaces for biospecific recognition reactions [96,97]. As it turned out, streptavidin with the highly specific interaction to its ‘ligand’ biotin also offers many advantages for tests of biosensor configurations and concepts, in which the solid surface of a signal transducer in contact with a liquid medium that contains the analyte has to be functionalized in such a way that the selective and specific interaction between ‘receptor’ and analyte is optimized while simultaneously all other non-specific binding is minimized.

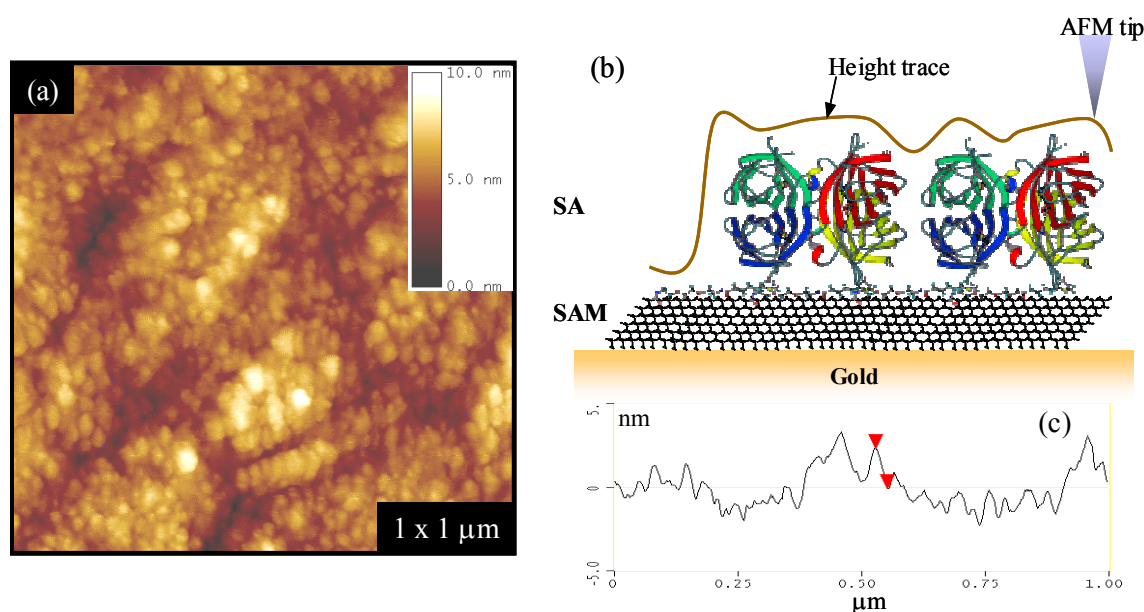


**Figure 5.25.** (a) Tapping mode AFM image of the immobilized streptavidin (SA) layer on the mixed SAMs. The rms roughness was 1.05 nm. (b) Schematic drawing of the immobilization of SA. (c) Cross section of the image (a).

Once the mixed thiols providing the recognition site to bind streptavidin were assembled on the gold, the substrate was immersed in the prepared streptavidin (SA) solution of 1  $\mu\text{M}$  in PBS for 1 hr. Figure 5.25 (a) shows typical AFM image of the immobilized streptavidin to the SAM layer. The morphology of SA modified surface was dramatically changed from that of SAMs. The SA is a tetramer with a two-fold symmetry of the binding pockets, on each side, and the dimensions of the single SA crystal was estimated to be  $\sim 5.0 \times 4.5 \times 4.5 \text{ nm}^3$  [98].

Due to the adsorption of the bulky SA molecules onto the biotin, the significantly increasing of optical thickness (3.3 nm) was calculated using SPR measurement (chapter 3.2.4). However it is difficult to estimate the thickness difference between the substrate and SA layer. The AFM tip can scan only the top of the surface, so the AFM image provides the information of the topography (Figure 5.25 (b)). The calculated rms roughness from the image of SA layer (Figure 5.25 (a)) was 1.05 nm ( $1 \times 1 \mu\text{m}^2$  in dimension). The surface was smoother than the mixed thiol layer (rms roughness was 1.37), which means the high affinity constant and the stability of the streptavidin-biotin complex allow for reliable bio-functionalization. The streptavidin is filled closely in the surface by high density with a uniform grain size of 35~40 nm width and 2 nm height. The hybridization efficiency in a DNA chip is known to be dependent on how much of the surface is covered with the probe. The large density of SA promises the much immobilization of the catcher probes on SA layer.

Peptide nucleic acid (PNA), a polyamide DNA mimic, has inspired the development of a variety of hybridization-based methods for the detection, quantification, purification and characterization of nucleic acids owing to the stability of the PNA/DNA duplex. PNA probes complementary to a specific sequence of Round-up Ready<sup>TM</sup> soybean were immobilized onto a sensor surface via a self-assembled matrix employing streptavidin/biotin binding.

The biotinylated PNAs (P-RR-15, 500 nM in PBS for 1 hr) as catcher probes could be easily immobilized on the SA layer due to the strong affinity of streptavidin-biotin after SA binding onto the SAMs, subsequently. The surface morphology of the PNA attached layer (Figure 5.26 (a)) was changed little from the SA layer (Figure 5.26 (a)). The length of PNA having 15 bases is 6 nm with 1 nm diameter approximately (after MM2 energy minimization using CS Chem 3D Pro<sup>®</sup>). It is difficult for the PNA probe attached to SA to stand without any supports especially after drying the surface. We could assume that PNAs lay flat like the schematic drawing (Figure 5.26 (b)). Therefore the roughness (0.77 nm) of the surface was smaller than that of the SA layer (1.05 nm). However the PNA probe could be free from the surface in water in order to hybridize with DNA targets.

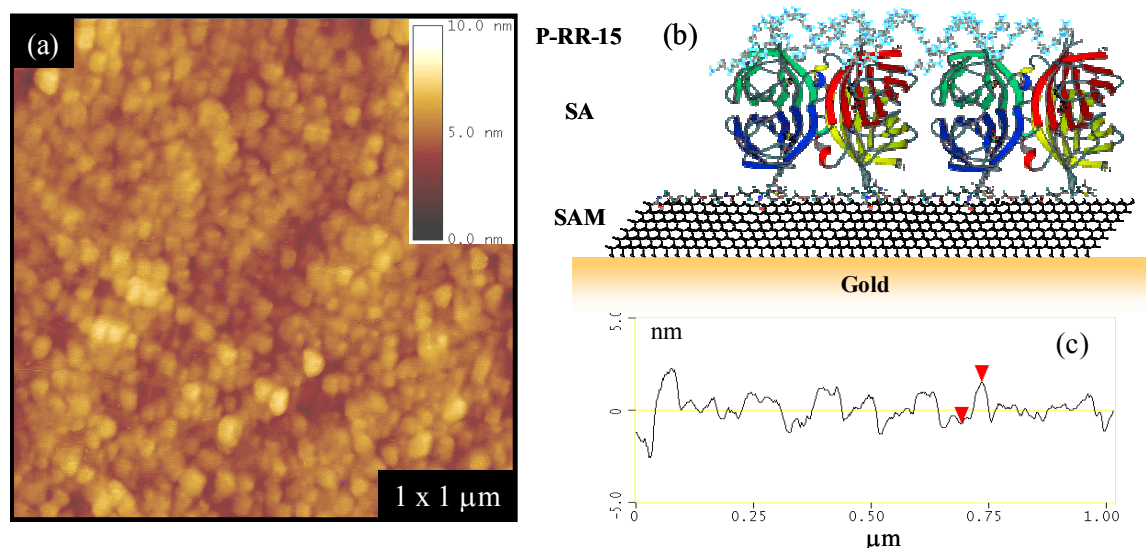


**Figure 5.26.** (a) Tapping mode AFM image of the immobilized PNA probe (P-RR-15) layer on the streptavidin layer. The rms roughness was 0.77 nm. (b) Schematic drawing of the immobilization of probe. (c) Cross section of the image (a).

Finally, the target DNA (T-RR-125, 100 nM) amplified using PCR with Round-up Ready<sup>TM</sup> soybean solution was prepared in 10 mM PB. The substrate immobilized with PNA having



specific recognition site against the target DNA was immersed in the DNA solution for 6 hrs (the hybridization between PNA/PCR was observed very slow from kinetic data in chapter 5.5)

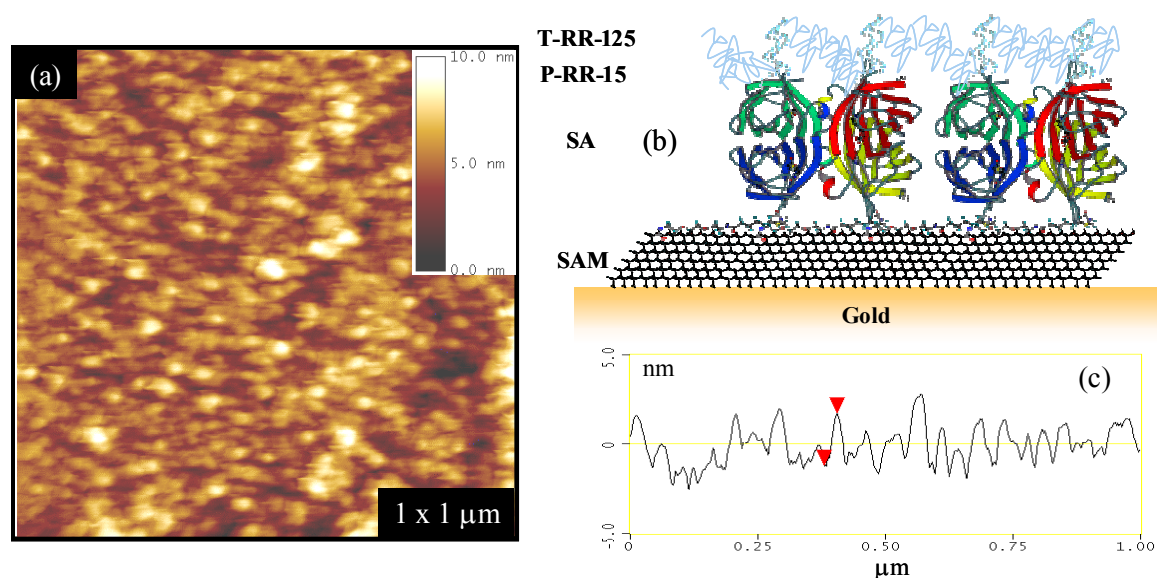


**Figure 5.27.** (a) Tapping mode AFM image after hybridization between PNA probe (P-RR-15) and PCR target (T-RR-125). The rms roughness was 1.10 nm. (b) Schematic drawing of the hybridization. (c) Cross section of the image (a).

The morphology after hybridization with long DNA target having 125 bases to surface attached PNA probe was changed slightly (Figure 5.27 (a)). In 10 mM PB solution, the target PCR can recognize the specific base sequences in PNA probe as evaluated in the previous kinetic analysis (in chapter 5.5). However the process of surface drying after hybridization resulted the free part of single stranded PCR target stick to the surface. These physically attached PCR targets (not matched part) made the surface rough (rms roughness was 1.10 nm) a little. In the AFM image (Figure 5.27 (a)) the dots were analyzed with 3~4 nm height which is corresponding to the length of 15 mer duplex (2.5~3.4 Å/ bp) [99-101]. However it is not clear to identify the DNA target quantitatively from the surface. The surface morphology change after the hybridization from PNA layers gives the clear demonstration for the existence of bound target DNA to the PNA immobilized surface. Nevertheless, some difficulties are still remaining such as a quantification of DNA detection. The AFM measurement in aqueous buffers could be useful to investigate the *in situ* hybridization [102-104].



## 5.6 Conclusion

SPFS is shown to allow for an in depth study of the hybridization reaction between surface attached PNAs which are designed for the detection of the GMO Round-up Ready<sup>TM</sup> soybean (RR soybean) and oligonucleotide DNA targets from solution. The optimized PNA sensor matrix constructed *via* SAM strategies allowed for kinetic measurements as well as for a quantitative determination of affinity constants. Moreover, it provided sufficient sensitivity to distinguish a single base mismatch in the hybridization of chromophore-labeled DNA targets (oligonucleotides and PCR products from RR soybean). The binding of fluorophore-labeled DNA targets to PNA probes resulted in a change of the thickness, reflectivity, and fluorescence intensity. The biomolecular interaction between PNA and DNA was analyzed by three different experiments using a simple Langmuir model. The association rate constant,  $k_{on}$ , and the dissociation rate constant,  $k_{off}$ , are obtained by separately fitting selected sections of the data of the association and the dissociation phase, respectively, to a simple bimolecular interaction model.

It is essential to evaluate the effect of the ionic strength for the hybridization between PNA probe and DNA target, because the amplified PCR product from GMO should be in low ionic strength to prevent re-hybridization. The ionic strength does not play a significant role in PNA/PCR hybridization. Therefore, all kinetic measurements were carried out in low ionic strength (10 mM PB)

In a kinetic analysis, 4 different experiments were demonstrated. The global analysis turned out to be the fastest and most reliable method to determine association rate constants because it analyses only early stages of the binding. For rather stable complexes like a hybrid of two 15mer oligonucleotides with zero mismatch a 10 min rinsing phase is not sufficient to see a significant dissociation that can be analyzed quantitatively. However, it is very well suited to obtain the dissociation rate in the case of a single base mismatched double strand during the rinsing step resulting in a visible loss of fluorescence intensity that allows for a quantitative determination of  $k_{off}$  in addition to  $k_{on}$ , and hence can also give the affinity constant  $K_A$ .

The typical titration experiment allows for the determination of the Langmuir adsorption isotherm and, hence, the affinity constant  $K_A$  based on the evaluation of surface coverages. However, by increasing the concentration and, hence, the occupancy of the probe binding sites, the interface is more and more charged resulting (especially for long DNA targets, at the low ionic strength used in these experiments) in an increasingly significant Coulombic barrier

for the hybridization at the sensor surface. As a consequence the (averaged) affinity constant can be significantly lower than that found by the global analysis or by kinetic-titration experiments at low bulk concentrations (relative to  $K_D = K_A^{-1}$ ), i.e., low surface coverages.

The kinetic and equilibrium coverage measurements that are done in the kinetic-titration experiment clearly revealed the influence of the interfacial charging effect. For each concentration  $c_0$  of the bulk solution the association and dissociation of the target to and from the sensor surface can be quantified and then also an apparent (concentration dependent) affinity constant can be determined.

The single kinetic analysis is a fast approach to compare both fully matched and one mismatched duplex formation. It is important to determine the target concentration for single kinetic analysis due to the different  $K_D$  values of targets desired to compare. Otherwise, the surface would have different coverage with target on the same probe sensor matrix resulting in different fluorescence intensity. Therefore, the titration experiment should be performed firstly to determine the  $K_D$  value. All mismatch discriminations were carried out successfully with significant differences even at very long target DNA concentrations (PCR products) by single kinetic experiments.

In order to investigate the effect of probe PNA in terms of length and sequence for high sensing efficiency, 3 different probes were immobilized and characterized with complementary matched target (MM0) and one base mismatched target (MM1). The short probes showed fast association rate; besides, a fast dissociation phase was measured due to the low stability compared to the long probe. For that reason, the short probe could be used to discriminate mismatched duplexes. Once, the probe is fixed with specific one, the length effect of target DNA was studied with oligomer (15 bases), and PCR targets (125 and 169 bases). The SPFS technique provided enough signals for a quantitative analysis. However, the fluorescence intensity was influenced by the distance of the chromophors attached to the DNA target from the surface. The fluorescence intensity of oligomer DNA targets was found to be a higher than those of long PCR targets. The chromophors attached PCR target is far from evanescence field resulting in reduced fluorescence intensity. Therefore, the optimized surface architecture according to the target analyte is desired for the detection with high sensitivity.

The limit of detection (LOD) measurement was satisfied with 1.4 pM of PCR target based on PNA/DNA hybridization with high sensitivity and selectivity. Furthermore, the GMO presenting 0.01 % in mixed PCR targets with 99.99 % impurity was able to be detected.

Finally, the specific binding at the functional molecule was characterized by tapping mode AFM in air. The information of surface structure and the change of morphology for adsorbed molecules were compared to each layer of sensor surface.

## 5.7 References

- [1] (a) Commission Regulation (EC) 258/97 of the European Parliament and of the Council concerning Novel Foods and Novel Food Ingredients. *Off. J. Eur. Communities* 1997, *L* 43, 1-5.  
  
(b) Commission Regulation (EC) 50/2000 of Jan 10, 2000, on the labeling of foodstuffs and food ingredients containing additives and flavorings that have been genetically modified or have been produced from genetically modified organisms. *Off. J. Eur. Communities* 2000, *L* 6, 15.  
  
(c) Regulation (EC) 1829/2003 of the European Parliament and the Council of the European Union on genetically modified food and feed. *Off. J. Eur. Union* 2003, *L*268, 1-23.  
  
(d) The European Parliament and the Council of the European Union Regulation (EC) 1830/2003 concerning the traceability and labeling of genetically modified organisms and the traceability of food and feed products produced from genetically modified organisms and amending Directive 2001/ 18/EC. *Off. J. Eur. Union* 2003, *L*268, 24-28.  
  
(e) Commission Regulation (EC) 65/2004 establishing a system for the development and assignment of unique identifiers for genetically modified organisms. *Off. J. Eur. Union* 2004, *L*10, 5-10.
- [2] Matsuoka, T.; Kuribara, H.; Takubo, K.; Akiyama, H.; et al. *J. Agric. Food Chem.* 2002, *50*, 2100-2109.
- [3] Anklam, E. *Anal. Chim. Acta.* 1999, *393*, 177-179.
- [4] Quist, D.; Chapela, I. H. *Nature* 2001, *414*, 541.
- [5] Metz, M.; Futterer, J. *Nature* 2002, *416*, 10.
- [6] Mann, C. C. *Science* 2002, *295*, 1617.
- [7] Quist, D.; Chapela, I. H. *Nature* 2002, *416*, 11.
- [8] Meyer, R. *Food Control.* 1999, *10*, 391-399.
- [9] Wurz, A.; Bluth, A.; Zeltz, C.; Pfeifer, C.; Willmund R. *Food Control.* 1999, *10*, 385-389.
- [10] Feriotto, G.; Borgatti, M.; Mischiati, C.; Bianchi, N.; Gambari, R. *J. Agric. Food Chem.* 2002, *50*, 955-962.
- [11] Nielsen, P. -E.; Egholm, M.; Berg, R. -H.; Buchardt, O. *Science* 1991, *254*, 1497-1500.
- [12] Egholm, M.; Buchardt, O.; Christensen, L.; Behrens, C.; Freier, S. -M.; et al. *Nature* 1993, *365*, 566-568.
- [13] Nielsen, P. -E.; Christensen, L. *J. Am. Chem. Soc.* 1996, *118*, 2287-2288.
- [14] Mugweru, A.; Wang, B. -Q.; Rusling, J. *Anal. Chem.* 2004, *76*, 5557-5563.
- [15] Bottomley, L. -A.; Poggi, M. -A.; Shen, S. -X. *Anal. Chem.* 2004, *76*, 5685-5689.

- [16] Ha, T. -H.; Kim, S.; Lim, G.; Kim, K. *Biosens. Bioelectron.* 2004, 20, 378-389.
- [17] [1] Jonsson, U.; Fagerstam, L.; Ivarsson, B.; Johnsson, B.; Karlsson, *Biotechniques* 1991, 11, 620-627.
- [18] Vadgama, P.; Crump, P. W. *Analyst.* 1992, 117, 1657-1670.
- [19] Malmqvist, M. *Nature* 1993, 361, 186-187.
- [20] Ha, T. -H.; Kim, S.; Lim, G.; Kim, K. *Biosens. Bioelectron.* 2004, 20, 378-389.
- [21] Knoll, W. *Ann. Rev. Phys. Chem.* 1998, 49, 565-634.
- [22] Liebermann, T.; Knoll, W.; Sluka, P.; Herrmann, R. *Colloids. Surf. A.* 2000, 169, 337-350.
- [23] Liebermann, T.; Knoll, W. *Colloids. Surf. A.* 2000, 171, 115-130.
- [24] Vasilev, K.; Knoll, W.; Kreiter, M. *J. Chem. Phys.* 2004, 120, 3439-3445.
- [25] Knoll, W.; Liley, M.; Piscevic, D.; Spinke, J.; Tarlov, M. -J. *Adv. Biophys.* 1997, 34, 231-251.
- [26] Germini, A.; Zanetti, A.; Salati, C.; Rossi, S.; Marchelli, R. *J. Agric. Food Chem.* 2004, 52, 3275-3280.
- [27] Germini, A.; Mezzelani, A.; Lesignoli, F.; Corradini, R.; Marchelli, R.; et al. *Agric. Food Chem.* 2004, 52, 4535-4540.
- [28] Yao, D.; Kim, J.; Yu, F.; Nielsen, P. -E.; Sinner, E. -K.; Knoll, W. *Biophys. J.* 2005, 88, 2745-2751.
- [29] Spinke, J.; Liley, M.; Guder, H. -J.; Angermaier, L.; Knoll, W. *Langmuir* 1993, 9, 1821-1825.
- [30] Knoll, W.; Park, H.; Sinner, E. -K.; Yao, D.; Yu, F. *Surf. Sci.* 2004, 570, 30-42.
- [31] Roden, L. -D.; Myszkal, D. -G. *Biochem. Biophys. Res. Commun.* 1996, 225, 1073-1077.
- [32] Mol, N. -J.; Plomp, E.; Fischer, M. -J. -E.; Ruijtenbeek, R. *Anal. Biochem.* 2000, 279, 61-70.
- [33] Morton, T. -A.; Myszkal, D. -G.; Chaiken, I. -M. *Anal. Biochem.* 1995, 227, 176-185.
- [34] Kambhampati, D.; Nielsen P. -E.; Knoll, W. *Biosens. Bioelectron.* 2001, 16, 1109-1118.
- [35] Tawa, K.; Knoll, W. *Nucleic Acids Res.* 2004, 32, 2372-2377.
- [36] O'Donovan, M.C.; Oefner, P.J.; Roberts, S.C.; et al. *Genomics* 1998, 52, 44-49.
- [37] Jones, A.C.; Hoogendoorn, B.; O'Donovan, M.C.; et al. *Am. J. Hum. Genet.* 1999, 65, 1196.
- [38] Zhu, L.; Lee, H.K.; Lin, B.C.; et al. *Electrophoresis* 2001, 22, 3683-3687.

- [39] Stanssens, P.; Zabeau, M.; Meersseman, G.; et al. *Genome Res.* 2004, 14, 126-133.
- [40] Jensen, K. K.; Orum, H.; Nielsen, P. E.; Nordén, B. *Biochemistry* 1997, 36, 5072-5077.
- [41] Dueholm, K. L.; Nielsen, P. E. *New J. Chem.* 1997, 21, 19-31.
- [42] Yu, F.; Yao, D.; Knoll, W. *Nucleic Acids Res.* 2004, 32, e75.
- [43] Kosaganov, Y.-N.; Stetsenko, D. -A.; Lubyako, E. -N.; Kvitko, N. -P.; Lazurkin, Y. -S.; Nielsen, P. -E. *Biochem.* 2000, 39, 11742-11747.
- [44] Tomac, S.; Sarkar, M.; Ratilainen, T.; Wittung, P.; Nielsen, P. -E.; Norden, B. *J Am Chem Soc.* 1996, 118, 5544-5552.
- [45] Tsourkas, A.; Behlke, M. A.; Rose, S. D.; Bao, G. *Nucleic Acids Res.* 2003, 31, 1319-1330.
- [46] Peyret, N.; Seneviratne, P.A.; Allawi, H.T.; SantaLucia, J. *Biochemistry* 1999, 38, 3468-3477.
- [47] Allawi, H.T.; SantaLucia, J. *Nucleic Acids Res.* 1998, 26, 2694-2701.
- [48] Allawi, H.T.; SantaLucia, J. *Biochemistry* 1997, 36, 10581-10594.
- [49] Allawi, H.T.; SantaLucia, J. *Biochemistry* 1998, 37, 9435-9444.
- [50] SantaLucia, J. *Proc. Natl. Acad.* 1998, 95, 1460-1465.
- [51] Mathews, D. H.; Sabina, J.; Zuker, M.; Turner, D. H. *J. Mol. Biol.* 1999, 288, 911-940.
- [52] Luscombe, N. M.; Laskowski, R. A.; Thornton, J. M. *Nucl. Acids Res.* 2001, 29, 2860-2874.
- [53] Todd, A. K.; Adams, A.; Thorpe, J. H.; Denny, W. A.; Wakelin, L. P.; Cardin, C. J. *J. Med. Chem.* 1999, 25, 536-540.
- [54] Liu, J.; Malinina, L.; Huynh-Dinh, T.; Subirana, J. A. *FEBS Letters* 1998, 438, 211-214.
- [55] Gao, Y.; Sriram, M.; Wang, A. H.-J. *Nucl. Acids Res.* 1993, 21, 4093-4101.
- [56] Rulisek, L.; Havlas, Z. *J. Am. Chem. Soc.* 2000, 122, 10428-10439.
- [57] Tereshko, V.; Wilds, C. J.; Minasov, G.; Prakash, T. P.; Maier, M. A.; Howard, A.; et al. *Nucl. Acids Res.* 2001, 29, 1208-1215.
- [58] Vollenhofer, S.; Burg, K.; Schmidt, J.; Kroath, H. *J. Agric. Food Chem.* 1999, 47, 5038-5043.
- [59] Lipp, M.; Anklam, E.; Stave, J. W. *J. AOAC Int.* 2000, 83, 919-927.
- [60] Vollenhofer, S.; Burg, K.; Schmidt, J.; Kroath, H. *Dtsch. Lebensm. Rundsch.* 1999, 95, 275-278.
- [61] Studer, E.; Rhyner, C.; Lüthy, J.; Hübner, P. *Z. Lebensm.-Unters. Forsch.* 1998, 207, 207-213.

- [62] Meyer, R. *Z. Lebensm.-Unters. Forsch.* 1995, 201, 583-586.
- [63] Meyer, R.; Chardonens, F.; Hubner, P.; Luthy, J. *Z. Lebensm.-Unters. Forsch.* 1996, 203, 339-344.
- [64] Hupfer, C.; Hotzel, H.; Sachse, K.; Engel, K. H. *Z. Lebensm.-Unters. Forsch.* 1998, 206, 203-207.
- [65] Hassan-Hauser, C.; Mayer, W.; Hortner, H. *Z. Lebensm.-Unters. Forsch.* 1998, 206, 83-87.
- [66] Vadgama, P.; Crump, P. W. *Analyst* 1992, 117, 1657-1670.
- [67] Yao, D.; Kim, J.; Yu, F.; Nielsen, P. -E.; Sinner, E. -K.; Knoll, W. *Biophys. J.* 2005, 88, 2745-2751.
- [68] Zorn, M.; Gibbons, R.; Sonzogni, W. *Environ. Sci. Technol.* 1999, 33, 2291-2295.
- [69] MacNaught, A. D.; Wiolinson, A. *IUPAC Compendium of Chemical Technology*. 1997, Blackwell Science.
- [70] Yu, F.; Persson, B.; Löfås, S.; Knoll, W. *J. Am. Chem. Soc.* 2004, 126, 8902-8903.
- [71] Myszka, D. G.; Morton, T. A.; Doyle, M. L.; Chaiken, I. M. *Biophys. Chem.* 1997, 6, 127-137.
- [72] Sjölander, S.; Urbaniczky, C. *Anal Chem* 1991, 63, 2338-2345.
- [73] Yao, D.; Tu, F.; Kim, J.; Scholz, J.; Nielsen, P. - E.; Shinner, E. - K.; Konll, W. *Nucleic Acids Research* 2004, 32, No. 22 e177.
- [74] Liebermann, T.; Knoll, W. *Colloids Surf. A.* 2000, 171 115-130.
- [75] Zizlsperger, M.; Knoll, W. *Prog. Colloid Polym. Sci.* 1998, 109, 244-253.
- [76] Hickel, W.; Kamp, D.; Knoll, W. *Nature* 1989, 339, 186-190.
- [77] Hickel, W.; Knoll, W. *Thin Solid Films* 1990, 187, 349-356.
- [78] Binnig, G.; Rohrer, H.; Gerber, Ch. and Weibel, E. *Phys. Rev. Lett.* 1982, 49, 5761.
- [79] Binnig, G.; Quate, CF.; Gerber, Ch. *Phys. Rev. L&t.* 1986, 56, 930-933.
- [80] Millan, K.M.; Mikkelsen, S.R. *Anal. Chem.* 1993, 65, 2317–2323.
- [81] Hashimoto, K.; Ito, K.; Ishimori, Y. *Anal. Chem.* 1994, 66, 3830–3833
- [82] Xu, X.H.; Bard, A.J. *J. Am. Chem. Soc.* 1995, 117, 2627–3631.
- [83] Herne, T.; Tarlov, M.J. *J. Am. Chem. Soc.* 1997, 119, 8916–8920.
- [84] Kanno, T.; Tanaka, H. *Appl. Phys. Lett.* 2001, 77, 3848.
- [85] Huang, E.; Zhou, F.; Deng, L. *Langmuir* 2000, 16, 3272.
- [86] Häußling, L.; Ringsdorf, H.; Schmitt, F.J.; Knoll, W. *Langmnir* 1837, 7, 1991.
- [87] Sagiv, J. *J. Am. Chem. Soc.* 1980, 102, 92.

- [88] Bain, C.D.; Whitesides, G.M. *Adv. Mater.* 1989, 4, 110.
- [89] Muller, W.; Ringsdorf, H.; Rump, E.; Zhang, X.; Angermaier, L.; Knoll, W.; Spinke, J. *J. Biomater. Sci. Polymer, Edn.* 1994, 6, 481.
- [90] Spinke, J.; Liley, M.; Schmitt, F.J.; Guder, H.J.; Angermaier, L.; Knoll, W. *J. Chem. Phys.* 1993, 99, 7012.
- [91] Schmitt, F.J.; Knoll, W. *Biophys. J.* 1991, 60, 716.
- [92] Bain, C. D.; Whitesides, G. M. *J. Am. Chem. Soc.* 1989, 111, 7164.
- [93] Ulman, A.; Evans, S. D.; Shnidman, Y.; Sharma, R.; Eilers, E.; Chang, J. C. *J. Am. Chem. Soc.* 1991, 113, 1499.
- [94] John, P.; Folkers, P. E.; Whitesides, G. M. *J. Phys. Chem.* 1994, 98, 563-571
- [95] Tamada, T.; Hara, M.; Sasabe, H.; Knoll, W. *Langmuir* 1997, 13, 1558-1566.
- [96] Dontha, N.; Nowall, W. B.; Kuhr, W.G. *Anal. Chem.* 1997, 69, 2619–2625.
- [97] Gorton, L.; Lindgren, A.; Larsson, T.; Munteanu, F. D.; Ruzgas, T.; Gazaryan, I. *Anal. Chim. Acta.* 1999, 400, 91–108.
- [98] Weisser, M.; Tovar, G.; Mittler-Neher, S.; et al. *Biosens. Bioelectron.* 1999, 14, 405-411.
- [99] Saenger, W. *Principles of Nucleic Acid Structure* 1984, Springer- Verlag, New York.
- [100] Pohl, E. M.; Jovin, T. M. *J. Mol. Biol.* 1972, 67, 375-396.
- [101] Ivanov, VI.; Minchenkova, L.E.; Schyolkina, A.K.; Pole- tayev, A.I. *Biopolymers* 1973, 12, 89-110.
- [102] Hansma, H.G.; Bezanilla, M.; Zenhausern, F.I; Adrian, M.; Sinsheimer, R.L. *Nucleic Acids Res.* 1993, 21, 505–512.
- [103] Hansma, H.G.; Laney, D.E. *Biophys. J.* 1996, 70, 1933–1939.
- [104] Magonov, S.N.; Elings, V.; Papkov, V.S. *Polymer* 1996, 38, 297–307.



## CHAPTER 6

# SUMMARY

---

Surface plasmon field-enhanced fluorescence spectroscopy (SPFS) uses the enhanced electromagnetic field of a surface plasmon for the excitation of surface-confined fluorophores placed near the metal-dielectric interface. SPFS was used in an in depth study of the hybridization reaction between surface attached probes and fluorescently (Cy5) labelled targets. The rate constants based on a simple Langmuir model for association ( $k_{on}$ ), dissociation ( $k_{off}$ ), and the affinity ( $K_A = k_{on}/k_{off}$ ) for the interaction of probes/targets were determined by using SPFS in hybridization kinetics.

In order to achieve high sensitivity and selectivity, a well-established architecture was used for the sensor surface by applying self-assembly strategies using peptide nucleic acid (PNA) probes on the streptavidin layer as catcher probes *via* the streptavidin/biotin binding. Peptide nucleic acids (PNAs) have attracted great attention as sensing probes for DNA targets owing to the stability of the duplex.

The presented study has clearly demonstrated the influence of the ionic strength on PNA/DNA hybridization on the sensor surface. The ionic strength does not play a dominant role on PNA/DNA hybridization kinetics primarily due to the PNA's neutral backbone in both MM1 and MM0 cases using different lengths of oligonucleotides. However, the fluorescence intensity was affected by the change in distance between the Au-surface and PNA/DNA duplex induced by change of the ionic strength. The ionic strength dependence for DNA target detection was quantified by varying the ionic strength from pure water to 1 M phosphate buffer (PB). A window of maximum fluorescence was found between 10 and 100 mM PB. Furthermore, the discrimination between fully matched and single base mismatched hybridization was accomplished with a significant difference of affinity constant. The best discrimination was achieved using a 11mer PNA.

The kinetics and thermodynamics of the fully matched 11mer PNA/DNA hybrids on the surface was studied over a range of temperature based on the Langmuir adsorption isotherm at equilibrium using the self-assembled sensor matrix. By increasing the temperature, the shifts of the Langmuir adsorption isotherm were observed. The thermodynamic parameters, enthalpy and entropy, for PNA/DNA hybridization on the surface were calculated.

SPFS further permitted a detailed study of surface-mediated hybridization reactions between surface attached PNA probes and genetically modified organism (GMO) targets amplified by polymerase chain reaction (PCR) using a template gene extracted from Round-up Ready<sup>TM</sup> soybean (RR soybean).

In a kinetic analysis, four different experiments were demonstrated. The global analysis was found to be the fastest and most reliable method to determine association rate constants because it probes only the early stages of the binding. The typical titration experiment involves the determination of the Langmuir adsorption isotherm and, hence, the affinity constant  $K_A$  based on the evaluation of surface coverages. By increasing the concentration the occupancy of the probe binding sites, the interface is further charged, resulting in an increasingly significant Coulombic barrier for the hybridization at the sensor surface. The kinetic and equilibrium coverage measurements in the kinetic-titration experiment clearly revealed the influence of the interfacial charging effect. The single kinetic analysis is a rapid approach to compare the duplex formation both fully matched and single base mismatched sequences.

The effect of probe PNAs immobilized on the surface was investigated for better sensing properties. The reliable detection limit of the PCR target and the quantitative kinetic analysis were measured by using the PNA attached sensor surface due to the high sequence specificity and stability of duplex. The limit of detection (LOD) (1.4 pM of PCR target) was found based on PNA/DNA hybridization with high sensitivity and selectivity. Furthermore, 0.01% GMO in mixed PCR targets with 99.99 % impurity could be detected.

Finally, the specific binding of targets by PNA probe on the sensor substrate was characterized by tapping-mode AFM in air. The surface morphology change after hybridization gave a clear demonstration for the presence of bound target DNA to the PNA immobilized surface.

# CHAPTER 7

## SUPPLEMENT

---

### 7.1 Abbreviations

ATR	Attenuated total reflection
bp	Base pairs
Cy5	Cyanine dye
Da	Dalton (g/mol)
DNA	Deoxyribonucleic acid
FRET	Fluorescence resonance energy transfer
GMO	Genetically modified organism
$h$	Planck's constant
HeNe	Helium-Neon
$\vec{k}$	Wave vector
$K_A$	Affinity constant
$k_{on}$	Association rate
$k_{off}$	Dissociation rate
LASFN9	High refractive index glass from Schott
LBL	Layer-by-layer
LOD	Limit of detection
MM0	Complementary match (base pair)
MM1	Single base mismatch (base pair)
n	Refractive index
PCR	Polymerase chain reaction
PBS	Phosphate buffered saline (buffer)
PDMS	Polydimethylsiloxane
PMT	Photo multiplier tube
PNA	Peptide nucleic acid
PSP	Plasmon surface polariton
rpm	Revolutions per minute
RR	Round-up Ready <sup>TM</sup>
RU	Resonance unit
S0, S1	Singlet electronic state of a molecule
SA	Streptavidin
SAM	Self-assembled monolayer
SD	Standard deviation
SERS	Surface enhanced Raman spectroscopy
SPDS	Surface plasmon diffraction sensor
SPFM	Surface plasmon fluorescence microscopy
SPFS	Surface plasmon fluorescence spectroscopy
SP, SPP	Surface plasmon polariton
SPR	Surface plasmon resonance
TE	Transversal electric (s-) polarization
TIR	Total internal reflection
TM	Transversal magnetic (p-) polarization
UV	Ultraviolet

## 7.2 List of Figures

**Figure 1.1.** A typical biosensor consists of a receptor and an electronic device.

**Figure 2.1.** Schematic drawing of total internal reflection and surface plasmon excitation in the Kretschmann geometry.

**Figure 2.2.** Schematic drawing of the charges and the electromagnetic field of surface plasmons.

**Figure 2.3.** Dispersion relation of photons traveling in the prism.

**Figure 2.4.** Dispersion relation of plasmon surface polaritons (PSP) at a metal/dielectric interface before and after the adsorption of an analyte layer.

**Figure 2.5.** Jablonski diagram.

**Figure 2.6.** Fluorescence scan curves and corresponding fluorescence kinetics.

**Figure 2.7.** Fluorescence at the metal/dielectric interface.

**Figure 2.8.** molecular interactions for self-assembly.

**Figure 2.9.** Self-assembled monolayers of alkanethiols on substrate (gold).

**Figure 2.10.** Structures of tetrameric streptavidin and biotin.

**Figure 2.11.** Interactions between streptavidin and biotin.

**Figure 2.12.** A typical kinetic curve of molecular interaction on the surface.

**Figure 2.13.** A typical set of global analysis.

**Figure 2.14.** A typical curve of Langmuir adsorption isotherm taken titration experiment.

**Figure 2.15.** A graphic overview of the steps involved in transcription and translation within the nucleus of the cell.

**Figure 2.16.** The base pairs of G-C and A-T.

**Figure 2.17.** The B form of the DNA helix.

**Figure 2.18.** Structures of double strand of PNA and DNA hybridization.

**Figure 2.19.** Schematic drawing of PCR.

**Figure 3.1.** Schematic draw of the surface plasmon field-enhanced fluorescence spectroscopy.

**Figure 3.2.** Schematic draw of flow cell and sample assembly.

**Figure 3.3.** Schematic draw of flow system for temperature experiment.

**Figure 3.4.** Angular scan curves of the reflectivity R according to the temperature.

**Figure 3.5.** Illustration of the self-assembled sensor matrix.

**Figure 3.6.** Molecular structures of (a) biotinylated thiol and (b) spacer thiol.

**Figure 3.7.** Kinetic SPR curves for each sensor layer.

**Figure 3.8.** SPFS measurement for specific and unspecific binding of DNA target to sensor surface.

**Figure 3.9.** Chemical structure of Cy5.

**Figure 3.10.** Electrophoresis patterns of PCR products in 2% agarose gel.

**Figure 3.11.** UV- vis. absorbance of RR-125.

**Figure 3.12.** A melt-quench protocol to separate double stranded PCR products.

**Figure 4.1.** Illustration of the self-assembled sensor matrix

**Figure 4.2.** Kinetics curves for 3 different PNA immobilizations during injection (black arrow) of biotinylated PNA to streptavidin in phosphate buffer solution.

**Figure 4.3** SPFS measurements for kinetic analysis of the association and dissociation phase.

**Figure 4.4** SPFS measurements for kinetic analysis of the association and dissociation phase (taken at  $\theta = 55.7^\circ$ ) at the surface.

**Figure 4.5** Hybridization kinetics for PNA 11mer (P-11) and DNA 11mer (T-11) at 7 different phosphate buffer solutions.

**Figure 4.6.** (a) Global analysis of PNA/DNA RR-15 hybridization at  $55.7^\circ$  in deionized water.

**Figure 4.7.** Fluorescence intensity of Cy5 labelled DNA in a range of ionic strength.

**Figure 4.8.** Fluorescence intensity vs. target concentration  $c_0$  at different ionic strength.

**Figure 4.9.** Titration curves for PNA (P-RR-11)/DNA (T-RR-11) hybridization at  $20 \pm 0.5^\circ\text{C}$ .

**Figure 4.10.** Titration curves for PNA (P-RR-11)/DNA (T-RR-11) hybridization at  $24 \pm 0.5^\circ\text{C}$ .

**Figure 4.11.** Titration curves for PNA (P-RR-11)/DNA (T-RR-11) hybridization at  $29 \pm 0.5^\circ\text{C}$ .

**Figure 4.12.** Titration curves for PNA (P-RR-11)/DNA (T-RR-11) hybridization at  $32 \pm 0.5^\circ\text{C}$ .

**Figure 4.13.** Temperature effect on the rate constants.

**Figure 4.14.** Normalized semi-logarithmic Langmuir adsorption isotherm curves, surface coverage *versus* concentration  $c_0$  for PNA (11mer)/DNA (11mer) hybridization at different temperature.

**Figure 4.15.** Reversible hybridization event for PNA (11mer)/DNA (11mer) hybridization at different temperature.

**Figure 4.16.** The van't Hoff plot from the titration experiment of the PNA (11mer)/DNA (11mer) hybridization in a range of temperature.

**Figure 5.1.** Illustration of the sensor matrix used in this study.

**Figure 5.2.** Global analysis of the association and dissociation phase of PNA (P-RR-15)/DNA (T-RR-15) hybridization in a solution containing 10 mM phosphate buffer solution.

**Figure 5.3.** Global analysis of PNA (P-RR-15)/DNA (T-RR-15) hybridization at high ionic strength, 137 mM NaCl added 10 mM phosphate buffer solution.

**Figure 5.4.** Titration curves for PNA (P-RR-15)/DNA (T-RR-15) hybridization.

**Figure 5.5.** Fluorescence intensity of the bulk concentration and the Langmuir isotherm.

**Figure 5.6.** Hybridization kinetics for PNA (P-RR-15)/DNA (T-RR-15) (MM0).

**Figure 5.7.** Hybridization kinetics for P-RR-11/T-RR-15, P-RR-13/T-RR-15, and P-RR-15/T-RR-15.

**Figure 5.8.** Hybridization kinetics for P-RR-15/T-RR-15 (MM0), P-RR-mis-15/T-RR-mis-15 (MM0), P-RR-mis-15/T-RR-15 (MM1), and (4) P-RR-15/T-RR-mis-15 (MM1).

**Figure 5.9.** Hybridization kinetics for DNA (D-RR-15)/DNA (T-RR-15) hybridization in 10 mM PB with 137 mM NaCl and DNA (D-RR-15)/DNA (T-RR-15) hybridization in 10 mM PB without NaCl.

**Figure 5.10.** Hybridization kinetics for DNA (D-RR-15)/DNA (T-RR-125) hybridization in 10 mM PB with 137 mM NaCl and DNA (D-RR-15)/DNA (T-RR-125) hybridization in 10 mM PB without NaCl.

**Figure 5.11.** Kinetic-titration curves for P-RR-15/T-RR-125 hybridization.

**Figure 5.12.** Langmuir isotherm for P-RR-15/T-RR-125 hybridization.

**Figure 5.13.** Kinetic-titration curves for P-RR-15/T-RR-169 hybridization.

**Figure 5.14.** Langmuir isotherm for P-RR-15/T-RR-169 hybridization.

**Figure 5.15.** Hybridization kinetics for P-RR-15/T-RR-125 (MM0, MM1)

**Figure 5.16.** Hybridization kinetics for P-RR-11/T-RR-169, P-RR-13/T-RR-169, and P-RR-15/T-RR-169.

**Figure 5.17.** Hybridization kinetics for P-RR-mis-11/T-RR-125, P-RR-mis-13/T-RR-125, and P-RR-mis-15/T-RR-125.

**Figure 5.18.** Limit of detection experiment for PCR target (T-RR-125) on the PNA probe (P-RR-15) in 10 mM PB.

**Figure 5.19.** Double-logarithmic plot of the binding of PCR target (T-RR-125) to the PNA probe (P-RR-15) surface.

**Figure 5.20.** Hybridization kinetics for P-RR-15/Mu-159 and P-RR-15/RR-125.

**Figure 5.21.** Fluorescence intensity upon the injection of mixed PCR targets.

**Figure 5.22.** SPM image of whole PNA probes and SPFM image after hybridization with target PCR (T-RR-125).

**Figure 5.23.** Tapping-mode AFM images of the gold substrates.

**Figure 5.24.** Tapping-mode AFM image of the mixed thiols modified gold substrate.

**Figure 5.25.** Tapping-mode AFM image of the immobilized streptavidin (SA) layer on the mixed SAMs.

**Figure 5.26.** Tapping-mode AFM image of the immobilized PNA probe (P-RR-15) layer on the streptavidin layer.

**Figure 5.27.** Tapping-mode AFM image after hybridization between PNA probe (P-RR-15) and PCR target (T-RR-125).

### 7.3 List of Tables

**Table 1.1** GMO Products: Benefits and Controversies.

**Table 3.1.** The optimized conditions to get desired temperature.

**Table 3.2.** Optical constants and determined thickness of sensor matrix measured by SPR.

**Table 3.3.** The sequences of PNA probes.

**Table 3.4.** Amplification primers.

**Table 3.5.** The sequences of PCRs.

**Table 4.1.** The chemical structures of thiols and the sequences of the PNA probes and DNA targets. <sup>a</sup> Mismatched base is underlined in the sequences of target DNA.

**Table 4.2** Apparent kinetic rate constants and equilibrium constants for MM0 PNA/DNA hybridizations.

**Table 4.3** Apparent kinetic rate constants and equilibrium constants for MM1 PNA/DNA hybridizations.

**Table 4.4** Rate constants and affinity constant for PNA 11mer (P-11) and DNA 11mer (T-11) hybridizations in different phosphate buffer solutions.

**Table 5.1.** The sequences of the probes and targets used in this study.

**Table 5.2.** Rate constants obtained by the single kinetic analysis (Figure 5.7).

**Table 5.3.** Rate constants obtained by the single kinetic analysis (Figure 5.8).

**Table 5.4.** Rate constants obtained by the kinetic-titration analysis for P-RR-15/T-RR-125.

**Table 5.5.** Rate constants obtained by the kinetic-titration analysis for PNA/DNA RR-125.

**Table 5.6.** Rate constants obtained by the single kinetic analysis (Figure 5.16).

**Table 5.7.** Rate constants obtained by the single kinetic analysis (Figure 5.17).

---

# CURRICULUM VITAE

---

## PERSONAL DATA

**Name:** 박혜영, Hyeyoung Park

**Date of Birth:** June 15, 1976

**Nationality:** Republic of Korea

## EDUCATION

**Ph. D (Nov. 2002 ~ Sep. 2005)**

Physical chemistry,

Mainz University, Max-Planck-Institute for Polymer Research, Mainz, Germany

**Master Degree (Mar. 1999 ~ Feb. 2001)**

Physical chemistry,

Hanyang University, Seoul, Korea

**Bachelor Degree (Mar. 1995 ~ Feb. 1999)**

Chemistry,

Kookmin University, Seoul, Korea

## PUBLICATIONS

1. **H. Park**, A. Germini, S. Sforza, R. Corradini, R. Marchelli, and W. Knoll, "The effect of ionic strength on PNA-DNA hybridization", *in preparation*.
2. **H. Park**, A. Germini, S. Sforza, R. Corradini, R. Marchelli, and W. Knoll, "Kinetic and affinity analysis of hybridization reactions between PNA probes and DNA targets using surface plasmon field-enhanced fluorescence spectroscopy (SPFS)", *Anal. chem.* **2005**, *Submitted*.
3. J. O. Kim, W. Shin, **H. Park**, H. Lee, "Effect of contact potential barrier of organic resists on atomic force microscope anodization lithography", *Colloid Surf. A-Physicochem. Eng. Asp.* **257**, 251-258, **2005**.
4. W. Knoll, **H. Park**, E.K. Sinner, D.F. Yao, and F. Yu, "Supramolecular interfacial architectures for optical biosensing with surface plasmons", *Surf. Sci.* **570**, 30-42, **2004**.
5. H.-J. Lee, **H. Park**, S. Koo and H. Lee, "Vertical alignments of single-walled carbon nanotubes on chemically functionalized silicon substrates", *MRS, Proc.* **739**, 199-204, **2003**.
6. **H. Park**, E. Kim, and H. Lee, "Synthesis of metal-azo dyes and their optical and thermal properties as recording materials for DVD-R", *Bull. Chem. Soc. Jpn.*, **75**, 2067-2070, **2002**.

## PRESENTATIONS

1. **H. Park**, A. Germini, S. Sforza, R. Corradini, R. Marchelli, and W. Knoll, "Detection of DNA amplicons and kinetics of PNA/DNA hybridization in buffer of different ionic strength by using surface plasmon optical techniques", *229<sup>th</sup> American Chemical Society National Meeting & Exposition*, San Diego, USA, **2005**.
  2. **H. Park**, A. Germini, S. Sforza, R. Corradini, R. Marchelli, and W. Knoll, "Detection of DNA amplicons and kinetics of PNA/DNA hybridization in buffer of different ionic strength by using surface plasmon optical techniques", *The Eighth World Congress on Biosensors*, Granada, Spain, **2004**.
-



- 
3. **H. Park**, and W. Knoll, "Kinetic analysis of hybridization between PNA and DNA using surface plasmon field-enhanced fluorescence spectroscopy", *MTB Joint Seminar*, Twente, Netherlands, Nov. **2004**.
  4. **H. Park**, and W. Knoll, "Supramolecular Interfacial Architectures for Optical Biosensing with Surface Plasmons", *30<sup>th</sup> anniversary conference of KSEAUK*, London, England, Sep. **2004**.
  5. **H. Park**, and W. Knoll, "Hybridization kinetics between PNA and DNA on the sensor surface", *Zürich-Mainz Joint Seminar*, Zürich, Switzerland, Aug. **2004**.
  6. **H. Park**, and W. Knoll, "Detection of DNA amplicons by PNA/DNA hybridization using surface plasmon field-enhanced fluorescence spectroscopy (SPFS)", *5th MPIP-CPI Joint Workshop*, Freiburg, Germany, Apr. **2004**.
  7. **H. Park**, and H. Lee, "The structural effects of organic films for nano-lithography by AFM on Si wafers", *30<sup>th</sup> anniversary conference of Vekni, Geseke*, Germany, sep. **2003**.

## **PATENTS**

1. **H. Park** and H. Lee, "Preparing ultra thin organic and polymer films by spin-coating method", *USA Patent*, 6716563, **2004**.
  2. **H. Park** and H. Lee, "Azo dyes and azo-metal complexes for atomic force microscope lithography", *Korea Patent*, 10-2002-0027428, **2002**.
  3. **H. Park** and H. Lee, "Synthesis of azo dyes and metal complexes", *Korea Patent*, 10-2001-0006879, **2001**.
  4. **H. Park** and H. Lee, "Synthesis of azo dyes containing heterocycle and metal complexes", *Korea Patent*, 10-2001-0006880, **2001**.
-